



# Backscatter Signal Analysis of Small-Footprint Full-Waveform Lidar Data

DISSERTATION

zur Erlangung des akademischen Grades eines

**Doktors der technischen Wissenschaften**  
**(Dr. techn.)**

eingereicht von

**Dipl.-Ing. Andreas Roncat**

Matrikelnummer 0025743

Forschungsgruppen Photogrammetrie und Fernerkundung  
Department für Geodäsie und Geoinformation  
Technische Universität Wien

Betreuung: Univ.-Prof. Dipl.-Ing. Dr.techn. Norbert Pfeifer

Diese Dissertation haben begutachtet:

---

Univ.-Prof. Dr.techn. Norbert Pfeifer

---

Univ.-Prof. Dr.-Ing. Uwe Stilla  
(TU München)

Wien, 24.07.2014

---

Dipl.-Ing. Andreas Roncat

# Backscatter Signal Analysis of Small-Footprint Full-Waveform Lidar Data

DISSERTATION

submitted in partial fulfillment of the requirements for the degree of

**Doktor der technischen Wissenschaften  
(Dr. techn.)**

by

**Dipl.-Ing. Andreas Roncat**

Registration Number 0025743

Research Groups Photogrammetry and Remote Sensing  
Department of Geodesy und Geoinformation  
Vienna University of Technology

Advisor: Univ.-Prof. Dipl.-Ing. Dr.techn. Norbert Pfeifer

The dissertation has been reviewed by:

---

Univ.-Prof. Dr.techn. Norbert Pfeifer

---

Univ.-Prof. Dr.-Ing. Uwe Stilla  
(TU München)

Wien, 24.07.2014

---

Dipl.-Ing. Andreas Roncat

# Erklärung zur Verfassung der Arbeit

## Author's Statement

Dipl.-Ing. Andreas Roncat  
Sperrgasse 14, 1150 Wien

Hiermit erkläre ich, dass ich diese Arbeit selbstständig verfasst habe, dass ich die verwendeten Quellen und Hilfsmittel vollständig angegeben habe und dass ich die Stellen der Arbeit – einschließlich Tabellen, Karten und Abbildungen –, die anderen Werken oder dem Internet im Wortlaut oder dem Sinn nach entnommen sind, auf jeden Fall unter Angabe der Quelle als Entlehnung kenntlich gemacht habe.

I hereby declare, that I independently drafted this manuscript, that all sources and references used are correctly cited and that the respective parts of this manuscript—including tables, maps and figures—which were included from other manuscripts or the internet, either semantically or syntactically, are made clearly evident in the text and all respective sources are correctly cited.

---

(Ort, Datum)

---

(Unterschrift Verfasser)

# Acknowledgements

First and foremost, I want to express the thanks to my supervisor Norbert Pfeifer for his support, his advices and guidance in the progress of this thesis. Then, I want to thank Uwe Stilla for providing the second review. Thanks also go to . . .

- . . . the many dear colleagues at the Research Groups Photogrammetry and Remote Sensing, formerly IPF, especially to Wolfgang Wagner and Thomas Melzer who introduced me to the field of full-waveform lidar
- . . . my current and former office mates: Marieke Geiger, Ana Djuricic, Jianzhong Zhang, Balázs Székely and Sajid Ghuffar who were exerted and successful in making room CB0306 a pleasant area for spending the working hours productively
- . . . my PhD “fellow sufferers” Werner Mücke and Clemens Nothegger not only but also for sharing their experiences during the progress of our theses
- . . . the experts in both lidar theory and practice from RIEGL Laser Measurement Systems with whom I spent many hours of interesting discussions, especially to Andreas Ullrich, Martin Pfennigbauer, Roland Schwarz and Nikolaus Studnicka
- . . . my co-authors of the papers finally leading to this thesis, in particular to Gunther Bergauer for giving the key-advice to work with uniform B-splines and for his consecutive mathematical support
- . . . Josef Jansa for his competent advice, his abundance of patience and his ability to transform a high-level scientific discussion into a punchline and the other way round
- . . . Sabine Gruber and Adnan Marvillo for proof-reading the manuscript
- . . . and last but not least to my family and friends for their support.

This thesis was to a large part funded by a Karl Neumaier PhD scholarship. I want to express my thanks to the funding committee in general and in particular to its long-time member Hellmuth Stachel, emeritus full professor of geometry at Vienna University of Technology. I additionally owe him a number of very illuminative insights when attending his equally interesting and elaborate lectures.



*„Ich hab’ ja gleich gewusst, dass Sie  
das interessieren wird.“*

*“I have known from the start you  
would be interested in this topic.”*

To the memory of

**Karl Kraus**

1939–2006

Professor of Photogrammetry  
at Vienna University of Technology  
from 1974 to 2006

# Kurzfassung

Dreidimensionale topographische Information für ausgedehnte Gebiete in hoher räumlicher Auflösung erreicht ein ständig steigendes Interesse in verschiedenen wissenschaftlichen Disziplinen und Anwendungsgebieten. Eine bedeutende Rolle kommt der direkt gewonnenen 3D-Information zu. Dieser Begriff bezieht sich auf die direkte Bestimmung von polaren 3D-Koordinaten, von denen eine die Entfernung zwischen Sensor und Objektoberfläche ist. Diese Dissertation beschäftigt sich mit einer Datenerfassungsmethode, die sowohl eine genaue Entfernungsbestimmung wie auch die Ableitung physikalischer Objektattribute erlaubt; dies wird durch die Aufzeichnung einer abgetasteten Wellenform eines ausgesandten Laserpulses und seiner Echos ermöglicht, die von einer gescannten Oberfläche stammen. Diese Methode wird daher Full-Waveform-Laserscanning oder auch Full-Waveform-Lidar genannt.

Mathematisch betrachtet ergibt sich das Echosignal im Wesentlichen aus einer Faltung, d.h. aus einem gleitenden Integral der Wellenform des ausgesandten Laserpulses multipliziert mit einer charakteristischen Funktion der vom Laserstrahl beleuchteten Objektoberfläche. Diese Funktion wird differentieller Rückstreuquerschnitt genannt und mit  $\sigma'(R)$  bezeichnet; seine Einheit ist m. Die Rekonstruktion des differentiellen Rückstreuquerschnittes mit Hilfe einer Rückfaltung bildet einen wesentlichen Teil dieser Arbeit, wobei eine Rückfaltungsmethode auf der Basis uniformer B-Splines besondere Berücksichtigung findet. Ist der differentielle Rückstreuquerschnitt bekannt, so können weitere physikalische Parameter der gescannten Oberfläche ermittelt werden: Integration liefert den Rückstreuquerschnitt  $\sigma[\text{m}^2]$ , durch Berücksichtigung der Entfernung  $R$  und des Einfallswinkels  $\vartheta$  können ein dimensionsloser Rückstreuoeffizient  $\gamma$  und, bei Vorliegen eines diffusen Reflexionsverhaltens der Oberfläche, ein Reflektivitätswert  $\rho_d$  ermittelt werden.

In dieser Dissertation werden die Möglichkeiten und Grenzen der Signalverarbeitung von Full-Waveform-Daten aufgezeigt, wofür theoretische Ableitungen, simulierte und tatsächliche Scandaten zum Einsatz kommen. Die Simulationen wurden für verschiedene Oberflächengeometrien erstellt, nämlich für Ebenen, parallele Halbebenen, Kugel-, Zylinder- und sinusoidale Oberflächen. Zusätzlich wurden zwei verschiedene Leistungsverteilungen im Laserstrahl untersucht; eine uniforme Verteilung, die im Nahfeld angenommen werden kann, sowie eine Gauß-förmige Verteilung, die näherungsweise im Fernfeld gilt.

Das Beispiel der parallelen Halbebenen erlaubt es, theoretische Grenzwerte für deren Trennbarkeit in den Full-Waveform-Signalen abzuleiten, sowohl für den differentiellen Rückstreuquerschnitt wie auch für das Echosignal. Daten aus mehreren ausgedehnten Lidar-Flugkampagnen wurden verwendet, um die Möglichkeiten der in dieser Arbeit vorgestellten Ansätze zu analysieren. Diese Datensätze ergaben übereinstimmend eine empirische Rechtfertigung dafür, jeden einzelnen ausgesandten Laserpuls in die Analyse miteinzubeziehen; sei es durch eine einfache radiometrische Korrektur mittels Amplitudennormalisierung oder aber die weitestgehende Eliminierung der Form dieses Pulses aus dem Antwortsignal durch Rückfaltung. Weiters konnte gezeigt werden, dass die Verwertung statistischer Momente aus dem zeitlichen Verlauf des differentiellen Rückstreuquerschnittes eine verbesserte Klassifizierung der gescannten Oberflächen ermöglichen könnte.

# Abstract

Three-dimensional topographic information in high spatial resolution for extended areas has gained steadily increasing interest in a number of scientific disciplines and applications. Within this field directly retrieved 3D data play a significant role. The term refers to the direct determination of 3D polar coordinates, one of them being the range (distance) from the sensor to the target surface. This thesis is dedicated to a data acquisition technique where both sophisticated ranging and derivation of physically meaningful object attributes are enabled by recording sampled copies of an emitted laser pulse and of its reflections from the scanned surfaces; this technique is therefore known as full-waveform laser scanning or full-waveform lidar.

In terms of mathematics, the return signals are substantially formed by a convolution (sliding integral) of the outgoing laser pulse's temporal profile and of a characteristic function for the surface illuminated by the laser pulse. This characteristic function is referred to as differential backscatter cross-section  $\sigma'(R)$  [m]; its reconstruction by means of deconvolution forms the core part of this thesis. Special emphasis is given to a deconvolution approach based on uniform B-splines. The knowledge of the differential backscatter cross-section of a target enables for calculating further physical target attributes: integration results in the backscatter cross-section  $\sigma$  [m<sup>2</sup>], correction for the range  $R$  and the local incidence angle  $\vartheta$  allow for the calculation of a dimensionless backscatter coefficient  $\gamma$  and—if diffuse reflectance behaviour of the target surface can be assumed—of a reflectance value  $\rho_d$ .

In this study the possibilities and limitations of signal processing of full-waveform lidar data are presented by means of theoretical derivations, simulated examples and real-world data sets. Simulations are provided for different target geometries, i.e. extended planes, parallel half-planes, spheres, cylinders and sinusoidal surfaces. Additionally, two different power density distributions within the laser footprint are simulated: a uniform distribution is used to represent the near field while a Gaussian distribution is used to represent the far field.

For the case of parallel half-planes, theoretical limits for their separability in the lidar return signal and in the differential backscatter cross-section are derived and presented. Data from multiple extended airborne lidar campaigns are analysed in order to assess



the performance of the presented approaches. These datasets give empirical justification for considering every emitted laser pulse in the full-waveform analysis: while some instabilities of the emitted laser power per pulse can be eliminated by amplitude normalization, deconvolution allows for decreasing the pulse's influence on the return signal at the highest possible level. It is additionally shown that the exploitation of statistical moments in the reconstructed differential backscatter cross-section curve may give valuable input to enhanced surface classification.

# Contents

Erklärung/Author's Statement . . . . .	i
Acknowledgements . . . . .	ii
Kurzfassung . . . . .	iv
Abstract . . . . .	vi
<b>Main Part</b>	<b>1</b>
<b>1 Introduction</b>	<b>1</b>
1.1 Lidar/Laser Scanning . . . . .	1
1.2 Airborne Laser Scanning . . . . .	4
1.3 Full-Waveform Laser Scanning . . . . .	5
1.4 Aim of this Thesis . . . . .	8
1.5 Structure of this Thesis . . . . .	9
<b>2 Physical Foundations of Full-Waveform Lidar</b>	<b>12</b>
2.1 The Radar Equation . . . . .	12
2.2 Lambertian Scattering . . . . .	17
2.3 Notes on the Geometry of the Laser Beam . . . . .	21
2.4 Forward Modeling of Full-Waveform Return Signals . . . . .	26
2.4.1 Related Work . . . . .	26
2.4.2 Alternative Approach for forward Modeling . . . . .	27
<b>3 Analysis of Full-Waveform Return Signals</b>	<b>30</b>
3.1 Approaches without Deconvolution . . . . .	30
3.1.1 Related Work . . . . .	30
3.1.1.1 Classical Detectors . . . . .	31
3.1.1.2 Finite-Mixture Model . . . . .	33
3.1.2 Own Contribution . . . . .	37
3.1.2.1 The Averaged Square Difference Function (ASDF) . . . . .	37
3.1.2.2 Derivation of Echo Parameters from the ASDF . . . . .	39
3.2 Approaches including Deconvolution . . . . .	39
3.2.1 Related Work . . . . .	40
3.2.1.1 Gaussian Decomposition . . . . .	40

3.2.1.2	Wiener Filter Deconvolution . . . . .	42
3.2.1.3	Expectation/Maximization Deconvolution . . . . .	44
3.2.2	Own Contribution: Deconvolution by Means of uniform B-Splines . . . . .	45
3.2.2.1	B-Spline Curves . . . . .	46
3.2.2.2	Deconvolution of B-Spline Curves . . . . .	46
3.3	Radiometric Calibration of Full-Waveform Lidar Data . . . . .	50
3.3.1	Theory and related Work . . . . .	50
3.3.1.1	Determination of the Calibration Constant . . . . .	52
3.3.1.2	Estimation of local normal Vectors in a Point Cloud . . . . .	53
3.3.2	Own Contribution . . . . .	54
3.3.2.1	Impact of the Instability of the System Waveform . . . . .	54
3.3.2.2	Extension of radiometric Calibration to uniform B-Splines . . . . .	59
3.3.2.3	Derivation of radiometrically calibrated Target Parameters by Means of statistical Moments . . . . .	63
<b>4</b>	<b>Numerical Examples</b>	<b>66</b>
4.1	Examples for forward Modeling of Lidar Return Waveforms . . . . .	66
4.1.1	Simulated dBCS for planar Targets . . . . .	68
4.1.2	Simulated dBCS for spherical Targets . . . . .	74
4.1.3	Simulated dBCS for cylindrical Targets . . . . .	75
4.1.4	Simulated dBCS for sinusoidal Targets . . . . .	76
4.1.5	Simulated total BCS . . . . .	78
4.1.6	Simulated recorded Echo Waveforms $P_r(t)$ . . . . .	81
4.2	Examples for Range Extraction using ASDF . . . . .	93
4.3	Examples concerning the Stability of System Waveforms and their Impact on radiometric Calibration . . . . .	96
4.4	Examples for Deconvolution based on uniform B-Splines . . . . .	103
4.4.1	Deconvolution of synthetic Data . . . . .	104
4.4.2	Deconvolution of Real-World Data . . . . .	110
4.4.3	Comparison to Gaussian Decomposition . . . . .	112
4.5	Examples for radiometric Calibration of B-spline-based Deconvolution . . . . .	116
4.6	Examples for Target Feature Extraction based on radiometric Calibration . . . . .	118
<b>5</b>	<b>Results and Discussion</b>	<b>122</b>
<b>6</b>	<b>Conclusion and Outlook</b>	<b>126</b>
<b>Appendix</b>		<b>128</b>
<b>A</b>	<b>Convolution in Time Domain</b>	<b>128</b>
A.1	Construction of uniform B-Splines by repetitive Convolution . . . . .	132
A.2	Convolution of Gaussian Distributions and Functions . . . . .	134

<b>B</b>	<b>The Convolution Theorem</b>	<b>137</b>
<b>C</b>	<b>Examples of dBCS Synthesis in Detail</b>	<b>139</b>
C.1	Simulated dBCS for extended planar Targets . . . . .	139
C.2	Simulated dBCS for parallel planar Targets with Offsets . . . . .	141
C.3	Simulated dBCS for spherical Targets . . . . .	146
C.4	Simulated dBCS for cylindrical Targets . . . . .	153
C.5	Simulated dBCS for sinusoidal Targets . . . . .	160
C.5.1	Circular Wavefronts . . . . .	160
C.5.2	Parallel Wavefronts . . . . .	166
<b>D</b>	<b>Examples for simulated recorded Echo Waveforms in Detail</b>	<b>190</b>
D.1	Simulated recorded Echo Waveforms for planar Targets . . . . .	190
D.2	Simulated recorded Echo Waveforms for spherical Targets . . . . .	192
D.3	Simulated recorded Echo Waveforms for cylindrical Targets . . . . .	193
D.4	Simulated recorded Echo Waveforms for sinusoidal Targets . . . . .	194
	<b>References</b>	<b>199</b>
	<b>Bibliography</b>	<b>199</b>
	<b>WWW References</b>	<b>208</b>

# Introduction

The past years have seen an increasing demand as well as an increasing availability of three-dimensional topographic data in high spatial resolution. Lidar, an active three-dimensional remote sensing technique, is one of the leading techniques for gathering such data. Additionally to the geometric content of lidar data, special lidar systems allow for the extraction of physical information, too. The most detailed geometric and physical information in lidar is retrieved by the analysis of backscattered full-waveform lidar signals. This analysis is the main focus of this thesis.

This introductory chapter starts with describing the principles of lidar in Section 1.1. From the general perspective on lidar, the topic is narrowed down to airborne lidar in Section 1.2 and more specifically to full-waveform lidar in Section 1.3. Aim and structure of this thesis are presented in Sections 1.4 and 1.5, resp.

## 1.1 Lidar/Laser Scanning

The term *lidar* is an acronym for *light detection and ranging* and characterizes an active remote sensing technique. Synonyms for lidar are e.g. laser scanning, laser ranging, ladar (*laser detection and ranging*) and laser radar [Shan and Toth 2008; Wagner et al. 2006]. We will use the terms lidar and laser scanning synonymously in the subsequent text.

The primary output of lidar measurements are three-dimensional point clouds of scanned surfaces. At very close distances up to approx. 2 m, the point coordinates may be retrieved by triangulation. For longer distances, direct determination of the distance (range) is needed. This is performed by measuring the round-trip time of the transmitted laser signal. Such a signal may either be a continuous laser wave or a short laser pulse with a temporal length in the magnitude of a nanosecond [Beraldin et al. 2010].

Besides the ranging principle, laser scanning systems are also categorized by their platform carrier [Ullrich and Pfennigbauer 2011]:

**Airborne Laser Scanning (ALS):** The platform is an aircraft.

**Terrestrial Laser Scanning (TLS):** The platform is commonly a tripod or a pillar, comparable to classical geodetic measurements.

**Mobile Laser Scanning (MLS):** The platform is a ground-based vehicle such as a car or a boat.

Three-dimensional point clouds from laser scanning measurements are retrieved as follows:

**1<sup>st</sup> dimension:** A short laser pulse or a continuous wave is emitted, deflected by a mirror, reflected by the target surface, and the round-trip time of the pulse's or wave's echo is determined. Multiplication with the group velocity of the laser (approx. the speed of light) gives the distance of the target along the path of the transmitted laser ray.

**2<sup>nd</sup> dimension:** For every transmitted pulse/wave, the rotation of the mirror changes.

**3<sup>rd</sup> dimension:** In case of ALS and MLS: the carrying vehicle moves along a path; in case of TLS: a second rotation mechanism enables for changing the attitude of the deflection mechanism.

Common laser wavelengths used in laser scanning are in the visible and near-infrared spectrum, e.g. 532 nm, 905 nm, 1064 nm and 1550 nm, depending on the purpose of the laser scanning campaign. While for topographic use, a wavelength in the near infrared is favourable, green laser light (532 nm) can penetrate the water column and is therefore favourable for hydrographic purposes [Irish and Lillycrop 1999; Mandlbürger et al. 2011]. An overview is given in Figure 1.1.

Furthermore, also within the range of near infrared, the reflectance of materials may vary significantly, as shown in Figure 1.2. See e.g. the huge decay in the reflectance of snow from 1064 nm to 1550 nm.

The following section, as the rest of this thesis, is dedicated to ALS.

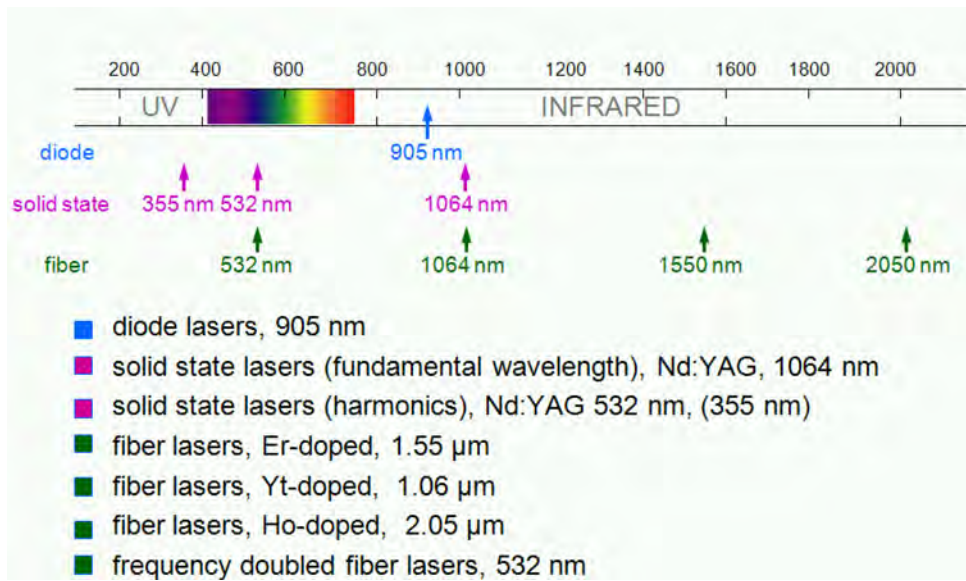


Figure 1.1: Typical laser wavelengths for lidar instruments [Pfennigbauer and Ullrich 2011].

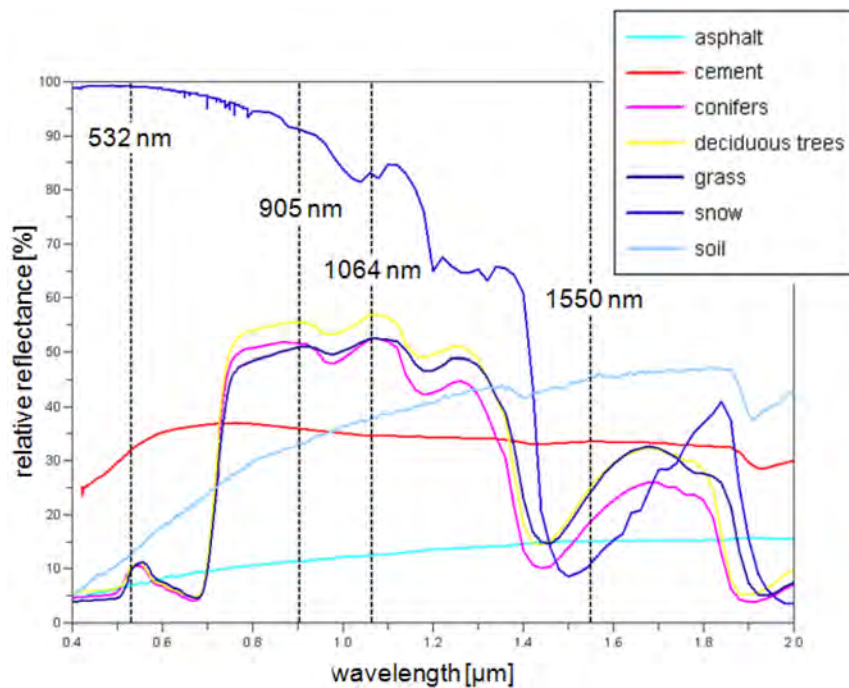
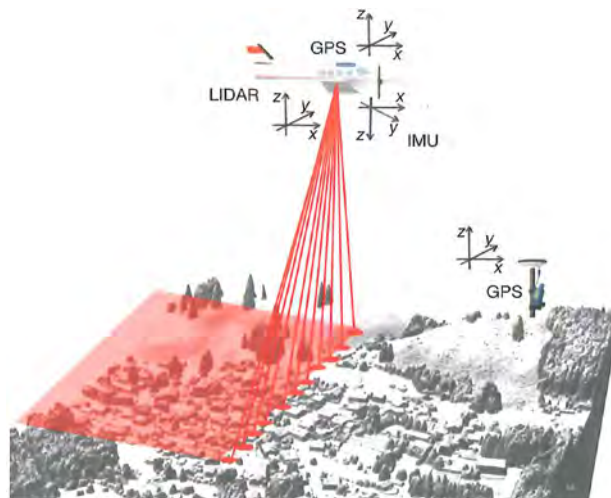


Figure 1.2: Reflectance values of selected vegetation types and materials in the visible and near-infrared spectrum [Pfennigbauer and Ullrich 2011].

## 1.2 Airborne Laser Scanning

In the past twenty years, ALS has played a dominant role in the retrieval of high-resolution three-dimensional topographic data over large areas. The products of ALS campaigns, from the raw three-dimensional point clouds to subsequently derived digital models, have been in use in a lot of scientific fields and applications, among them hydrology [Cobby et al. 2001; Mandlburger et al. 2009], archaeology [Doneus et al. 2008], forestry [Næsset and Gobakken 2005], geomorphology [Höfle and Rutzinger 2011], 3D city modeling [Dorninger and Pfeifer 2008; Zhou et al. 2004], detection and reconstruction of power lines [Ritter and Bengler 2012].

ALS data are acquired strip-wise (see Figure 1.3) with the aircraft's flight trajectories being typically nearly parallel to each other. The scanned areas per strip normally show some overlap. On the one hand, this gives a higher point density in such areas, allowing for a more detailed and accurate reconstruction of the scanned surface. On the other hand, it additionally allows for a geometric quality check in form of calculation and removal of height differences between overlapping strips. For this task, various strip adjustment techniques have been developed [e.g. Habib et al. 2009; Kager 2004; Ressler et al. 2011].



**Figure 1.3:** Schematic illustration of ALS data acquisition [Beraldin et al. 2010].

Besides the categorization of lidar systems according to their ranging principle or their carrier platform, several other criteria may be applied which are summarized in Figure 1.4. The focus in this thesis is on pulsed, monostatic lidar systems recording time and amplitude applying a multi-photon detection mechanism, as indicated by the gray-hatched blocks in this figure.



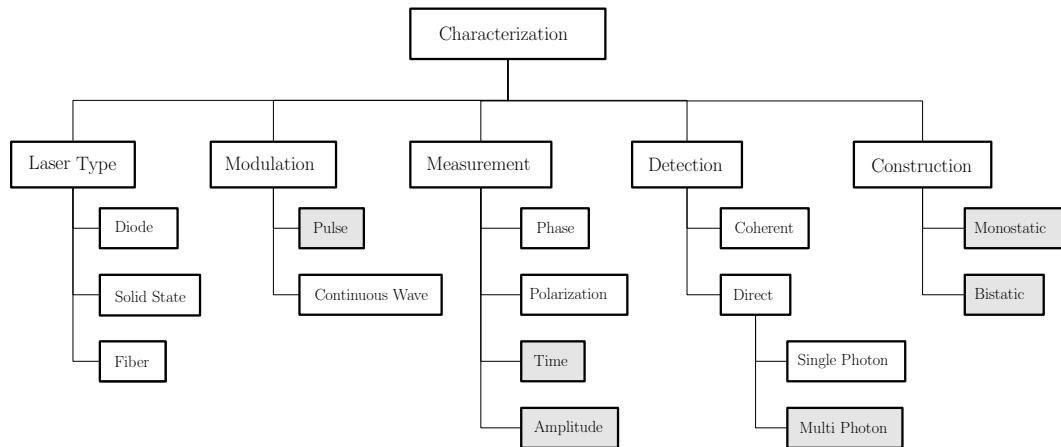


**Figure 1.4:** Characterization of laser ranging systems (adapted from [Stilla and Jutzi 2008] and [Pfennigbauer and Ullrich 2011]). The gray-hatched blocks denote the configurations focused on in this thesis. Strictly speaking, we deal with bistatic systems. However, in the case of airborne systems, the distance between emitter and receiver optics is very small in comparison to the ranges to the targets. Thus, this case is also treated as monostatic configuration.

If these time and amplitude recordings are sampled in a high frequency in the order of 1 ns, one speaks of (full-)waveform lidar [Mallet and Bretar 2009]. This configuration will be the focus of the next section and of the rest of this text.

### 1.3 Full-Waveform Laser Scanning

The term Full-Waveform (FWF) refers to the case where all samples of both the emitted pulse and all of its echoes are recorded [Ullrich and Pfennigbauer 2011], which is the type of laser scanning data we are going to deal with in this thesis. An example for such sampled waveforms, as retrieved by a Riegl LMS-Q560 system [Riegl LMS 2014], is shown in Figure 1.5.

The following instrument parameters are of special interest in FWF lidar [Beraldin et al. 2010; Hollaus et al. 2014]:

**Pulse length:** The length of the emitted laser pulse is a limiting factor for the discrimination of two subsequent echoes (see Sections 2.1 and 4.1.1).

**Sampling interval:** According to the sampling theorem, this quantity determines the highest frequency which can still be reconstructed from the recorded signal. Together with the pulse length, it also influences the ranging accuracy.

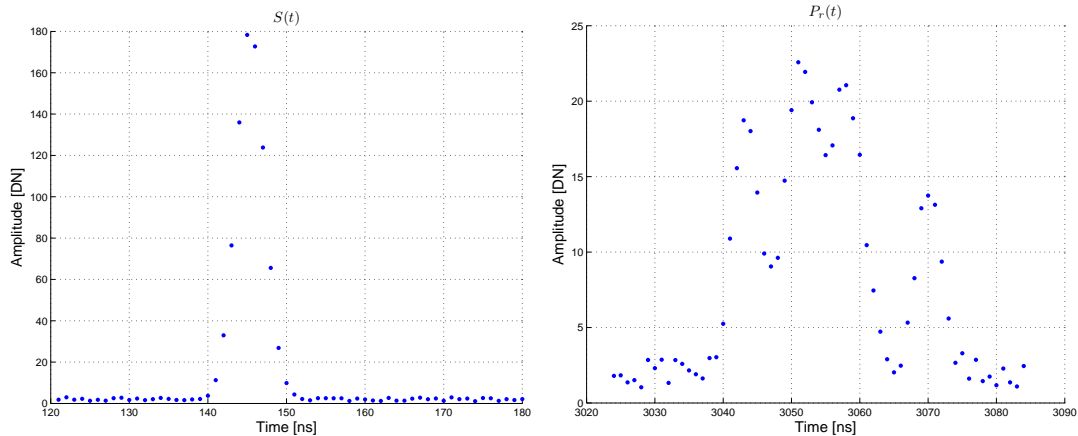


**Figure 1.5:** Waveform samples representing the transmitted laser pulse (left) and its echoes (right).

**Beam width:** The laser beam is considered as circular cone of opening angle  $\beta_t$ . This  $\beta_t$  commonly refers to the angle where the power density has fallen to  $1/e^2$  of the maximum power density [cf. [ISO 2006](#)].

**Bit depth of amplitude recording:** besides constraining the detection of weak echoes, it mainly affects the resolved radiometric details of radiometric calibration.

**Laser wavelength:** This applies mainly to radiometric calibration using natural targets or reflectivity assumptions in homogeneous areas (see [Section 3.3](#)).

Table [1.1](#) lists the system parameters of currently available FWF airborne lidar systems [[Hollaus et al. 2014](#)]. Further types of laser scanning data closely related to FWF data are [[Ullrich and Pfennigbauer 2011](#)]:

**Echo-Waveform Data:** The samples of all echo waveforms are recorded.

**Tightly-coupled echo signal samples:** Selectable echo-signal samples are recorded.

**Loosely-coupled echo signal samples:** Only some echo samples per shot are recorded.

**Online-processed waveform data:** Neither pulse samples nor echo samples are stored but the target range and echo features are calculated in real-time from the waveforms.

Besides using a single laser wavelength at once, there exist approaches for multi-wavelength lidar and hyperspectral lidar. While the first refers to sensors operating at two or

Manufacturer	Model	Scanning mode	Max. PRR	Max. scan angle	Mult. pulses	Max. range
AHAB	Chiroptera	Palmer scan	400 kHz	$\pm 20^\circ$	yes	1500 m
Leica Geosystems	ALS60	Osc. mirror	200 kHz	$\pm 37.5^\circ$	yes	6300 m
	ALS70 CM	Osc./rot. mirror	120 kHz	$\pm 37.5^\circ$	yes	1850 m
	ALS70 HP	Osc./rot. mirror	120 kHz	$\pm 37.5^\circ$	yes	4400 m
	ALS70 HA	Osc./rot. mirror	120 kHz	$\pm 37.5^\circ$	yes	6300 m
	Optech	Aquarius	Osc. mirror	70 kHz	$\pm 25^\circ$	no
Gemini		Osc. mirror	125 kHz	$\pm 25^\circ$	yes	4000 m
Orion		Osc. mirror	125 kHz	$\pm 30^\circ$	yes	4000 m
Pegasus		Osc. mirror	125 kHz	$\pm 32.5^\circ$	yes	2500 m
Riegl LMS	Q680i	Rot. pyramid	400 kHz	$\pm 30^\circ$	yes	3000 m
	Q780	Rot. pyramid	400 kHz	$\pm 30^\circ$	yes	5400 m

Manufacturer	Model	Pulse length	Sampl. interval	Beam width	Bit depth	Wavelength
AHAB	Chiroptera	$4 \pm 1$ ns	0.55 ns	0.55 mrad	N/A	$1 \mu\text{m}$
Leica Geosystems	ALS60	5 ns	1 ns	0.22 mrad	8 bit	1064 nm
	ALS70 CM	N/A	1 ns	0.22 mrad	8 bit	1064 nm
	ALS70 HP	N/A	1 ns	0.22 mrad	8 bit	1064 nm
	ALS70 HA	N/A	1 ns	0.22 mrad	8 bit	1064 nm
	Optech	Aquarius	N/A	1 ns	N/A	12 bit
Gemini		N/A	1 ns	0.35 mrad	12 bit	1064 nm
Orion		N/A	1 ns	0.35 mrad	12 bit	1064 nm
				1.13 mrad		1541 nm
Riegl LMS	Pegasus	N/A	1 ns	0.28 mrad	12 bit	1064 nm
	Q680i	4 ns	1 ns	$\leq 0.5$ mrad	$2 \times 8$ bit	1550 nm
	Q780	4 ns	1 ns	$\leq 0.5$ mrad	$2 \times 8$ bit	1550 nm

**Table 1.1:** Currently available airborne small-footprint topographic full-waveform lidar systems and their characteristic system parameters. Max. PRR ... maximal pulse repetition rate. ALS70 CM/HP, Gemini, Optech, Orion and Pegasus are actually able to scan in a higher PRR but the PRR of the FWF digitizer is limited to the given value [Leica Geosystems 2014; Optech Inc. 2014]. Data for Aquarius refer to the topographic mode.

more wavelgents, in most cases considerably separated, in the latter a certain wavelength range is covered by several sensors at high and equally spaced spectral resolution [Pfennigbauer and Ullrich 2011]. E.g., Briese et al. [2012] combined data from scanners operating at 532 nm, 1064 nm and 1550 nm in an urban area to produce active multi-channel radiometric images without shadows, comparable to “true” orthophotos.

Hyperspectral terrestrial lidar systems have been successfully tested to derive 3D information of single trees together with target characteristics such as the normalized differenced vegetation index (NDVI) or the water index for tree classification [Hakala et al. 2012; Kaasalainen et al. 2010]. The system used in the mentioned references consists of 16 channels, each separated by 35 nm; because of low laser intensity at lower wavelengths, 8 channels were used at wavelengths of 542, 606, 672, 707, 740, 775, 878 and 981 nm.

## 1.4 Aim of this Thesis

The aim of this thesis is to develop, implement and test innovative methods which overcome limitations existent in standard methods for signal analysis of FWF lidar data. It summarizes the author’s contribution to this topic, embedded in the context of approaches presented in relevant literature of this field.

These approaches can be grouped into approaches aiming at empirical target characterization on the one side and approaches aiming at physical target characterization via reconstruction of the scattering process at the target on the other side. The approaches of the first group start with the search for (tentative) echoes in the backscattered lidar signal, followed by the estimation of *echo* parameters. The second group starts with deconvolution of the backscattered lidar signal by the originally transmitted signal, followed by echo detection and physical *target* characterization; the last step is achieved by radiometric calibration. This distinction is reflected by the structure of the respective chapter in this thesis (Chapter 3).

The mentioned contribution of the author comprises

- the extraction and localization of echoes by correlation techniques,
- investigations on the impact of the transmitted pulse’s energy and shape variation on radiometric calibration,
- theoretical investigation supported by numerical sampling for understanding the echo shape as convolution of emitted pulse and the target’s differential backscatter cross-section
- the development of a linear deconvolution approach based on uniform B-splines and

- subsequent radiometric calibration and the calculation of target features based on statistical moments of the radiometrically calibrated deconvolution.

The first item in the above list belongs to the first group of approaches while all other items apply to the second group.

## 1.5 Structure of this Thesis

The rest of this thesis is organized as follows: Chapter 2 presents the physical background of FWF lidar. The analysis of the backscattered return signals is focused on in Chapter 3. Numerical examples are given in the subsequent chapter, while the results of these examples are discussed in Chapter 5 and the conclusions are given in Chapter 6.

Parts of this document are based on publications authored and co-authored by the writer of this thesis. The respective sections and references are given in the following list:

### Section 2.1

[[Roncat et al. 2014a](#)] Roncat, A., Morsdorf, F., Briese, C., Wagner, W., and Pfeifer, N. [2014a]. “Laser Pulse Interaction with Forest Canopy: Geometric and Radiometric Issues”. In: *Forestry Applications of Airborne Laser Scanning – Concepts and Case Studies*. Vol. 27. Ed. by M. Maltamo, E. Næsset, and J. Vauhkonen. Managing Forest Ecosystems. Dordrecht, The Netherlands: Springer Netherlands. Chap. 2, pp. 19–41. isbn: 978-94-017-8662-1. doi: [10.1007/978-94-017-8663-8\\_2](https://doi.org/10.1007/978-94-017-8663-8_2)

### Section 3.1.2

[[Wagner et al. 2007](#)] Wagner, W., Roncat, A., Melzer, T., and Ullrich, A. [2007]. “Waveform Analysis Techniques in Airborne Laser Scanning”. In: *ISPRS Workshop “Laser Scanning 2007 and SilviLaser 2007”*. *International Archives of the Photogrammetry, Remote Sensing and Spatial Information Sciences 36 (Part 3/W52)*. Ed. by P. Rönholm, H. Hyyppä, and J. Hyyppä, pp. 413–418. url: [http://www.isprs.org/proceedings/XXXVI/3-W52/final\\_papers/Wagner\\_2007\\_keynote.pdf](http://www.isprs.org/proceedings/XXXVI/3-W52/final_papers/Wagner_2007_keynote.pdf)

[[Roncat et al. 2008](#)] Roncat, A., Wagner, W., Melzer, T., and Ullrich, A. [2008]. “Echo Detection and Localization in Full-Waveform Airborne Laser Scanner Data using the Averaged Square Difference Function Estimator”. In: *The Photogrammetric Journal of Finland* 21 [1], pp. 62–75. url: [http://foto.hut.fi/seura/julkaisut/pjf/pjf\\_e/2008/Roncat\\_et\\_al\\_2008\\_PJF.pdf](http://foto.hut.fi/seura/julkaisut/pjf/pjf_e/2008/Roncat_et_al_2008_PJF.pdf)

### Section 3.2.1.1

[Roncat et al. 2014a] (see above)

### Section 3.2.2

[Roncat et al. 2010] Roncat, A., Bergauer, G., and Pfeifer, N. [2010]. “Retrieval of the Backscatter Cross-Section in Full-Waveform Lidar Data using B-Splines”. In: *PCV 2010 – ISPRS Technical Commission III Symposium on Photogrammetric Computer Vision and Image Analysis. International Archives of the Photogrammetry, Remote Sensing and Spatial Information Sciences 38 (Part 3B)*. ed. by N. Paparoditis, M. Pierrot-Deseilligny, C. Mallet, and O. Tournaire, pp. 137–142. url: [http://www.isprs.org/proceedings/XXXVIII/part3/b/pdf/137\\_XXXVIII-part3B.pdf](http://www.isprs.org/proceedings/XXXVIII/part3/b/pdf/137_XXXVIII-part3B.pdf)

[Roncat et al. 2011a] Roncat, A., Bergauer, G., and Pfeifer, N. [2011a]. “B-Spline Deconvolution for Differential Target Cross-Section Determination in Full-Waveform Laser Scanner Data”. In: *ISPRS Journal of Photogrammetry and Remote Sensing* 66 [4], pp. 418–428. doi: [10.1016/j.isprsjprs.2011.02.002](https://doi.org/10.1016/j.isprsjprs.2011.02.002)

### Section 3.3.2

[Roncat et al. 2011b] Roncat, A., Lehner, H., and Briese, C. [2011b]. “Laser Pulse Variations and their Influence on radiometric Calibration of Full-Waveform Laser Scanner Data”. In: *ISPRS Workshop Laser Scanning 2011. International Archives of the Photogrammetry, Remote Sensing and Spatial Information Sciences 38 (Part 5/W12)*. Ed. by D. D. Lichti and A. F. Habib, pp. 137–142. doi: [10.5194/isprsarchives-XXXVIII-5-W12-37-2011](https://doi.org/10.5194/isprsarchives-XXXVIII-5-W12-37-2011)

[Lehner et al. 2011] Lehner, H., Kager, H., Roncat, A., and Zlinszky, A. [2011]. “Consideration of laser pulse fluctuations and automatic gain control in radiometric calibration of airborne laser scanning data”. In: *Proceedings of 6th ISPRS Student Consortium and WG VI/5 Summer School*. Fayetteville State University, North Carolina. url: [http://publik.tuwien.ac.at/files/PubDat\\_199484.pdf](http://publik.tuwien.ac.at/files/PubDat_199484.pdf)

[Roncat et al. 2012] Roncat, A., Pfeifer, N., and Briese, C. [2012]. “A linear approach for radiometric calibration of full-waveform Lidar data”. In: *Proc. SPIE 8537, Image and Signal Processing for Remote Sensing XVIII*. doi: [10.1117/12.970305](https://doi.org/10.1117/12.970305)

[Roncat et al. 2014b] Roncat, A., Briese, C., Jansa, J., and Pfeifer, N. [2014b]. “Radiometrically Calibrated Features of Full-Waveform Lidar Point Clouds based on Statistical Moments”. In: *IEEE Geoscience and Remote Sensing Letters* 11 [2], pp. 549–553. doi: [10.1109/LGRS.2013.2274557](https://doi.org/10.1109/LGRS.2013.2274557)

### **Section 4.3**

[\[Roncat et al. 2011b\]](#) (see above)

### **Section 4.4**

[\[Roncat et al. 2010\]](#) (see above)

[\[Roncat et al. 2011a\]](#) (see above)

### **Section 4.5**

[\[Roncat et al. 2012\]](#) (see above)

### **Section 4.6**

[\[Roncat et al. 2014b\]](#) (see above)

# Physical Foundations of Full-Waveform Lidar

This chapter presents the underlying physical concepts for the analysis of small-footprint full-waveform lidar data. The text is mainly based on the presentation given in [\[Roncat et al. 2014a\]](#).

## 2.1 The Radar Equation

Let the transmitted power of a laser be  $P_t$  [W]. Assuming constant energy distribution within the cone formed by the laser beam, the power density  $e_L$  at a scattering planar target of infinite expansion hit orthogonally by the laser ray is

$$e_L = \frac{P_t}{A_L}. \quad (2.1)$$

This quantity is given in  $\text{W}/\text{m}^2$ . The term  $A_L$  [ $\text{m}^2$ ] is the area of the laser footprint, i.e. the area formed by the intersection of the cone and a sphere with centre at the laser's position  $O$  and radius  $R$  corresponding to the distance from the laser to the target (see Figure 2.1). Let the solid angle of this cone be  $\Omega$  [sr] =  $2\pi(1 - \cos \beta_t/2)$ , with  $\beta_t$  [rad] being the opening angle of this cone. We retrieve for  $A_L$  [\[Wagner et al. 2006\]](#):

$$A_L = R^2\Omega = 2\pi R^2 \left(1 - \cos \left(\frac{\beta_t}{2}\right)\right) \simeq 2\pi R^2 \left(1 - 1 + \frac{\beta_t^2}{8}\right) = \frac{\pi R^2 \beta_t^2}{4}, \quad (2.2)$$

using  $\cos x = 1 - x^2/2 + x^2/4! - \dots$  and truncating the Taylor expansion after the quadratic term.



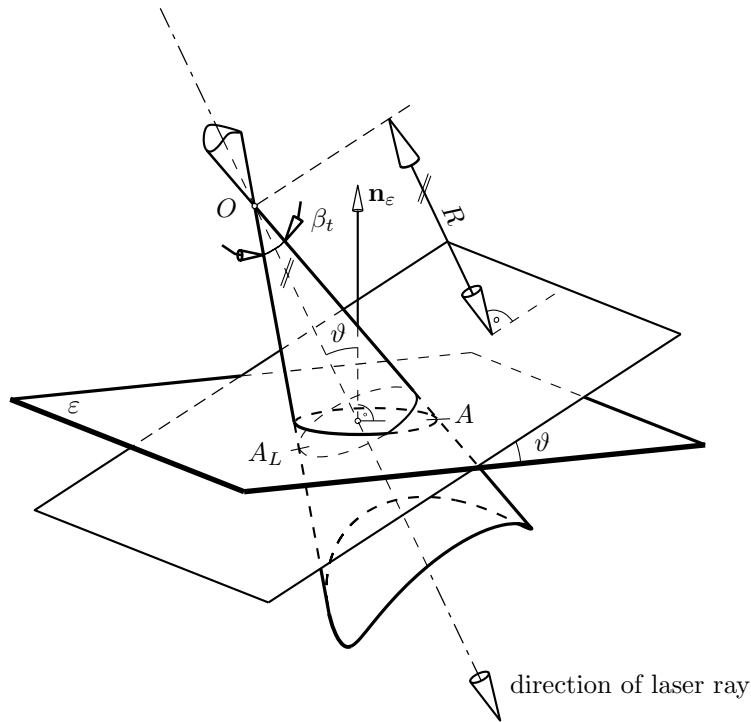


**Figure 2.1:** Laser footprint area  $A_L$  and illuminated target area  $A$  of an extended target in the plane  $\varepsilon$  located at a distance  $R$  from the laser origin  $O$  [Roncat et al. 2012]. The angle  $\vartheta$  formed by the laser ray and the normal of  $\varepsilon$  is called *incidence angle*.

Assuming a constant power density distribution within the laser footprint, this power density amounts to

$$e_L = \frac{P_t}{A_L}.$$

Consequently, the power density at the target (irradiance) results to

$$e = \frac{P_t}{A},$$

with  $A$  as the effective receiving area of the target. We assume the target to be within an infinite plane  $\varepsilon$  whose normal forms an angle  $\vartheta$  with the laser beam; see Figure 2.1. This angle is called *incidence angle*.

With small opening angle  $\beta_t$  of the laser beam, the illuminated area of the target amounts to

$$A \simeq \frac{A_L}{\cos \vartheta}$$

and therefore  $e \simeq e_L \cos \vartheta$ . The total power intercepted by the target is

$$P_{it} = eA = \frac{4P_t}{\pi R^2 \beta_t^2} A_L.$$

In the case of lidar, the used wavelength is typically very small in comparison to the size of the scanned targets. Thus, the effective area for collision is the projected illuminated area of the scattering target. The scattered, i.e. re-radiated power, results to

$$P_{st} = \rho P_{it} \cos \vartheta = \rho \frac{4P_t}{\pi R^2 \beta_t^2} A_L \cos \vartheta$$

with  $\rho$  being the target reflectivity in the wavelength of the laser. The actual scattering mechanism may be very complex; the basic quantity representing the surface's scattering characteristics is its bi-directional reflectance distribution function (BRDF) [Nicodemus et al. 1977]. As this BRDF is based on the ratio of infinitesimal functions, it cannot be directly measured. The most general measurable configuration is represented by the bi-conical reflectance factor. In this model, the scattering mechanism is taken into account in a simplified version by just considering an aggregated value and introducing a cone with projected solid angle  $\Omega_S$  representing the integral over all possible directions [Schaepman-Strub et al. 2006]:

$$\Omega_S = \iint \cos \vartheta_S \sin \vartheta_S d\vartheta_S d\varphi_S \quad (2.3)$$

with  $\sin \vartheta_S d\vartheta_S d\varphi_S$  being the differential surface element on the unit sphere, formed by differential changes in the scattering angle  $\vartheta_S$  and in azimuth  $\varphi_S$ .

With the receiver located at a distance  $R$  from the target, we get as echo power density at the receiver:

$$e_e = \rho \frac{P_{st}}{\Omega_S R^2} = \rho \frac{4P_t}{\pi R^4 \beta_t^2} \frac{1}{\Omega_S} A_L \cos \vartheta.$$

We finally retrieve as the echo power at the receiver  $P_e = e_e \pi D_r^2 / 4$  where  $D_r$  [m] is the aperture diameter of the receiver optics. The combination of all mentioned effects gives [Jelalian 1992]

$$P_e = P_t \frac{D_r^2}{4\pi R^4 \beta_t^2} \frac{4\pi}{\Omega_S} \rho A_L \cos \vartheta. \quad (2.4)$$

This formula is known as *radar equation*. It is valid in the far field, i.e. the extent of the region of interest is way smaller than the distance  $R$  to the laser [Woodhouse 2006]. The last terms in the radar equation describe target characteristics which are summarized to the *scattering cross-section*  $\sigma$ :

$$\sigma := \frac{4\pi}{\Omega_S} \rho A_L \cos \vartheta. \quad (2.5)$$

Figure 2.2 sketches the transmission of a laser pulse, the scattering process at a target and the recording of the echoes. In the further text, we will only consider the monostatic

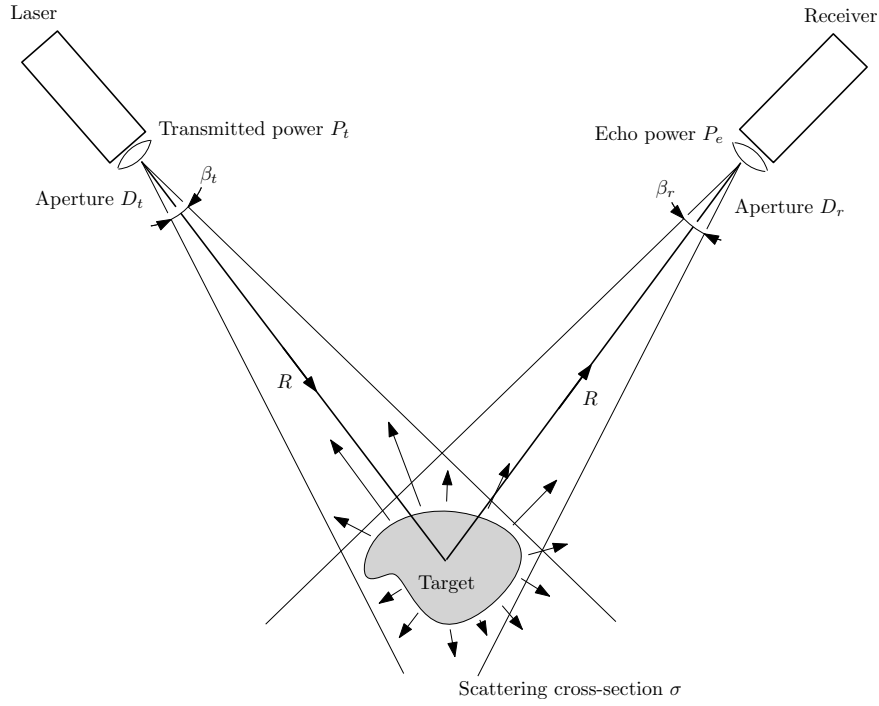


**Figure 2.2:** Laser pulse interaction with an extended target [Wagner et al. 2006]. In case of the laser and the receiver being close together,  $\sigma$  is called *backscatter* cross-section.

case where laser and receiver are very close together. As a consequence, the receiver observes the echo signal *backscattered* from the target.

Thus, this  $\sigma$  is a *backscatter cross-section* in the context of this thesis. It has the unit of  $m^2$  and corresponds to the effective area of collision between laser ray and the target w.r.t. reflectivity and directionality.

Taking a varying laser power over time  $P_t(t)$ , systematic and atmospheric effects into account, we get [Wagner et al. 2006]:

$$P_e(t) = \frac{D_r^2}{4\pi R^4 \beta_t^2} P_t \left( t - \frac{2R}{v_g} \right) \sigma \eta_{\text{SYS}} \eta_{\text{ATM}} \quad (2.6)$$

with  $v_g$  being the group velocity of the laser (approximately the speed of light in vacuum),  $\eta_{\text{ATM}}$  the atmospheric transmission factor, and  $\eta_{\text{SYS}}$  the system transmission factor.

If multiple targets are present, the echo signal results to a superposition of single echoes along the laser ray at different ranges  $R_i$ . Their respective time delay is  $2R_i/v_g$  so that we can use time and range interchangeably in this context. Targets very close to

each other act as a cluster. The maximum cluster size  $\Delta R$ , i.e. the minimum distance between two targets still being separable, depends on laser wavelength, pulse width and target reflectivity. For such a cluster at a range  $R_i \pm \Delta R$  we retrieve [Wagner et al. 2006]:

$$P_{e,i}(t) = \frac{D_r^2}{4\pi\beta_t^2} \eta_{\text{SYS}} \eta_{\text{ATM}} \int_{R_i - \Delta R}^{R_i + \Delta R} \frac{1}{R^4} P_t \left( t - \frac{2R}{v_g} \right) \sigma'_i(R) dR \quad (2.7)$$

with  $\sigma'_i(R) = d\sigma/dR$  being the derivative of the backscatter cross-section w.r.t. the range. It is called *differential backscatter cross-section* (short: dBCS) further on. Since  $\sigma'_i(R)$  is zero outside the interval  $[R_i - \Delta R, R_i + \Delta R]$ , the term

$$\int_{R_i - \Delta R}^{R_i + \Delta R} P_t \left( t - \frac{2R}{v_g} \right) \sigma'_i(R) dR = \int_{-\infty}^{\infty} P_t \left( t - \frac{2R}{v_g} \right) \sigma'_i(R) dR = P_t(t) \otimes \sigma'_i(t)$$

is the convolution of the transmitted laser power with the differential backscatter cross-section, denoted by the operator  $\otimes$ .

Assuming that  $\Delta R \ll R_i$ , Equation (2.7) can be approximated by

$$\begin{aligned} P_{e,i}(t) &\simeq \frac{D_r^2}{4\pi\beta_t^2 R_i^4} \eta_{\text{SYS}} \eta_{\text{ATM}} \int_{R_i - \Delta R}^{R_i + \Delta R} P_t \left( t - \frac{2R}{v_g} \right) \sigma'_i(R) dR \\ &= \frac{D_r^2}{4\pi\beta_t^2 R_i^4} \eta_{\text{SYS}} \eta_{\text{ATM}} P_t(t) \otimes \sigma'_i(t). \end{aligned}$$

Receiver electronics do not allow to record  $P_t(t)$  and  $P_e(t)$  directly; instead, their convolution with the scanner's system response function  $\Gamma(t)$  is recorded. This yields

$$\begin{aligned} P_{e,i}(t) \otimes \Gamma(t) &= \frac{D_r^2}{4\pi\beta_t^2 R_i^4} \eta_{\text{SYS}} \eta_{\text{ATM}} P_t(t) \otimes \sigma'_i(t) \otimes \Gamma(t) \\ &= \frac{D_r^2}{4\pi\beta_t^2 R_i^4} \eta_{\text{SYS}} \eta_{\text{ATM}} P_t(t) \otimes \Gamma(t) \otimes \sigma'_i(t) \end{aligned}$$

because convolution is commutative (see Chapter A in the appendix). Thus, we can define  $P_t(t) \otimes \Gamma(t)$  as *system waveform*  $S(t)$ , the quantity actually recorded when a copy of the transmitted laser pulse is stored. Summing up all  $N$  echoes of such a pulse, we get the *recorded echo power*  $P_r(t)$  as

$$P_r(t) = \sum_{i=1}^N P_{e,i}(t) \otimes \Gamma(t) = \frac{D_r^2}{4\pi\beta_t^2} \eta_{\text{SYS}} \eta_{\text{ATM}} \sum_{i=1}^N \frac{1}{R_i^4} S(t) \otimes \sigma'_i(t). \quad (2.8)$$

The primary output of airborne lidar campaigns are three-dimensional area-wide point clouds. Full-waveform lidar allows for a precise determination for the range  $R_i$  of a

target and subsequently for its three-dimensional position. For the derivation of physical target properties, the first goal is to determine the backscatter cross-section  $\sigma_i$ . For this purpose, we re-group Equation (2.8) and retrieve:

$$\sigma'_i(t) = \frac{4\pi\beta_t^2 R_i^4}{D_r^2 \eta_{\text{SYS}} \eta_{\text{ATM}}} P_r(t) \otimes^{-1} S(t).$$

The operator  $\otimes^{-1}$  denotes deconvolution, i.e. the inverse of convolution. It is an ill-posed task and needs additional constraints for a stable solution [Tikhonov and Arsenin 1977]. Approaches used for deconvolution in lidar research are treated in detail in Section 3.2.

After range determination and deconvolution, the term  $\beta_t^2/(D_r^2 \eta_{\text{SYS}} \eta_{\text{ATM}})$  remains as unknown quantity. While some of its components are known to system designers of lidar systems, they cannot be easily separated in an inversion.

As last step for the calculation of the backscatter cross-section, we need to solve the integral

$$\sigma_i = \int_{-\infty}^{\infty} \sigma'_i(t) dt. \quad (2.9)$$

The solutions for  $\sigma_i$  and the derivation of further radiometric quantities from given  $S(t)$  and  $P_r(t)$ , known as *radiometric calibration*, are described in Section 3.3. Some of these derivations assume the targets to be Lambertian scatterers. The underlying physics are presented in the following section.

## 2.2 Lambertian Scattering

This scattering mechanism is also known as diffuse scattering and appears in the interaction of an electromagnetic wave with rough target surfaces. A common criterion for classifying smooth and rough surfaces is the *Fraunhofer criterion* [Schanda 1986]: Considering two rays reflected at different levels on the surface being one standard deviation  $s_h$  apart from each other, their phase difference  $\Delta\varphi$  results to

$$\Delta\varphi = 2s_h \frac{2\pi}{\lambda} \cos \vartheta,$$

with  $\lambda$  being the used wavelength and  $\vartheta$  being the incidence angle. In the far field, for smooth surfaces the maximum phase difference is  $\Delta\varphi < \pi/8$  which gives

$$s_h < \frac{\lambda}{32 \cos \vartheta}.$$

In the case of lidar, the used wavelength is in the range of  $1 \mu\text{m}$  (see Table 1.1), so that for orthogonal incidence, only surfaces with  $s_h < 31 \text{ nm}$  are considered as smooth. As a consequence, most surface types can be considered as rough in this spectrum [Wagner et al. 2003]. An ideal rough surface is characterized by scattering the incident power

uniformly within a hemisphere, so that the integration limits in Equation (2.3) amount to 0 and  $2\pi$  for  $\varphi_S$ ; for  $\vartheta_S$ , they result in 0 and  $\pi/2$ . This gives:

$$\begin{aligned}\Omega_S &= \int_0^{2\pi} \int_0^{\pi/2} \cos \vartheta_S \sin \vartheta_S \, d\vartheta_S d\varphi_S = 2\pi \int_0^{\pi/2} \frac{\sin 2\vartheta_S}{2} d\vartheta_S = \pi \left[ -\frac{\cos 2\vartheta_S}{2} \right]_0^{\pi/2} \\ &= \pi \left( \frac{1}{2} + \frac{1}{2} \right) = \pi,\end{aligned}$$

so that the effective scattering cone for Lambertian scattering has an opening angle of  $\beta_S = 2 \arccos(1 - \Omega_S/(2\pi)) = 2\pi/3$ . In the absolute opposite case of specular reflection,  $\Omega_S = 0 \Rightarrow \beta_S = 0$  so that only one single direction remains in which energy is re-radiated, which is determined by Snell's law. Evaluating Equation (2.5) for an extended target with  $\Omega_S = \pi$ , we get

$$\sigma_L = 4\rho A_L \cos \vartheta. \quad (2.10)$$

Following the examples and the reflectivity of different materials given by [Wagner et al. \[2003\]](#), we will now illustrate the behaviour of  $\sigma$  for examples of

- “point-like” circular targets within the laser footprint: maple leaves ( $\rho = 0.4$ ) and maize leaves ( $\rho = 0.9$ ),
- “linear” targets of small width in comparison to the laser footprint: copper wires ( $\rho = 0.9$ ) and stainless steel wires ( $\rho = 0.2 - 0.6$ ),
- extended targets: asphalt ( $\rho = 0.2$ ), snow ( $\rho = 0.25$ ), terra cotta ( $\rho = 0.3$ ) and dry silty soil ( $\rho = 0.6$ ),

each in dependency of size and incidence angles.

For circular targets within the laser footprint of radius  $r < R \sin(\beta_t/2)$ , we get

$$\sigma_{L,c} = 4\rho\pi r^2 \cos \vartheta.$$

If the target is linear, e.g. a wire of length  $l > R \sin(\beta_t/2)$  and width  $w \ll R \sin(\beta_t/2)$ , the corresponding  $\sigma$  results to

$$\sigma_{L,l} = 4\rho w R \beta_t \cos \vartheta,$$

yielding an  $R^{-3}$  dependency of  $P_e(t)$  to  $P_t(t)$  in the radar equation. In the case of an extended target, we get

$$\sigma_{L,e} = 4\rho A_L \cos \vartheta = \pi\rho R^2 \beta_t^2 \cos \vartheta$$

which corresponds to an  $R^{-2}$  dependency of  $P_e(t)$  to  $P_t(t)$  in the radar equation.

The synthetic examples shown in Figures 2.3 – 2.5 illustrate  $\sigma$  for the mentioned target types. The range  $R$  was chosen to 1000 m and the transmitter beamwidth to  $\beta_t = 0.5$  mrad, yielding a laser footprint of 50 cm diameter and  $A_L = 0.196 \text{ m}^2$ .

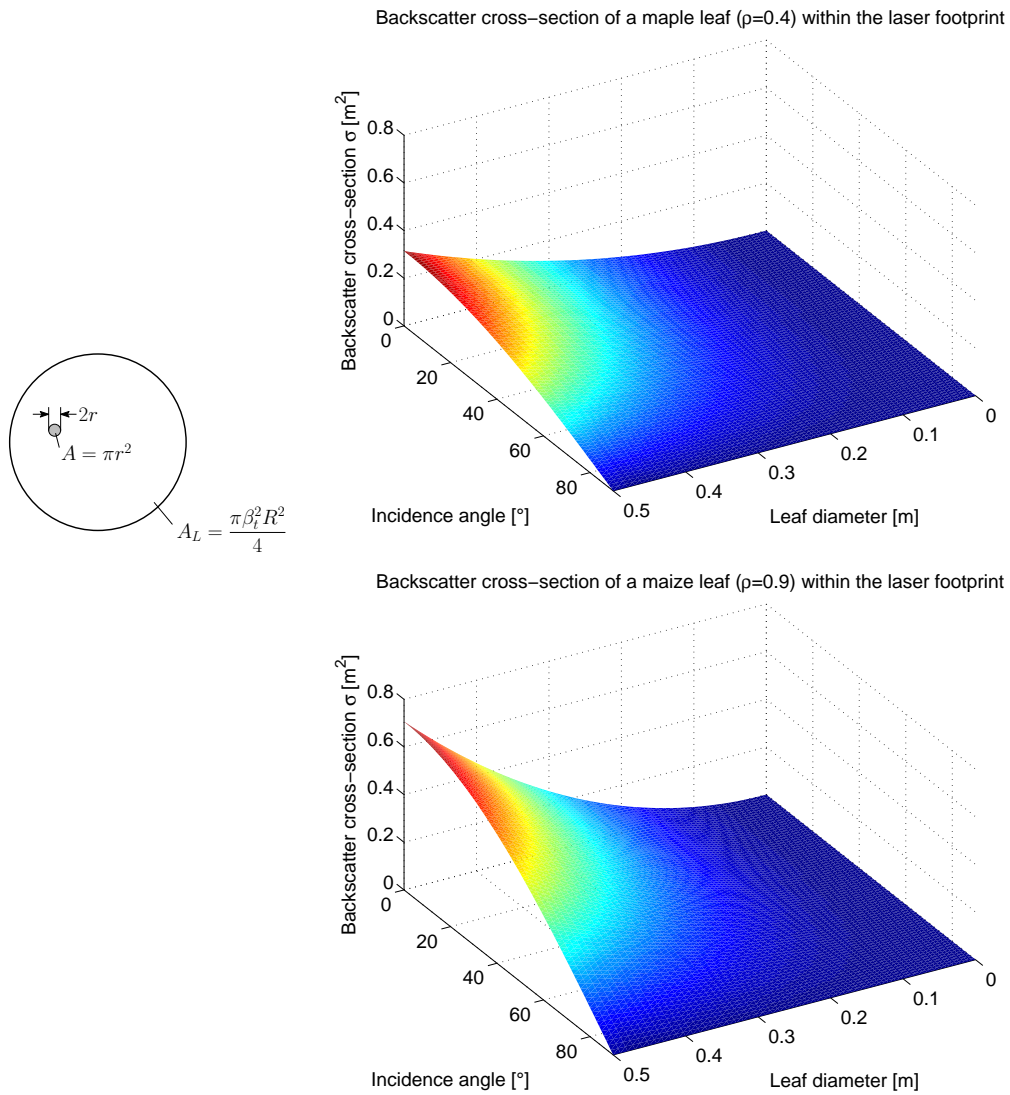
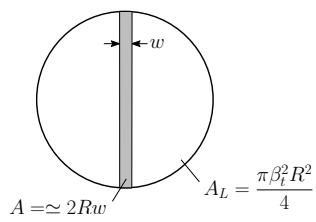
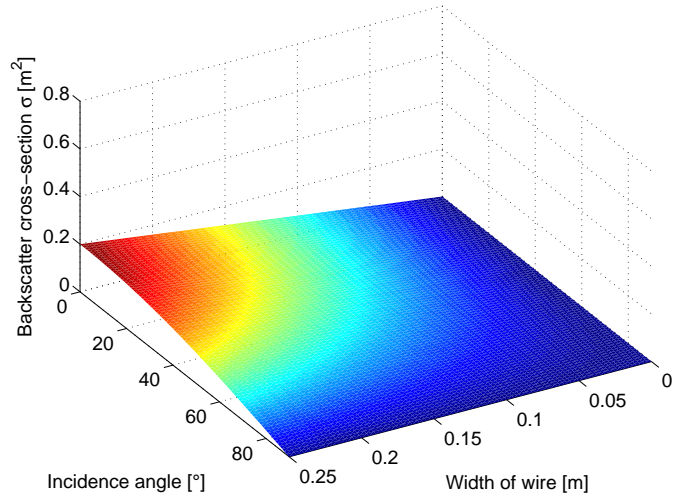


**Figure 2.3:** Backscatter cross-section for maple leaves (top,  $\rho = 0.4$ ) and maize leaves (bottom,  $\rho = 0.9$ ), dependent on leaf radius  $r$  and incidence angle  $\vartheta$ .



Backscatter cross-section of a stainless steel wire ( $\rho=0.9$ ) within the laser footprint



Backscatter cross-section of a copper wire ( $\rho=0.9$ ) within the laser footprint

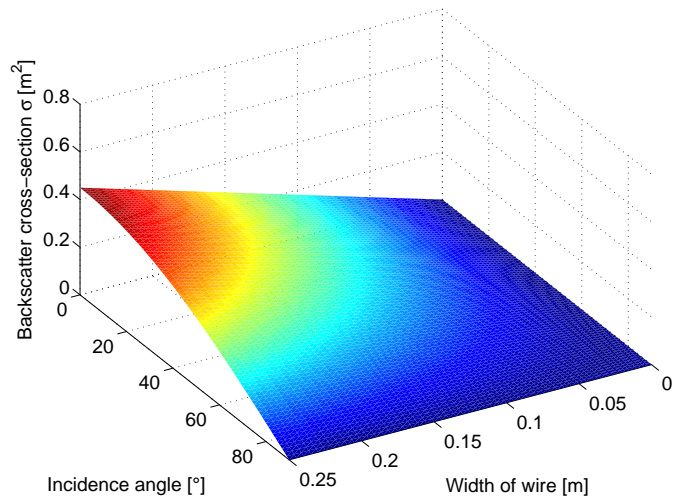


**Figure 2.4:** Backscatter cross-section for linear targets (wires) made of stainless steel (top,  $\rho = 0.4$ ) and copper (bottom, ( $\rho = 0.9$ ), dependent on the width  $w$  of the wire and incidence angle  $\vartheta$ .



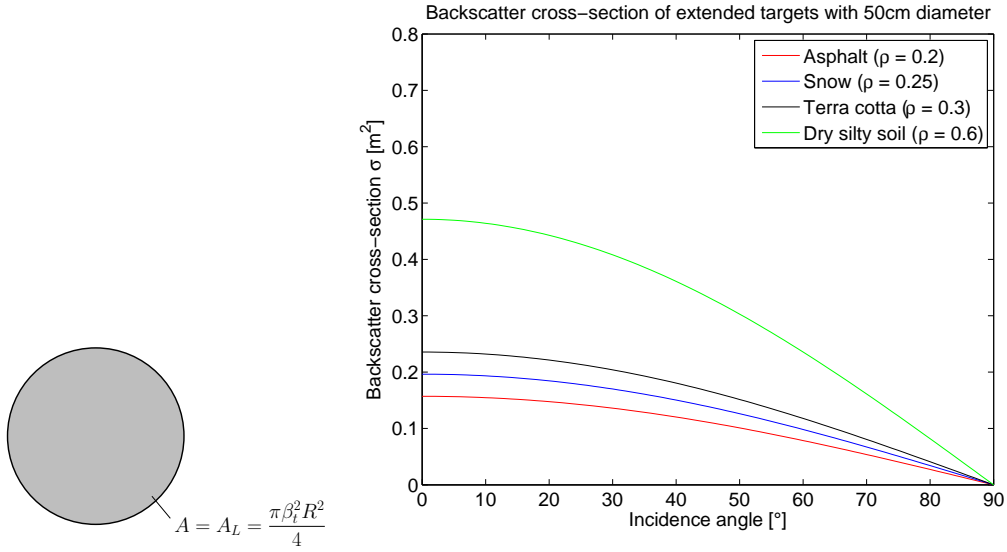


**Figure 2.5:** Backscatter cross-section for extended targets: asphalt (red,  $\rho = 0.2$ ), snow (blue,  $\rho = 0.25$ ), terra cotta (black,  $\rho = 0.3$ ) and dry silty soil (green,  $\rho = 0.6$ ), dependent on the incidence angle  $\vartheta$ .

### 2.3 Notes on the Geometry of the Laser Beam

As mentioned in the introduction of this thesis, the primary output of lidar campaigns are three-dimensional point clouds. The question may arise which point and consequently, which range  $R$ , is representative for a target. For answering this question, we will take a closer look on the geometry of the laser beam and its intersection with a target.

Let us consider the simple case of an extended planar target, located in a plane  $\varepsilon'$ . Let the normal vector of this plane form an angle  $\vartheta$  with the central axis of the laser beam; this beam is considered as a circular cone  $\Phi$  with opening angle  $\beta_t$ ; its apex is the laser origin  $O$ . The surfaces of equal range  $R$  are spheres around  $O$ . Thus, the corresponding range isolines in  $\varepsilon'$  are concentric circles around the laser origin's foot of perpendicular,  $O'$ . The radius of such a circle corresponding to the range  $R$  is

$$r = \sqrt{R^2 - OO'^2} = \sqrt{R^2 - O\varepsilon'^2}.$$

The intersection of  $\Phi$  with  $\varepsilon'$  is a conic section  $c'$ . In realistic circumstances, this conic section is an ellipse with major semi-axis  $a$  and centre  $N'$ ; see Figure 2.6.

The variations of the incidence angle  $\vartheta$  and of the  $R^2$  term of the radar equation are small within the laser footprint, as the illustrations in Figure 2.7 indicate. Thus, for uniform power density within the laser beam, the main factor influencing  $\sigma'(R)$  is the

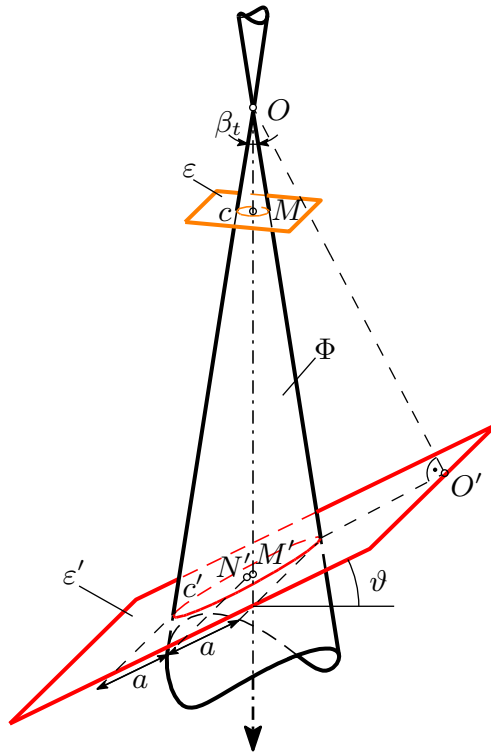


**Figure 2.6:** Offset between the centre  $N'$  of the conic section (ellipse)  $c'$  and the intersection  $M'$  of the laser beam cone's axis with the plane  $\varepsilon' \supset c'$ .

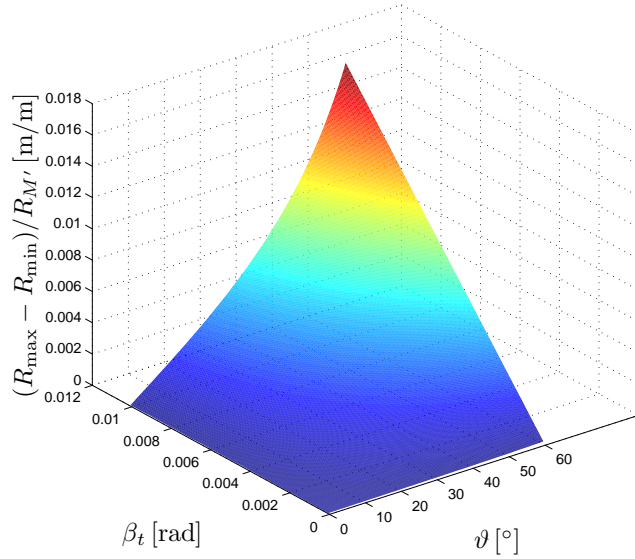
range distribution  $\psi(R)$  within the area of  $c'$ . This distribution  $\psi(R)$  results from the arc lengths of the respective range isolines (circular arcs) within the conic section  $c'$ .

Both the intersection of the laser beam axis with the target plane,  $M'$ , and the centre  $N'$  of the ellipse  $c'$  are justified choices for a point being representative for the target. It shall be noted that these two points do not coincide in general:  $c'$  can be considered as the perspective image (perspective centre  $O$ , image plane  $\varepsilon'$ ) of a circle  $c$  with centre  $M$  located in a plane  $\varepsilon$ . This plane is orthogonal to the laser beam's axis (see Figure 2.6). As is known from descriptive geometry [cf. [Wunderlich 1966](#)], the image of  $M'$  under an orthogonal projection onto a plane  $\parallel \varepsilon^1$  results in a focus of the image of  $c'$  under this orthogonal projection. There are two cases where  $M'$  coincides with  $N'$ :

1. the laser beam  $\Phi$  is a cylinder, i.e.  $\beta_t$  equals zero; consequently, the central projection which maps  $c \mapsto c'$  degenerates to a parallel projection, and

<sup>1</sup>the projection rays of this orthogonal projection are therefore parallel to the axis of  $\Phi$

Maximum difference in range, normalized by  $R_{M'}$



Maximum difference in incidence angle

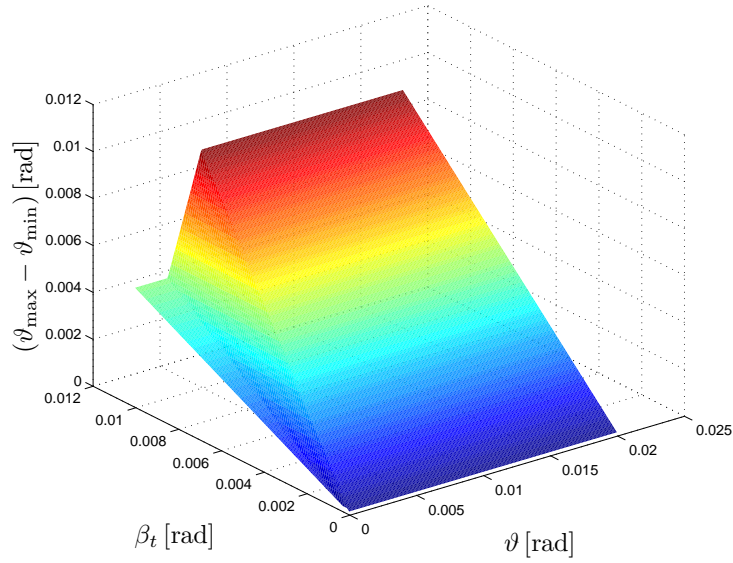


**Figure 2.7:** Top: Maximum differences in range within the laser footprint, normalized by  $R_{M'}$ . Bottom: Maximum differences in incidence angle within the laser footprint in dependence of  $\beta_t$  and  $\vartheta$ . This maximum difference amounts to  $\beta_t/2$  for  $\vartheta < \beta_t/4$ , to  $2\vartheta$  for  $\beta_t/4 \leq \vartheta < \beta_t/2$  and to  $\beta_t$  for  $\vartheta \geq \beta_t/2$ . For better comparability, all angular quantities are given in rad in the illustration at the bottom.

2. the plane  $\varepsilon'$  is perpendicular to the laser beam's central axis; in this case,  $c'$  is a circle and therefore centre and foci coincide.

In the first case, the range isolines are the intersections of parallel planes with  $\varepsilon'$ . These lines are perpendicular to the major axis of  $c'$ . Each such line segment inside  $c'$  is symmetric w.r.t. its major axis; moreover, there is another line segment of the same length in a mirror-symmetrical position to the minor axis of  $c'$ . Thus, the range distribution  $\psi(R)$  within the area of  $c'$  is a semi-ellipse [cf. [Wagner et al. 2004](#)]; its line of symmetry corresponds to the range isoline segment passing through  $M' = N'$ .

In the second case, the range isoline passing through  $M' = N'$  degenerates to the origin's foot of perpendicular  $O'$  and represents the *shortest* appearing range; its arc length is therefore zero. This means that the value of the range distribution for  $R = \overline{OO'}$  yields  $\psi(\overline{OO'}) = 0$  as well. As a consequence, there is no influence of this distance on the recorded echo waveform or on  $\sigma'(R)$  either. The arc lengths of the range isolines increase linearly with radius  $r$ , resulting in a linear function of value  $2\pi r$  in the interval  $r \in [0, a]$  and zero outside, with  $a = R_{M'} \tan(\beta_t/2)$  being the radius of the circle resulting from the intersection  $\Phi \cap \varepsilon'$ . Thus, the range distribution in dependency of  $R$  within the laser footprint results to a square-root function, i.e.

$$\psi(R) = 2\pi\sqrt{R^2 - \overline{O\varepsilon'}^2}$$

in the interval

$$R \in \left[ \overline{O\varepsilon'}, \sqrt{\overline{O\varepsilon'}^2 + a^2} \right]$$

and zero outside this interval. The two explained range distributions are given in Figure 2.8.

If both conditions necessary for  $M' = N'$  apply at once, i.e. both cylindrical beam shape and orthogonal incidence hold, all ranges  $R$  within the laser footprint are equal; consequently, the range distribution  $\psi(R)$  and the differential backscatter cross-section  $\sigma'(R)$  both result in the Dirac impulse.

For fixed angles  $\vartheta$  (incidence) and  $\beta_t$  (beam width), the offset  $e = \overline{N'M'}$  is a linear function in  $R_{M'} = \overline{OM'}$ . Figure 2.9 illustrates the amount of this offset in dependency of  $\vartheta$  and  $\beta_t$ , normalized by  $R_{M'}$ .

The offset effects derived in this section are of lower importance for small-footprint lidar systems. However, in the case of a large-footprint system, the situation is different. We will take NASA's LVIS (*Laser Vegetation Imaging Sensor* resp. *Land, Vegetation, and Ice Sensor*) as an example: This system operates with a beam divergence of  $\beta_t = 8$  mrad and at ranges in the order of  $R = 10$  km [[Blair et al. 1999](#)]. We therefore retrieve a footprint diameter of 80 m at the given range. The offset  $e$  results to 8.5 cm for an

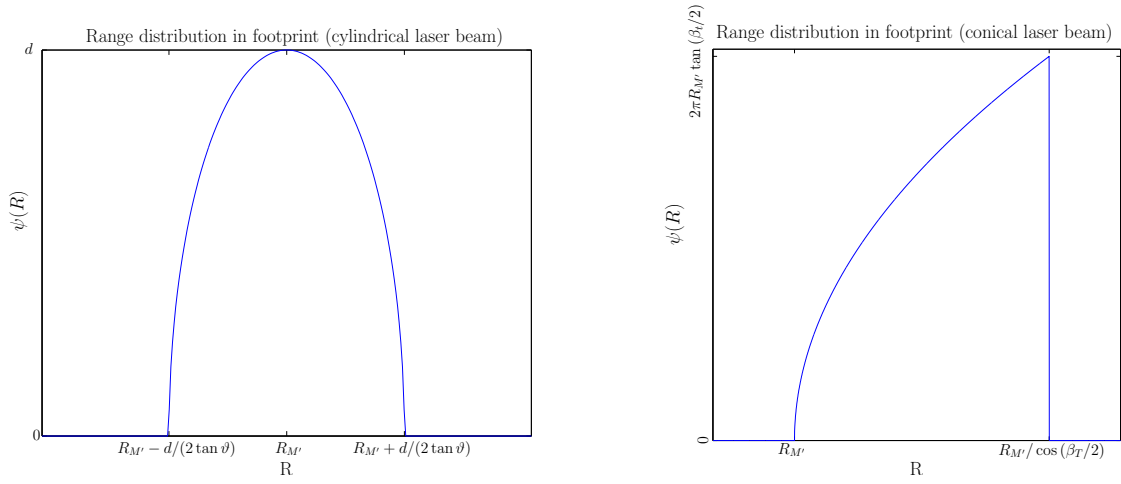


**Figure 2.8:** Range distribution  $\psi(R)$  within the laser footprint. Left: cylindrical beam shape (diameter  $d$ ), target plane normal inclined by the angle  $\vartheta$ . Right: conical beam shape (opening angle  $\beta_t$ ),  $\vartheta = 0$ . The value  $R_{M'}$  refers to the distance  $\overline{OM'}$  =  $\overline{ON'}$ . In the right image, additionally  $R_{M'} = \overline{O\varepsilon'}$  holds.

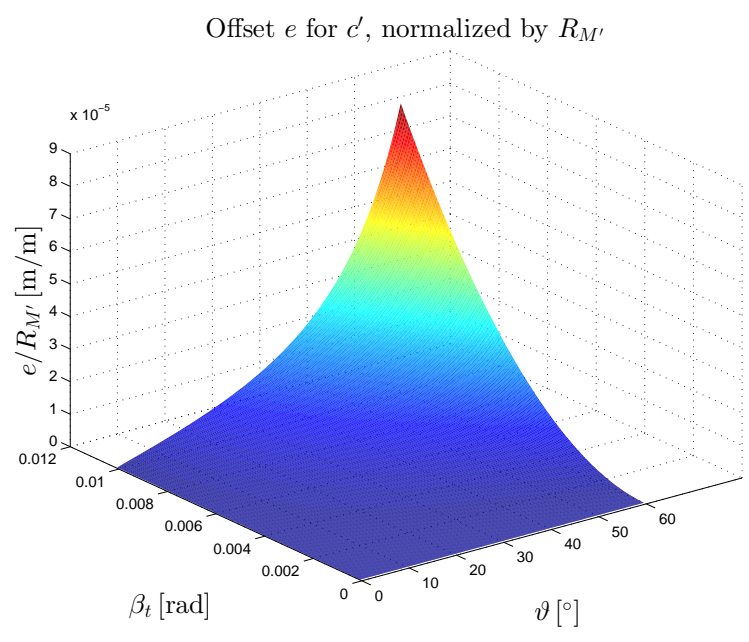


**Figure 2.9:** Offset  $e = \overline{N'M'}$  for the ellipse  $c'$ , normalized by  $R_{M'}$ .

incidence angle  $\vartheta = 30^\circ$  and to 18 cm for  $\vartheta = 45^\circ$ , in the latter case exceeding the spatial equivalent of the sampling interval.

An issue geometrically equivalent to the offset  $e$  for the ellipse  $c$  is found in vision metrology concerning the elliptic images of circular reference targets [e.g. [Otepka 2004](#)].

To resume, we have noted that the search for a point and a range representing a target is not trivial, even in the simple case of an extended planar target. However, the beam widths of commercial small-footprint lidar systems are typically  $< 1$  mrad and provide Gaussian power density distribution (see [Table 1.1](#)). Therefore, in practice the (unproblematic) first case is much more likely to appear than the second case.

## 2.4 Forward Modeling of Full-Waveform Return Signals

Based on the findings of the previous section, these paragraphs are dedicated to the synthesis of the differential backscatter cross-section  $\sigma'(R)$  stemming from targets of different size and shape as well as orientation to the laser beam. The relevant literature in lidar studies contains various approaches for this synthesis; four of them will be presented in the next section. An alternative approach, incorporating the results of the last preceding section, will be presented in [Section 2.4.2](#).

### 2.4.1 Related Work

[Steinvall \[2000\]](#) investigated the differential backscatter cross-section and the total backscatter cross-section from simple objects (cones, spheres, paraboloids and cylinders) being co-axial with the laser beam. The beam is considered to be cylindrical, i.e. without any beam divergence. Objects of specular and diffuse reflectance were considered in this paper.

In [\[Jutzi 2007\]](#), the focus is on the differential backscatter cross-section of planar and spherical surfaces. [Morsdorf et al. \[2007\]](#) employed a ray-tracing approach using the software POVRay<sup>2</sup> for simulating the differential backscatter cross-section from forest canopies. These canopies were modeled as fractal models. The laser was assumed as spotlight with defined beam divergence. This approach was extended to radiative transfer modeling in [\[Morsdorf et al. 2009\]](#). The result of this approach was a discretized version of  $\sigma'(R)$  in the form  $\sigma'[R_i]$ ; each discrete value represents the sum of all contributing canopy parts within the range interval  $[R_i - \Delta R; R_i + \Delta R)$  with  $(R_{i+1} - R_i) = 2\Delta R$ .

A subdivision of the laser beam into sub-beams, as proposed by [Kukko and Hyypä \[2007\]](#), is incorporated in the approach presented in the following section.

---

<sup>2</sup><http://www.povray.org/>

## 2.4.2 Alternative Approach for forward Modeling

As shown in Section 2.3, a representative range for a target is well defined for cylindrical shape of the laser beam and extended planar targets, but less well defined in other cases. This fact serves as motivation for approximating the conical laser beam by a subdivision based on cylindrical sub-beams. We start this subdivision with the intersection of the laser beam cone with a plane orthogonal to the central axis of this cone. This intersection yields a circular disc of radius  $r$ . We approximate this disc by a regular partitioning of it: First, the circular disc is subdivided into  $n$  radial zones of equal width  $\Delta r = r/n$ . The circle at the boundary of each zone is approximated by a polygon of  $6i$  vertices, placed isotropically along this circle. Together with the centre of the circular disc, we retrieve

$$1 + \sum_{i=1}^n 6i = 1 + 6 \frac{n(n+1)}{2}$$

vertices in total, e.g. 331 vertices for  $n = 10$  and 30301 vertices for  $n = 100$ . The conical laser beam is now substituted by cylinders representing sub-beams, one passing through each of the centres of the Voronoi cells retrieved by triangulation of the vertices and through the laser origin  $O$ .

The fraction of total laser energy represented by a sub-beam is adjusted by the according power density  $d(\cdot)$  in the original laser beam, and additionally by the contribution of the respective Voronoi cell w.r.t. the area of the whole beam. We use uniform and Gaussian-shape power density models; the latter corresponds to the  $1/e^2$  definition, i.e. the radius  $r$  of the circular disc is the locus where the power density has fallen to  $1/e^2$  of the maximum power density in the centre [cf. ISO 2006]. Thus, the radius  $r$  corresponds to the double of the underlying normal distribution's standard deviation  $s$ :

$$d(r) = \frac{1}{e^2} d(0) = \frac{1}{e^2} \frac{1}{\sqrt{2\pi}s} = \frac{1}{\sqrt{2\pi}s} e^{-r^2/(2s^2)}.$$

The natural logarithm of the above formula gives

$$-2 = -\frac{r^2}{2s^2} \implies r^2 = 4s^2 \implies r = 2s,$$

as both  $r$  and  $s$  are positive quantities.

Figure 2.10 shows illustrations for Gaussian-shape and uniform beam approximations by cylindrical sub-beams in  $n = 10$  radial zones. Both variants represent the same total laser energy; the beam divergence  $\beta_t$  was chosen to the rather high value of 333 mrad in this illustrations for better visibility.

In addition to the representation of different power density distributions within the laser footprint, it is also possible to model the differential backscatter cross-section for planar and other surfaces. For each sub-beam, the corresponding portion  $\sigma_i$  of  $\sigma$  is retrieved by

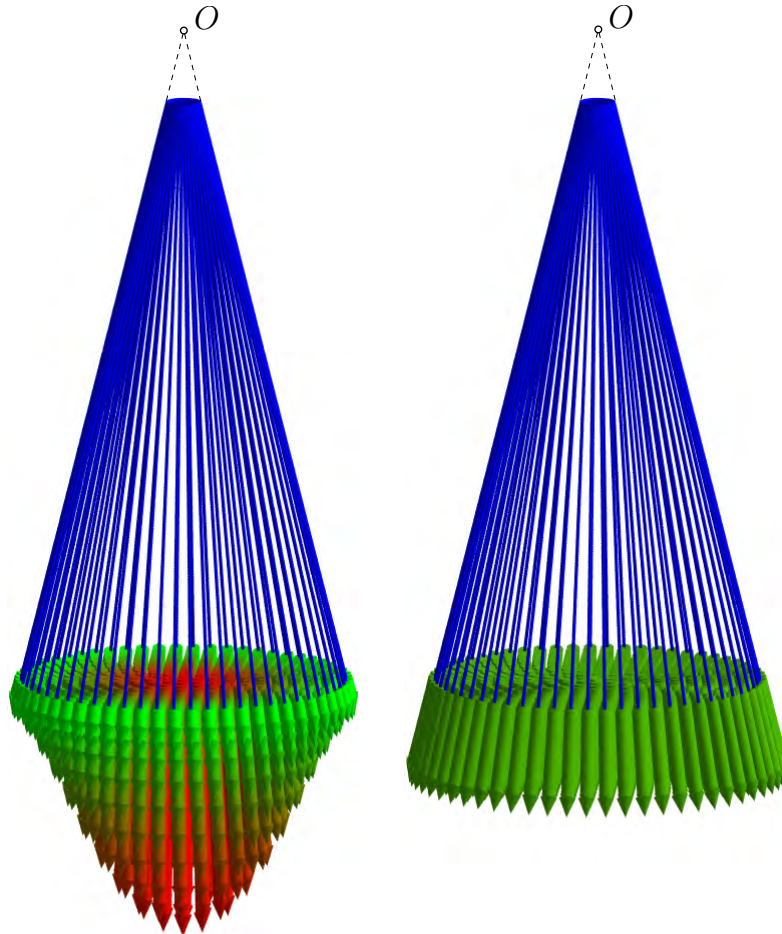


**Figure 2.10:** Conical laser beams approximated by cylindrical sub-beams. Left: Gaussian power-density distribution, right: uniform power-density distribution.



- intersecting the middle axis of the cylinder with the respective surface,
- in case of a real intersection point: calculating the range  $R$  and applying the  $R^2$  law, as we can locally substitute the target surface by its tangent plane at the intersection point,
- calculating the local incidence angle  $\vartheta$  by means of this tangent plane and applying the correction w.r.t.  $\cos \vartheta$  (Lambertian reflectance).

Calculating a histogram of these  $\sigma_i$  portions w.r.t. the corresponding  $R_i$  results in the numerical estimate of the dBCS  $\sigma'(R)$ ; the sum of all  $\sigma_i$  portions gives the numerical estimate of the BCS  $\sigma$  for the target.

In Section 4.1, examples of  $\sigma'(R)$  and  $\sigma$  are given and analysed for

- planes perpendicular and in arbitrary angle to the axis of the laser beam's circular cone,
- spheres,
- cylinders and
- sinusoidal surfaces

in the two mentioned power density distribution configurations.

# Analysis of Full-Waveform Return Signals

In this chapter, techniques for the analysis of FWF data are presented. The chapter begins in Section 3.1 with techniques working without deconvolution, aiming at the retrieval of 3D points and additional *echo* parameters. The approaches involving deconvolution and thus enabling for the extraction of *target* parameters are described in Section 3.2. The subsequent section 3.3 deals with approaches for radiometric calibration whose goal is the assignment of physically meaningful attributes to the targets. These sections are each further subdivided into subsections presenting related work and such describing the author's own contribution to this field.

An overview of the approaches presented in this chapter is given in Table 3.1 [Roncat et al. 2014a].

## 3.1 Approaches without Deconvolution

As mentioned above, these approaches deliver the ranges of the targets, possibly accompanied by *echo* parameters. In general, these echo parameters are dependent on the used instrument, e.g. the temporal profile of the emitted pulse and on parameters of the flight mission, e.g. the altitude of the aircraft.

### 3.1.1 Related Work

This section describes classical detectors for extracting the targets' ranges and the fit of a finite mixture model to the echo waveform. The parameters of these finite mixtures may also be considered as echo parameters.

Approach	# Echoes	Range	Amplitude	Continuous Modeling	Additional Echo Parameters	Deconvolution	Radiometric Calibration
Classical Detectors	•	•	•	—	—	—	~
Finite Mixture Model	•	•	•	•	•	—	•
<i>Correlation/ASDF</i>	•	•	—	—	◇	—	—
Wiener filter	◇	◇	—	•	◇	•	◇
Gaussian Decomposition	—	○	•	•	○	•	•
Expectation/Maximization (EM)	•	•	—	—	—	•	◇
<i>B-splines</i>	◇	◇	—	•	◇	•	◇

**Table 3.1:** FWF data analysis techniques and their outputs. Contributions by the author of this thesis are written in italics. • ... primary results, ○ ... results based on initial estimates provided by another technique, ◇ ... possible, but not originally intended, ~ ... approximately possible (e.g. with some further assumptions), — ... not provided by the approach

### 3.1.1.1 Classical Detectors

In this section, five classical detectors for signal processing are described, each aimed at detecting and locating the pulse and its echoes in the sampled system waveform  $S[t]$  and recorded echo waveform  $P_r[t]$ . Both are sampled with digitization interval  $\Delta t$ , thus  $t = j\Delta t$  with  $j \in \mathbb{Z}$ .

For each found echo at position  $t_{.,i}$ , its range is calculated by

$$R_i = \frac{c}{2} (t_{.,i} - t_{.,s})$$

where  $t_{.,s}$  is the determined position of the laser pulse in  $S[t]$  and the subscript  $\cdot$  is the place holder for the used method.

**Peak detection** This detector takes as  $t_{pd,s}$  the timestamp of the sample with maximum amplitude in  $S[t]$  [Jutzi and Stilla 2003]. The same is done for segments of  $P_r[t]$ . The segment limits are determined by the first and last of subsequent samples exceeding a certain threshold, e.g. 20% of the maximum amplitude of  $P_r[t]$  [Wagner et al.

2004]. Subsample location can be achieved by determining the zero crossings of the first derivative of  $S[t]$  [Gonzalez and Woods 2008]:

$$\frac{\partial S[j\Delta t]}{\partial t} = S[(j+1)\Delta t] - S[j\Delta t]. \quad (3.1)$$

The first derivative of  $P_r[t]$  is derived analogously; the zero crossings are determined by linear interpolation [Wagner et al. 2004]. Another possibility for subsample location is to determine the peak of a parabola passing through the maximum and its left and right neighbours (see Section 3.1.2.1).

**Zero crossing of second derivative** This method aims at locating the zero crossings  $t_{\text{infl},}$  of the *second* derivatives, i.e. their inflection points. This second derivative is given as [Gonzalez and Woods 2008]

$$\frac{\partial^2 S[j\Delta t]}{\partial t^2} = S[(j+1)\Delta t] - 2S[j\Delta t] + S[(j-1)\Delta t] \quad (3.2)$$

in case of the system waveform and analogously for  $P_r[t]$ . Again, a subsample location can be derived by linear interpolation.

**Leading edge (threshold)** With this method, pulse and echoes are extracted at positions  $t_{\text{thr},}$  where the leading edges of  $S[t]$  and  $P_r[t]$  exceed a certain threshold, typically given as a percentage of the maximum amplitude appearing in the respective time series [Jutzi and Stilla 2003; Wagner et al. 2004]. Sub-sample location is achieved by linear interpolation.

**Constant fraction determination** This method is aimed at determining zero crossings  $t_{\text{cf},}$  in the difference of the original signal and a shifted, attenuated copy of it [Jutzi and Stilla 2003; Wagner et al. 2004]:

$$S_{\text{cf}}[t] = S[t] - a \cdot S[t + \tau] \text{ and } P_{r,\text{cf}}[t] = P_r[t] - a \cdot P_r[t + \tau].$$

The delay  $\tau$  is typically chosen as the full width at half maximum (FWHM) of the system waveform, rounded to an integer multiple of the sampling interval  $\Delta t$  [Jutzi 2007] and the attenuation factor  $a$  is chosen within the interval  $[0, 1]$ .

**Center of gravity** The center of gravity (CoG) of a time series is found as its weighted mean:

$$\begin{aligned} t_{\text{cog},s} &= \left( \sum_{j=j-}^{j+} S[j\Delta t] \right)^{-1} \left( \sum_{j=j-}^{j+} j\Delta t S[j\Delta t] \right), \\ t_{\text{cog},i} &= \left( \sum_{k=k_{i-}}^{k_{i+}} P_r[k\Delta t] \right)^{-1} \left( \sum_{k=k_{i-}}^{k_{i+}} k\Delta t P_r[k\Delta t] \right). \end{aligned} \quad (3.3)$$

The limits  $j-$ ,  $j+$ ,  $k_{i-}$  and  $k_{i+}$  of the waveform segments are the first and last of subsequent samples exceeding a certain threshold, e.g. 20% of the maximum amplitude [Wagner et al. 2004]. If the signal areas are surrounded by Gaussian noise with mean 0, these indices do not need to be determined exactly [Jutzi 2007].

Figure 3.1 illustrates the performance of the presented detectors by means of a complex echo waveform recorded with an Optech ALTM 3100 instrument [Optech Inc. 2014]. The numerical results are given in Table 3.2.

Method	$t_{,S}$	$t_{,1}$	$t_{,2}$	$t_{,3}$	$t_{,4}$	$t_{,5}$
pd	19.65	8980.00	9002.00	9033.00	9088.00	–
infl	14.91	8977.14	8996.67	9000.33	9028.50	9084.50
thr	11.72	8972.61	9023.47	9079.60	–	–
cf	22.73	8983.42	9035.72	9068.09	9091.21	–
cog	21.38	8991.28	9034.75	9089.54	–	–

Method	$R_{,1}$	$R_{,2}$	$R_{,3}$	$R_{,4}$	$R_{,5}$
pd	1342.76	1346.05	1350.70	1358.94	–
infl	1343.04	1345.96	1346.51	1350.73	1359.10
thr	1342.84	1350.46	1358.87	–	–
cf	1342.81	1350.65	1355.50	1358.96	–
cog	1344.19	1350.70	1358.91	–	–

**Table 3.2:** Numerical results of echo detection using classical detectors for the example shown in Figure 3.1. Time stamps are given in ns and ranges are given in m.

### 3.1.1.2 Finite-Mixture Model

In [Mallet et al. 2010], echo waveforms are decomposed to a finite-mixture model using a Monte Carlo sampler in a marked point process. Originally developed for fitting a mixture of *Generalized Gaussian* functions to the echo waveform in a least-squares approach [Chauve et al. 2007], the method was enlarged to three families of functions. The first one are the already mentioned Generalized Gaussian functions of the form

$$f(t) = Ae^{-\frac{(t-\mu)^{\alpha^2}}{2\sigma^2}} \quad (3.4)$$

with the parameters: Amplitude  $A$  (comparable to  $\hat{P}_i$  in Gaussian Decomposition, see Section 3.2.1), the mean  $\mu$  (comparable to  $\mu_i$  in Gaussian Decomposition), the standard deviation  $\sigma$  (comparable to  $s_{p,i}$  in Gaussian Decomposition) and shape parameter  $\alpha^2$ . For  $\alpha^2 = 2$ ,  $f(t)$  is a Gaussian function.

The second family is the one of *Nakagami* functions which are generalized  $\chi$  distributions of the form

$$f(t) = A \frac{2\xi^\xi}{\omega\Gamma(\xi)} \left(\frac{t-s}{\omega}\right)^{2\xi-1} e^{-\xi\frac{(t-s)^2}{\omega}} \quad (3.5)$$

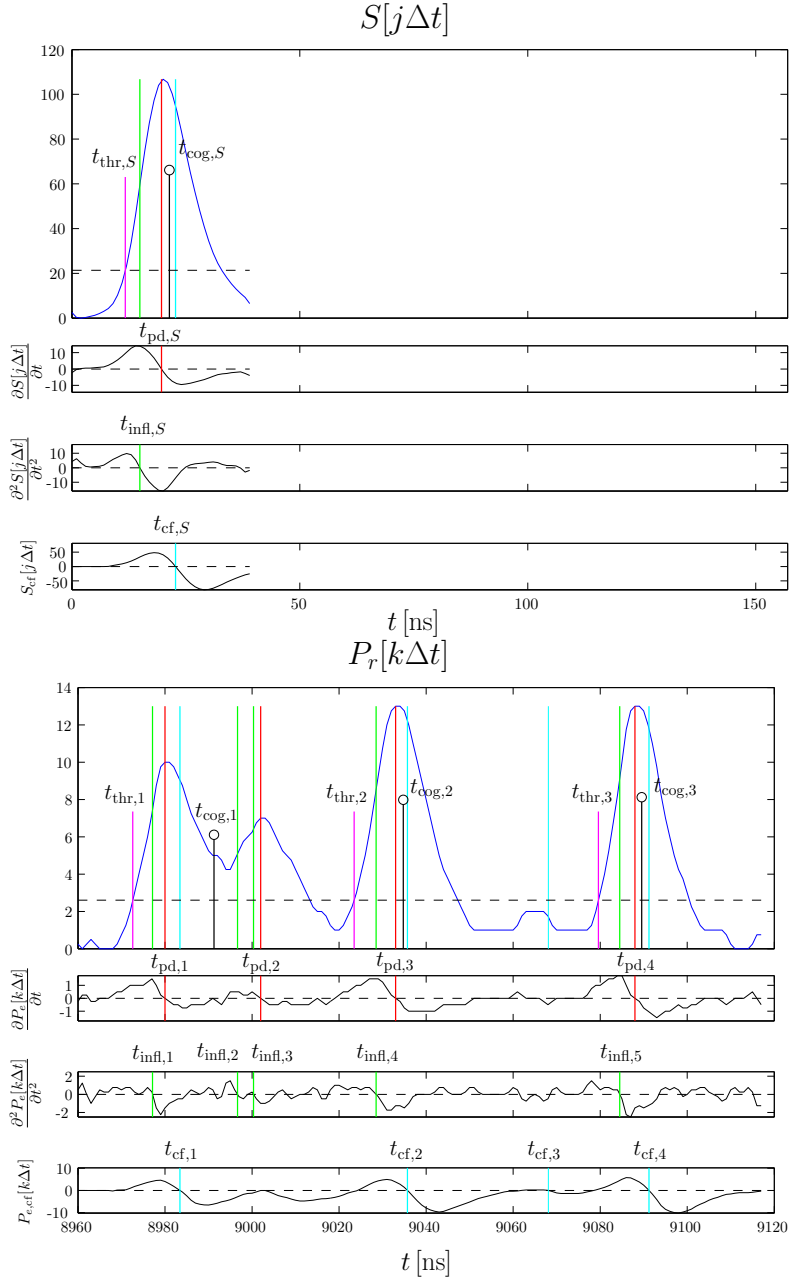


**Figure 3.1:** Pulse and echo detection by classical detectors in a sampled system waveform  $S[t]$  (top) and recorded echo waveform  $P_r[t]$  (bottom). Both waveforms were filtered by a binomial filter for noise suppression. The red lines indicate detected peaks found as zero crossings of the first derivatives, the green lines indicate inflection points (zero crossings of second derivatives). Lines in cyan give the echoes found by the constant fraction method whereas the leading edge is shown in magenta, at the point the waveform exceeds a certain threshold (black dashed line). The centers of gravity are depicted as black circles. The corresponding numerical values are given in Table 3.2.

with parameters  $A$  (amplitude),  $s$  (shift),  $\xi$  (shape parameter) and  $\omega$ . The latter is a parameter for skewness and spreading of the function along the  $t$  axis. The last set of functions is the one of *Burr* functions having the form

$$f(t) = A \frac{bc}{a} \left( \frac{t-s}{a} \right)^{-b-1} \left( 1 + \left( \frac{t-s}{a} \right)^{-b} \right)^{-c-1} \quad (3.6)$$

with parameters  $A$  (amplitude),  $s$  (shift),  $b$ ,  $a$  (spreading along the  $t$  axis) and  $c$ . Examples for Generalized Gaussian functions, Nakagami functions and Burr functions are shown in Figures 3.2 – 3.4.

For each waveform, an a-priori probability for the number of echoes was assigned, based on the distribution found in a test area. The estimation is intended to limit the number of echoes according to the minimum description length principle. Convergence of the algorithm is reached by simulated annealing.

In the examples given by [Mallet et al. 2010], the vast majority of cases resulted to Generalized Gaussian functions, followed by Nakagami and Burr.

Please note that not all base functions in finite-mixture models are suited for the reconstruction of the dBCS. Gaussian Decomposition is one of such cases allowing for interpretability of the function parameters in the context of deconvolution and dBCS reconstruction under certain assumptions; see Sections 4.4.3 and A.2. However, a link of function parameters to object attributes might still be possible, as the results of Mallet et al. 2011 have shown.

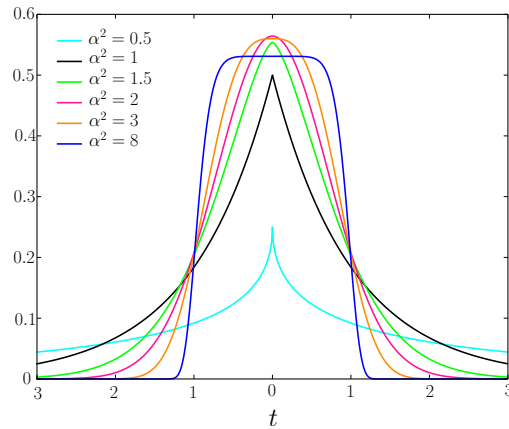


**Figure 3.2:** Left: Generalized Gaussian functions (Equation (3.4)) with varying shape parameter  $\alpha^2$ ;  $\mu = 0$ ,  $A = \sigma = 1$ . Source: [http://upload.wikimedia.org/wikipedia/commons/1/10/Generalized\\_normal\\_densities.svg](http://upload.wikimedia.org/wikipedia/commons/1/10/Generalized_normal_densities.svg).

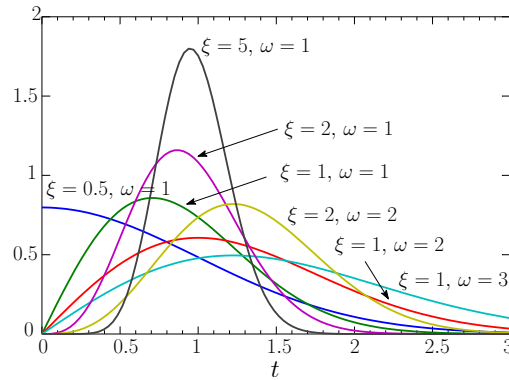


**Figure 3.3:** Nakagami functions (Equation (3.5)) for different  $\xi$  and  $\omega$ ;  $A = 1$ ,  $s = 0$ . Source: [http://upload.wikimedia.org/wikipedia/commons/d/d0/Nakagami\\_pdf.svg](http://upload.wikimedia.org/wikipedia/commons/d/d0/Nakagami_pdf.svg).

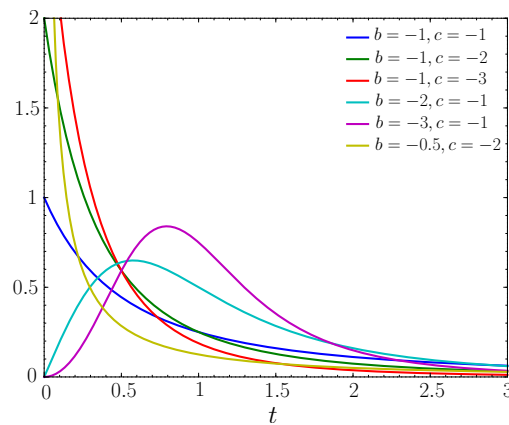


**Figure 3.4:** Burr functions (Equation (3.6)) for different values of  $b$  and  $c$ ;  $A = a = 1$ ,  $s = 0$ . Source: [http://upload.wikimedia.org/wikipedia/commons/d/d0/Burr\\_pdf.svg](http://upload.wikimedia.org/wikipedia/commons/d/d0/Burr_pdf.svg).



### 3.1.2 Own Contribution

This section deals with the extraction and localization of echoes in FWF data by means of the Averaged Square Difference Function (ASDF) as presented in [Jacovitti and Scarano 1993]. This function is closely related to the correlation function. The presentation follows the references [Roncat et al. 2008] and [Wagner et al. 2007].

#### 3.1.2.1 The Averaged Square Difference Function (ASDF)

The Averaged Square Difference Function (ASDF) is a time delay estimation technique based on the correlation of a sampled reference signal and the sampled return signal [Jacovitti and Scarano 1993]. In the case of FWF-ALS data, the reference signal is the sampled system waveform  $S[i\Delta t]$  and the return signal corresponds to the recorded echo waveform  $P_r[j\Delta t]$ . Both are equidistantly sampled time series with sampling interval  $\Delta t$ . A suitable distance measure between  $S[k\Delta t]$  and the shifted echo waveform  $P_r[k\Delta t + \tau]$  is the response value  $r_A$  of their ASDF which is defined as follows [Jacovitti and Scarano 1993]:

$$r_A(\tau, S, P_r) = \frac{1}{N} \sum_{k=1}^N (S[k\Delta t] - P_r[k\Delta t + \tau])^2 \quad (3.7)$$

where the time shift  $\tau = -N\Delta t, -(N-1)\Delta t, \dots, (N-1)\Delta t, N\Delta t$  is an integer multiple of the sampling interval  $\Delta t$ . Figure 3.5 shows an example for  $S[i\Delta t]$  and  $P_r[j\Delta t]$  and their ASDF response value  $r_A$ , recorded with a Riegl LMS-Q560 instrument.

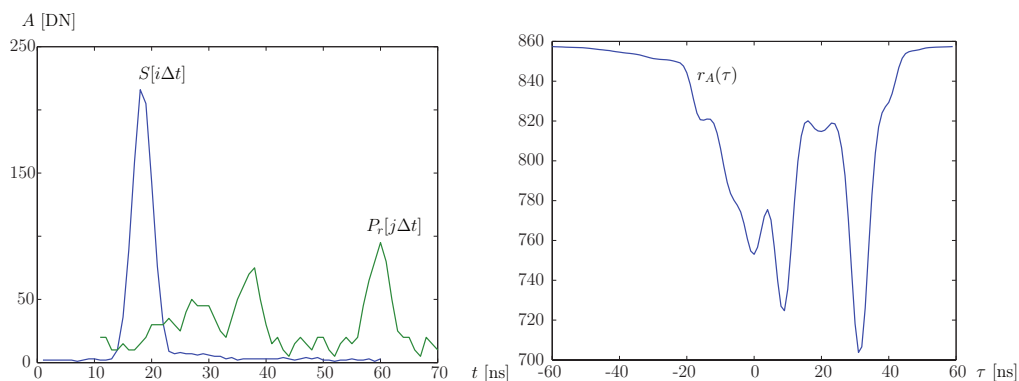


**Figure 3.5:** Left: A sampled system waveform  $S[i\Delta t]$  (blue) and its recorded echo waveform  $P_r[j\Delta t]$  (green). Right: resulting response values  $r_A(\tau, S, P_r)$  of their ASDF.

The goal is to detect and to localize precisely the echoes of the system waveform. As  $r_A(\tau, S, P_r)$  becomes minimal at  $r_A(0, S, S)$ , i.e.  $P_r$  is an exact copy of  $S$  and  $\tau = 0$ , we consider such integer values  $d$  as candidate positions for echoes fulfilling

$$d = \arg \min_{\tau} (r_A(\tau, S, P_r)). \quad (3.8)$$

In the following text, we will always take  $S[i\Delta t]$  as second and  $P_r[j\Delta t]$  as third argument so that we will shortly refer to the ASDF response value as  $r_A(\tau)$ .

Since multiple echoes may appear, not only the global minimum of  $r_A(\tau)$ , but also its local minima have to be taken into account. To retrieve initial estimates for those minima, several criteria for minima detection have been applied as follows:

- classical minimum detection:  $r_A(\tau)$  has to be lower or equal than its “neighbours”  $r_A(\tau - \Delta t)$  and  $r_A(\tau + \Delta t)$
- first discrete derivative

$$\frac{dr_A(\tau)}{d\tau} := \frac{1}{2} (r_A(\tau + \Delta t) - r_A(\tau - \Delta t)).$$

Change in sign (from negative to positive) in the first derivative at  $\tau = d$ :

$$\frac{dr_A(d - \Delta t)}{d\tau} < 0 \text{ and } \frac{dr_A(d + \Delta t)}{d\tau} > 0.$$

The first derivatives of the neighbouring points are used to decrease the sensitivity of the algorithm to saw tooth distortions in the waveform. The above criteria are also applied to detect local maxima of  $r_A(\tau)$  using  $-r_A(\tau)$ . To make the echo detection more robust, three additional criteria are applied:

- To avoid the detection of noise peaks, the maximum of  $P_r[j\Delta t]$  has to be greater or equal than a certain threshold which is empirically chosen by means of selected waveforms.
- To avoid the detection of subsequent minima in a minimal “plateau” of  $t_A(\tau)$ , there has to be a local maximum of  $t_A(\tau)$  at a position  $d_3$  between two subsequent local minima at positions  $d_1$  and  $d_2$ , i.e.  $d_1 < d_3 < d_2$ .
- Subtle local minima as shown in Figure 3.6 ( $\min_1$  and  $\min_4$ ) are suppressed by the following threshold criterion

$$\max\{r_{\max,l} - r_A(d), r_{\max,r} - r_A(d)\} \geq \Delta r_A := 0.3(\max(r_A(\tau)) - \min(r_A(\tau)))$$

where  $r_{\max,l}$  and  $r_{\max,r}$  are the response values of the left and right neighbouring local maxima of  $r_A(d)$ . This threshold was empirically selected.

After the echo detection, the echo positions were estimated with sub-sampling accuracy by using parabola fitting [Jacovitti and Scarano 1993]. Given a coarsely estimated echo at a position  $d$ , its fine position  $d_f$ , i.e. the peak of the parabola is at

$$d_f = -\frac{\Delta t}{2} \frac{r_A(d + \Delta t) - r_A(d - \Delta t)}{r_A(d + \Delta t) - 2r_A(d) + r_A(d - \Delta t)} + d. \quad (3.9)$$

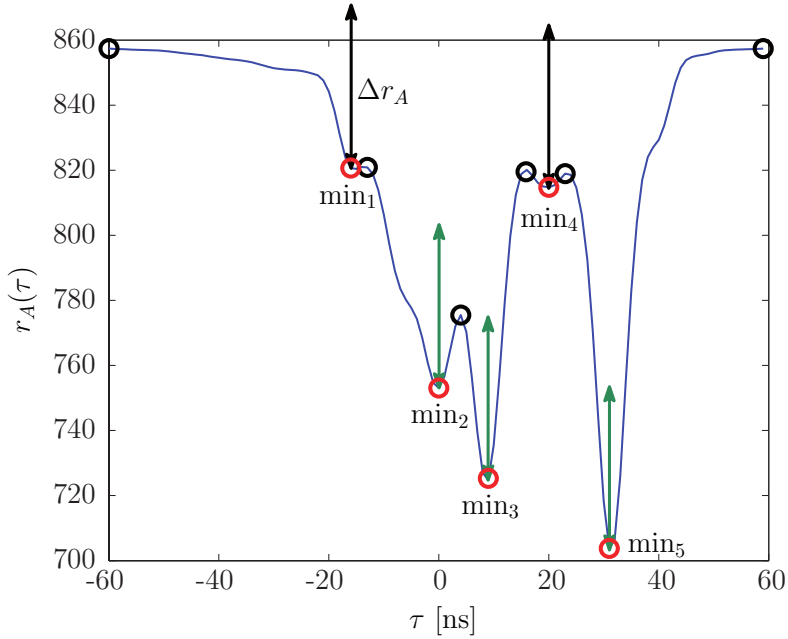


**Figure 3.6:** Application of different criteria for robust echo detection: Red circles: local minima, black circles: local maxima. The length of the arrows equals  $\Delta r_A$ . Green arrow: echo candidate accepted, black arrow: echo candidate rejected because of threshold criterion.

### 3.1.2.2 Derivation of Echo Parameters from the ASDF

Let us consider the fitted parabola from the above section. It is a quadratic function with its apex at the position  $\tau = d_f$  so that we can express the parabola fit of  $r_A(\tau)$  around  $d_f$  as

$$r_A(\tau) = a(\tau - d_f)^2 + r_0.$$

While  $d_f$  gives the echo location,  $a$  can be considered as a vertical scaling parameter of  $r_A$  at the echo position and as an echo attribute.

A second attribute is the *significance level*  $s$  of an echo, defined as the minimum of the difference to the neighbouring maxima in  $r_A$ :

$$l_s := \min \{r_{\max,l} - r_A(d), r_{\max,r} - r_A(d)\}. \quad (3.10)$$

The values of  $l_s$  are in the interval  $[0, 1]$ . The two echo parameters  $a$  and  $l_s$  are illustrated for a whole ALS flight strip in Section 4.2.

## 3.2 Approaches including Deconvolution

The techniques described in this section aim at the removal of the system waveform's influence on the shape of the received echo waveform via deconvolution. This removal is

a pre-requisite for the determination of *target* parameters, i.e. quantities only dependent on physical properties of the scattering surface within the laser footprint at the used wavelength.

### 3.2.1 Related Work

#### 3.2.1.1 Gaussian Decomposition

This technique, also referred to as Gaussian Mixture Model [Mallet et al. 2010], is aimed at modeling the recorded echo waveform  $P_r(t)$  as sum of Gaussian functions, i.e. scaled normal distributions [Hofton et al. 2000; Wagner et al. 2006]:

$$P_r(t) = \sum_{i=1}^N \hat{P}_{r,i} e^{-\frac{t-t_i}{s_i^2}} = \sum_{i=1}^N \hat{P}_{r,i} \sqrt{2\pi} s_i \mathcal{N}(t_i, s_i^2), \quad (3.11)$$

so each scatterer is represented by a normal distribution with mean  $t_i$  and variance  $s_i^2$ , scaled by the factor  $\hat{P}_{r,i} \sqrt{2\pi} s_i$  (see also Section A.2 in the appendix).

The fit is aimed at minimizing the squared sum of the residuals, i.e.

$$\left| \sum_{j=1}^{\#j} \left( \sum_{i=1}^N \hat{P}_{r,i} e^{-\frac{t_j-t_i}{s_i^2}} \right) - P_r[t_j] \right|^2 \rightarrow \min.$$

with  $\#j$  being the number of samples in the recorded echo waveform. The fit is established by non-linear optimization, e.g. the Levenberg-Marquardt algorithm [Wagner et al. 2006]. A crucial point is the determination of the model complexity represented by the number of scatterers  $N$ . This might either be done using classical detectors (see Section 3.1.1.1), correlation (see Section 3.1.2.1) or by means of statistical criteria. Examples for such criteria are the Minimum Description Length or the Akaike Information Criterion [Hernández-Marín et al. 2007]. Mallet et al. [2010] determine the number of scatterers in a marked-point process. In the example given in Figure 3.7,  $P_r(t)$  was modeled as sum of four Gaussian functions [cf. Wagner et al. 2008].

The technique of Gaussian decomposition was introduced in the lidar community by Hofton et al. [2000]. In this reference, the approach was applied to Laser Vegetation Imaging Sensor (LVIS) waveform data. Wagner et al. [2006] extended the approach by modeling the system waveform  $S(t)$  as Gaussian function as well:

$$S(t) = \hat{S} e^{-\frac{t-t_s}{s_s^2}} = \hat{S} \sqrt{2\pi} s_s \mathcal{N}(t_s, s_s^2). \quad (3.12)$$

In analogy to the recorded echo waveform, the best fit to the sampled values  $S[t]$  is also found by non-linear estimation.

With  $S(t)$  being a Gaussian function, we can reconsider the convolution properties of Gaussian functions (see Section A.2 in the appendix for the derivation): The convolution of two Gaussians  $S(t)$  and  $\bar{\sigma}_i^t(t)$  again gives a Gaussian  $P_{r,i}(t)$  where

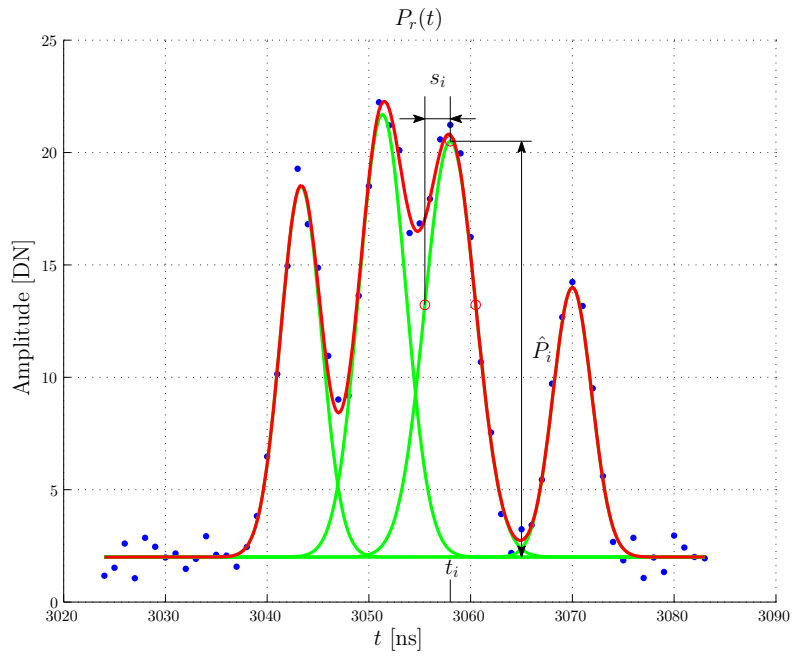


**Figure 3.7:** Recorded echo waveform  $P_r(t)$ , modeled as sum of four Gaussian functions. The original sampled values  $P_r[t]$  are indicated by the blue dots.

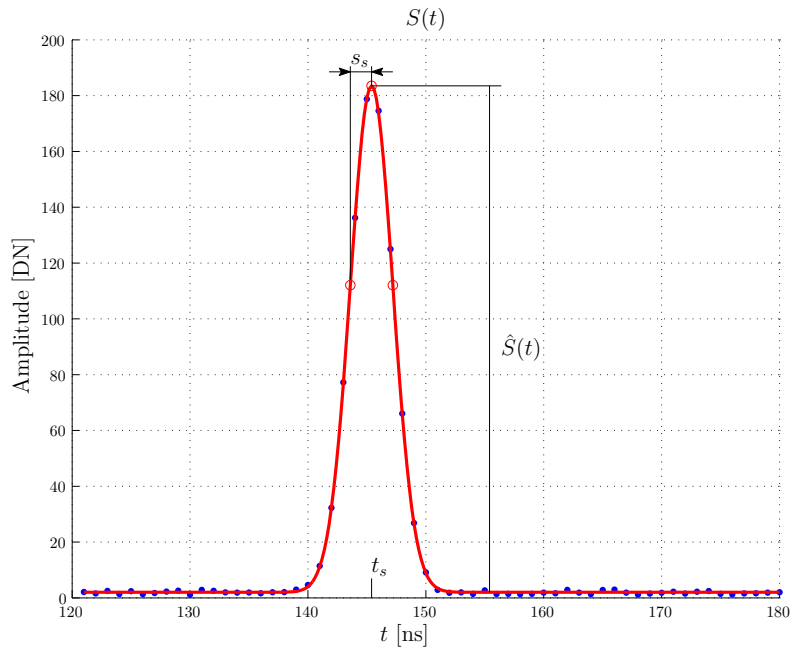


**Figure 3.8:** Modeling the system waveform  $S(t)$  as Gaussian function. The original sampled values  $S[t]$  are indicated by the blue dots.

- the resulting mean  $t_i$  is the sum of the operands' means:

$$t_i = t_s + t_{\sigma,i},$$

- the resulting variance  $s_i$  is the sum of the operands' variances:

$$s_i^2 = s_s^2 + s_{\sigma,i}^2,$$

- the resulting scaling factor w.r.t. the underlying normal distribution  $\mathcal{N}(t_i, s_i^2)$  is the product of the operands' scaling factors:

$$P_{r,i}(t) = 2\pi \left( \hat{S} s_s \right) \left( \hat{C}_i s_{\sigma,i} \right).$$

For the inverse operation, i.e. the deconvolution  $\bar{\sigma}'_i(t) = P_{r,i}(t) \otimes^{-1} S(t)$ , we retrieve a Gaussian function with the parameters

$$t_{\sigma,i} = t_i - t_s \quad (3.13)$$

$$s_{\sigma,i}^2 = s_i^2 - s_s^2 \quad (3.14)$$

$$\hat{C}_i = \sqrt{2\pi} \frac{\hat{P}_i s_i}{\hat{S} s_s s_{\sigma,i}} \quad (3.15)$$

being the mean, variance and peak amplitude. The relation to the underlying normal distribution is therefore given by

$$\bar{\sigma}'_i(t) = \hat{C}_i \sqrt{2\pi} s_{\sigma,i} \mathcal{N}(t_{\sigma,i}, s_{\sigma,i}^2) = \frac{\hat{P}_i s_i}{\hat{S} s_s} \mathcal{N}(t_i - t_s, s_i^2 - s_s^2). \quad (3.16)$$

Figure 3.9 shows the result of the deconvolution of  $P_r(t)$  by  $S(t)$  of Figure 3.7 and 3.8, resp. Since  $P_r(t)$  consists of four Gaussian functions, the deconvolution  $\bar{\sigma}'(t)$  represents four scatterers.

### 3.2.1.2 Wiener Filter Deconvolution

Again, the recorded echo waveform  $P_r(t)$  is modeled as the convolution of the system waveform  $S(t)$  and a scaled version of the differential backscatter cross-section  $\bar{\sigma}'(t)$ :

$$P_r(t) = S(t) \otimes \bar{\sigma}'(t).$$

Using the Fourier transform, we get [Weisstein 2014a]

$$\underline{P}_r(\omega) = \underline{S}(\omega) \cdot \underline{\bar{\sigma}}'(\omega)$$

and we can retrieve  $\bar{\sigma}'(t)$  by

$$\underline{\bar{\sigma}}'(\omega) = \frac{\underline{P}_r(\omega)}{\underline{S}(\omega)}$$

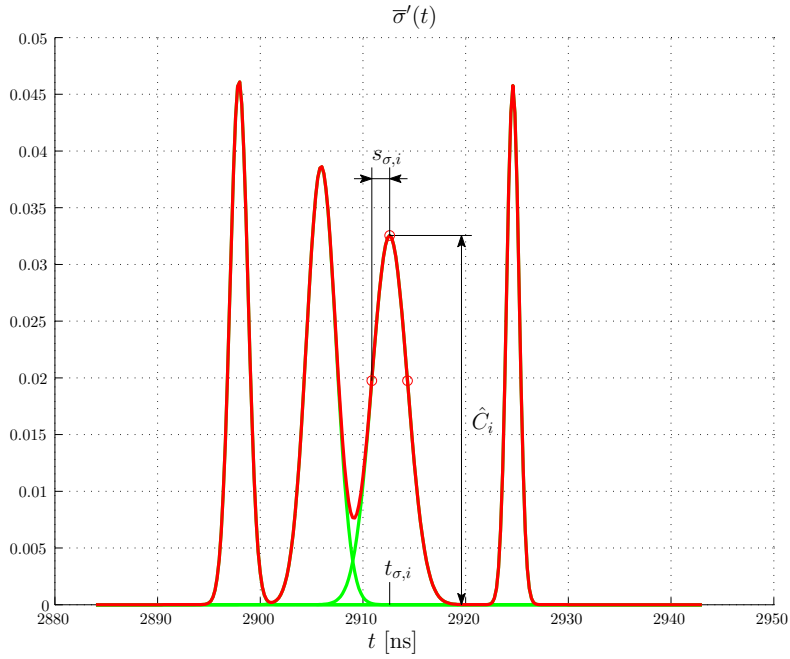


**Figure 3.9:** Deconvolution  $\bar{\sigma}'(t) = P_r(t) \otimes^{-1} S(t)$ .

and the inverse Fourier transform.

Unlike the Gaussian Decomposition approach presented in Section 3.2.1.1, deconvolution is performed on the sampled waveforms  $S[t]$  and  $P_r[t]$ ; we denote their (discrete) Fourier transforms in the subsequent text as  $\underline{S}[\omega]$  and  $\underline{P}_r[\omega]$ , resp.

In presence of noise, the direct solution by the division of spectra may become unstable because this division tends to amplify the noise at high frequencies; the system waveform and the recorded echo waveform are therefore modeled with an additional noise term  $n[t]$  [Jutzi and Stilla 2006]:

$$S_n[t] = S[t] + n[t] \text{ and } P_{r,n}[t] = P_r[t] + n[t].$$

For noise suppression, a Wiener Filter is used, minimizing the mean squared error between  $\underline{\sigma}'[\omega]$  its estimate  $\hat{\underline{\sigma}}'[\omega]$ :

$$W[\omega] = \frac{|P_r[\omega]|^2}{|P_r[\omega]|^2 + |N[\omega]|^2} \quad (3.17)$$

with  $\underline{N}[\omega]$  being the Fourier transform of the noise term  $n[t]$ . This noise term is estimated by analysing the non-signal part of  $S[t]$  and  $P_r[t]$ .

In case of orthogonal incidence ( $\vartheta = 0$ ),  $\underline{P}_r[\omega] \sim \underline{S}[\omega]$ ; thus, the Wiener filter can be estimated as [Jutzi and Stilla 2006]

$$\hat{W}[\omega] = \frac{|\underline{S}[\omega]|^2}{|\underline{S}[\omega]|^2 + |\underline{N}[\omega]|^2}.$$

A “noise-free” estimation of the system waveform’s Fourier transform,  $\hat{\underline{S}}[\omega]$ , is retrieved by lowpass filtering  $S_n[t]$  with a binomial filter in time domain and subsequent Fourier transformation. We finally get the Fourier transform of the deconvolution as

$$\hat{\underline{\sigma}}'[\omega] = \frac{P_{r,n}[\omega]}{\hat{\underline{S}}[\omega]} \hat{W}[\omega] \quad (3.18)$$

and  $\hat{\sigma}'[t]$  by the inverse Fourier transformation.

Jutzi and Stilla [2006] fit a superposition of Gaussians to  $\hat{\sigma}'[t]$  for target localization ( $t_{\sigma,i}$ ) and assigning additional parameters amplitude  $A_i$  and width  $s_{\sigma,i}$  to these targets:

$$\hat{\sigma}'(t) = \sum_{i=1}^N A_{\sigma,i} e^{-\frac{(t-t_{\sigma,i})^2}{2s_{\sigma,i}^2}}$$

aiming at

$$\sum_{i=1}^N \sum_{j=1}^{\#j} \left( A_{\sigma,i} e^{-\frac{(t_j-t_{\sigma,i})^2}{2s_{\sigma,i}^2}} - \hat{\sigma}'[t_j] \right)^2 \rightarrow \min .$$

The whole approach is therefore referred to as “hybrid deconvolve-decompose approach” by Parrish et al. [2011]. In the same reference, filtering the deconvolution by a lowpass Gaussian filter before the fitting of Gaussians is suggested in order to avoid ringing artefacts.

The final fitting of Gaussians to the deconvolution is done in a similar way as the derivation of *echo* amplitude and width in Gaussian Decomposition (see Section 3.2.1.1). However, for performing the deconvolution in Gaussian Decomposition, the system waveform is required to be a Gaussian function as well. This is not the case in Wiener-Filter deconvolution.

### 3.2.1.3 Expectation/Maximization Deconvolution

This approach is aimed at performing a discrete deconvolution in time domain. Convolution is set up as [Parrish and Nowak 2009]

$$P_r[t] = S[t] \otimes \bar{\sigma}'[t] + n[t] \quad (3.19)$$

with  $n[t]$  being an additional noise term as in Section 3.2.1.2. This noise term is assumed as Gaussian noise of mean 0 and variance  $s_n^2$ . Deconvolution is formulated as a Bayesian



estimation problem, incorporating additional knowledge: The ideal deconvolution is set up as a train of spikes, each of them representing a scattering target. The prior is the probability density of such a spike at each sampled point in time, each timestamp is considered as independent of the others [Parrish and Nowak 2009].

The numerical solution to this problem is found in an iterative two-step procedure known as Expectation/Maximization (EM) [Kay 1993]:

**Expectation step (E):** Determination of the average log-likelihood of the complete data (signal and noise components)

**Maximization step (M):** This average log-likelihood function of the complete data is maximized.

For the deconvolution problem, this means that the actual deconvolution is performed in the expectation step

$$\hat{z}^{(k)}[t] = \hat{\sigma}'^{(k)}[t] + S^*[t] \otimes \left( P_r[t] - S[t] \otimes \hat{\sigma}'^{(k)}[t] \right) \quad (3.20)$$

with  $k$  denoting the iteration counter,  $S^*[t]$  denoting the complex conjugate of the discrete system waveform  $S[t]$  and  $\hat{z}^{(k)}[t]$  being the estimate of the missing data in the procedure. The M-step, also referred to as denoising step, is given as

$$\hat{\sigma}'^{(k+1)}[t] = \frac{\max\{(\hat{z}^{(k)}[t])^2 - \tau s_n^2, 0\}}{\hat{z}^{(k)}[t]} \quad (3.21)$$

with the *tuning parameter*  $\tau$  controlling the model complexity, i.e. the number of spikes. This  $\tau$  is inversely related to the prior probability of a spike at a specific location. In an empirical study by Parrish et al. [2011],  $\tau$  resulted to 0.1.

Iteration is stopped when the relative difference between two subsequent estimates of  $\hat{\sigma}'[t]$  falls below a certain threshold, e.g.  $10^{-3}$  [Parrish and Nowak 2009].

### 3.2.2 Own Contribution: Deconvolution by Means of uniform B-Splines

In this section, a B-spline-based deconvolution algorithm is presented in detail, based on the study by Roncat et al. [2011a]. We start with the basic definitions, present curve fitting of both system and recorded waveform, and introduce a least-squares deconvolution approach.

### 3.2.2.1 B-Spline Curves

A uniform B-spline  $B_l^n(t)$  is a piecewise continuous polynomial function of degree  $n$  with  $C^{n-1}$  continuity, being positive in the interval  $[l\Delta t; (n+l+1)\Delta t]$  and zero outside. Starting with the  $B_l^0(t)$  being step functions, the uniform B-splines of higher degrees are constructed by repetitive convolution, as described in detail in Section A.1 in the appendix. A B-spline curve  $\gamma(t) = (\gamma_1(t), \dots, \gamma_m(t))^\top \in \mathbb{R}^m$  of degree  $n$  is defined as a linear combination of B-splines

$$\gamma(t) = \sum_{i=1}^{i_{\max}} \mathbf{b}_i B_i^n(t). \quad (3.22)$$

The  $\mathbf{b}_i \in \mathbb{R}^m$  are called *control points*.

Fitting a B-spline curve to observations is a linear least-squares problem

$$\sum_{j=1}^{j_{\max}} \left( y(t_j) - \sum_{i=1}^{i_{\max}} \mathbf{b}_i B_i^n(t_j) \right)^2 \rightarrow \min., \quad (3.23)$$

where in our case the  $y(t_j)$  denote the observed amplitude values of the recorded waveform at time  $t_j$  and the  $\mathbf{b}_i$  denote the unknown control points.

In the case of full-waveform laser scanning, the values of  $t$  are given in a “natural” way by the recorded time stamps, i.e.  $t_j = \Delta t, 2\Delta t, \dots, j_{\max}\Delta t$ . The dimension of the  $\mathbf{b}_i$  is 1, i.e.  $\mathbf{b}_i = b_i$ . With the knot vector spacing  $\Delta u \geq \Delta t$ , and  $t_j$  as above, the minimization of Equation (3.23) has a unique solution, if, additionally,  $i_{\max}\Delta u \geq j_{\max}\Delta t$ . With  $\Delta u = \Delta t$ , the system is not overdetermined. It is explicitly noted that no multiplicity at the end points of the knot vector is introduced, which would lead to the interpolation of the first and the last control point.

### 3.2.2.2 Deconvolution of B-Spline Curves

The convolution of two B-splines  $B_{l_1}^{n_1}(t) \otimes B_{l_2}^{n_2}(t)$  with uniform knot vector gives the B-spline  $B_{l_1+l_2-1}^{n_1+n_2+1}(t)$ ; see Section A.1 for details.

Aiming at full-waveform laser scanning, the system waveform (subscript  $s$ ) and the scaled differential backscatter cross-section (abbreviated by dBCS, subscript  $\sigma$ ) are convolved to result in the recorded echo waveform (subscript  $r$ ). The degrees  $n_s$  and  $n_\sigma$  of the B-spline curves approximating the system waveform and the (yet unknown) scaled dBCS, respectively, can be chosen arbitrarily. However, literature on curve fitting focuses mainly on cubic B-splines [e.g. Farin 2002; Prautzsch et al. 2002]. Degrees below 3 lead to curves which are too inflexible for fitting, whereas higher degrees do not provide additional advantages, unless  $C^3$  and higher-order continuity is required.

The degree  $n_r$  of the approximating B-spline curve representing the received echo waveform is  $n_r = n_s + n_\sigma + 1$  (see Equation (A.5)). The length of the knot vector of this curve is  $k_{\max} = i_{\max} + j_{\max} - 1$ .

Defining the B-spline approximation of the emitted waveform as

$$S(t) := \sum_{i=1}^{i_{\max}} b_{i,s} B_i^{n_s}(t),$$

the one representing the (still unknown) scaled dBCS as

$$\bar{\sigma}'(t) := \sum_{j=1}^{j_{\max}} b_{j,\sigma} B_j^{n_\sigma}(t),$$

and the one representing the received echo waveform as

$$\begin{aligned} P_r(t) &:= \sum_{k=1}^{k_{\max}=i_{\max}+j_{\max}-1} b_{k,r} B_k^{n_r}(t) \\ &= \sum_{i=1}^{i_{\max}} \sum_{j=1}^{j_{\max}} (b_{i,s} B_i^{n_s}(t)) \otimes (b_{j,\sigma} B_j^{n_\sigma}(t)) \end{aligned}$$

and, therefore (see Equation (A.5))

$$P_r(t) = \sum_{i=1}^{i_{\max}} \sum_{j=1}^{j_{\max}} (b_{i,s} b_{j,\sigma}) \underbrace{(B_i^{n_s}(t) \otimes B_j^{n_\sigma}(t))}_{B_{i+j-1}^{n_s+n_\sigma+1} = B_{i+j-1}^{n_r}},$$

this yields for the values of the received waveform's control points

$$b_{k,r} = \sum_{i,j:i+j-1=k} b_{i,s} b_{j,\sigma}. \quad (3.24)$$

The values of the control points of the scaled dBCS,  $b_{j,\sigma}$ , can be determined using the scheme of Equation (3.24). Interpreting this equation as an observation equation for least squares adjustment, the control points of the recorded echo waveform are the observations. The control points of the emitted waveform are known quantities, and the control points of the scaled dBCS are the unknowns. The observations are acquired in a regular sequence with the same device, thus equal weighting is suggested.

The least-squares deconvolution has a redundancy of

$$\#\text{observations} - \#\text{unknowns} = (i_{\max} + j_{\max} - 1) - j_{\max} = i_{\max} - 1$$

Thus, in theory the redundancy only depends on the number of knots in the emitted waveform, but not on the length of the received waveform. However, the number of

knots of the received waveform,  $k_{\max}$ , has to be  $\geq i_{\max}$  to solve the equation system. The normal equation matrix of this system has a band form with a width of  $n_s + 1$ .

The disadvantage of the adjustment technique described above is that the parameters of the curve representing the emitted waveform,  $b_{i,s}$  are treated as constants in Equation (3.24), neglecting the fact that they were estimated in a least-squares adjustment. This can be overcome by an overall adjustment (i.e. curve fitting and deconvolution) following the general case for adjustment [cf. Mikhail 1976] after the single steps. In this case, the results of curve fitting and deconvolution serve as initial values for the parameters in the overall adjustment. Equation (3.23) gives the setup for the observation equations whereas Equation (3.24) gives the one for the constraints:

$$\begin{aligned} \mathbf{A}_1 \mathbf{x} &= \mathbf{y} + \mathbf{e} & \mathbf{A}_2 \mathbf{x} &= \mathbf{o} \\ \mathbf{A}_1 &= \begin{pmatrix} \mathbf{M}_\varepsilon & \mathbf{o} & \mathbf{o} \\ \mathbf{o} & \mathbf{o} & \mathbf{M}_\rho \end{pmatrix} & \mathbf{A}_2 &= (\mathbf{G}_\sigma, \mathbf{G}_\varepsilon, -\mathbf{I}) \\ \mathbf{x}^\top &= (\mathbf{b}_\varepsilon^\top, \mathbf{b}_\sigma^\top, \mathbf{b}_\rho^\top) & \mathbf{y}^\top &= (\mathbf{y}_\varepsilon^\top, \mathbf{y}_\rho^\top) \end{aligned}$$

so that the whole equation system reads as follows:

$$\begin{pmatrix} \mathbf{A}_1^\top \mathbf{A}_1 & \mathbf{A}_2^\top \\ \mathbf{A}_2 & \mathbf{o} \end{pmatrix} \begin{pmatrix} \mathbf{x} \\ \boldsymbol{\lambda} \end{pmatrix} = \begin{pmatrix} \mathbf{A}_1^\top \mathbf{y} \\ \mathbf{o} \end{pmatrix} \quad (3.25)$$

with

- $\mathbf{M}_\varepsilon$  ... Jacobian Matrix of Equation (3.23) w.r.t. unknown control points  $\mathbf{b}_\varepsilon$
- $\mathbf{M}_\rho$  ... Jacobian Matrix of Equation (3.23) w.r.t. unknown control points  $\mathbf{b}_\rho$
- $\mathbf{G}_\varepsilon$  ... Jacobian Matrix of Equation (3.24) w.r.t. unknown control points  $\mathbf{b}_\varepsilon$
- $\mathbf{G}_\sigma$  ... Jacobian Matrix of Equation (3.24) w.r.t. unknown control points  $\mathbf{b}_\sigma$

Since observations and constraints are linear and bi-linear equations, resp., the algorithm is expected to converge fast and almost surely. The investigations on empirical data already carried out did not show evidence for divergence.

A sample result for B-spline curve fitting and deconvolution is shown in Figure 3.10.

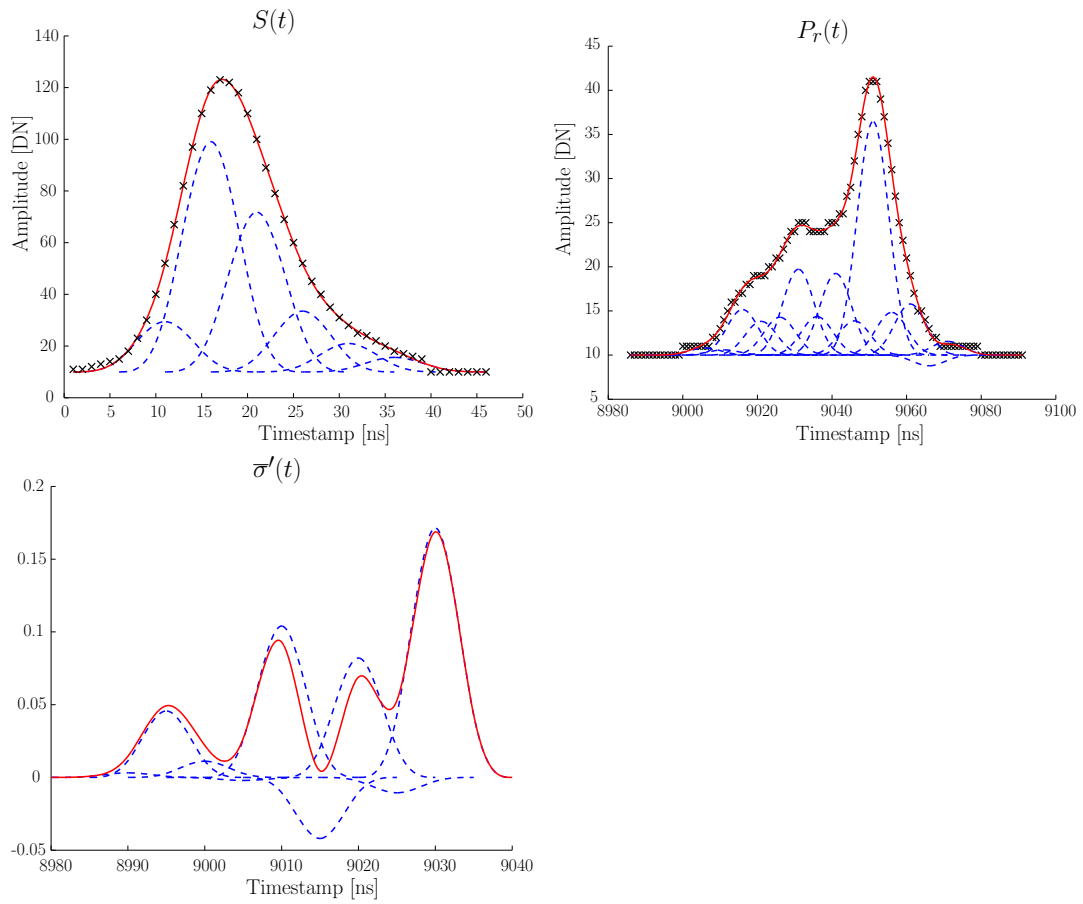


**Figure 3.10:** B-spline deconvolution of a received echo waveform by a system waveform, as recorded by an Optech ALTM 3100 system. Top: System waveform  $S(t)$  (left) and echo waveform  $P_r(t)$  (right). Bottom: Deconvolution  $\bar{\sigma}'(t)$ . The blue dashed curves indicate the single B-splines whereas the red solid curves represent the resulting B-spline curves of degree  $n_s = 3$ ,  $n_r = 7$  and  $n_\sigma = 7 - 3 - 1 = 3$ , resp. From [Roncat et al. 2012].

### 3.3 Radiometric Calibration of Full-Waveform Lidar Data

This section deals with the assignment of physically meaningful attributes to extracted targets and/or a deconvolved lidar waveform.

#### 3.3.1 Theory and related Work

The deconvolution approaches presented in Section 3.2 resulted in scaled versions  $\bar{\sigma}'(t)$  of the differential backscatter cross-section:

$$\sigma'(t) = \frac{4\pi\beta_t^2}{\eta_{\text{SYS}}\eta_{\text{ATM}}D_r^2} R^4 \bar{\sigma}'(t).$$

The right-hand side of this equation contains a constant factor

$$C_{\text{CAL}} := \frac{4\pi\beta_t^2}{\eta_{\text{SYS}}\eta_{\text{ATM}}D_r^2}$$

and a range-dependent factor

$$\tilde{\sigma}'(t) := R^4 \bar{\sigma}'(t).$$

The constant factor  $C_{\text{CAL}}$  is known as *calibration constant* [Wagner et al. 2006]. It summarizes the unknown yet constant parameters in the radar equation. Depending on the deconvolution approach and the temporal stability of the system waveform's shape, alternative versions for  $C_{\text{CAL}}$  have been proposed [cf. Briese et al. 2008; Roncat et al. 2012; Wagner 2010]; see also Section 3.3.2 of this thesis. The determination of the calibration constant is the core task within radiometric calibration which will be treated in detail in the subsequent sections.

Having determined  $C_{\text{CAL}}$ , the last step for calculating the backscatter cross-section  $\sigma$  of a target is to solve the integral in Equation (2.9):

$$\sigma = \int_{-\infty}^{\infty} \sigma'(t) dt.$$

If the resulting  $\sigma'(t)$  is a sum of Gaussian functions or B-splines, this task is straightforward (see Sections A.1 and A.2). In case of a discrete result  $\sigma'[t]$ , the integral is to be replaced by a sum and  $dt$  is to be replaced by the sampling interval  $\Delta t$ .

The backscatter cross-section  $\sigma$  is a physical target quantity for all first targets hit by a single laser shot. The subsequently hit targets are partly shadowed by the previous ones so that a physical meaning cannot be attributed to their  $\sigma$ . This quantity has the dimension of an area and is independent of the parameters of the system waveform. However, the influences of the laser footprint area  $A_L$  and the incidence angle  $\vartheta$  (see Figure 2.1) still remain. Elimination of the range influence leads to the introduction

of the *backscatter coefficient*  $\gamma$  and the *normalized backscatter cross-section*  $\sigma^0$  [Wagner 2010; Woodhouse 2006]:

$$\gamma = \frac{\sigma}{A \cos \vartheta} = \frac{\sigma}{A_L} = \frac{4\sigma}{\pi R^2 \beta_t^2}, \quad (3.26)$$

$$\sigma^0 = \frac{\sigma}{A} = \frac{4\sigma \cos \vartheta}{\pi R^2 \beta_t^2}. \quad (3.27)$$

Both  $\gamma$  and  $\sigma^0$  are dimensionless quantities. While the backscatter coefficient can be determined without knowledge of the target's orientation, for the calculation of the normalized backscatter cross-section, this orientation needs to be determined in form of the incidence angle  $\vartheta$ . Within this task, the target's normal vector needs to be calculated; approaches for this task are presented in Section 3.3.1.2. With the knowledge of the local normal vector, the incidence angle  $\vartheta$  can be calculated as well as  $\sigma^0$ . Furthermore, assuming Lambertian scattering (see Section 2.2), we may also derive the diffuse reflectance  $\rho_d$  [Briese et al. 2012; Lehner and Briese 2010]:

$$\rho_d = \frac{\sigma}{\pi R^2 \beta_t^2 \cos \vartheta} = \frac{\gamma}{4 \cos \vartheta} = \frac{\sigma^0}{4 \cos^2 \vartheta}. \quad (3.28)$$

In this context, also the term *reflectance factor* is used, referring to the ratio of the reflectance of the target to that of a perfectly diffuse surface measured in similar illumination and geometry [Kaasalainen et al. 2009].

The backscatter coefficient  $\gamma$  and the normalized backscatter cross-section  $\sigma^0$  are *target parameters* dependent on the orientation of the illuminated target w.r.t. to the laser beam and the actual size of the target, resp. In contrast, the diffuse reflectance  $\rho_d$  is a *target surface parameter*. With the knowledge of the transmitter beamwidth  $\beta_t$  and of the calibration constant  $C_{CAL}$  together with the extraction of the range  $R$ , the parameter  $\gamma$  is well defined. The determination of  $\sigma^0$  requires additional information about the neighbourhood of the target and if an extended target is present; this also holds for  $\rho_d$ , for which a further assumption about the reflectance behaviour has to be made. If this assumption of diffuse scattering is not valid, i.e. the solid angle of the effective scattering cone  $\Omega_S < \pi$ , the reconstructed reflectance might result to values greater than 1.

Concerning the practical workflow of radiometric calibration of full-waveform lidar data, Briese et al. [2012] suggest an 8-step procedure, which is presented here in a slightly altered version:

1. Selection of the in-situ reference targets based on the ALS flight plan
2. Determination of the incidence-angle dependent reflectance  $\rho_d$  of the reference surfaces utilizing a spectrometer or reflectometer that operates at the same lidar wavelength

3. If atmospheric conditions do not allow to treat  $\eta_{\text{ATM}}$  as a constant: recording of meteorological data (aerosol type, visibility, water vapour, etc. for the estimation of an atmospheric model) during the flight mission in order to estimate the atmospheric transmission factor
4. Full-waveform decomposition (echo extraction and estimation of echo parameters)
5. Direct georeferencing of the ALS echoes and maybe strip adjustment in order to get an advanced relative and absolute georeferencing of the ALS data
6. Estimation of  $C_{\text{CAL}}$  based on the ALS echoes within the in-situ reference targets (e.g. defined by a polygon area)
7. Radiometric calibration of all echoes based on the determined value of  $C_{\text{CAL}}$
8. Estimation of the local surface normal in order to consider the local incidence angle  $\vartheta$

Compared to [Briese et al. 2012], steps 6 and 8 were switched because we aim at the determination of  $\sigma$  by deconvolution as first result (see next section) and derive  $\gamma$  and  $\rho_d$  subsequently. The cited paper aims at the direct determination of the diffuse reflectance  $\rho_d$  using the results of Gaussian Decomposition.

### 3.3.1.1 Determination of the Calibration Constant

With the findings of the previous section, we retrieve for the backscatter cross-section

$$\sigma = C_{\text{CAL}} R^4 \underbrace{\int_{-\infty}^{\infty} \bar{\sigma}'(t) dt}_{:=\bar{\sigma}} = R^2 \beta_t^2 \cos \vartheta \rho_d$$

so that the calibration constant results in

$$C_{\text{CAL}} = \frac{\rho_d \beta_t^2 \cos \vartheta}{\bar{\sigma}} R^2. \quad (3.29)$$

Different strategies have been suggested in the relevant literature for establishing a reference area of known diffuse reflectance  $\rho_d$  (see points 1 and 2 of the workflow given above), e.g.

- selecting an area where a uniform diffuse reflectance can be assumed, e.g. a paved asphalt road with  $\rho_d = 0.2$  [Wagner et al. 2006],
- placing portable tarps of calibrated reflectance in an area of interest during acquisition time of the scan [Ahokas et al. 2006; Kaasalainen et al. 2007],



- determining the diffuse reflectance of material present in the scanned area under laboratory conditions, e.g. for sand and gravel [Kaasalainen et al. 2009], or
- determining the diffuse reflectance in-situ for material present in the scanned area, simultaneously to the lidar campaign. This is achieved with a reflectometer (operating at the same wavelength as the lidar instrument) and small reference targets of calibrated diffuse reflectance such as Spectralon<sup>®</sup>. For both the scanned surface and the reference targets, the reflectance is determined for different incidence angles [Briese et al. 2008; Lehner and Briese 2010].

With the knowledge of  $\rho_d$ , of  $\bar{\sigma}$  by deconvolution and of  $R$  by range extraction, we are only left with the estimation of the local normal vector for determining a representative  $C_{\text{CAL}}$ . It typically results to the mean value in the respective reference area [Lehner and Briese 2010]. Together with the direction of the laser beam, the incidence angle  $\vartheta$  can be derived from this normal vector. We will focus on its determination in the next section.

### 3.3.1.2 Estimation of local normal Vectors in a Point Cloud

Note that at this point, we leave the laser beam cone as area of interest. The focus is now laid on the spatial *neighbourhood* of the target. Various neighbourhood definitions for 3D point clouds exist in the literature, e.g.

- Filin and Pfeifer [2005] present a vertical and slope-adaptive cylindrical neighbourhood definition.
- Nothegger and Dorninger [2007] evaluate the increase of the smallest eigenvalue of the covariance matrix with growing neighbourhood size  $n$  (point count). The number  $n_o$  being the lowest where no significant increase in the smallest eigenvalue can be recognized is considered as optimal neighbourhood size.
- Demantké et al. [2011] suggest a spherical neighbourhood definition, whose radius is chosen by a similarity and entropy criterion, resp. Moreover, the dimensionality of the neighbourhood (1D—linear, 2D—planar or 3D) is determined by the ratio of eigenvalues of the neighbourhood’s covariance matrix.<sup>1</sup>
- Abed et al. [2012] perform a repeated search for the optimal set of neighbours in a local planar environment by applying an angle threshold criterion w.r.t. a horizontal plane containing the neighbourhood’s center of gravity.

Given the set of neighbours, the local normal vector is commonly found by eigenanalysis of the neighbourhood’s covariance matrix [Filin and Pfeifer 2005]: The eigenvector corresponding to the smallest eigenvalue is the local normal vector.

---

<sup>1</sup>In case of a 1D neighbourhood, a unique normal vector cannot be determined.

Instead of the covariance matrix, also the *point distribution tensor* can be taken into account [Ritter and Bengler 2012]. This tensor is closely related to the covariance matrix, however it is reduced to the current target point instead of the center of gravity. Furthermore, the points are weighted inversely to their distance to the current target point. The neighbourhood is limited by a cut-off distance.

Kirchhof et al. [2008] perform a pre-segmentation of the scanned scene into penetrable and impenetrable objects using cross-correlation of  $S[t]$  and  $P_r[t]$ . The set of points belonging to impenetrable objects is partitioned into planar patches and these patches are fitted iteratively in a robust approach using RANSAC. The planes' parameters already give the normal vectors.

Otepka et al. [2013] give an extensive review on additional point attributes retrieved from the neighbourhood of the respective point in images and point clouds. Besides investigating geometric attributes, they also deal with attributes of radiometric nature. In this reference, a point feature categorization in four levels is suggested:

**Level 0:** directly determined coordinates or raw measurements

**Level 1:** improved coordinates (e.g. by strip adjustment) and features obtained by further processing of the measurements of a single points

**Level 2:** features calculated from the spatial neighbourhood of the point

**Level 3:** features obtained by combination of the three lower levels with other data sources.

Concerning FWF lidar, the raw sampled amplitude values are an example of a level-0 feature; the backscatter cross-section  $\sigma$  belongs to level 1 whereas the diffuse reflectance  $\rho_d$  belongs to level 2. An RGB colouring stemming from aerial images might be an additional level-3 feature.

### 3.3.2 Own Contribution

#### 3.3.2.1 Impact of the Instability of the System Waveform

Based on [Roncat et al. 2011b], this section presents the error propagation from the system waveform parameters to the calibration constant in Gaussian Decomposition. Let us re-consider the Gaussian model of system waveform  $S(t)$  and recorded echo waveform  $P_r(t)$ :

$$S(t) = \hat{S} e^{-\frac{(t-t_s)^2}{2s_s^2}} \quad P_r(t) = \sum_{i=1}^N \hat{P}_i e^{-\frac{(t-t_i)^2}{2s_{p,i}^2}}$$

with

$$\hat{P}_i = \frac{D_r^2}{4\pi R_i^4 \beta_t^2} \frac{\hat{S} s_s}{s_{p,i}} \sigma_i \eta_{\text{SYS}} \eta_{\text{ATM}}$$

Separating the parameters of the reflecting surface from the other parameters of  $\hat{P}_i$  leads to the introduction of the calibration constant for Gaussian Decomposition,  $C_{\text{CAL,GD}}$  [Briese et al. 2008; Wagner et al. 2006]:

$$\sigma_i = C_{\text{CAL,GD}} R_i^4 \hat{P}_i s_{p,i} \quad (3.30)$$

with

$$C_{\text{CAL,GD}} = \frac{4\pi\beta_t^2}{\eta_{\text{SYS}}\eta_{\text{ATM}}D_r^2\hat{S}s_s} = \frac{4\pi\sqrt{2\pi}\beta_t^2}{\eta_{\text{SYS}}\eta_{\text{ATM}}D_r^2E_s}. \quad (3.31)$$

The term  $E_s = \sqrt{2\pi}\hat{S}s_s$  refers to the energy (integral) of the system waveform. The parameters of the system waveform are normally regarded as unknown (or known up to a constant factor since  $S(t)$  is stored in a damped version) but constant quantities. This is also reflected in file format specifications such as the ASPRS LAS 1.3 and LAS 1.4 (LASer File Format Exchange, [ASPRS 2014]), Riegl's SDC and SDW file formats [Riegl LMS 2014]. Both do not represent the transmitted laser pulse<sup>2</sup>. However, there has been empirical evidence that the transmitted laser pulse cannot be regarded as "constant enough" for proper radiometric calibration [cf. Bretar et al. 2009; Mallet 2011]. Another evidence is given in Figure 3.11 which shows the sample of 2,000 randomly chosen system waveforms of a large lidar campaign.

In [Wagner 2010], a different version of the calibration constant is therefore formulated, without  $\hat{S}$  in the denominator:

$$\bar{C}_{\text{CAL,GD}} = \frac{4\pi\beta_t^2}{\eta_{\text{SYS}}\eta_{\text{ATM}}D_r^2s_s}. \quad (3.32)$$

The observation of  $S(t)$  and the determination of  $\hat{S}$  (up to a constant factor) and  $s_s$  allow us to study the influence of their variations on  $C_{\text{CAL,GD}}$ .

For this analysis, we first write the partial derivatives of  $C_{\text{CAL,GD}}$  w.r.t.  $\hat{S}$  and  $s_s$ :

$$\frac{\partial C_{\text{CAL,GD}}}{\partial \hat{S}} = -\frac{1}{\hat{S}} C_{\text{CAL,GD}} \quad (3.33)$$

$$\frac{\partial C_{\text{CAL,GD}}}{\partial s_s} = -\frac{1}{s_s} C_{\text{CAL,GD}} \quad (3.34)$$

---

<sup>2</sup>It is though possible to store information on the system waveform in the open full-waveform file standard *PulseWaves* [PulseWaves 2014]. In contrast to the mentioned LAS and SDC/SDW formats, *PulseWaves* is rather focused on the raw waveforms than on already extracted targets with additional features.

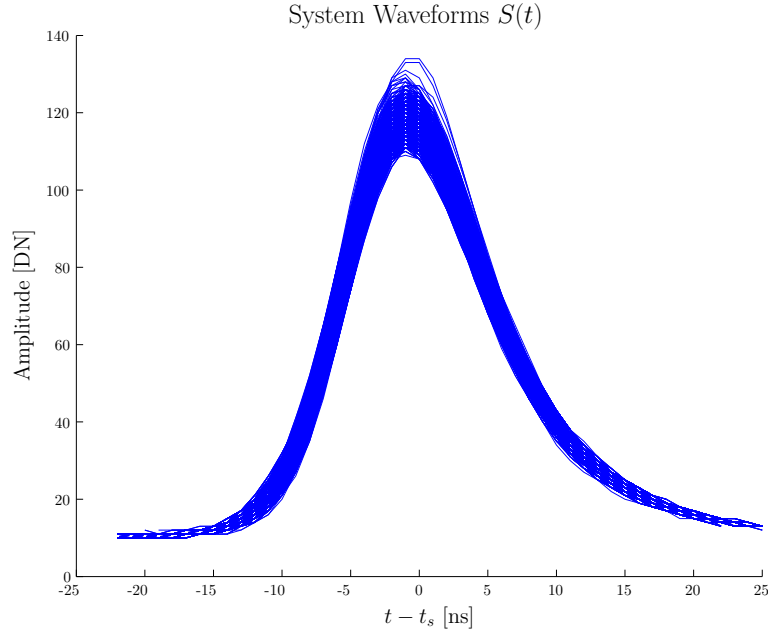


**Figure 3.11:** Overlay of 2 000 randomly chosen system waveforms  $S(t)$  of a large lidar campaign equipped with an Optech ALTM 3100 instrument. The waveforms' timestamps are reduced to their peak positions  $t_s$ . The image illustrates the necessity to take the variation of the amplitude  $\hat{S}$  into account for radiometric calibration. From [Roncat et al. 2013].

Following the law of error propagation, this yields for the variance  $\varsigma_{C_{CAL,GD}}^2$  [Mikhail 1976]<sup>3</sup>:

$$\varsigma_{C_{CAL,GD}}^2 = \left( \frac{\partial C_{CAL,GD}}{\partial \hat{S}}, \frac{\partial C_{CAL,GD}}{\partial s_s} \right) \begin{pmatrix} \varsigma_{\hat{S}}^2 & \varrho \varsigma_{\hat{S}} \varsigma_{s_s} \\ \varrho \varsigma_{\hat{S}} \varsigma_{s_s} & \varsigma_{s_s}^2 \end{pmatrix} \begin{pmatrix} \frac{\partial C_{CAL,GD}}{\partial \hat{S}} \\ \frac{\partial C_{CAL,GD}}{\partial s_s} \end{pmatrix} \quad (3.35)$$

with  $\varrho$  as the correlation coefficient of  $\hat{S}$  and  $s_s$ .  $\varsigma_{\hat{S}}^2$  and  $\varsigma_{s_s}^2$  denote the variances of  $\hat{S}$  and  $s_s$ , resp. Reordering Equation (3.35) gives

$$\begin{aligned} \varsigma_{C_{CAL,GD}}^2 &= \left( \frac{\partial C_{CAL,GD}}{\partial \hat{S}} \right)^2 \varsigma_{\hat{S}}^2 + \left( \frac{\partial C_{CAL,GD}}{\partial s_s} \right)^2 \varsigma_{s_s}^2 \\ &+ 2\varrho \frac{\partial C_{CAL,GD}}{\partial \hat{S}} \frac{\partial C_{CAL,GD}}{\partial s_s} \varsigma_{\hat{S}} \varsigma_{s_s}. \end{aligned}$$

<sup>3</sup>Alternative writings  $\varsigma$  and  $\varrho$  of the Greek lowercase letters *sigma* (standard deviation) and *rho* (correlation coefficient) are used to avoid confusion with the backscatter cross-section  $\sigma$  and the reflectance  $\rho$ .

The relative deviation of  $C_{\text{CAL,GD}}$  is therefore given by

$$\frac{\varsigma_{C_{\text{CAL,GD}}}^2}{C_{\text{CAL,GD}}^2} = \frac{\varsigma_{\hat{S}}^2}{\hat{S}^2} + \frac{\varsigma_{s_s}^2}{s_s^2} + 2\rho \frac{\varsigma_{\hat{S}}}{\hat{S}} \frac{\varsigma_{s_s}}{s_s}. \quad (3.36)$$

When assuming positive correlation between  $\hat{S}$  and  $s_s$  (empirically justified by the data sets investigated in this study, see Section 4.3), a lower bound of the relative deviation of  $C_{\text{CAL,GD}}$  is found by neglecting correlation ( $\rho = 0$ ):

$$\frac{\varsigma_{C_{\text{CAL,GD}}}^2}{C_{\text{CAL,GD}}^2} \geq \frac{\varsigma_{\hat{S}}^2}{\hat{S}^2} + \frac{\varsigma_{s_s}^2}{s_s^2}$$

Figure 3.12 shows the relation of these three relative deviations for different levels of correlation. A detailed numerical evaluation is presented in Section 4.3.

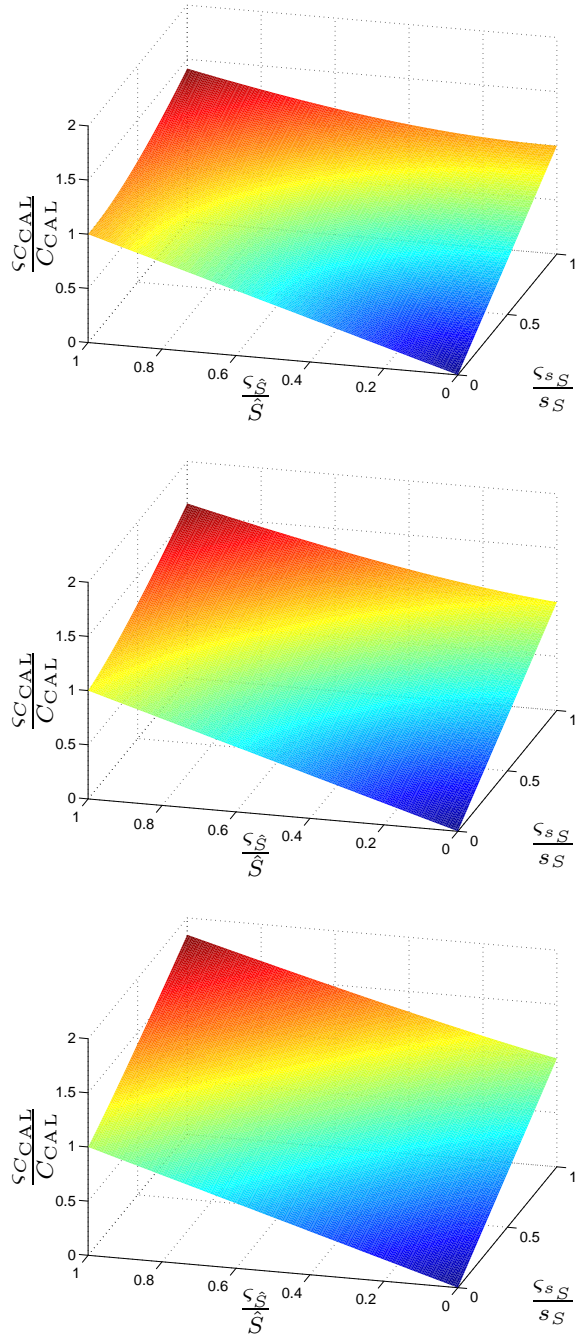


**Figure 3.12:** Error propagation of the relative deviations of the system waveform's amplitude  $\hat{S}$  and the width  $s_s$  resulting in the relative deviation of the calibration constant  $C_{CAL,GD}$ . Top: no correlation between  $\hat{S}$  and  $s_s$ . Center:  $\rho = 0.3$ . Bottom:  $\rho = 0.7$ .

### 3.3.2.2 Extension of radiometric Calibration to uniform B-Splines

This section follows the presentation given in [Roncat et al. 2012].

B-spline deconvolution relies on fitting the waveforms to a mixture of base functions with beneficial convolution properties (see Chapter A in the appendix for details), resulting in a fitted model of the system waveform recorded echo waveform

$$S(t) = \sum_{i=1}^{i_{\max}} b_{i,s} B_i^{n_s}(t) \text{ and } P_r(t) := \sum_{k=1}^{k_{\max}} b_{k,r} B_k^{n_r}(t),$$

respectively. In Gaussian Decomposition, we need to determine some parameters of  $P_r(t)$  in advance, namely the number of Gaussians,  $N$ , and initial estimates for their amplitudes  $\hat{P}_i$ , peak positions  $t_i$  and widths (variances)  $s_{p,i}^2$ , as already stated. The curve fitting is solved by non-linear optimization. In the case of B-spline deconvolution, the knot distance  $\Delta u$  and the degrees  $n_s$  and  $n_r$  need to be determined in advance. Furthermore, the signal part of  $S(t)$  and  $P_r(t)$  should be extracted from the waveforms for noise reduction, e.g. by applying a Schmitt trigger [Schmitt 1938].

As mentioned previously, we introduce a scaled version of the differential backscatter cross-section for deconvolution:

$$\bar{\sigma}'(t) = \frac{D_r^2 \eta_{\text{SYS}} \eta_{\text{ATM}}}{4\pi R^4 \beta_t^2} \sigma'(t) = P_r(t) \otimes^{-1} S(t). \quad (3.37)$$

Note that this equation refers to the deconvolution of the *whole* backscattered waveform; it is a uniform B-spline curve of degree  $n_\sigma = n_r - n_s - 1$  and  $j_{\max} = k_{\max} - i_{\max} + 1$  control points  $b_{j,\sigma}$ . In contrast, Gaussian Decomposition allows for solving the deconvolution implicitly (see Chapter A in the appendix). For retrieving  $\bar{\sigma}'(t)$  by using B-spline deconvolution, we have to solve an overdetermined linear equation system (Equation (3.24)).

Looking back at Equation (3.37), we can extract  $\beta_t$ ,  $D_r$ ,  $\eta_{\text{SYS}}$  and  $\eta_{\text{ATM}}$  as unknown, but constant parameters. We have already discussed the instability of  $S(t)$  in Section 3.3.2.1, motivating to take every single system waveform into account. Thus, we finally get as calibration constant  $C_{\text{CAL},B}$

$$C_{\text{CAL},B} = \frac{4\pi \beta_t^2}{\eta_{\text{SYS}} \eta_{\text{ATM}} D_r^2} \quad (3.38)$$

where the subscript  $B$  denotes the B-spline approach, in contrast to other techniques demanding for a different definition of this constant.

**Notes to the influence of the range  $R$ .** In order to retrieve physically meaningful values for  $\sigma'(t)$ , the influence of the range  $R$  has to be corrected. In Gaussian decomposition, the range  $R_i$  of the  $i$ -th scatterer is retrieved by multiplying the temporal peak position  $(t_i - t_s)$  by half the group velocity of the laser ray,  $v_g$ . In B-spline deconvolution, not single scatterers are extracted, but we operate on the whole waveforms. As a consequence, there is no explicit range for a scatterer. However, we can limit the range to a minimum and maximum in  $\sigma'(t)$ , i.e.

$$R_{\min} = \frac{j_{\min} \Delta t v_g}{2} \text{ and } R_{\max} = \frac{j_{\max} \Delta t v_g}{2}.$$

Typical signal lengths for the Riegl LMS-Q560 and LMS-Q680 are 10 ns and 50 ns for  $S(t)$  and  $P_r(t)$ , respectively. This gives a length of 30 ns for  $\sigma'(t)$ , corresponding to  $R_{\max} - R_{\min} \simeq 450$  cm and a maximum difference of  $\Delta R \simeq \pm 225$  cm to the mean range  $R_{\text{mean}}$  of  $\sigma'(t)$ . The use of  $R_{\text{mean}}$  for further calculations results in a maximum relative error of

$$\epsilon = \frac{(R_{\text{mean}} \pm \Delta R)^4}{R_{\text{mean}}^4} - 1. \quad (3.39)$$

Figure 3.13 shows  $\epsilon$  in dependence of  $R_{\text{mean}}$  and  $\Delta R$ . It can be seen that the absolute value of  $\epsilon$  is lower than 0.05 for ranges greater than 500 m. For shorter distances and/or greater  $\Delta R$ , it is preferable to take the single B-splines of the deconvolution  $\bar{\sigma}'(t)$  into account: As an example, let the knot distance be  $\Delta u = 4$  ns and the degree  $n_\sigma = 3$ . We retrieve  $\Delta R = (4 * (3 + 1))/2$  ns  $\simeq 120$  cm so that  $\epsilon$  does not exceed  $\pm 0.05$  for distances greater than 200 m. Typical distances in ALS mostly exceed this value. Furthermore, the sampled amplitudes are commonly given in 8-bit resolution so that the influence of  $\Delta R$  for radiometric calibration can be regarded as negligible.

We can therefore eliminate a great part of the range influence for the whole deconvolution by multiplying each B-spline  $j$  with its mean range  $R_{j,\text{mean}}$  to the power of 4, so every base function  $B_j^{n_\sigma}$  is scaled by an individual, but known factor  $\tilde{b}_{j,\sigma}$ :

$$\tilde{\sigma}'(t) := \sum_{j=1}^{j_{\max}} \underbrace{R_{j,\text{mean}}^4 b_{j,\sigma}}_{=: \tilde{b}_{j,\sigma}} B_j^{n_\sigma} = \frac{\eta_{\text{SYS}} \eta_{\text{ATM}} D_r^2}{4\pi \beta_t^2} \sigma'(t).$$

With the above results for range determination and the respective solution for  $C_{\text{CAL,B}}$ , we can formulate the dBCS as

$$\sigma'(t) = C_{\text{CAL,B}} \tilde{\sigma}'(t) \quad (3.40)$$

and consequently its integral  $\sigma$  as (cf. Equation (A.6) in the appendix)

$$\sigma = C_{\text{CAL,B}} \int_{-\infty}^{\infty} \tilde{\sigma}'(t) dt = C_{\text{CAL,B}} \Delta t \sum_{j=1}^{j_{\max}} \tilde{b}_{j,\sigma}. \quad (3.41)$$



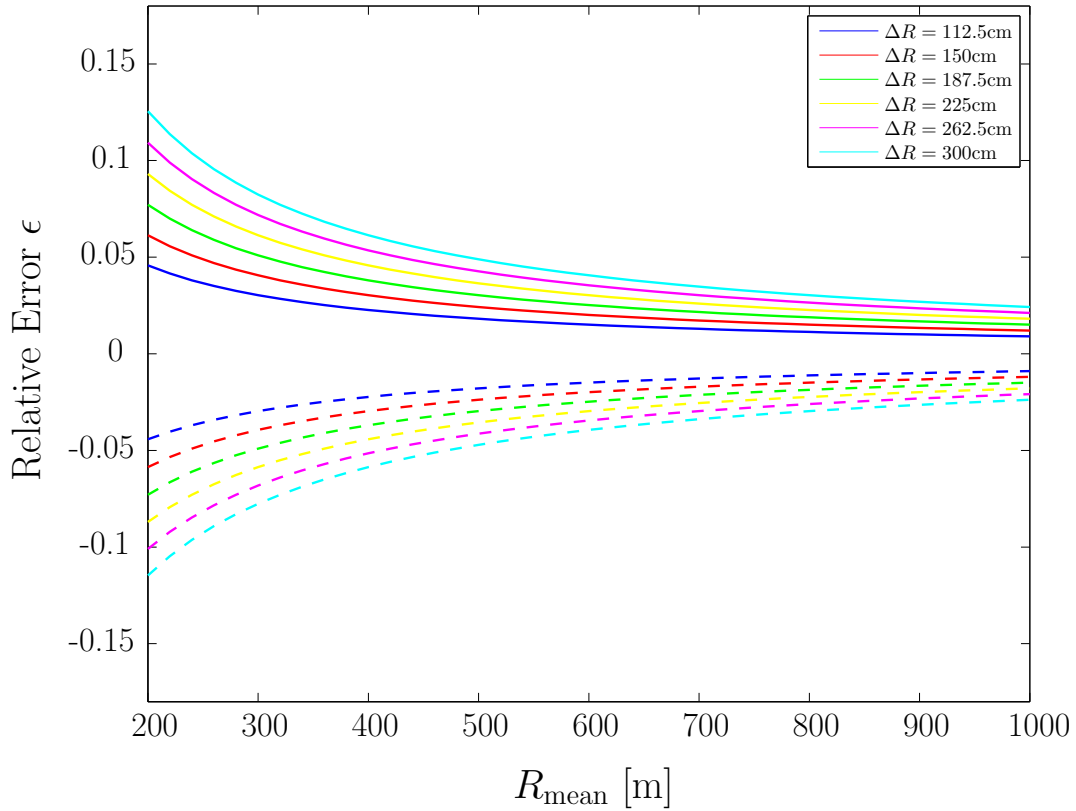
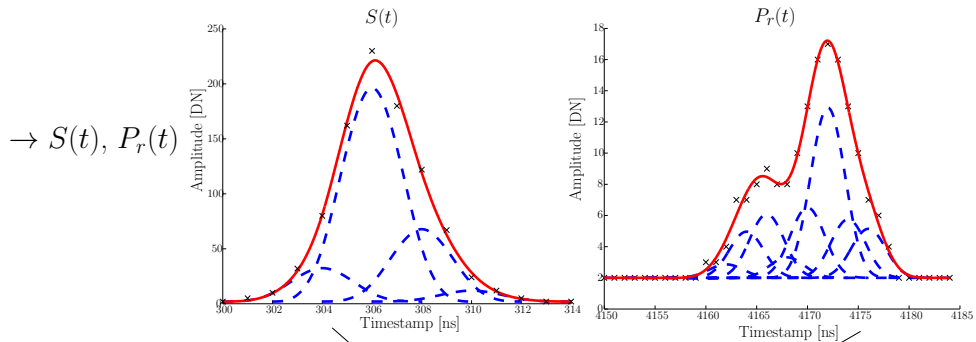


**Figure 3.13:** Maximum relative error  $\epsilon$  for different signal lengths  $\Delta R$  and ranges  $R_{\text{mean}}$ . The solid lines correspond to the  $\Delta R > 0$  and the dashed lines to the  $\Delta R < 0$ .

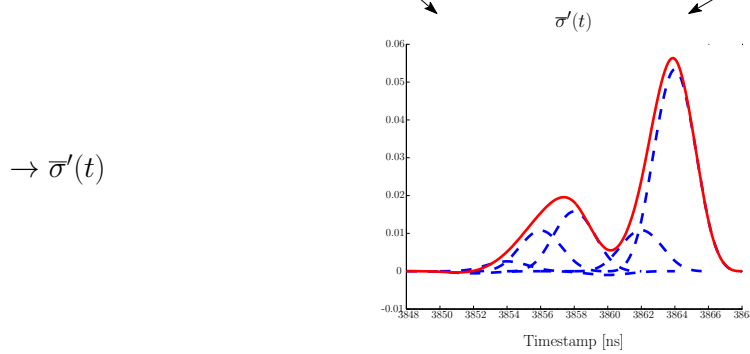
The workflow of determining  $\sigma$  with this approach is illustrated in Figure 3.14, using an example acquired with a RIEGL LMS-Q560 system. Following the suggestions in Section 3.2.2, the degrees  $n_s$  and  $n_r$  were chosen to 3 and 7, respectively, and the knot distance to  $\Delta u = 2$  ns.

The next section presents a technique to extract a discrete number of targets from  $\sigma'(t)$  together with the assignment of the BCS  $\sigma$  and further parameters of such targets.

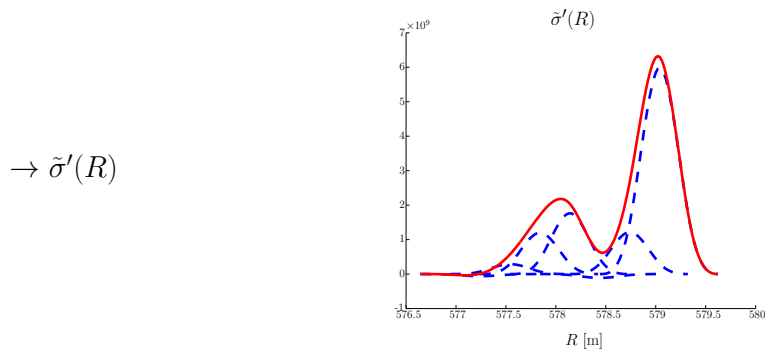
Model system waveform and recorded echo waveform as **continuous functions**



**Deconvolution**



**Range correction and transformation to metric domain**



**Integration**

$\rightarrow \sigma$   $\sigma = 4.62590 \times 10^9 C_{\text{CAL,B}} [\text{m}^2]$

**Figure 3.14:** Workflow for retrieving  $\sigma$  using B-spline deconvolution. This example stems from data acquired with a RIEGL LMS-Q560 system. The crosses in the diagrams at the top indicate the originally sampled amplitude values. The blue curves are the single B-splines forming the fitted B-spline curves (in red). From [Roncat et al. 2012].

### 3.3.2.3 Derivation of radiometrically calibrated Target Parameters by Means of statistical Moments

This section is mainly based on the study presented in [Roncat et al. 2014b].

A univariate function  $f(x)$  can be considered as a probability density function if  $f(x) \geq 0$  for all  $x$  and its integral equals 1. For such functions, *statistical moments* are defined as given below. Provided that the dBCS of a target is non-negative, a physical necessity, its first statistical moment of  $\sigma'_i(t)$ , the mean  $m_{1,i}$ , is defined as

$$m_{1,i} := \frac{1}{\int_{-\infty}^{\infty} \sigma'_i(t) dt} \int_{-\infty}^{\infty} t \sigma'_i(t) dt = \frac{1}{\sigma_i} \int_{-\infty}^{\infty} t \sigma'_i(t) dt. \quad (3.42)$$

The *central* moments of degree  $n \in \mathbb{N}$  ( $n > 1$ ) are defined as:

$$\bar{m}_{n,i} := \frac{1}{\sigma_i} \int_{-\infty}^{\infty} (t - m_{1,i})^n \sigma'_i(t) dt. \quad (3.43)$$

The second central moment  $\bar{m}_{2,i}$  is referred to as variance, its square root as standard deviation. We will concentrate on the central moments of degree 2 to 4 in the subsequent text.

In the case of discrete functions, the integral is to be replaced by a sum. The statistical moments of B-spline curves can be derived analytically since these curves consist of piecewise continuous polynomial functions.

In this section, we describe the determination of the number of targets in a dBCS derived by B-spline deconvolution, the localization and subsequent derivation of target features from the central moments of higher order. The dBCS is a piecewise continuous univariate polynomial of low degree, so that its roots, derivatives and integral can be calculated analytically. The number of targets is calculated by extracting local minima in the dBCS from roots of its first derivative. It results to the number of local minima plus 1. The positions of the  $i$ -th and  $(i + 1)$ -th minimum are taken as lower and upper bound  $t_{l,i}$  and  $t_{u,i}$  of a dBCS segment contributing to a target  $i$ , with  $t_{l,i+1} = t_{u,i}$ . The corresponding segment  $\sigma'_i(t)$  is defined as  $\sigma'_i(t) := \sigma'(t)$  for  $t \in [t_{l,i}, t_{u,i})$  and 0 elsewhere. Its integral  $\sigma_i$  gives the BCS of the  $i$ -th target. In analogy to Gaussian Decomposition, the mean  $m_{1,i}$  is taken as the location of this target. The central moments of higher degree are calculated using the formulas given above. Figure 3.15 shows an example for this procedure, stemming from an ALS data set recorded with an Optech ALTM 3100 system.

Due to noise, small negative parts may appear in the dBCS. Since such negative parts contradict both the underlying physical model and the prerequisites for a probability density function, these parts are eliminated from further analysis; instead of their

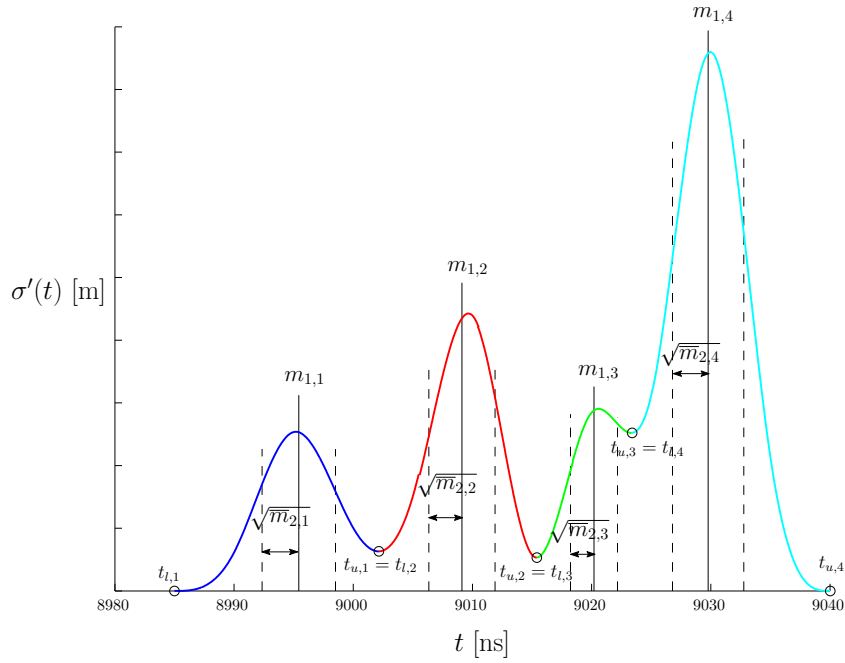


**Figure 3.15:** Example for target extraction and localization and feature derivation based on statistical moments of the dBCS. The target location is set to the mean  $m_{1,i}$  of the segment between the  $i$ -th and  $(i + 1)$ -th local minimum; its backscatter cross-section  $\sigma_i$  is the area under the curve in this segment. The image further shows the square roots of the second central moments (variances), the standard deviations  $\sqrt{m_{2,i}}$ .

minima, the neighbouring roots (zero crossings) of the dBCS next to a minimum are used as limits for the subsequent calculations.

An extended example for the presented feature extraction is given in Section 4.6.

In addition to uniform B-splines, also other deconvolution approaches may (partly) be used for such a feature assignment, e.g. :

- Gaussian Decomposition (Section 3.2.1.1) aims at reconstructing the echo signal as superposition of Gaussian functions, i.e. scaled normal distributions. Since the system waveform is a Gaussian, the output of the deconvolution results to a Gaussian as well. Normal distributions are fully characterized by their first (mean) and second central moment (variance), so that the higher moments do not contain further information.
- EM-Deconvolution (Section 3.2.1.3) is targeted at deconvolving the echo waveform by the system waveform into a train of spikes (one per target) in a discrete

time series. Thus, no statistical moments besides the mean can be derived from the deconvolution.

- Wiener-Filter (Section 3.2.1.2) and regularized least-squares deconvolution [Wang et al. 2009] reconstruct the dBCS by discrete deconvolution in time domain and spectra division in the frequency domain, resp. Moments of arbitrary order can be derived from the resulting function which is a discrete function though. In [Jutzi and Stilla 2006], the deconvolution is eventually fitted to a superposition of Gaussian functions, therefore assumptions on the shape of the dBCS are made.

# Numerical Examples

In this chapter, the theoretical derivations of Section 2.4 and Chapter 3 are empirically investigated by means of numerical examples.

The chapter starts with the simulation of the dBCS  $\sigma'(t)$ , its integral  $\sigma$  and forward-modeled recorded echo waveforms  $P_r(t)$  for different beam and target types in Section 4.1. Examples for target extraction and localization using a correlation-based technique are presented in Section 4.2. While Section 4.3 illustrates the impact of system waveform  $S(t)$  variations on radiometric calibration using the example of two extended lidar campaigns, Sections 4.4 and 4.5 deal with examples for B-spline deconvolution of lidar waveforms, and subsequent radiometric calibration of this deconvolution. Target extraction and target feature calculation from such radiometrically calibrated waveform deconvolutions are illustrated in Section 4.6. The results are highlighted and discussed in Chapter 5.

The examples presented in Section 4.3 – 4.6 originate from publications by the author of this thesis (among co-authors).

## 4.1 Examples for forward Modeling of Lidar Return Waveforms

This section focuses on the synthesis of the dBCS  $\sigma'(R)$  and its integral, the BCS  $\sigma$ , as appearing in the interaction of a laser ray with targets of different size, shape and orientation. The synthetic echo waveforms  $P_r(t)$ , resulting from the convolution of the respective dBCS and a synthetic system waveform  $S(t)$ , are given as well. To simulate realistic results, these system waveforms were modeled as Gaussian functions, obtained by a least-squares fit from real  $S(t)$  examples recorded by an instrument of (a) the RIEGL LMS-Q series and (b) the Optech ALTM series, resp.

The primary goal of this section is to investigate (a) the temporal shape of the dBCS, (b) the amount of the overall BCS and (c) the temporal shape of the recorded echo waveform in the different settings. In addition to the variations of the target parameters, also two different power density distributions within the laser footprint are considered, i.e. Gaussian distribution and uniform distribution. According to scattering theory, the first distribution can be expected in the far field whereas a Gaussian distribution is expected in the near field [Jutzi 2007].

In case of the first, the standard deviation of the Gaussian is chosen to  $1/4$  of the laser beam's opening angle, corresponding to the  $1/e^2$  specification [cf. ISO 2006]. The target surface is assumed to be of diffuse Lambertian reflectance behaviour with  $\rho_d = 1$ .

The simulation of an echo waveform  $P_r(t)$  could include further aspects like scattering in the atmosphere or multiple scattering at the object. This is not considered here.

The target configurations in detail:

**Extended planar target:** This is an extended target for which the effect of the incidence angle (i.e. tilt of the plane w.r.t. the laser ray) on the broadening of the resulting echoes is of primary interest.

**Two parallel half-planes:** In this configuration, it is investigated up to which maximum incidence angle and up to which minimum offset of the two half-planes their contributions to the overall dBCS are still separable.

**Spherical target:** Here the main focus is on the behaviour of the dBCS when the sphere changes from a point-like object to an extended target, expressed by an increasing radius of the sphere. Second, a shift of the sphere from the axis of the beam cone towards its boundary is investigated.

**Cylindrical target:** Here the main focus is on the behaviour of the dBCS when the sphere changes from a line-like object to an extended target, expressed by an increasing radius of the cylinder. Second, a shift of the cylinder axis from the axis of the beam cone towards its boundary is investigated.

**Sinusoidal target:** The object of interest is a surface of (a) concentric circular sine waves and (b) parallel sine waves. Like the first configuration, this is an extended target, too. The focus is on the dBCS behaviour w.r.t. changing amplitude and wavelength; these two parameters mainly affect the surface roughness within the laser footprint. For parallel sine waves, also the impact of a varying incidence angle is investigated, as such a change happens when the target is in the center or and the boundary of an ALS flight strip, resp.

The laser ray is assumed as a filled cone of opening angle  $\beta_t = 0.5 \text{ mrad}$ , approximated by cylindrical sub-beams in 500 radial zones. Its origin (apex) is at the position  $(0, 0, 1000 \text{ m})^\top$  whereas the target surfaces are placed “around” the plane  $z = 0$ ; see the following sections for details. The intersection of this plane with the laser beam cone is a circle with radius 0.25 m. Its center is the origin of the coordinate system whose axes are aligned to the scanner coordinate system. All metric quantities are given in metres. Each example given in this section is illustrated by a visualization of the target surface geometry, laser power distribution within the footprint and the backscatter strength, corresponding to the cosine of the local incidence angle. An example for such a visualization is given in Figure 4.1 below, depicting laser illumination and backscatter for a sinusoidal surface.

For reasons of clarity, only selected examples are presented in this section while the full range of simulations is presented in Chapter C in the appendix.

#### 4.1.1 Simulated dBCS for planar Targets

The plane is given as  $\varepsilon(\vartheta) = \mathbf{n}(\vartheta)^\top \mathbf{x} - d = 0$ , with  $\mathbf{n}(\vartheta) = (0, \sin \vartheta, \cos \vartheta)^\top$  and  $d = 0$ , i.e. plane contains the origin in all variants. The angle  $\vartheta$  varies from  $0^\circ$  to  $60^\circ$  in steps of  $10^\circ$ . Two example configurations for  $\vartheta$  equalling  $30^\circ$  and  $60^\circ$  are given in Figure 4.2 and in Figures C.1 and C.2 in the appendix. The two different power density configurations affect significantly the shape of the corresponding dBCS: While the Gaussian configuration results in a Gaussian-shaped dBCS, the uniform configuration gives a semi-ellipse-like dBCS, as outlined in Section 2.3 and in [Wagner et al. 2004].

In the case of two parallel half planes, the first half-plane follows the parametrization as given above whereas for the second, parallel, half-plane, the parameter  $d = \Delta z$ . This  $d_z$  varies from 0 to 1 m in steps of 0.2 m. The boundary of the half-planes is the plane  $x = 0$ .

The example of two parallel half planes leads us to the question which offset  $\Delta z_{\min}$  between the half planes has to be exceeded so that their contributions to the dBCS may still be attributed to two separate targets, i.e. that they form two separate maxima in the dBCS.

For a Gaussian power density distribution within the laser footprint, this minimum offset in range direction,  $\Delta R_{\min}$  is related to the standard deviations  $s_\sigma$  of these two dBCS contributions as follows [Wagner et al. 2008]<sup>1</sup>:

$$\Delta R_{\min} = 2s_\sigma.$$

The boundary of the laser beam was defined as the locus where the power density has fallen to  $1/e^2$  of its maximum value. Thus, it corresponds to a distance of  $2s$  from the

---

<sup>1</sup>In this reference, the minimum separation distance is referred to as “pulse duration” because the width of the system waveform  $s_s$  instead of  $s_\sigma$  was taken into account.



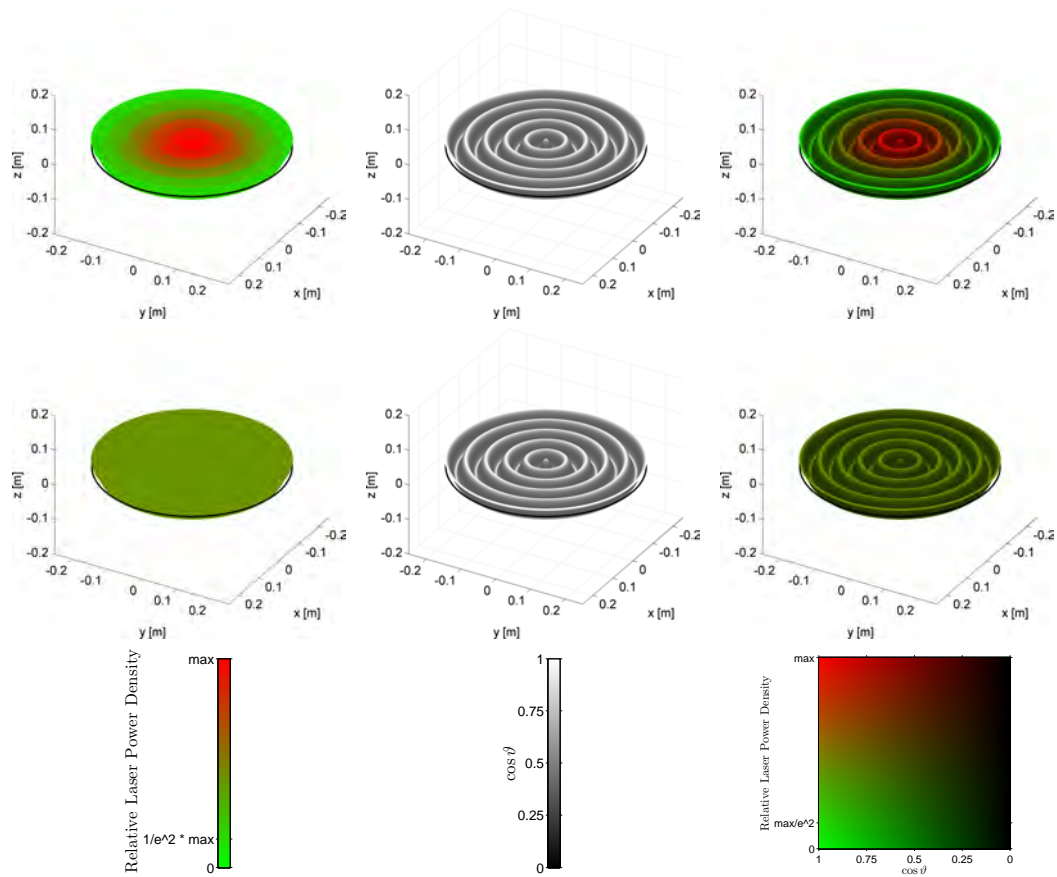


**Figure 4.1:** Illustration of laser illumination and backscatter strength for a sinusoidal target with circular wavefronts. Top row: Gaussian laser power density distribution; second row: uniform laser power density distribution. Bottom row: Legends. Left: Laser illumination at the target. The black circle is the intersection of the laser beam cone with the plane  $z = 0$ . In the Gaussian case, it corresponds to the locus where the laser power density has fallen to  $1/e^2$  of its maximum value. Center: Cosine of the local incidence angle, equivalent to the local backscatter strength. Right: Combination of the two effects.

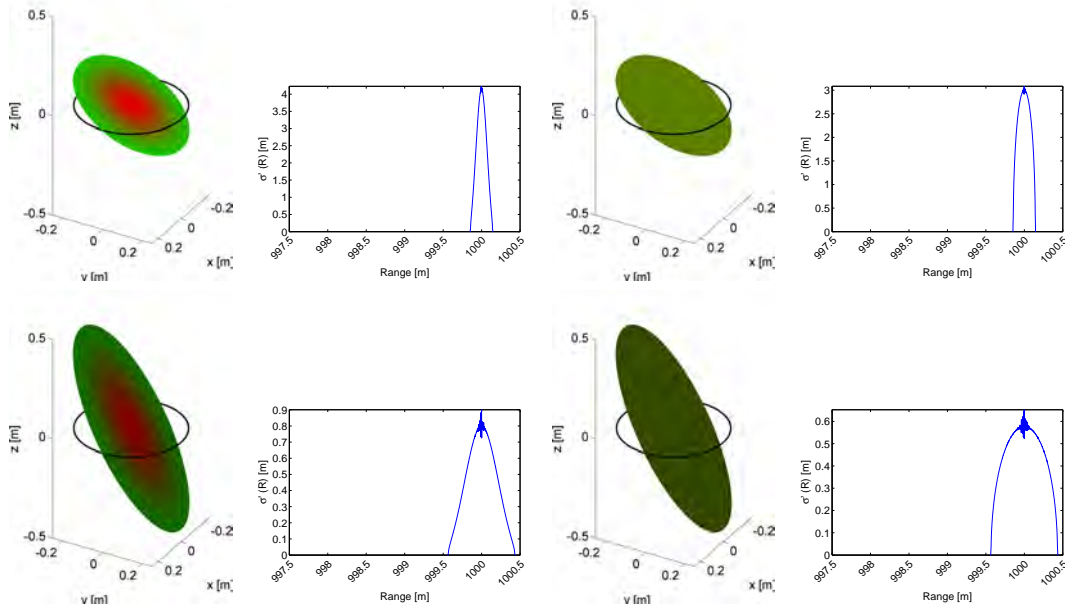


**Figure 4.2:** Differential backscatter cross-section for extended planar targets with incidence angle  $\vartheta$  of  $30^\circ$  (top) and  $60^\circ$  (bottom). The left side refers to Gaussian power density distribution whereas the right side refers to uniform density distribution within the laser footprint.

axis of the laser beam cone (see Section 2.4.2). At a range  $R$  between the laser source and the target, this gives

$$2s = R \tan\left(\frac{\beta_t}{2}\right). \quad (4.1)$$

For small  $\beta_t$ , we may locally approximate the laser beam cone by a circular cylinder  $\Phi$  of radius  $2s$  and retrieve the power density distribution at the target planes as result of a parallel projection. Same holds for the projection in range direction, i.e. for the dBCS, and we retrieve (see [Pfennigbauer et al. 2013] and Figure 4.4, left):

$$s_\sigma = s \tan \vartheta = \frac{R}{2} \tan\left(\frac{\beta_t}{2}\right) \tan \vartheta. \quad (4.2)$$

The offset  $\Delta z$  between two parallel half planes is measured along their common normal  $\mathbf{n}_\varepsilon$ . In range direction, we get

$$\Delta R = \frac{\Delta z}{\cos \vartheta}, \quad (4.3)$$

as shown on the right of Figure 4.4.

Summarizing the above findings, we retrieve

$$\frac{\Delta z_{\min}}{\cos \vartheta} = R \tan\left(\frac{\beta_t}{2}\right) \tan \vartheta$$

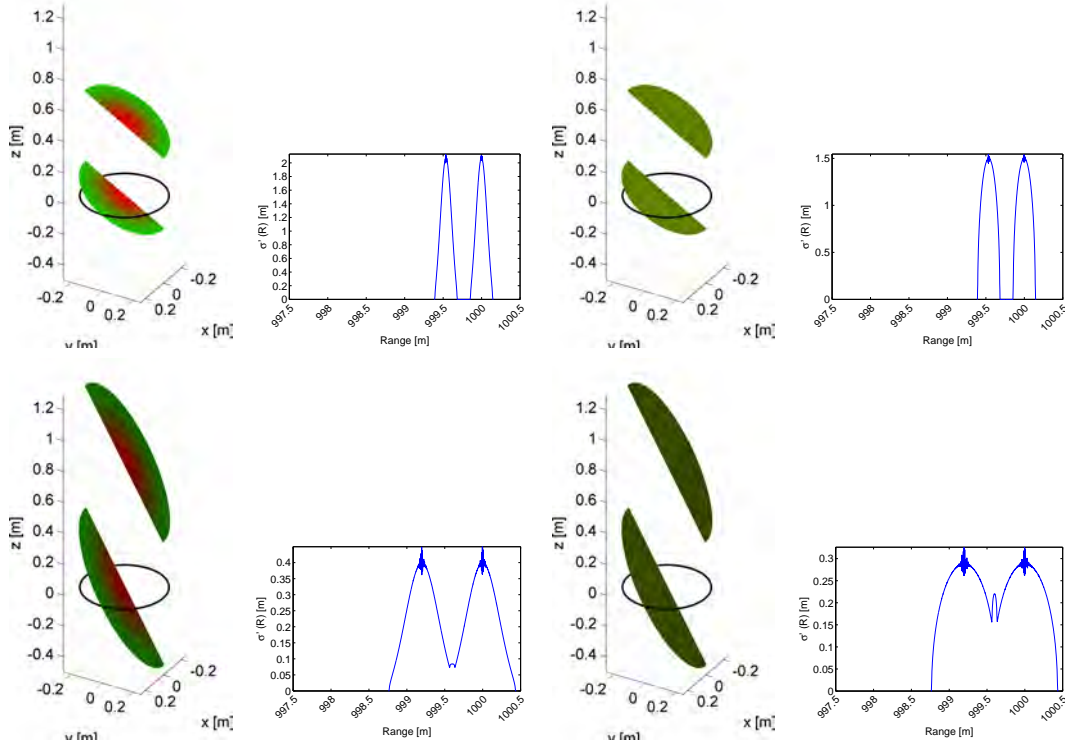


**Figure 4.3:** Differential backscatter cross-section for half-plane targets (offset  $\Delta z = 0.4$  m) with incidence angle  $\vartheta$  of  $30^\circ$  (top) and  $60^\circ$  (bottom). The left side refers to Gaussian power density distribution whereas the right side refers to uniform density distribution within the laser footprint.

and finally

$$\Delta z_{\min} = R \tan\left(\frac{\beta_t}{2}\right) \sin \vartheta. \quad (4.4)$$

We see that the range  $R$  and the transmitter beamwidth  $\beta_t$  only appear in combination and can be replaced by the laser footprint diameter  $d_f = 2R \tan(\beta_t/2)$ . We can now set up a criterion for the presence of two separate maxima in the dBCS and, as a consequence, for target separation:

$$\Delta z - \frac{d_f}{2} \sin \vartheta \begin{cases} > 0 \dots \text{two separate maxima in dBCS,} \\ \leq 0 \dots \text{only one maximum in dBCS.} \end{cases} \quad (4.5)$$

As the maximum value of the sine function is 1, we see that the two half-planar targets form two separate maxima in the dBCS if  $\Delta z > 1/2 d_f$ .

If the system waveform  $S(t)$  is of Gaussian shape, the above result can be analogously applied to the recorded echo waveform  $P_r(t)$  in time domain if  $s_\sigma$  is replaced by  $s_i = 2\sqrt{s_s^2 + s_\sigma^2}/v_g$  and  $\Delta R$  by  $2\Delta R/v_g$ .

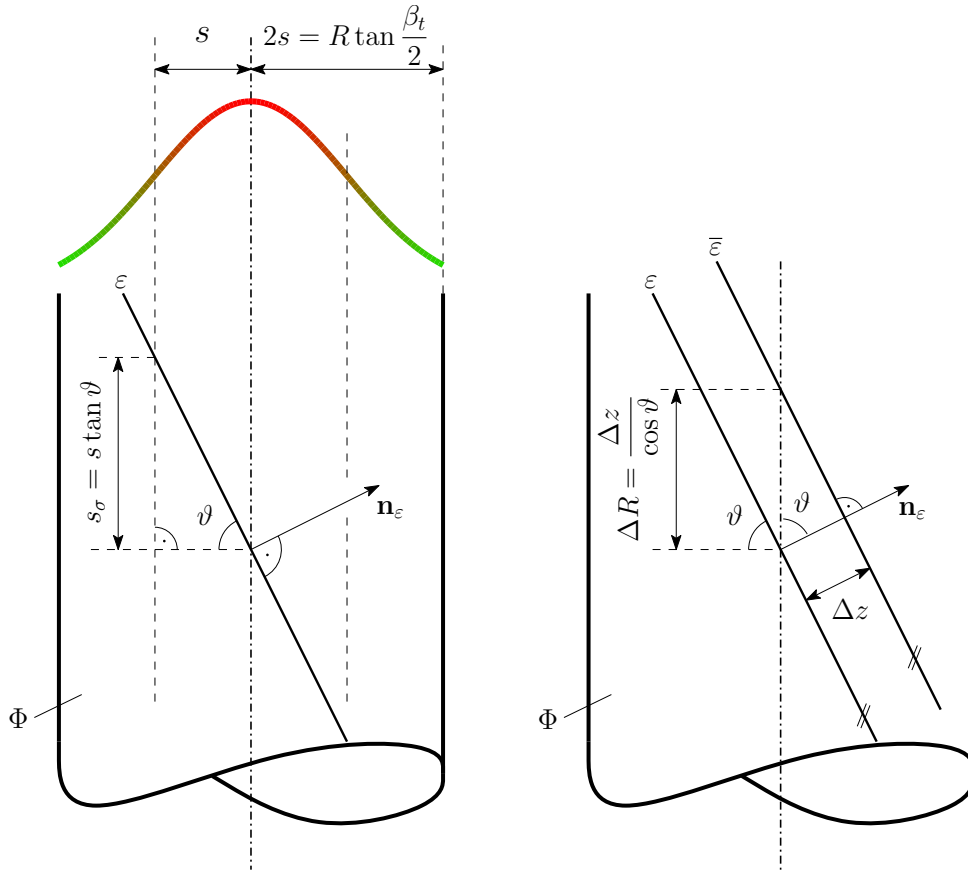


**Figure 4.4:** Left: Geometric derivation for the standard deviation  $s_\sigma$  of the dBCS in case of a planar target and Gaussian power density distribution within the footprint (indicated by the Gaussian curve at the top). Right: Relation of target separation distance  $\Delta z$  and range difference  $\Delta R$  for parallel planes  $\varepsilon$  and  $\bar{\varepsilon}$  at an incidence angle  $\vartheta$ .

We are now seeking for the minimal temporal offset  $\Delta t_{\min}$  where  $P_r(t)$  still shows two separate maxima, and further for the relation of this  $\Delta t_{\min}$  to the spatial offset  $\Delta z$ :

$$\Delta t_{\min} = \frac{2}{v_g} 2s_i = \frac{4}{v_g} \sqrt{s_s^2 + s_\sigma^2} = \frac{4}{v_g} \sqrt{\left( s_s^2 + \left( \frac{d_f}{4} \tan \vartheta \right)^2 \right)},$$

$$\Delta t = \frac{2}{v_g} \frac{\Delta z}{\cos \vartheta}.$$

In analogy to Equation (4.5), we want to determine a  $\Delta z_{\min}$  ensuring  $\Delta t \geq \Delta t_{\min}$ . This

gives

$$\frac{\Delta z_{\min}}{\cos \vartheta} = 2 \sqrt{\left( s_s^2 + \left( \frac{d_f}{4} \tan \vartheta \right)^2 \right)}$$

and, finally

$$\Delta z_{\min} = 2 \sqrt{\left( s_s^2 \cos^2 \vartheta + \frac{d_f^2}{16} \sin^2 \vartheta \right)}.$$

Figure 4.5 depicts the values of  $\Delta z_{\min}$  w.r.t. footprint diameter  $d_f$  and incidence angle  $\vartheta$  for two different system waveform configurations. The first is based the RIEGL LMS-Q series and the second on the Optech ALTM series by setting  $s_s$  to 1.7 ns (equivalent to 51 cm in range domain) and 4.8 ns (144 cm), resp. [Optech Inc. 2014; Riegl LMS 2014]. Note that in the first example,  $\Delta z_{\min}$  is much lower than in the second one because of the lower  $s_s$ ; due to this fact, the influence of the incidence angle becomes though much more significant with increasing footprint diameter than in the second case. Moreover, we see that  $\Delta z_{\min}$  decreases for growing incidence angle in the shown cases. The left illustration indicates that is not true for the large-footprint case.

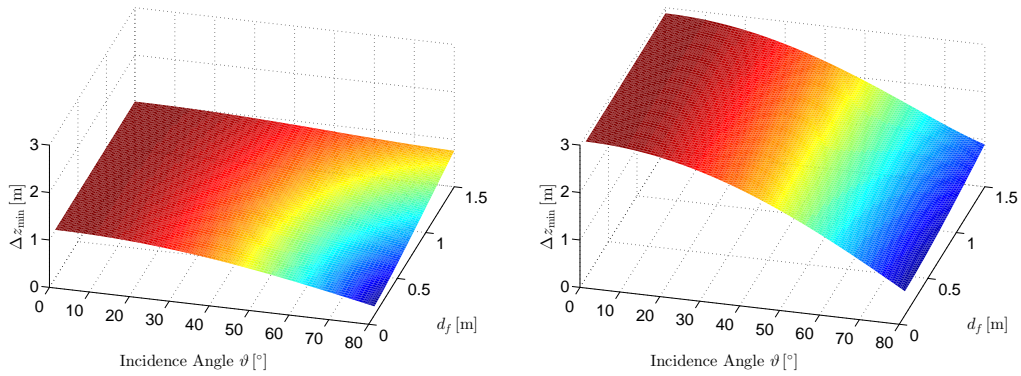


**Figure 4.5:** Minimum offset  $\Delta z_{\min}$  of two parallel half planes to allow two separate maxima in the recorded echo waveform  $P_r(t)$ , given in dependence of the laser footprint diameter  $d_f$ , the incidence angle  $\vartheta$  and the width of the system waveform  $S(t)$ , expressed by the standard deviation  $s_s$ . Left:  $s_s = 51$  cm, right:  $s_s = 144$  cm.

### 4.1.2 Simulated dBCS for spherical Targets

The spheres are given as  $(x - m_x)^2 + (y - m_y)^2 + (z - m_z)^2 - r^2 = 0$ . The  $x$  coordinate of the spheres' center is always 0, its  $y$  coordinate  $m_y$  is taken as a shift parameter and varies from 0 to 0.25 m in steps of 0.05 m. The radius  $r$  is set to 0.025, 0.05, 0.1, 0.2, 0.3, 0.4 and 0.5 m; the  $z$  coordinate of the sphere's center is chosen to  $-r$  so that the "highest" point of the sphere is in the reference plane  $z = 0$  for every example. Figure 4.6 shows the dBCS for spheres of radius 0.05, 0.2 and 0.5 m, all with offset  $m_y = 0.1$  m.

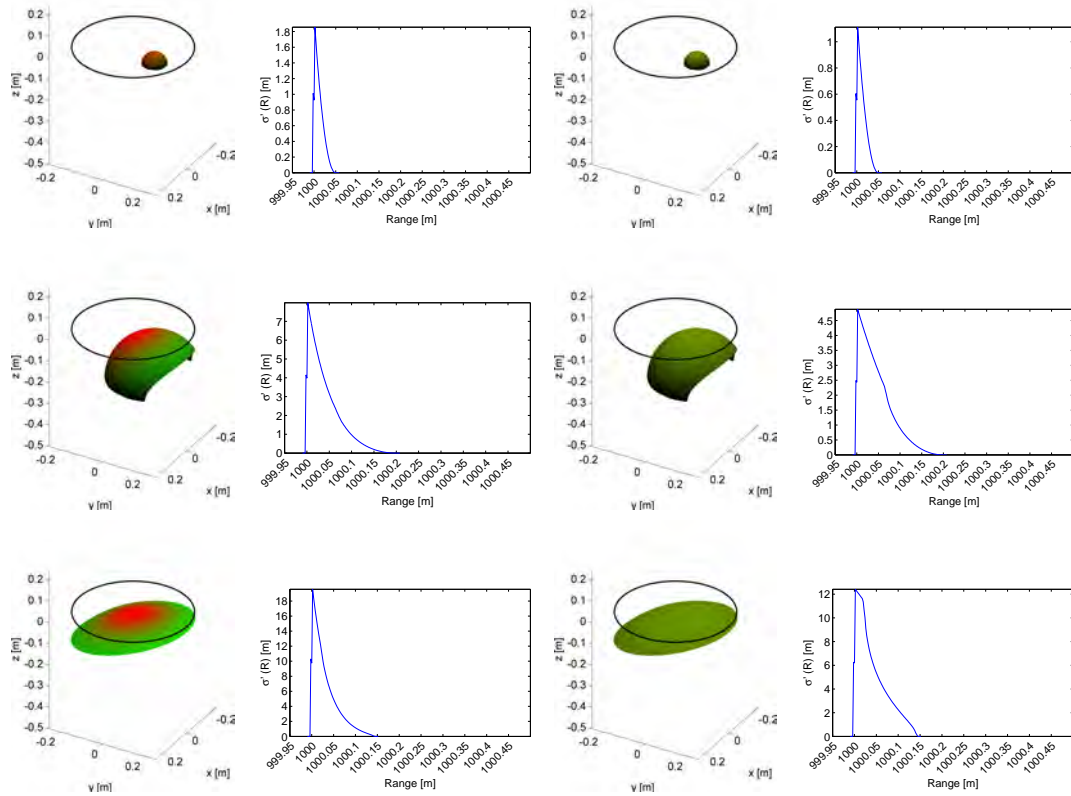


**Figure 4.6:** Differential backscatter cross-section for spherical targets of radius  $r = 0.05$ , 0.2 and 0.5 m (from top to bottom) and shift  $m_y = 0.1$  m.

It is interesting to note that in the uniform case, the dBCS is independent of  $m_y$  as long as the sphere stays as a whole within the laser footprint, i.e.  $r + m_y < d_f/2$ . If this threshold is exceeded, a discontinuity in the slope of the right part of the dBCS is visible. If  $r > d_f/2$ ,  $\sigma'(R)$  has a discontinuity at its right part. These two phenomena are also present in the Gaussian case, but much less pronounced due to the low power density at the boundary of the footprint. Additionally, different numerical values of the dBCS and as a consequence also for the BCS  $\sigma$  (see Section 4.1.5) are retrieved in the uniform and

the Gaussian case, resp. See also Figures C.8 to C.14 in the appendix for full detail.

### 4.1.3 Simulated dBCS for cylindrical Targets

In analogy to the spherical example, the cylinder is given as  $(y - m_y)^2 + (z - m_z)^2 - r^2 = 0$ . The cylinder's axis is parallel to the  $x$  axis, its  $y$  coordinate  $m_y$  is taken as a shift parameter and varies from 0 to 0.25 m in steps of 0.05 m. The radius  $r$  is set to 0.025, 0.05, 0.1, 0.2, 0.3, 0.4 and 0.5 m; the  $z$  coordinate of the cylinder's center is chosen to  $-r$  so that the "highest" generatrix is in the reference plane  $z = 0$ . In contrast to the spherical configuration, the difference between the Gaussian and the uniform case is less present both in shape and numerical values of the dBCS; see Figures 4.7 and C.15 to C.21 in the appendix. One reason for that result is that parts of the generatrices pass the full diameter of the laser footprint if  $r > m_y$ .

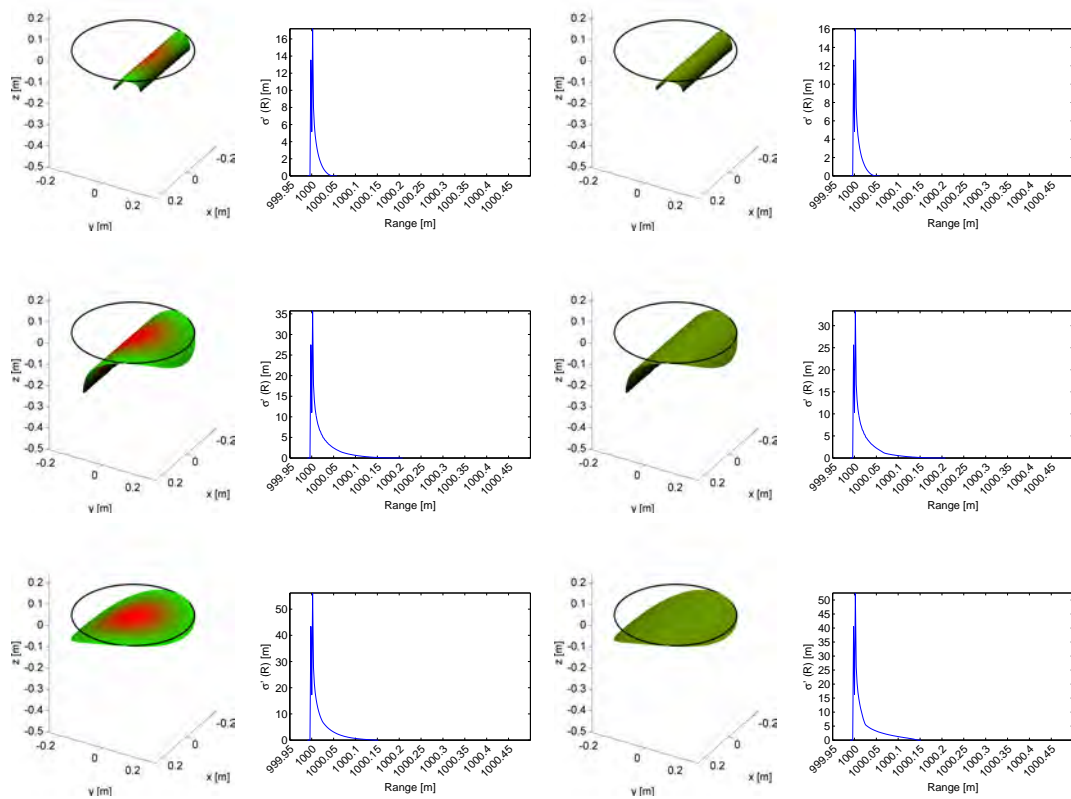


**Figure 4.7:** Differential backscatter cross-section for cylindrical targets of radius  $r = 0.05, 0.2$  and  $0.5$  m (from top to bottom) and shift  $m_y = 0.1$  m.

#### 4.1.4 Simulated dBCS for sinusoidal Targets

In contrast to the two previous sections, only extended targets are taken into account here. While we first consider sinusoidal surfaces with circular wavefronts, also surfaces with parallel wavefronts are dealt with. In the case of circular wavefronts, these surfaces are given as

$$z(x, y) = a \cos \left( 2\pi \frac{\sqrt{x^2 + y^2}}{\lambda} \right).$$

The surface parameters  $a$  (amplitude) and  $\lambda$  (wavelength) vary from 0.01 to 0.05 m in steps of 0.01 m and from 0.05 to 0.25 m in steps of 0.05 m, resp. We see from the examples given in Figure 4.8 and in the Figures C.22 to C.27 in the appendix that the Gaussian and the uniform case result in similar dBCS shapes and values for many configurations; furthermore, each dBCS has a local maximum at the start and at the end of their non-zero domains. The ratio of the dBCS values at the first and the second maximum is though dependent on the wavelength.

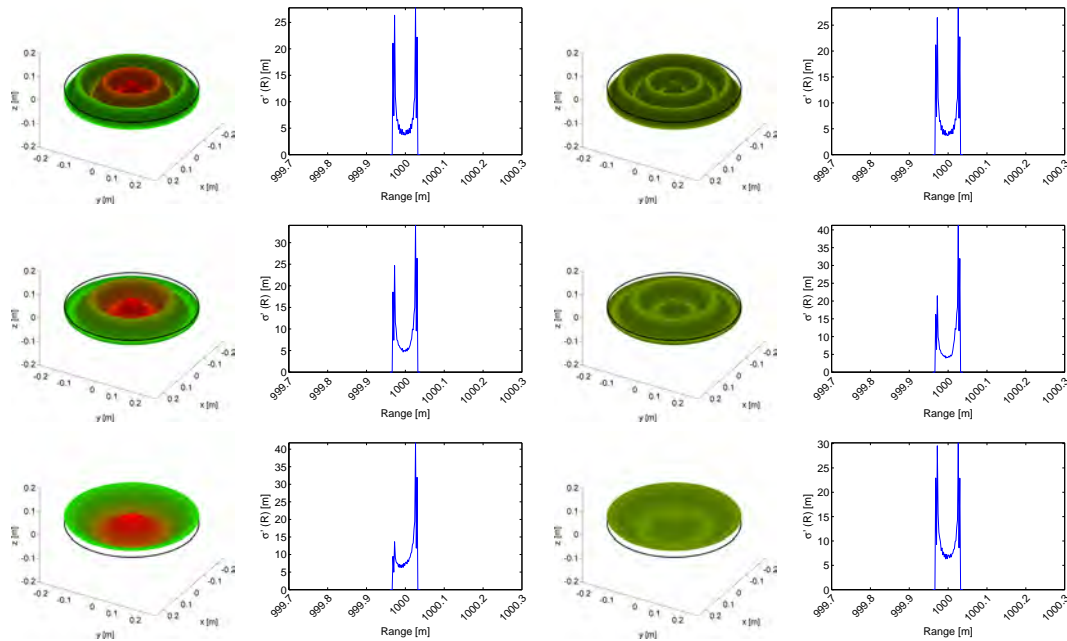


**Figure 4.8:** Differential backscatter cross-section for sinusoidal targets of amplitude  $a = 0.03$  m, wavelength  $\lambda = 0.1, 0.5$  and  $0.2$  m (from top to bottom).

The example was continued with sinusoidal surfaces with parallel wavefronts. Additionally, these sinusoidal surfaces were tilted w.r.t. to the laser beam axis in order to investigate the effect of a changing incidence angle, as appearing in an ALS scan line going from the centre of a flight strip to its outline. The tilt angle, equivalent to a mean incidence angle, was chosen to  $0$  (centre),  $10$ ,  $20$  and  $30^\circ$  (outline). While the non-tilted variant is comparable to the situation for circular wavefronts, the tilted versions



show multiple local maxima and even zero parts in the dBCS because of shadowed areas within the target (see Figure 4.9 below and Figures C.28 to C.51 in the appendix).

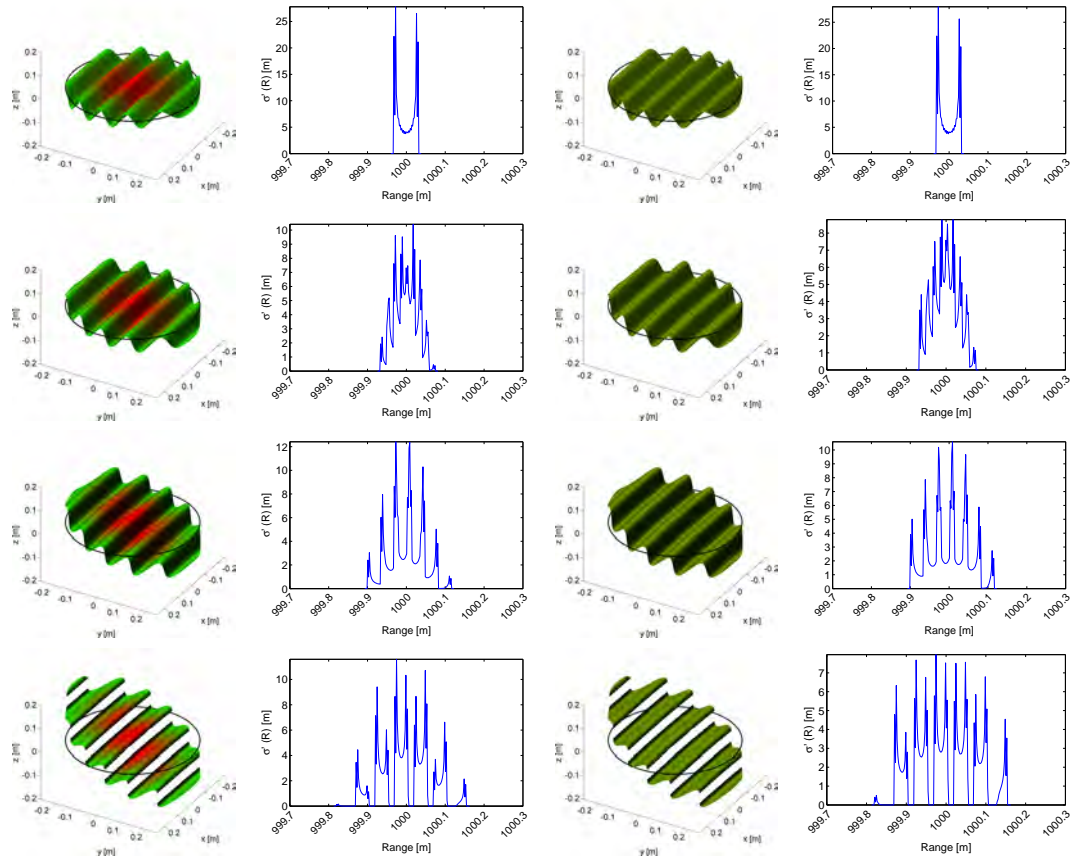


**Figure 4.9:** Differential backscatter cross-section for sinusoidal targets with parallel wavefronts. The amplitude was chosen to  $a = 0.03$  m and the wavelength to  $\lambda = 0.1$ . The tilt angles w.r.t. to the laser beam axis are 0, 10, 20 and 30° (from top to bottom).

### 4.1.5 Simulated total BCS

Additionally to the temporal (and thus spatial) shape, also the integral  $\sigma$  of the respective dBCS was investigated for the different target shapes. As expected, the only variation in the planar cases resulted from the incidence angle  $\vartheta$  (see Figure 4.10); the resulting  $\sigma = \pi/4$  for  $\vartheta = 0$  being the upper limit for all other variants.

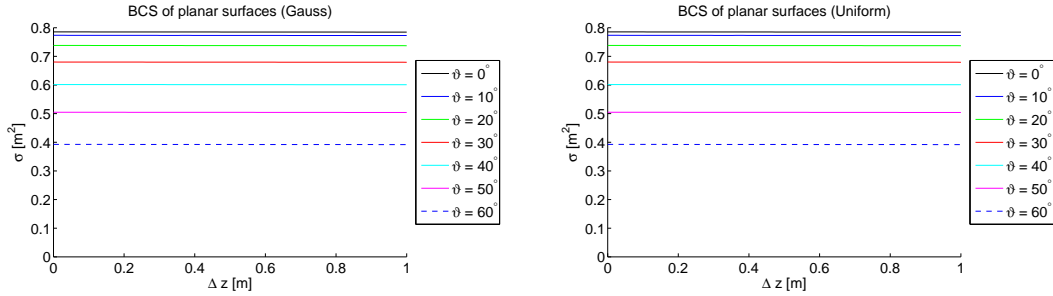


**Figure 4.10:** Total BCS  $\sigma$  for planar targets w.r.t. incidence angle  $\vartheta$  and offset  $\Delta z$ . Left: Gaussian power density distribution; right: uniform power density distribution.

As mentioned previously, in the spherical case  $\sigma$  stays constant for a specific radius in the uniform case if the whole sphere remains within the laser footprint; the bigger the radius, the less the offset  $m_y$  affects the value of the BCS and the closer it gets to the one of the non-tilted plane, as Figure 4.11 indicates. Similar results are found for the cylindrical case (see Figure 4.12).

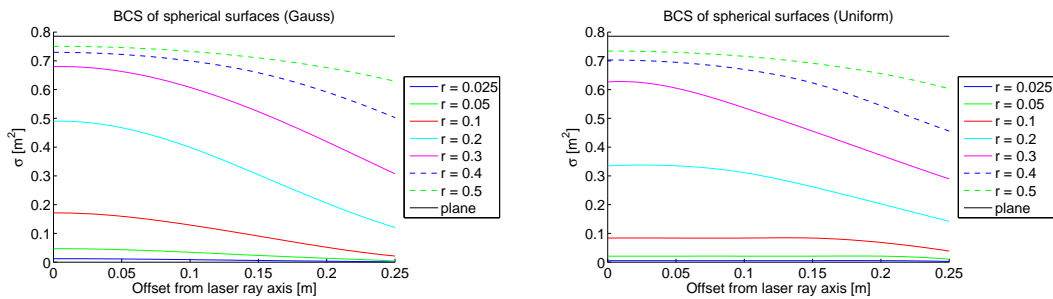


**Figure 4.11:** Total BCS  $\sigma$  for spherical targets w.r.t. offset  $m_y$  and radius  $r$ . Left: Gaussian power density distribution; right: uniform power density distribution.

For sinusoidal surfaces with circular wavefronts, the BCS  $\sigma$  decreases with increasing amplitude  $a$  while it increases with increasing wavelength  $\lambda$ ; the upper limit is again formed by the horizontal plane which corresponds to  $a = 0$  and/or  $\lambda = \infty$ , as Figure 4.13 shows. For the case of parallel wavefronts, the resulting  $\sigma$  are each very similar to the corresponding one for circular wavefronts in the non-tilted case. However, the situation is more complicated if  $\vartheta \neq 0$ . Depending on the wavelength, the illuminated parts of the

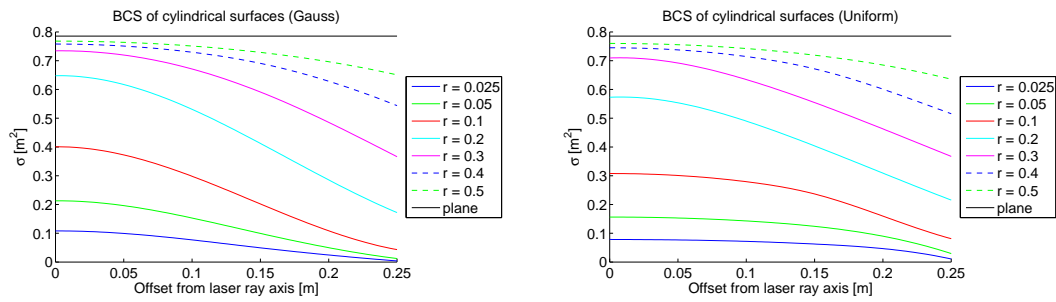


**Figure 4.12:** Total BCS  $\sigma$  for cylindrical targets w.r.t. offset  $m_y$  and radius  $r$ . Left: Gaussian power density distribution; right: uniform power density distribution.

target may act like a set of parallel planes orthogonal to the laser beam so that the BCS of a plane with the same  $\vartheta$  may be even exceeded (see Figure 4.14).

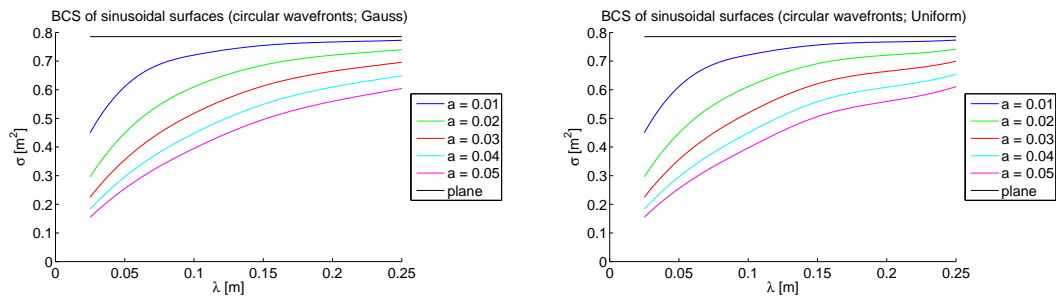


**Figure 4.13:** Total BCS  $\sigma$  for sinusoidal targets with circular wavefronts w.r.t. wavelength  $\lambda$  and amplitude  $a$ . Left: Gaussian power density distribution; right: uniform power density distribution.

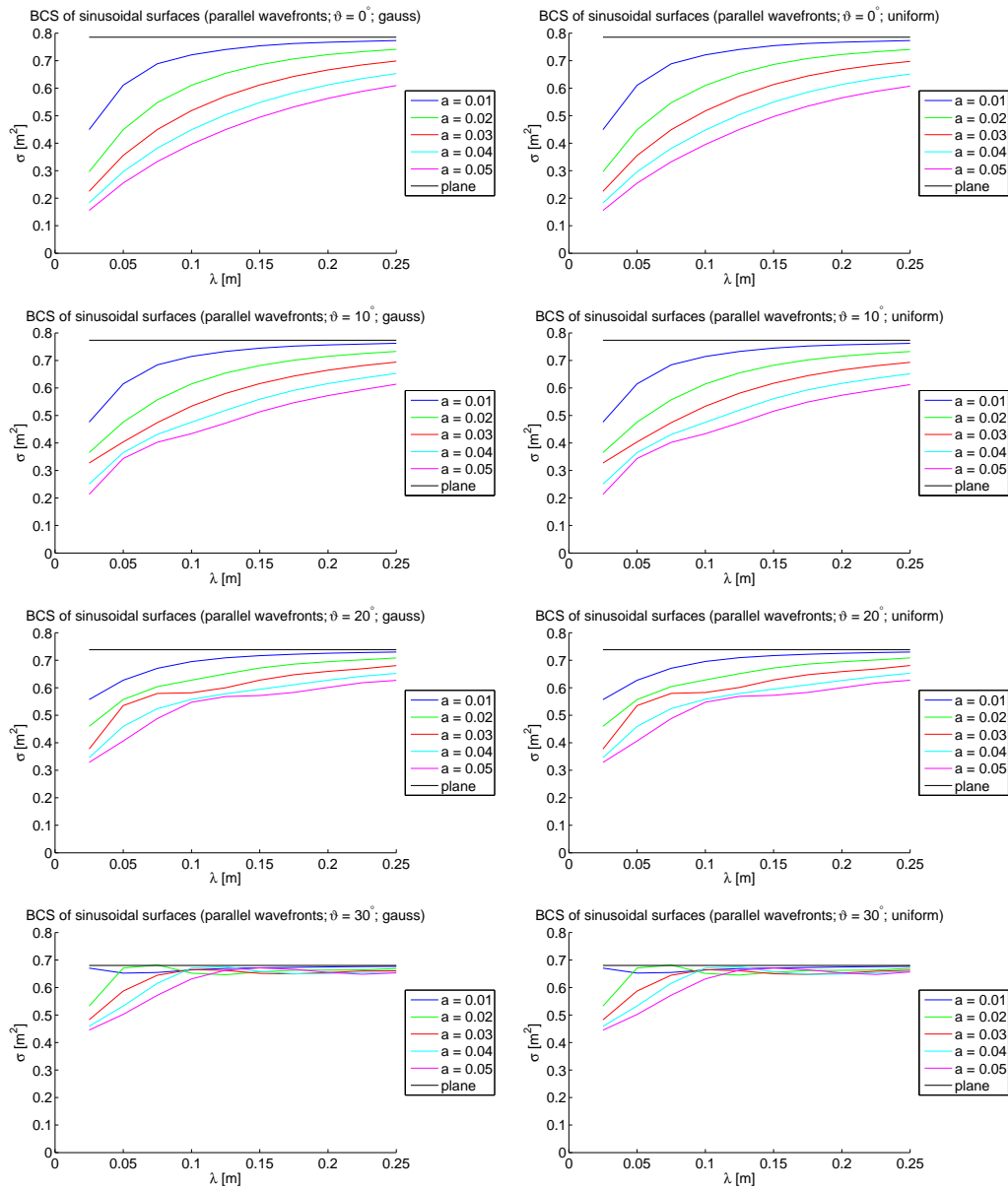


**Figure 4.14:** Total BCS  $\sigma$  for sinusoidal targets with parallel wavefronts w.r.t. wavelength  $\lambda$  and amplitude  $a$ . Left: Gaussian power density distribution; right: uniform power density distribution. The incidence angle increases from  $0^\circ$  (top) to  $30^\circ$  (bottom) in steps of  $10^\circ$ .

#### 4.1.6 Simulated recorded Echo Waveforms $P_r(t)$

As stated at the beginning of Section 4.1, recorded echo waveforms were simulated using system waveforms corresponding to the RIEGL LMS-Q series ( $s_s = 1.7$  ns) and to the Optech ALTM series ( $s_s = 4.8$  ns). These values were obtained by least-squares fit of real  $S(t)$  examples from extended ALS campaigns. These system waveforms were then convolved with the dBCS  $\sigma'(t)$ .

The results for the planar cases in Figures 4.15 and 4.16 clearly confirm the findings of Section 4.1.1 concerning separability w.r.t. offset  $\Delta z$  and incidence angle  $\vartheta$ . Figures D.1 and D.2 contain a detailed overview of the investigated configurations.

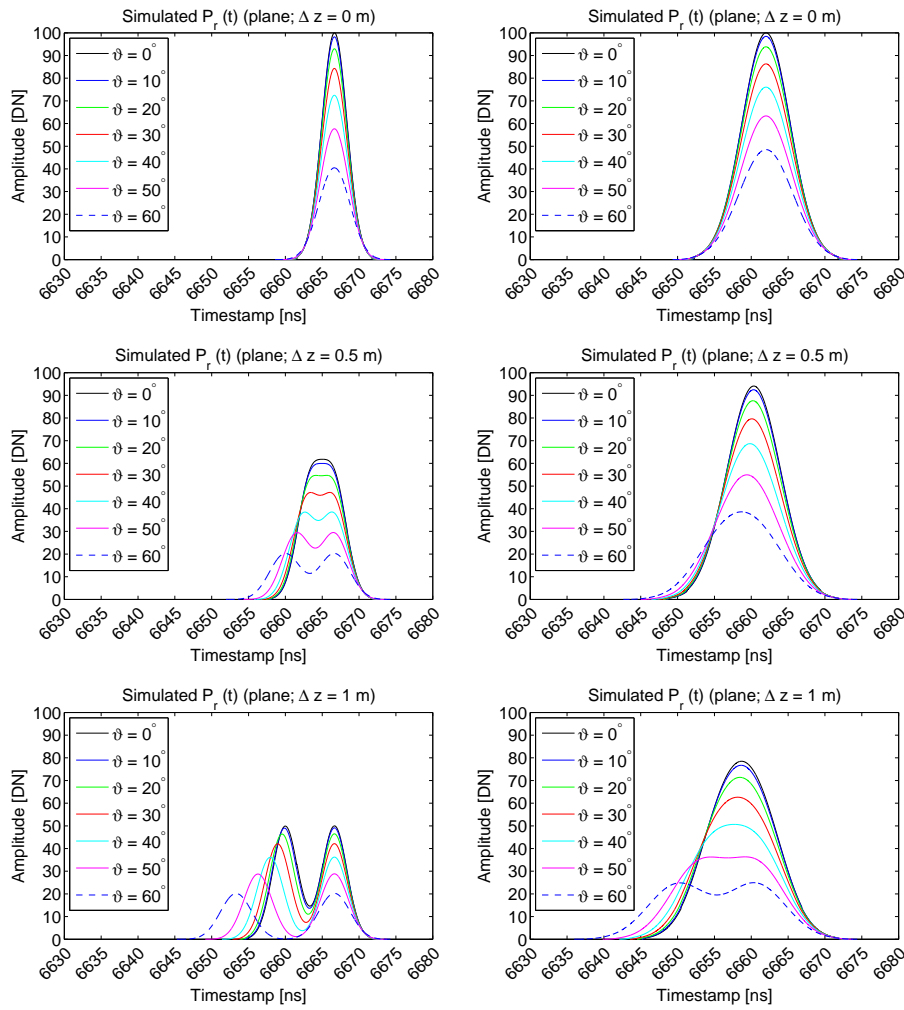


**Figure 4.15:** Simulated recorded echo waveforms  $P_r(t)$  for planar targets, retrieved by convolution of the simulated dBCS of the various configurations and Gaussian-shaped (standard deviation  $s_s$ ) system waveform  $S(t)$ . Left:  $s_s = 1.7$  ns (Gauss), right:  $s_s = 4.8$  ns (Gauss). The offset  $\Delta z$  varies from 0 (top), 0.5 m (middle) and 1 m (bottom).

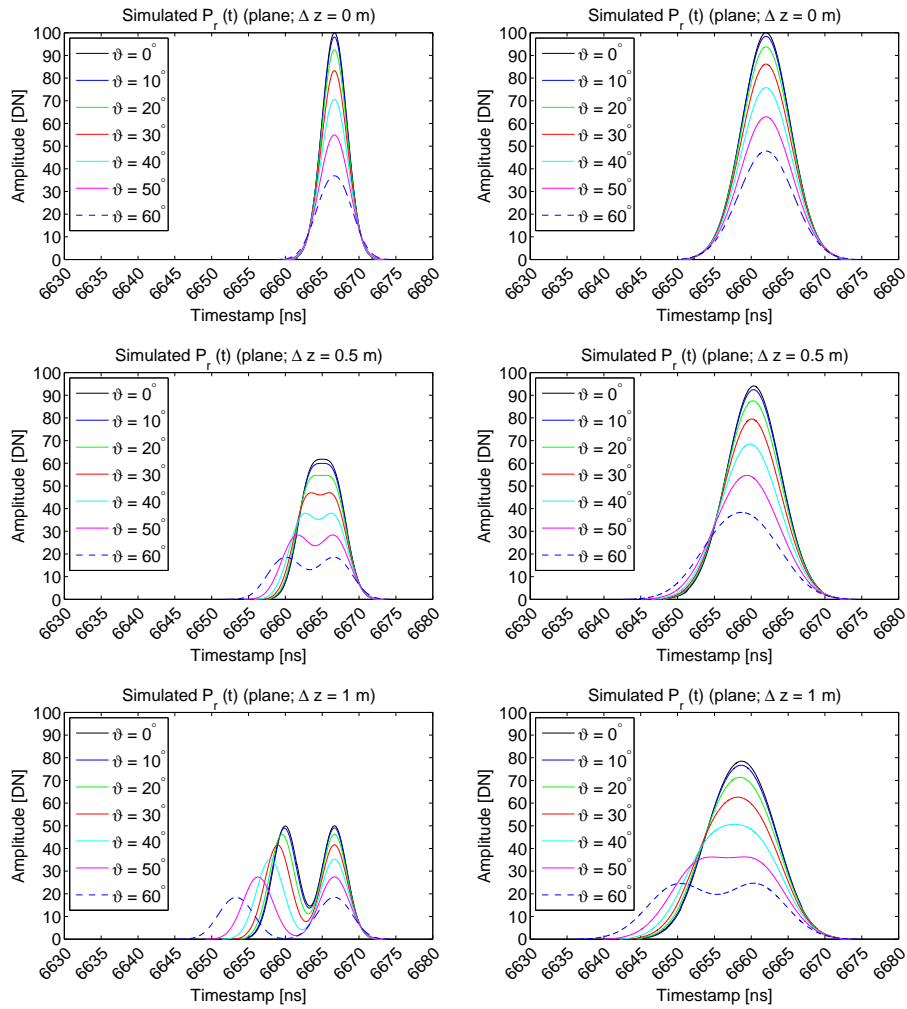


**Figure 4.16:** Continuation of Figure 4.15 for uniform power density distribution within the laser footprint.

For the spherical and the cylindrical examples, in the uniform case some waveforms were identical although the offsets to the laser beam axis were different—in accordance to the corresponding case for their respective dBCS; see Sections 4.1.2 and 4.1.3. As was expected, the amplitude increased quadratically with the radius in the spherical examples and linearly in the cylindrical examples, as visible in Figures 4.17 to 4.20. A detailed overview is given in Sections D.2 and D.3 in the appendix.

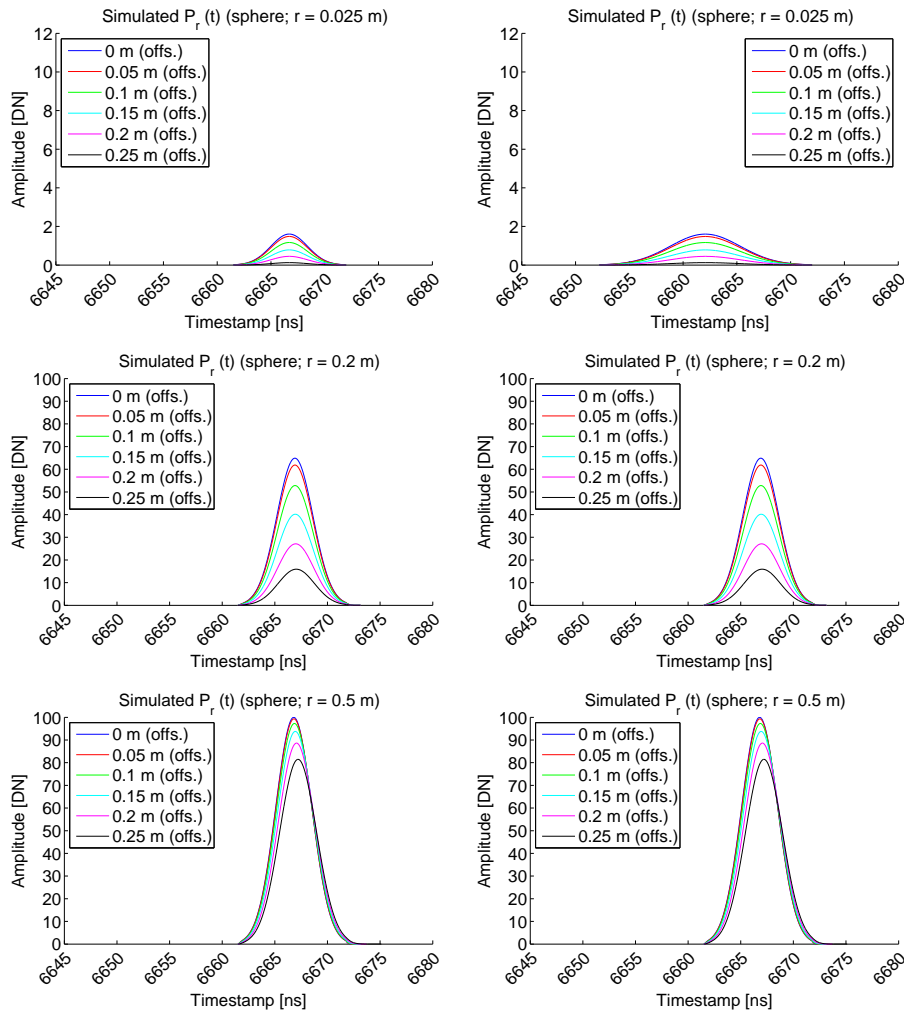


**Figure 4.17:** Simulated recorded echo waveforms  $P_r(t)$  for spherical targets, retrieved by convolution of the simulated dBCS of the various configurations and Gaussian-shaped (standard deviation  $s_s$ ) system waveform  $S(t)$ . Left:  $s_s = 1.7$  ns (Gauss), right:  $s_s = 4.8$  ns (Gauss). The radius  $r$  varies from 0.025 m (top), 0.2 m (middle) to 0.5 m (bottom).

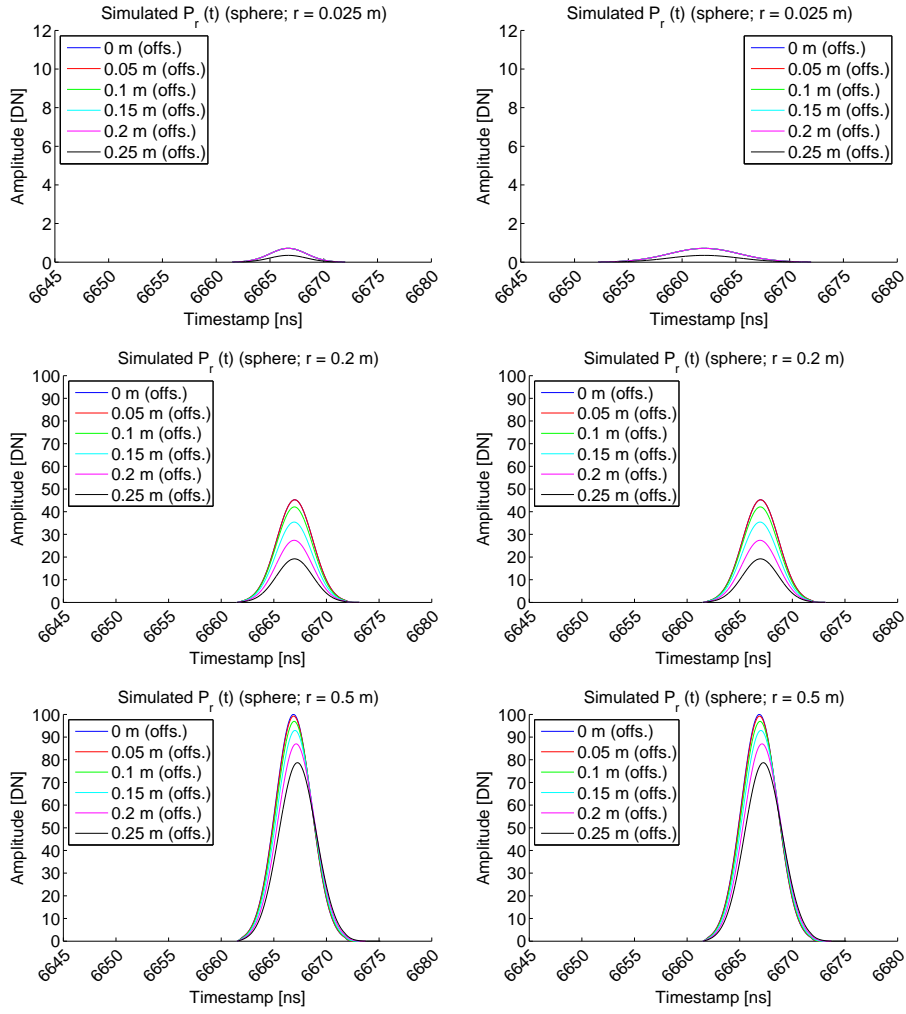


**Figure 4.18:** Continuation of Figure 4.17 for uniform power density distribution within the laser footprint.



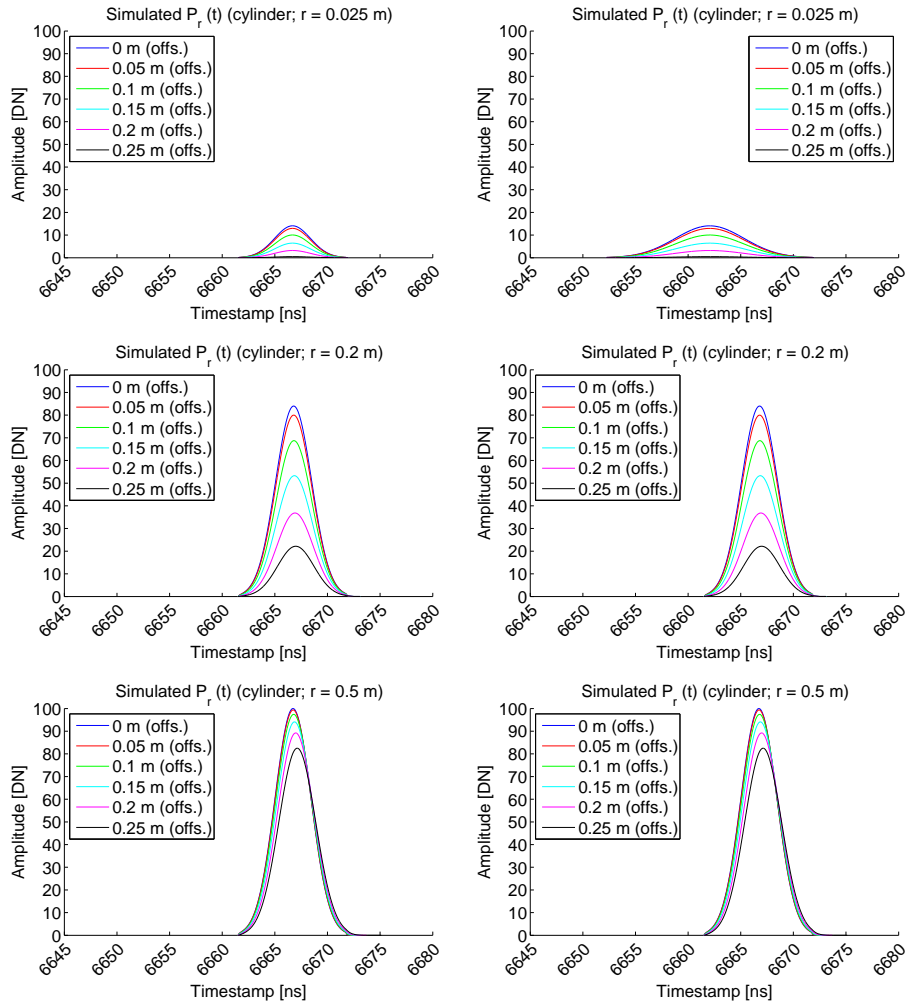


**Figure 4.19:** Simulated recorded echo waveforms  $P_r(t)$  for cylindrical targets, retrieved by convolution of the simulated dBCS of the various configurations and Gaussian-shaped (standard deviation  $s_s$ ) system waveform  $S(t)$ . Left:  $s_s = 1.7$  ns (Gauss), right:  $s_s = 4.8$  ns (Gauss). The radius  $r$  varies from 0.025 m (top), 0.2 m (middle) to 0.5 m (bottom).

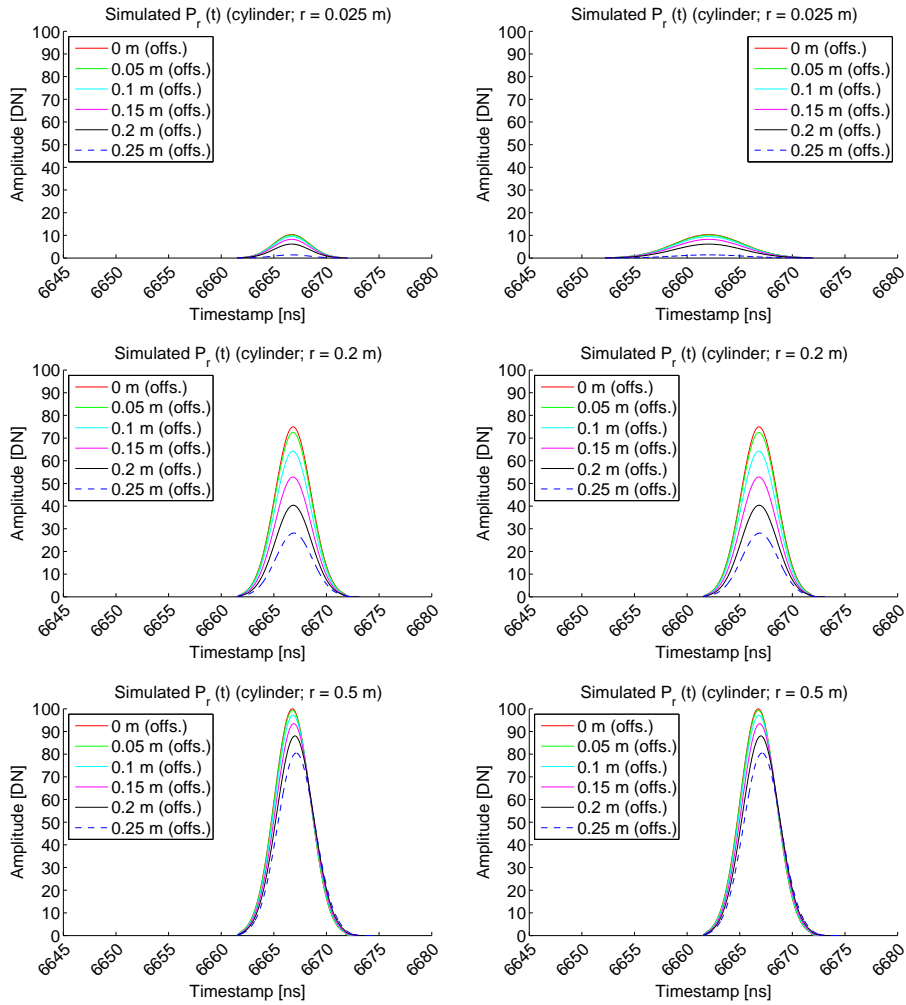


**Figure 4.20:** Continuation of Figure 4.19 for uniform power density distribution within the laser footprint.

For sinusoidal target surfaces, the resulting recorded echo waveforms are of special interest in the case of parallel wavefronts: with increasing incidence angle  $\vartheta$ , the influence of the amplitude  $a$  decreases and surfaces with higher (surface) amplitude  $a$  may result in a higher echo amplitude, in contrast to the examples with  $\vartheta = 0$ . See Figures 4.21 to 4.26 and Section D.4 in the appendix.

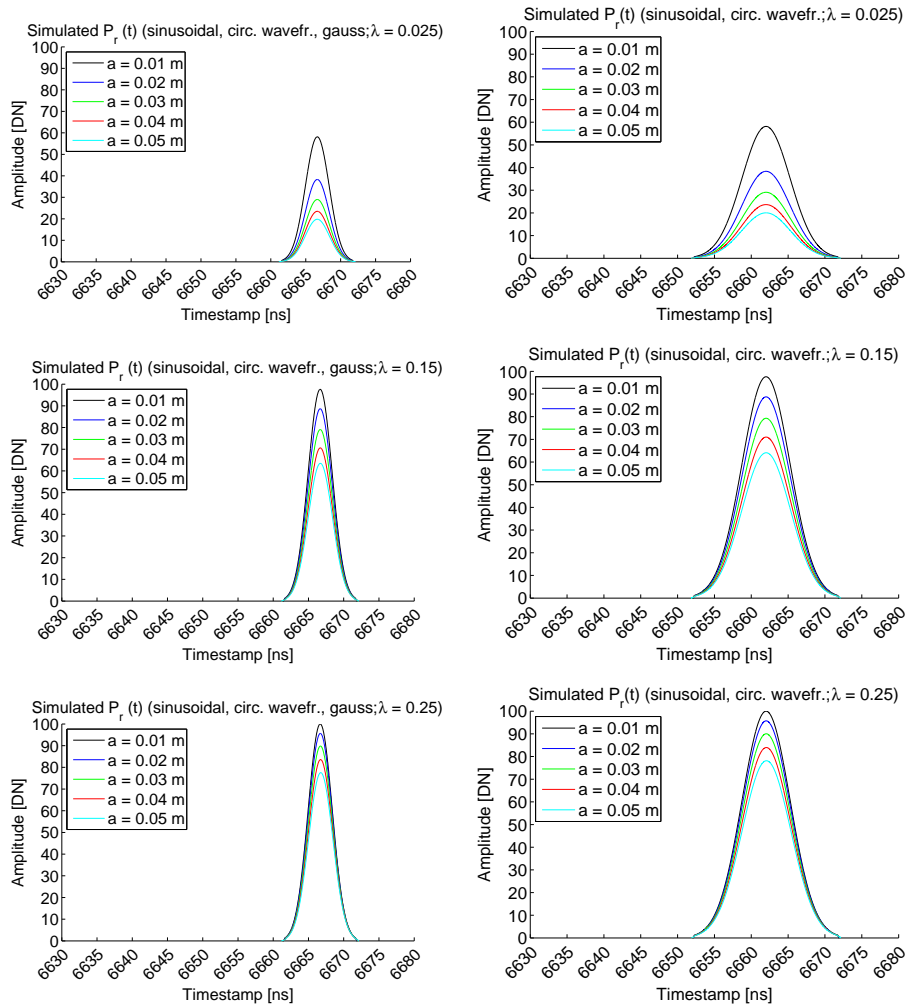


**Figure 4.21:** Simulated recorded echo waveforms  $P_r(t)$  for sinusoidal targets with circular wavefronts, retrieved by convolution of the simulated dBCS of the various configurations and Gaussian-shaped (standard deviation  $s_s$ ) system waveform  $S(t)$ . Left:  $s_s = 1.7$  ns (Gauss), right:  $s_s = 4.8$  ns (Gauss). The wavelength  $\lambda$  varies from 0.025 m (top) to 0.15 m (middle), to 0.25 m (bottom).

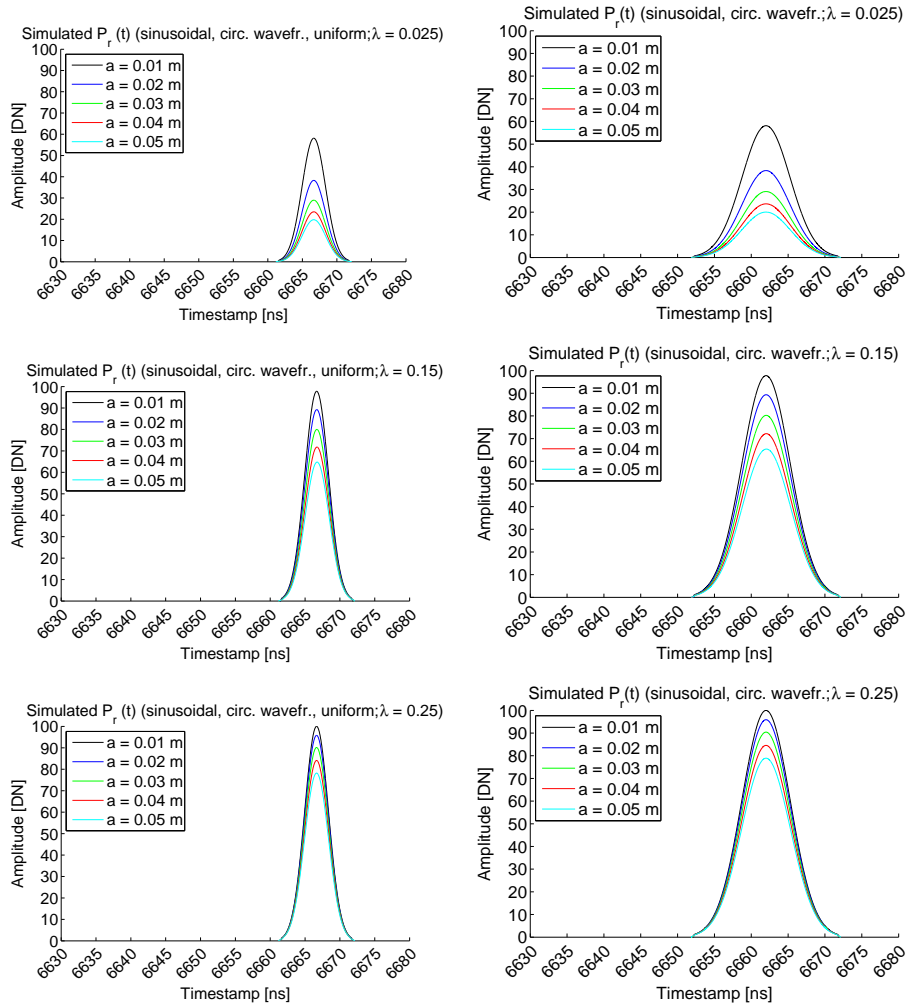


**Figure 4.22:** Continuation of Figure 4.21 for uniform power density distribution within the laser footprint.

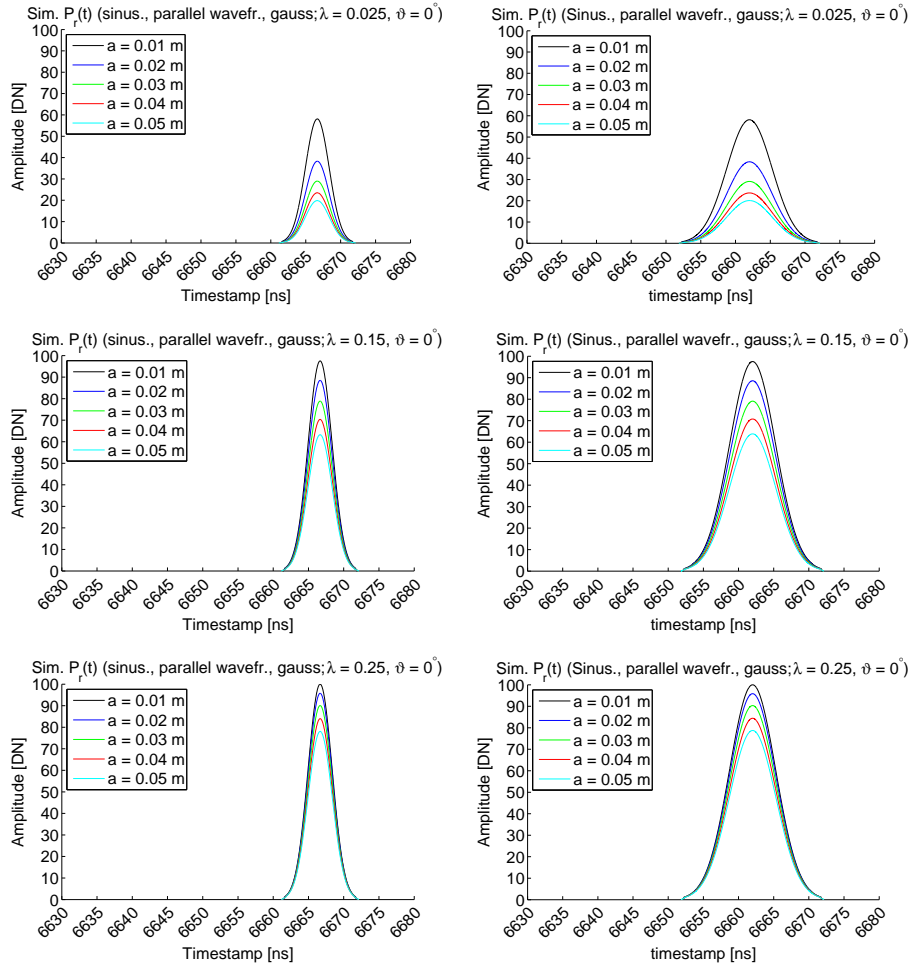


**Figure 4.23:** Simulated recorded echo waveforms  $P_r(t)$  for sinusoidal targets with parallel wavefronts, retrieved by convolution of the simulated dBCS of the various configurations and Gaussian-shaped (standard deviation  $s_s$ ) system waveform  $S(t)$ . Left:  $s_s = 1.7$  ns (Gauss), right:  $s_s = 4.8$  ns (Gauss). The wavelength  $\lambda$  varies from 0.025 m (top) to 0.15 m (middle), to 0.25 m (bottom).

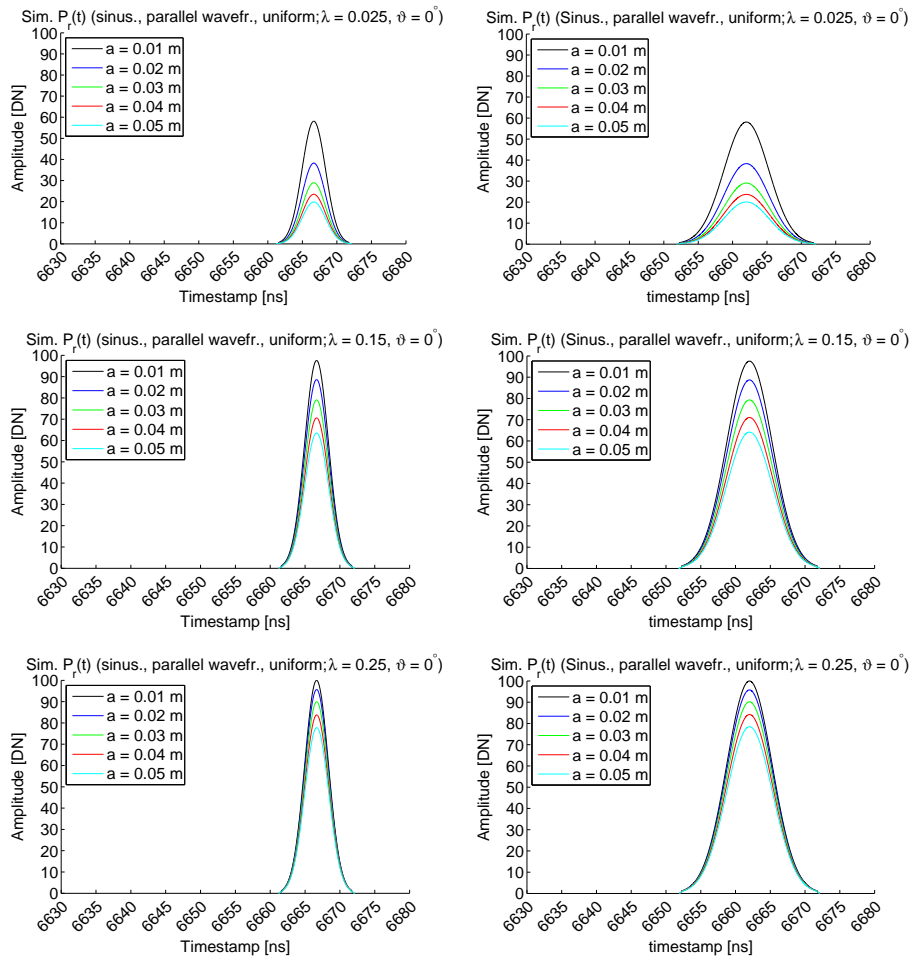


**Figure 4.24:** Continuation of Figure 4.23 for uniform power density distribution within the laser footprint.

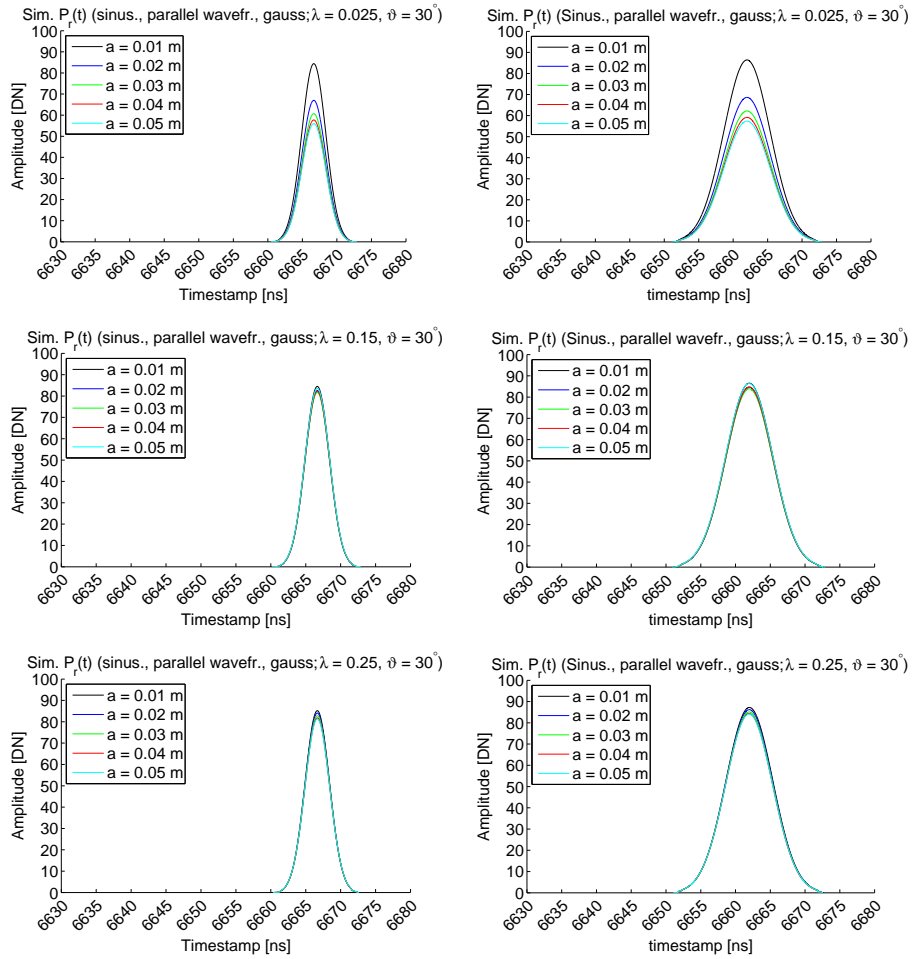


**Figure 4.25:** Simulated recorded echo waveforms  $P_r(t)$  for sinusoidal targets with parallel wavefronts and tilt angle  $\vartheta = 30^\circ$ , retrieved by convolution of the simulated dBCS of the various configurations and Gaussian-shaped (standard deviation  $s_s$ ) system waveform  $S(t)$ . Left:  $s_s = 1.7$  ns (Gauss), right:  $s_s = 4.8$  ns (Gauss). The wavelength  $\lambda$  varies from 0.025 m (top) to 0.15 m (middle), to 0.25 m (bottom).

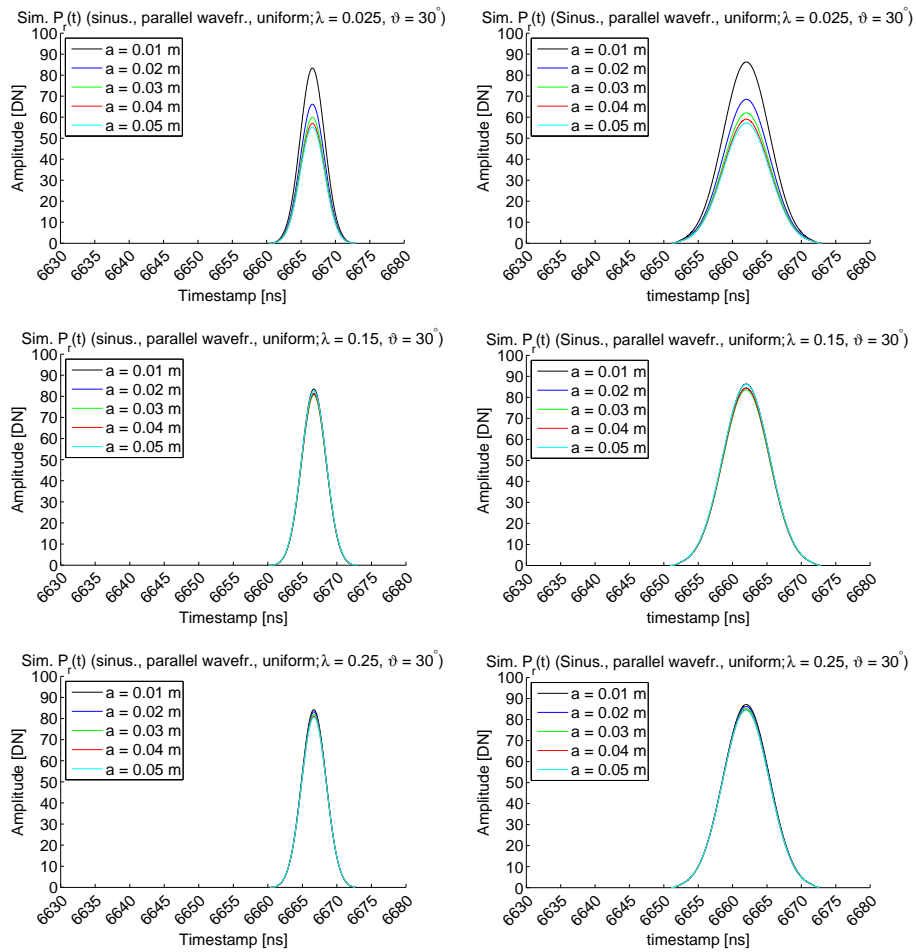


**Figure 4.26:** Continuation of Figure 4.25 for uniform power density distribution within the laser footprint.



## 4.2 Examples for Range Extraction and Echo Feature Calculation using a Correlation/ASDF-based Method

For the examples of this section, as well as for Section 4.6 and Chapter 6, we chose a test site around the village Obergurgl (Tyrol, Austria) where built-up areas, open terrain, high and low vegetation were present, as well as flat areas and steep slopes (see Figures 4.27 and 4.28). The 3D point cloud (approx. 1 pt/m<sup>2</sup>) was calculated from the extracted echoes in the full waveform and the direct georeferencing information of a single flight strip in a big lidar campaign. This campaign covered large parts of the Ötztal Alps and was operated with an Optech ALTM 3100 instrument. Apart from FWF and direct georeferencing data, also ranges and intensity (amplitude) values directly retrieved by the instrument were available; see [Roncat et al. 2013] for more details on the campaign.



**Figure 4.27:** Orthophoto of the test area in Obergurgl (Tyrol, Austria). Orthophoto: [www.geoimage.at](http://www.geoimage.at) ©, accessed on July 18, 2013. Coordinates given in UTM, Zone 32N.

Besides computing the point cloud, the *echo* attributes  $a$  (parabola scaling) and  $l_s$  (significance level) were additionally derived for each point. The visualization in Figure 4.29 shows that high vegetation is quite well visible. A detailed analysis concerning the geometric performance of the ASDF technique in this dataset containing an extensive cross-validation is given in Chapter 5.

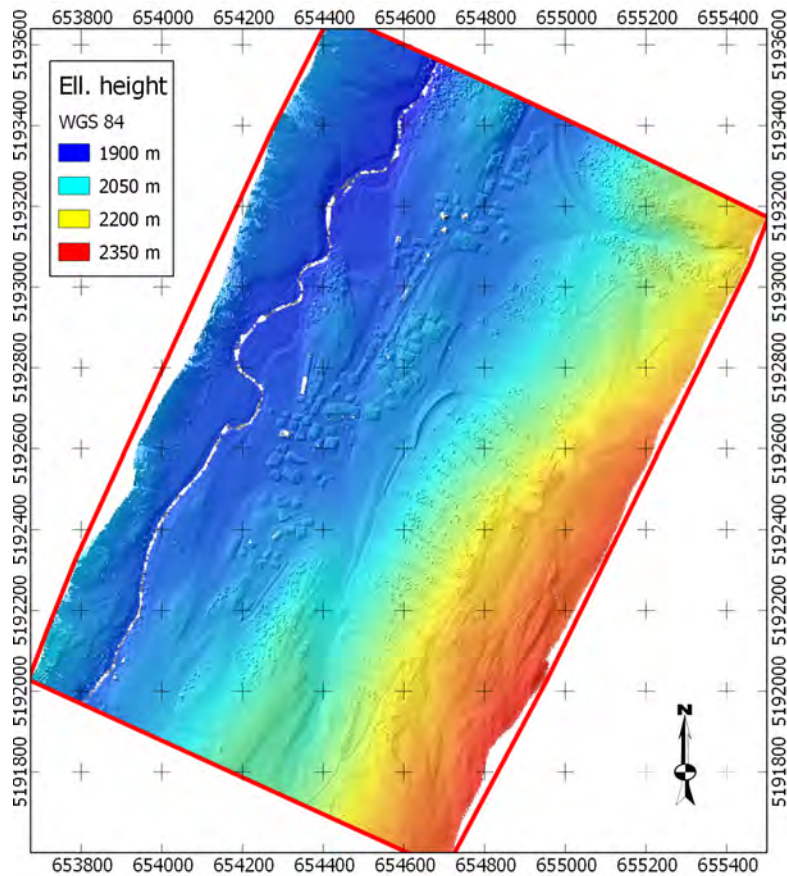


**Figure 4.28:** Digital surface model of the test area. Coordinates given in UTM, Zone 32N.

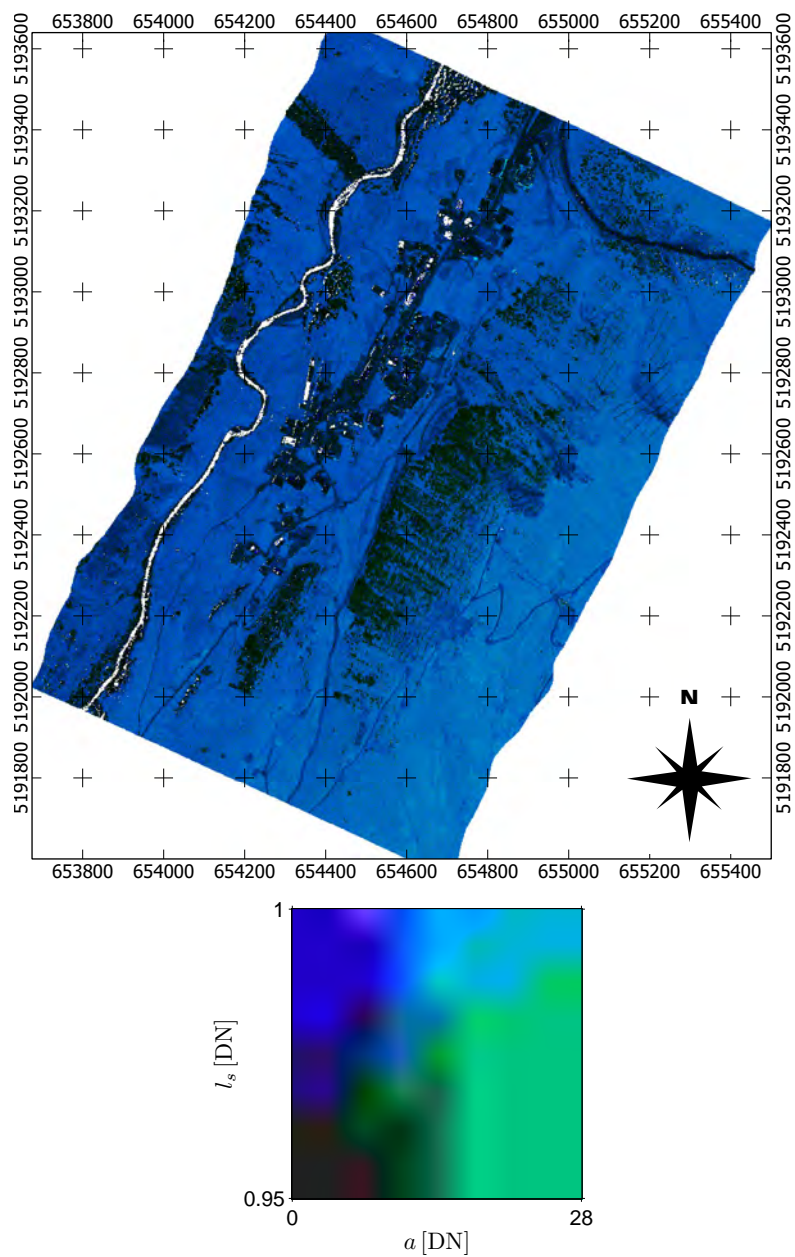


**Figure 4.29:** Top view of the ALS point cloud of the test area (cf. Figure 4.27), coloured-coded using the ASDF parabola scaling  $a$  (green channel) and the ASDF significance level  $l_s$  (blue channel).

### 4.3 Examples concerning the Stability of System Waveforms and their Impact on radiometric Calibration

Empirical analysis was carried out on the example of two full-waveform ALS campaigns. The campaigns took place over the Schönbrunn area in Vienna, Austria on August 20, 2004 and May 4, 2005, resp. Both were operated with a Riegl LMS-Q560 instrument [Riegl LMS 2014]. The first campaign consisted of eleven flight strips with 1.9 million to 2.9 million laser pulses per flight strip and 26.4 million laser pulses in total. The scanner was operated at a pulse repetition rate of 50 kHz.

The second campaign contained 13 flight strips with 3.6 million to 5.0 million laser pulses per flight strip, resulting in approx. 53.1 million laser pulses all together. The pulse repetition rate was 100 kHz. The scan layout of both campaigns is shown in Figure 4.30.

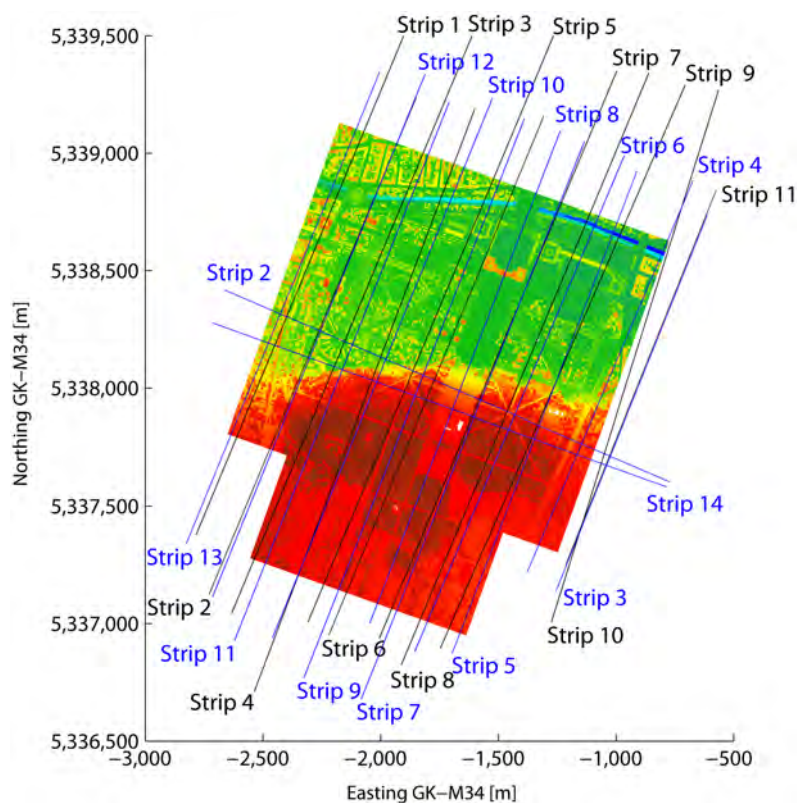


**Figure 4.30:** Digital surface model of the Schönbrunn area of Vienna overlaid with the flight trajectories of the two scanning campaigns of 2004 (black lines) and 2005 (blue lines).

The scan layouts of the two campaigns were nearly equivalent with the exception of the different pulse repetition rate and the two additional strips of the 2005 campaign

(strips 2 and 14). The two campaigns form therefore an ideal test data set for investigating the validity of the calibration constant among different flight strips and different scanning campaigns regarding the variation of the system waveforms.

For each recorded system waveform, its amplitude  $\hat{S}$  and width  $s_s$  were calculated using the Gaussian Decomposition algorithm suggested by [Wagner et al. \[2006\]](#). We based our analysis on histograms and other statistics (minimum, maximum, mean, standard deviation and relative standard deviation), calculated per flight strip for  $\hat{S}$  and  $s_s$ .

The 2004 campaign showed very similar distributions of  $\hat{S}$  (given in [Table 4.1](#) and [Figure 4.31](#)) with slightly different mean values per strip but very similar shapes. Only the flight strips 10 and 11 showed a noticeably higher skewness. The distributions of  $s_s$  per flight strip were practically identical (see [Table 4.2](#) and [Figure 4.32](#)).

Flight strip	min.	max.	$\mu_{\hat{S}}$	$\varsigma_{\hat{S}}$	$\varsigma_{\hat{S}}/\mu_{\hat{S}}$
1	193.4	264.3	226.0	7.3	0.032
2	190.7	259.4	224.0	7.2	0.032
3	188.3	256.8	<b>222.8</b>	<b>7.1</b>	<b>0.032</b>
4	192.3	257.3	223.5	7.2	0.032
5	192.6	<b>255.7</b>	223.2	7.2	0.032
6	191.6	260.8	224.6	7.3	0.032
7	<b>185.9</b>	260.8	225.5	7.3	0.032
8	192.3	265.7	225.9	7.3	0.032
9	193.8	262.8	226.9	7.4	0.033
10	198.4	265.6	<b>228.7</b>	<b>7.5</b>	<b>0.033</b>
11	<b>199.8</b>	<b>268.1</b>	228.4	7.5	0.033
Mean	—	—	225.4	7.3	0.032

**Table 4.1:** Statistics for the system waveform amplitudes  $\hat{S}$  of the 2004 campaign (unit: DN). Bold figures denote the minima and maxima per category for the whole campaign, resp.

The high similarity of the stripwise distributions of both  $\hat{S}$  and  $s_s$  in the 2004 campaign was not present in the other campaign. Especially the amplitudes showed a much higher variation which might be due to the higher pulse repetition rate. The mean values per flight strip ranged from 158.8 to 222.7 whereas the average value in the 2004 campaign was 225.4. However, the relative deviations per flight strip were comparable to those of the 2004 campaign, except for strip 2 where the relative deviation was more than three times higher. The two very small minimum amplitudes of strip 11 and 12 (1.2 and 3.6) are due to a erroneous recording, i.e. the digitizer was turned on although no laser pulse was emitted and only noise was recorded. [Table 4.3](#) and [Figure 4.33](#) contain the detailed figures and histograms.

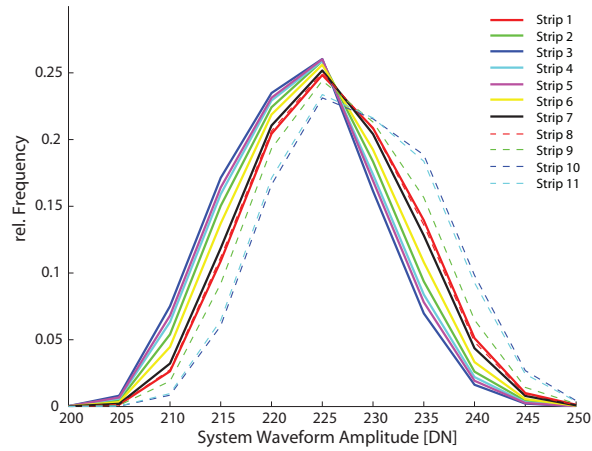


**Figure 4.31:** Histogram of the system waveform amplitudes  $\hat{S}$  per flight strip in the 2004 campaign (bin size: 5).

Flight strip	min.	max.	$\mu_{s_s}$	$\varsigma_{s_s}$	$\varsigma_{s_s}/\mu_{s_s}$
1	1.804	1.963	1.861	0.0138	0.00745
2	1.796	1.962	1.861	0.0139	0.00749
3	<b>1.806</b>	1.966	1.861	0.0140	0.00750
4	1.800	1.967	1.861	<b>0.0140</b>	<b>0.00751</b>
5	1.800	1.968	<b>1.861</b>	0.0139	0.00745
6	1.804	1.966	1.861	0.0139	0.00746
7	1.805	1.963	1.861	0.0139	0.00748
8	1.800	<b>1.980</b>	1.862	0.0139	0.00746
9	<b>1.795</b>	1.965	1.862	0.0139	0.00746
10	1.798	1.962	1.862	<b>0.0138</b>	<b>0.00743</b>
11	1.803	<b>1.961</b>	<b>1.862</b>	0.0139	0.00749
Mean	—	—	1.861	0.0139	0.00750

**Table 4.2:** Statistics for the system waveform widths  $s_s$  of the 2004 campaign (unit: ns). Bold figures denote the minima and maxima per category for the whole campaign, resp.

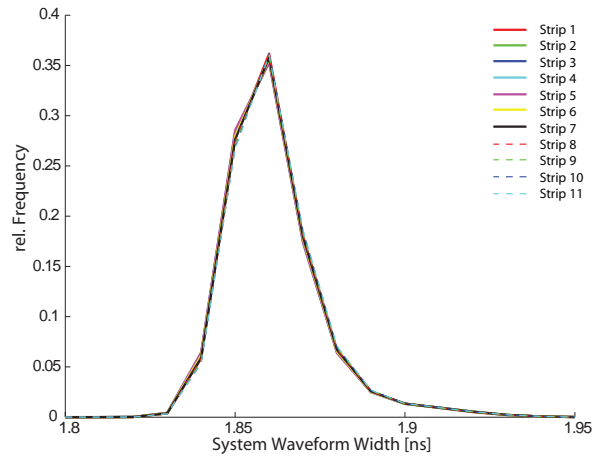


**Figure 4.32:** Histogram of the system waveform widths  $s_s$  per flight strip in the 2004 campaign (bin size: 0.01).

Flight strip	min.	max.	$\mu_{\hat{S}}$	$\varsigma_{\hat{S}}$	$\varsigma_{\hat{S}}/\mu_{\hat{S}}$
2	126.8	242.8	161.2	<b>19.5</b>	<b>0.121</b>
3	135.4	<b>185.1</b>	<b>158.8</b>	5.7	0.036
4	143.3	189.0	165.1	<b>5.5</b>	0.033
5	148.3	199.6	173.7	6.2	0.036
6	160.9	224.2	193.7	7.5	0.038
7	174.9	232.5	203.3	6.5	0.032
8	179.6	242.3	210.3	7.1	0.034
9	180.4	240.1	210.4	6.9	0.033
10	183.2	244.5	214.9	7.0	0.033
11	3.6	245.6	214.5	6.9	0.032
12	<b>1.2</b>	249.9	219.6	7.1	0.032
13	<b>188.9</b>	247.2	218.3	6.9	<b>0.032</b>
14	188.1	<b>252.8</b>	<b>222.7</b>	7.2	0.032
Mean	—	—	197.4	7.7	0.040

**Table 4.3:** Statistics for the system waveform amplitudes  $\hat{S}$  of the 2005 campaign (unit: DN). Bold figures denote the minima and maxima per category for the whole campaign, resp.

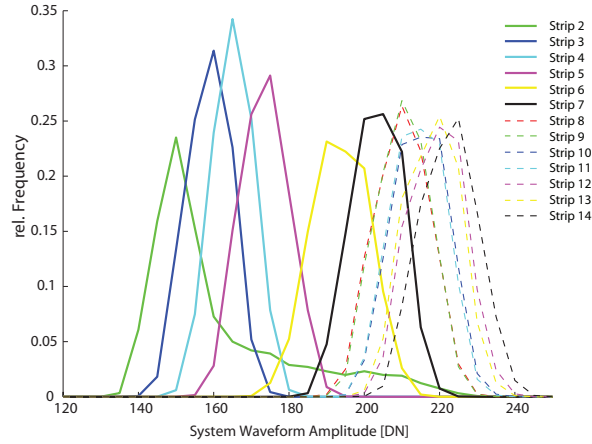


**Figure 4.33:** Histogram of the system waveform amplitudes  $\hat{S}$  per flight strip of the 2005 campaign (bin size: 5).

The average of the pulse widths  $s_s$  in the 2005 campaign differed about 1.5% from the average value of 2004 (1.835 ns vs. 1.861 ns) with lower relative deviations. All flight strips showed very similar distributions, in contrast to the distributions of  $\hat{S}$  (see Table 4.4 and Figure 4.5).

Flight strip	min.	max.	$\mu_{s_s}$	$\varsigma_{s_s}$	$\varsigma_{s_s}/\mu_{s_s}$
2	1.775	1.882	1.832	<b>0.00911</b>	<b>0.00497</b>
3	1.777	1.877	<b>1.832</b>	0.00894	0.00488
4	1.767	1.880	1.835	0.00871	0.00475
5	1.775	1.881	1.835	0.00840	0.00458
6	1.783	<b>1.873</b>	1.834	0.00786	0.00428
7	1.777	1.876	1.834	0.00770	0.00420
8	1.781	1.877	1.835	0.00763	0.00416
9	<b>1.786</b>	1.874	1.836	0.00763	0.00416
10	1.774	1.875	1.836	0.00761	0.00414
11	<b>0.363</b>	1.882	1.837	0.00765	0.00416
12	1.776	<b>2.207</b>	1.837	0.00756	0.00410
13	1.776	1.875	1.837	0.00756	0.00412
14	1.782	1.879	<b>1.838</b>	<b>0.00749</b>	<b>0.00408</b>
Mean	—	—	1.835	0.00800	0.00440

**Table 4.4:** Statistics for the system waveform widths  $s_s$  of the 2005 campaign (unit: ns). Bold figures denote the minima and maxima per category for the whole campaign, resp.

Besides the statistics of amplitudes and widths of the sytem waveforms, also their



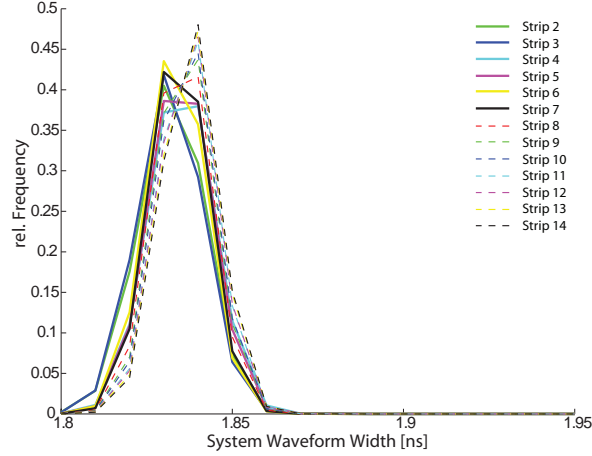


**Table 4.5:** Histogram of the system waveform widths  $s_s$  per flight strip of the 2005 campaign (bin size: 0.01).

correlation coefficients  $\rho$  were calculated per flight strip. Only positive correlation was found, varying from 0.23 to 0.24 in the 2004 campaign and from 0.02 to 0.18 in the campaign of 2005.

These results enable us for calculating upper bounds of their influence on the calibration constant by evaluating Equation (3.36). Taking the respective maximum values in Tables 4.1–4.4, we see that the relative deviation of  $C_{\text{CAL}}$  is

$$\begin{aligned} \frac{SC_{\text{CAL}}}{C_{\text{CAL}}} &\leq \sqrt{0.033^2 + 0.00751^2 + 2 \cdot 0.24 \cdot 0.033 \cdot 0.00751} \\ &= 0.0356 \end{aligned}$$

within the single flight strips of 2004,

$$\begin{aligned} \frac{SC_{\text{CAL}}}{C_{\text{CAL}}} &= \sqrt{0.121^2 + 0.00497^2 + 2 \cdot 0.14 \cdot 0.121 \cdot 0.00497} \\ &= 0.1218 \end{aligned}$$

for strip 2 of the 2005 campaign (where  $\rho = 0.14$ ) and

$$\begin{aligned} \frac{SC_{\text{CAL}}}{C_{\text{CAL}}} &\leq \sqrt{0.038^2 + 0.00488^2 + 2 \cdot 0.18 \cdot 0.038 \cdot 0.00488} \\ &= 0.0392 \end{aligned}$$

for all other single strips of this campaign. The variation of  $\hat{S}$  can be regarded as main influence quantity for the variation of  $C_{\text{CAL}}$  so that  $s_s$  and the correlation between these two parameters can be neglected.

Our results also apply if an other deconvolution technique than Gaussian Decomposition is performed. In this case, the right-hand side of Equation (3.31) is taken into

account so that the relative deviation of  $C_{\text{CAL}}$  is only dependent on the relative deviation of system waveform energy (integral),  $\varsigma_{E_S}/E_S$ . As Figure 4.34 shows, it resulted in a distribution similar to the one of the system waveforms' amplitudes. This was expected due to the small variations of the widths  $s_s$ .

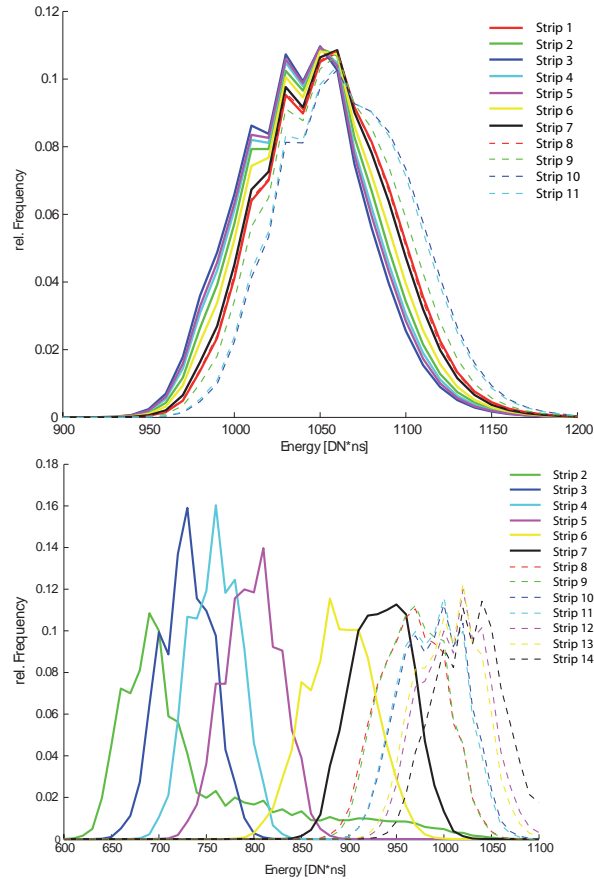


**Figure 4.34:** Histogram of the system waveform energy (integral)  $E_s$  per flight strip of the 2004 (top) and 2005 campaign (bottom). Bin size: 10 [DN ns].

## 4.4 Examples for Deconvolution based on uniform B-Splines

In this section the deconvolution of received echo waveforms, targeted at the computation of the scaled dBCS, will be demonstrated. First, two synthetic examples will be presented in Section 4.4.1. In both cases, the system waveform and the scaled differential backscatter cross-section are given. All of them are of degree 3, leading to the received echo waveform by convolution with degree 7. Second, we show a real-world example for B-spline deconvolution in Section 4.4.2 and analyse the same example by Gaussian Decomposition in Section 4.4.3.

For both synthetic examples, the amplitudes were normalized in the form that the value of the respectively greatest  $b_{i,\varepsilon}$  and  $b_{j,\sigma}$  was set to 1. Both examples use the same system waveform which is slightly asymmetrical (see Figure 4.35(a), solid line). Among its control points there are three with non-zero values (knot distance  $\Delta u = 1$  ns) so that the whole system waveform has a duration of 7 ns. The full width at half maximum (FWHM) which is commonly used to characterize the pulse length is 1.8 ns.

For the reconstruction of the scaled dBCS, both the synthetic system waveform and the synthetic waveform were sampled in 1 ns intervals. To present information about the stability of the proposed algorithm in the presence of noise, four sampling variants were made:

- noise-free (“×” markers in Figures 4.35 and 4.36)
- added Gaussian noise with  $\varsigma = 0.01$  (“+” markers in Figures 4.35 and 4.36)
- added Gaussian noise with  $\varsigma = 0.02$  (“.” markers in Figures 4.35 and 4.36)
- added Gaussian noise with  $\varsigma = 0.05$  (“o” markers in Figures 4.35 and 4.36)

The Gaussian noise was added additively to the sampled values. For each variant, the investigation was based on statistic quantities, namely the square root of the variance a posteriori of the adjustment,  $s_0$ , the root mean square error, r.m.s., and the normalized root mean square error, r.m.s.<sub>norm</sub>. The latter are defined as follows:

$$\text{r.m.s.}(f(t), g(t)) := \sqrt{\frac{1}{t_{\max} - t_{\min}} \int_{t_{\min}}^{t_{\max}} (f(t) - g(t))^2 dt}$$

and

$$\text{r.m.s.}_{\text{norm}}(f(t), g(t)) := \frac{\text{r.m.s.}(f(t), g(t))}{\text{r.m.s.}(g(t), 0)},$$

resp. In the examples treated here,  $t_{\min}$  is always equal to 0 and  $t_{\max}$  is equal to  $\Delta t i_{\max}$ ,  $\Delta t j_{\max}$  or  $\Delta t k_{\max}$ , resp. In detail, the error analysis consists of:

- $s_0$  of the estimated system waveform ( $\hat{S}(t)$ ) and received echo waveform ( $\hat{P}_r(t)$ ), root mean square errors  $\text{r.m.s.}(\hat{S}(t), S(t))$  and  $\text{r.m.s.}(\hat{P}_r(t), P_r(t))$ , and normalized r.m.s. errors  $\text{r.m.s.}_{\text{norm}}(\hat{S}(t), S(t))$  and  $\text{r.m.s.}_{\text{norm}}(\hat{P}_r(t), P_r(t))$  of these fitted curves (see Table 4.6), where  $S(t)$  and  $P_r(t)$  denote the synthetically generated system and received echo waveform
- $s_0$  of the deconvolution ( $\hat{\sigma}'(t)$ ) and root mean square errors  $\text{r.m.s.}(\hat{\sigma}'(t), \bar{\sigma}'(t))$  and  $\text{r.m.s.}_{\text{norm}}(\hat{\sigma}'(t), \bar{\sigma}'(t))$  of the scaled dBCS reconstructed by deconvolution in comparison to the synthetic scaled dBCS (see Tabs. 4.7(a) and 4.8(a), resp.)
- r.m.s. errors of the forward-modeled received echo waveform, i.e. convolution of fitted system waveform and reconstructed scaled dBCS  $\bar{P}_r(t) = \hat{S}(t) \otimes \hat{\sigma}'(t)$ , in comparison to the synthetic ( $\text{r.m.s.}(\bar{P}_r(t), P_r(t))$ ,  $\text{r.m.s.}_{\text{norm}}(\bar{P}_r(t), P_r(t))$ ) and fitted received echo waveform ( $\text{r.m.s.}(\hat{P}_r(t), P_r(t))$ ,  $\text{r.m.s.}_{\text{norm}}(\hat{P}_r(t), P_r(t))$ ). See Tables 4.7(b) and 4.8(b), resp.

#### 4.4.1 Deconvolution of synthetic Data

The deconvolution of one synthetic *asymmetric* scatterer is shown in Figure 4.35(b) (full duration: 7 ns). It is highly asymmetric with a steeper ascending slope. The convolution of system waveform and scaled dBCS leads to an asymmetric synthetic received echo waveform (full duration: 14 ns; see Figure 4.36(a)).

The synthetic scaled dBCS representing *three symmetrical* scatterers is shown in Figure 4.35(c) (full duration: 14 ns). The convolution of system waveform and scaled dBCS leads to a synthetic received echo waveform containing three echoes of different echo width (full duration: 21 ns; see Figure 4.36(b)). The whole scaled dBCS is symmetric, but the asymmetric system waveform leads to an asymmetric received echo waveform.

Table 4.6 gives an overview of the results of the curve fittings. In both cases, an error-free sampling in 1 ns intervals yields an approximation of the synthetic curves without noticeable deviation from the original curves, as was expected. Thus, in this case also the scaled dBCS can be reconstructed by deconvolution without significant deviation. In the case of curve fitting under noise, both the  $s_0$  and r.m.s. error increase according to the growing noise level. This is also valid for the deconvolution.

For the asymmetric scatterer, Figure 4.37(a) shows that the general shape of the scaled dBCS is estimated well, including the asymmetry. The noise levels of 1% of the system waveform and the received echo waveform result in 5% of the deconvolved scaled dBCS (value of 0.0473 in Table 4.7(a)). In the forward modeling, however, the error level of 0.01 is maintained, indicating that the deconvolution remains a task with poorly defined optimal values. With increasing noise level, the general shape of the scaled dBCS is maintained (figures are not shown). However, the deviations grow according to the noise level.

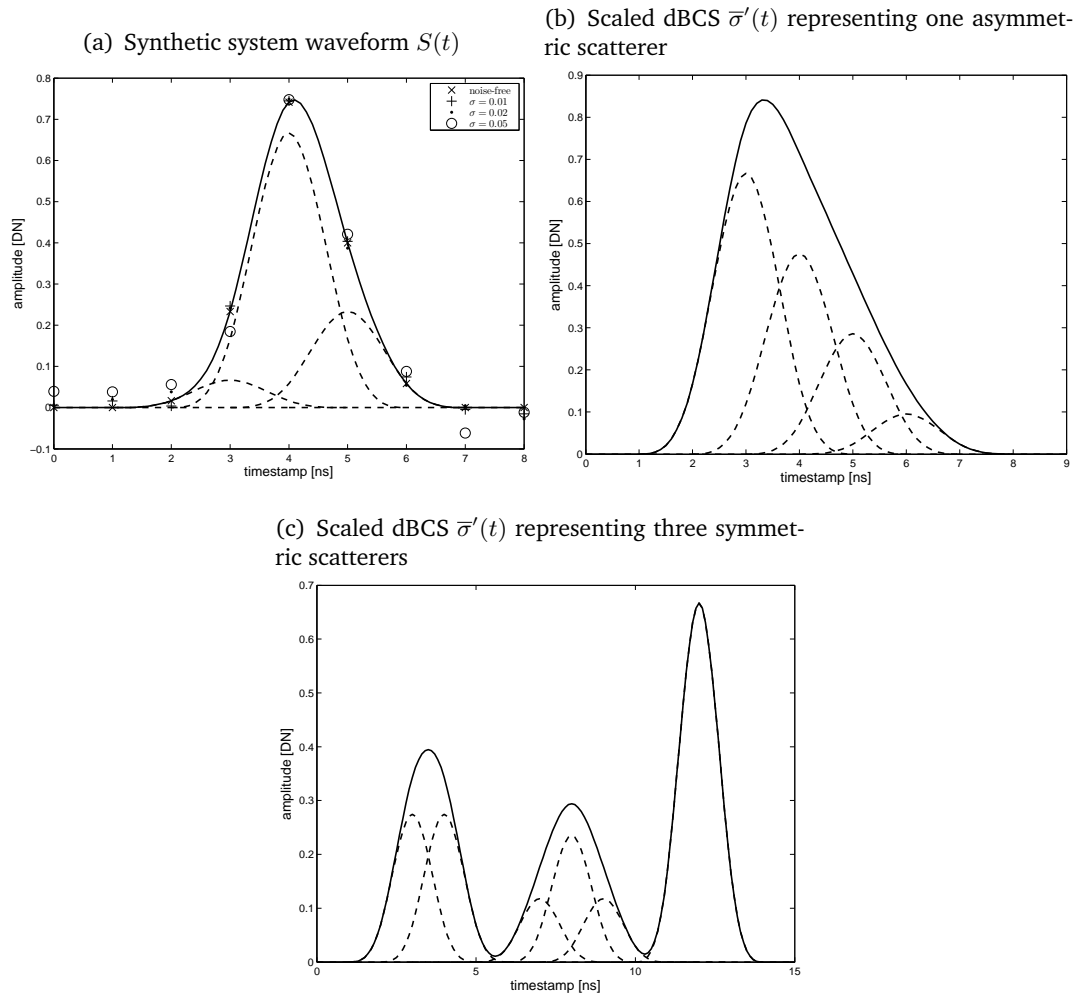


**Figure 4.35:** Construction of synthetic examples for B-spline convolution and deconvolution. B-splines are shown as solid lines, while their individual components are depicted as dashed curves. Image 4.35(a) shows the system waveform, 4.35(b) shows the scaled dBCS of a synthetic asymmetric scatterer, and 4.35(c) the scaled dBCS of three synthetic symmetric scatterers. Figure 4.36 shows the received echo waveforms corresponding to these data. “×”, “+”, “.” and “o” markers indicate sampled values without and with added Gaussian noise of different intensity.

(a) Synthetic received echo waveform  $P_r(t)$ : one asymmetric scatterer (b) Synthetic received echo waveform  $P_r(t)$ : three symmetric scatterers

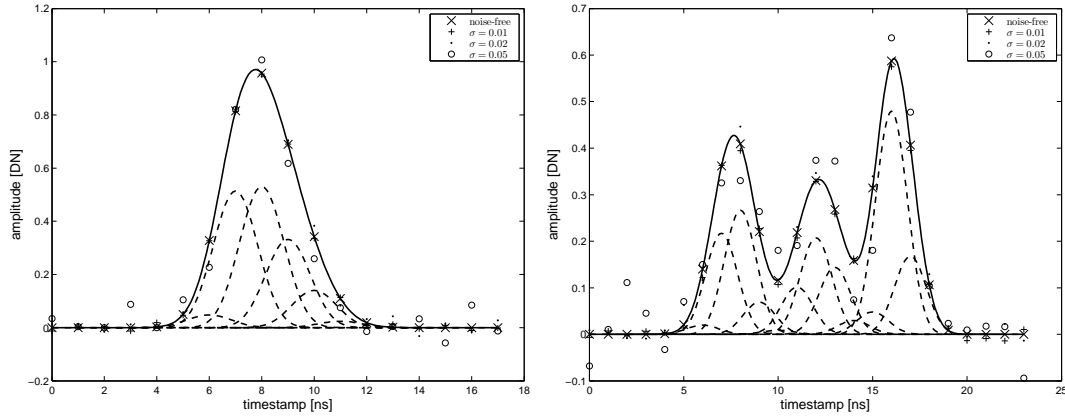


**Figure 4.36:** Synthetic received echo waveforms  $P_r(t)$  resulting from the convolution of the system waveform and the scaled dBCS of Figure 4.35. The solid line in image 4.36(a) is the convolution of the solid lines in Figures 4.35(a) and 4.35(b), whereas the solid line in image 4.36(b) is the convolution of the solid lines in Figures 4.35(a) and 4.35(c). “x”, “+”, “.” and “o” markers indicate sampled values without and with added Gaussian noise of different intensity.

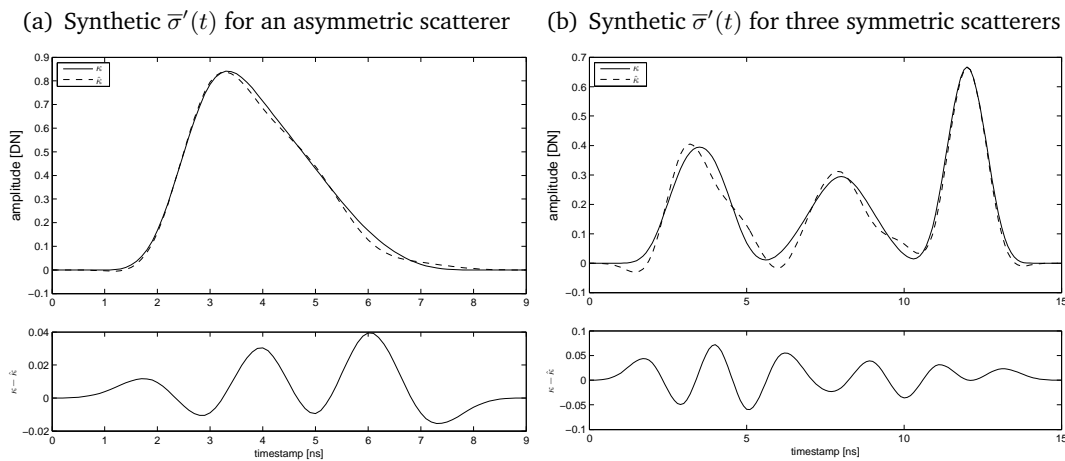


**Figure 4.37:** Top: Synthetic ( $\bar{\sigma}'(t)$ , solid line) vs. reconstructed scaled dBCS ( $\hat{\sigma}'(t)$ , dashed line), noise level  $\varsigma = 0.01$ . Bottom: Difference  $\bar{\sigma}'(t) - \hat{\sigma}'(t)$  of the two curves.

(a) System waveform			
noise level ( $\varsigma$ ), symbol	$s_0$	r.m.s. $(\hat{S}(t), S(t))$	r.m.s. <sub>norm</sub> $(\hat{S}(t), S(t))$
0 ( $\times$ )	0.0000	0.0000	0.0000
0.01 (+)	0.0148	0.0048	0.0155
0.02 ( $\cdot$ )	0.0167	0.0126	0.0411
0.05 ( $\circ$ )	0.0439	0.0307	0.0997

(b) Received echo waveform asymmetric echo			
noise level ( $\varsigma$ ), symbol	$s_0$	r.m.s. $(\hat{P}_r(t), P_r(t))$	r.m.s. <sub>norm</sub> $(\hat{P}_r(t), P_r(t))$
0 ( $\times$ )	0.0000	0.0000	0.0000
0.01 (+)	0.0109	0.0030	0.0082
0.02 ( $\cdot$ )	0.0203	0.0161	0.0437
0.05 ( $\circ$ )	0.0535	0.0416	0.1132

(c) received echo waveform three echoes			
noise level ( $\varsigma$ ), symbol	$s_0$	r.m.s. $(\hat{P}_r(t), P_r(t))$	r.m.s. <sub>norm</sub> $(\hat{P}_r(t), P_r(t))$
0 ( $\times$ )	0.0000	0.0000	0.0000
0.01 (+)	0.0095	0.0079	0.0339
0.02 ( $\cdot$ )	0.0103	0.0157	0.0674
0.05 ( $\circ$ )	0.0644	0.0522	0.2237

**Table 4.6:** Error analysis: Curve fitting of system waveform 4.6(a) and received echo waveforms 4.6(b), 4.6(c)

For the case of three symmetric scatterers, the estimated dBCS contains three modes (Figure 4.37). It is noticeable that the maxima of the synthetic, error-free and the estimated scaled dBCS deviate in the order of the noise level while the lateral deformation is more pronounced. The modes are shifted by less than 1 ns.

The difference from the forward models  $\bar{P}_r(t)$  to the fitted received echo waveforms  $\hat{P}_r(t)$ , Figure 4.38, demonstrate that the beginning and the end of the signals are the weakest part in the determination. Compared to the example of one single scatterer, it is noted that the deviations increase for the three scatterer case.

(a) Deconvolution				
noise level ( $\zeta$ ), symbol	$s_0$	r.m.s. $(\hat{\sigma}'(t), \bar{\sigma}'(t))$	r.m.s. $(\hat{\sigma}'(t), \bar{\sigma}'(t))$	r.m.s.norm $(\hat{\sigma}'(t), \bar{\sigma}'(t))$
0 ( $\times$ )	0.0000	0.0000	0.0000	0.0000
0.01 (+)	0.0413	0.0184	0.0473	0.0473
0.02 ( $\cdot$ )	0.1643	0.0639	0.1646	0.1646
0.05 ( $\circ$ )	0.0942	0.0709	0.1825	0.1825

(b) Forward modeling				
noise level ( $\zeta$ ), symbol	r.m.s. $(\hat{P}_r(t), P_r(t))$	r.m.s.norm $(\hat{P}_r(t), P_r(t))$	r.m.s. $(\bar{P}_r(t), \hat{P}_r(t))$	r.m.s.norm $(\bar{P}_r(t), \hat{P}_r(t))$
0 ( $\times$ )	0.0000	0.0000	0.0000	0.0000
0.01 (+)	0.0058	0.0158	0.0067	0.0183
0.02 ( $\cdot$ )	0.0296	0.0806	0.0304	0.0820
0.05 ( $\circ$ )	0.0348	0.0947	0.0156	0.0432

**Table 4.7:** Error analysis: Deconvolution 4.7(a) and forward modeling 4.7(b) of the received echo waveform containing one asymmetric echo

(a) Deconvolution				
noise level ( $\zeta$ ), symbol	$s_0$	r.m.s. $(\hat{\sigma}'(t), \bar{\sigma}'(t))$	r.m.s. $(\hat{\sigma}'(t), \bar{\sigma}'(t))$	r.m.s.norm $(\hat{\sigma}'(t), \bar{\sigma}'(t))$
0 ( $\times$ )	0.0000	0.0000	0.0000	0.0000
0.01 (+)	0.0543	0.0306	0.1270	0.1270
0.02 ( $\cdot$ )	0.0978	0.0463	0.1919	0.1919
0.05 ( $\circ$ )	0.1035	0.0980	0.4066	0.4066

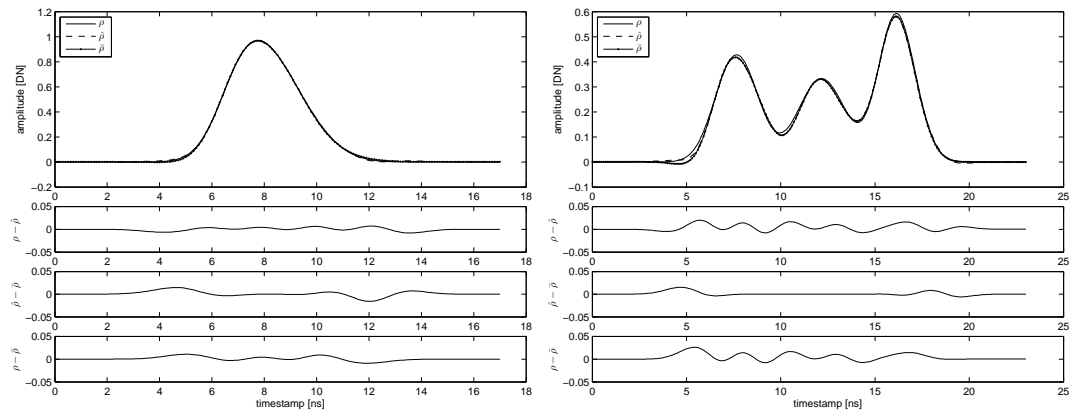
  

(b) Forward modeling				
noise level ( $\zeta$ ) symbol	r.m.s. $(\hat{P}_r(t), P_r(t))$	r.m.s.norm $(\hat{P}_r(t), P_r(t))$	r.m.s. $(\bar{P}_r(t), \hat{P}_r(t))$	r.m.s.norm $(\bar{P}_r(t), \hat{P}_r(t))$
0 ( $\times$ )	0.0000	0.0000	0.0000	0.0000
0.01 (+)	0.0104	0.0446	0.0067	0.0294
0.02 ( $\cdot$ )	0.0182	0.0778	0.0168	0.0707
0.05 ( $\circ$ )	0.0558	0.2390	0.0172	0.0713

**Table 4.8:** Error analysis: Deconvolution 4.8(a) and forward modeling 4.8(b) of the received echo waveform containing three echoes



(a) Received echo waveform of an asymmetric scatterer (b) Received echo waveform of three symmetric scatterers



**Figure 4.38:** Top: Synthetic ( $P_r(t)$ , solid line), approximated ( $\hat{P}_r(t)$ , dashed line) and forward-modeled received echo waveforms ( $\bar{P}_r(t)$ , dotted line), noise level  $\zeta = 0.01$ . Bottom: Differences of the the respective curves:  $P_r(t) - \hat{P}_r(t)$ ,  $\hat{P}_r(t) - \bar{P}_r(t)$ , and  $P_r(t) - \bar{P}_r(t)$  (from top to bottom).

#### 4.4.2 Deconvolution of Real-World Data

The next example (Figure 4.39) is based on real-world data, acquired during a flight mission in early 2007 in Burgenland, Eastern Austria [Doneus et al. 2008; Roncat et al. 2010]. The system waveform and the received echo waveform are recorded by a Riegl LMS-Q560 instrument [Riegl LMS 2014].

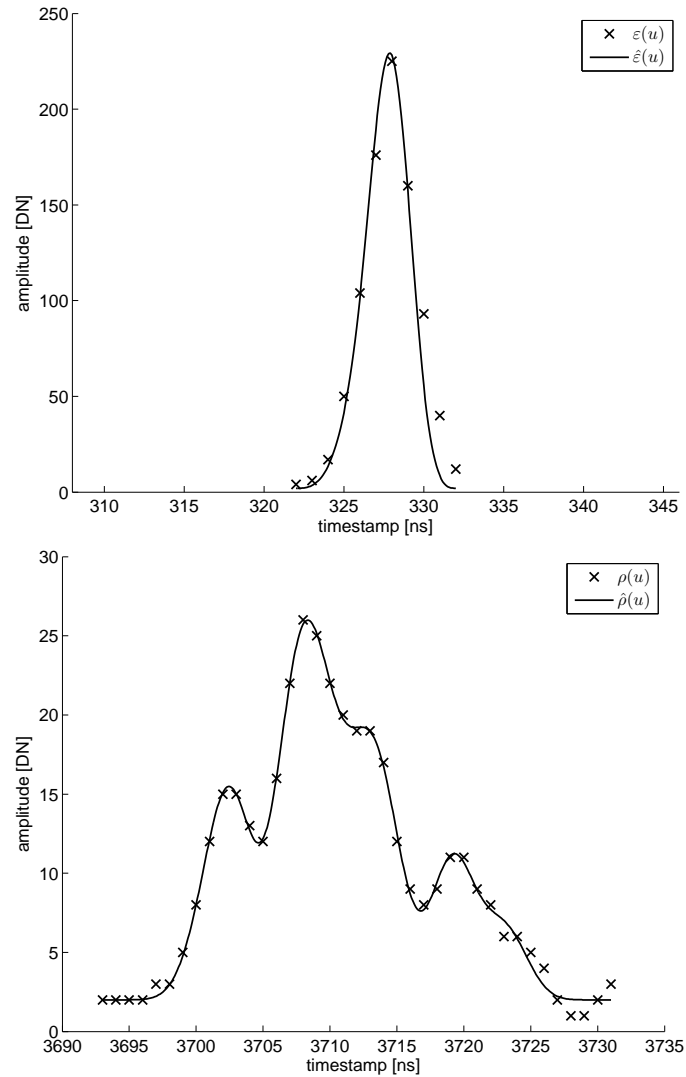


**Figure 4.39:** System waveform (top) and received echo waveform (bottom) recorded with a Riegl LMS-Q560 instrument. The sampled values  $S[t]$  and  $P_r[t]$  are depicted by the “ $\times$ ” markers, the B-spline approximations  $\hat{S}(t)$  and  $\hat{P}_r(t)$  by solid curves.

The system waveform is uni-modal and is modeled with a control polygon of length 2.

For the mathematical reasons given before, we choose a cubic B-spline curve to model the system waveform and the scaled dBCS. Furthermore, empirical tests carried out with data of the same flight campaign showed that curve fitting performed best (in the sense of lowest  $s_0$  values) with cubic B-spline curves in the case of system waveforms. To suppress noise, the spacing of the B-spline control points is chosen as twice the sampling interval, here 2 ns. This leads to a full duration of the system waveform of 10 ns, i.e. the power is strictly zero outside this interval. The FWHM is 3.8 ns. The  $s_0$  of B-spline curve fitting for the system waveform is 17.5<sup>2</sup>. Besides determining the vertices of the B-spline control polygon, an additional parameter has to be determined in the curve fitting due to hardware reasons: During A/D conversion in the waveform recording process of the LMS-Q560, a constant offset (DC offset) is added to the raw amplitude values since background radiation passing through the filter in front of the detector might cause negative amplitude values. However, these are outside of the allowed range of values of the recorder. Adding the DC offset keeps the amplitudes in the intended range of values which is typically [0 . . . 255] (1 byte).

As a consequence of the choice of degrees  $n_\varepsilon = 3$  and  $n_\sigma = 3$ , the received echo waveform is modeled as B-spline curve of degree  $n_\rho = n_\varepsilon + n_\sigma + 1 = 7$ . According to the system waveform, control points are spaced in 2 ns intervals as well. With 12 non-zero control points in total, the received echo waveform has a duration of 38 ns, for which the amplitude values are larger than zero. The temporal profile of the received echo waveform is multi-modal. Looking closer at the shape of the descending slope of the received echo waveform at approx. 3708–3715 ns suggests to assume two overlapping scatterers at this point. The distance of these scatterers is lower than the respective echo width so that no extra mode is visible. The same applies to the section from 3720–3730 ns (cf. Figure 4.40).

Again, a DC offset is determined within the least-squares adjustment for curve fitting. This curve fitting of the received echo waveform results in  $s_0 = 0.54$ .

The deconvolution yields a cubic B-spline curve representing the scaled dBCS with a length of 26 ns (see Figure 4.40, left). According to Section 3.2.2.2, the results of the separated curve fittings and deconvolution serve as initial values for an overall adjustment following the principle of the general case for adjustment. This procedure gives the control polygons for the curves  $\hat{S}(t)$ ,  $\hat{\sigma}'(t)$  and  $\hat{P}_r(t)$  (and the DC offsets) as results. Despite of the huge overlap of the scatterers in the received echo waveform  $\hat{P}_r(t)$ , the deconvolved B-spline curve  $\hat{\sigma}'(t)$  contains five clearly separated maxima, giving empirical evidence for the practicability of our inversion approach.

The r.m.s. and r.m.s.<sub>norm</sub> values of curve fitting and forward modeling are summarized in Table 4.9. Both the curve fitting of the received echo waveform and its discrete forward model agree well with the originally recorded received echo waveform. There

<sup>2</sup>For comparing this result with the ones of Section 4.4.1, please note that the amplitudes here are higher by a factor more than one hundred than in the case of the synthetic examples

is practically no difference between the forward-modeled and the fitted received echo waveform ( $\text{r.m.s.}_{\text{norm}}(\hat{P}_r(t), \hat{P}_r(t)) < 1\%$ , see Table 4.9).

$(f(t), g(t))$	r.m.s. $(f(t), g(t))$	r.m.s. $_{\text{norm}}(f(t), g(t))$
$(\hat{S}(t), S[t])$	18.96	0.169
$(\hat{P}_r(t), P_r[t])$	0.483	0.039
$(\bar{P}_r(t), P_r[t])$	0.479	0.039
$(\bar{P}_r(t), \hat{P}_r(t))$	0.084	0.007

**Table 4.9:** r.m.s. values of B-spline curve fitting and forward modeling for the example of Section 4.4.2

### 4.4.3 Comparison to Gaussian Decomposition

The analysis is continued with the example of Section 4.4.2, but concentrate now on the deconvolution results of Gaussian Decomposition. A standard implementation of Gaussian Decomposition, suggested by Wagner et al. [2006], models the received echo waveform with three Gaussian scatterers. The detailed results of parameter estimation, i.e. curve fitting, are given below (see Figure 4.41 and Table 4.10).

Echo ID	Position $(t_s, t_i)$ [ns]	Amplitude $(\hat{S}, \hat{P}_i)$ [DN]	$s_s, s_{p,i}$ [ns]
system waveform			
0	327.90	223.67	1.78
received echo waveform			
1	3701.70	9.32	1.39
2	3709.48	22.09	4.00
3	3720.44	7.30	2.81

**Table 4.10:** Results of Gaussian Decomposition for the example of Section 4.4.2

The deconvolution of two Gaussian functions results in a Gaussian function again. The amplitude, position and variance of the Gaussian function representing the system waveform are denoted as  $\hat{S}$ ,  $t_s$  and  $s_s^2$  and the ones representing a scatterer within the received echo waveform as  $\hat{P}_i$ ,  $t_i$  and  $s_{p,i}^2$ , resp. As given in Section 3.2.1.1, the deconvolution results in a Gaussian with parameters:

$$\hat{C}_i = \frac{\hat{P}_i s_{p,i}}{\hat{S} s_s}, \quad t_{\sigma,i} = t_i - t_s, \quad s_{\sigma,i}^2 = s_{p,i}^2 - s_s^2.$$

In the example presented here, one of the Gaussian functions representing individual scatterers has a  $s_{p,i}$  lower than the one of the system waveform,  $s_s$ . In this case, deconvolution does not yield a “proper” Gaussian function any more, i.e. a function of the general form  $e^{-x^2}$ , but one of the form  $e^{x^2}$  (see leftmost dashed curve in Figure 4.42).

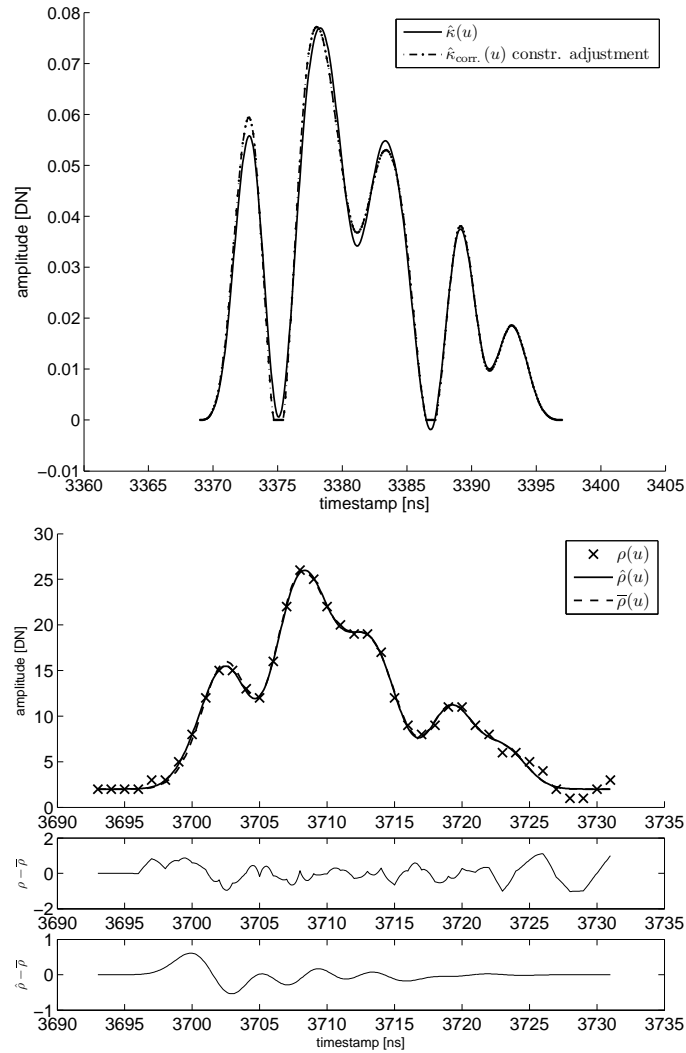


**Figure 4.40:** Top: Scaled dBCS retrieved by deconvolution, before  $(\hat{\sigma}'(t))$  and after constrained adjustment and correction  $(\hat{\sigma}'_{\text{corr.}}(t))$ . Bottom: Forward-modeled received echo waveform  $\bar{P}_r(t)$  (dashed line) in comparison to the sampled values  $P_r(t)$  (“x” markers) and the B-spline curve  $\hat{P}_r(t)$  retrieved by constrained adjustment (solid line). Images at the bottom show the differences  $P_r(t) - \bar{P}_r(t)$  and  $\hat{P}_r(t) - \bar{P}_r(t)$  (from top to bottom).

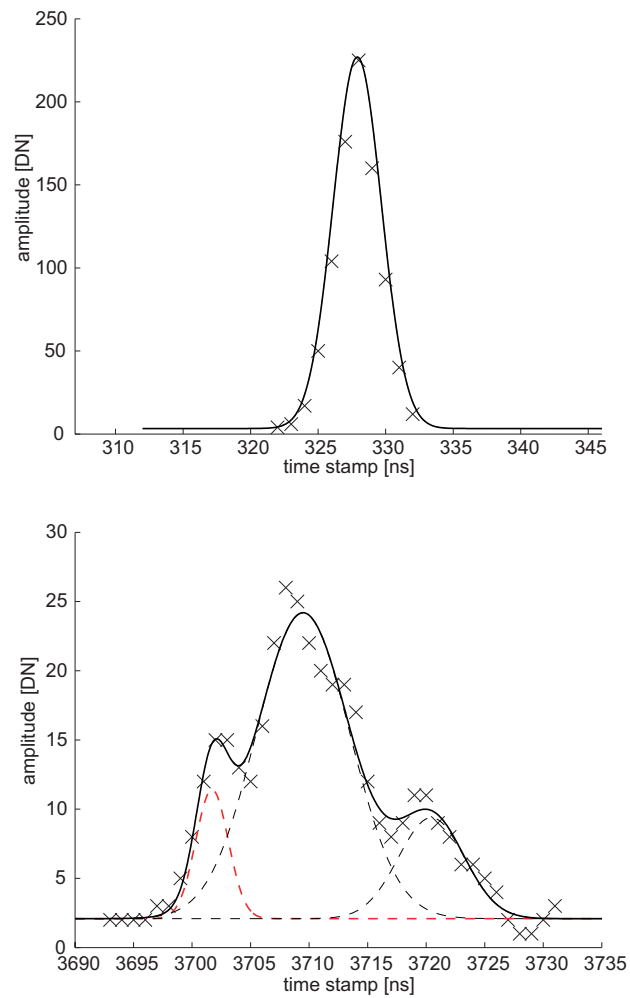


**Figure 4.41:** Results of Gaussian Decomposition for the emitted (top) and received (bottom) waveform. The sampled values are depicted by the “x” markers, the dashed curves show the Gaussian functions representing three individual scatterers and the solid curve shows the sum of the Gaussian functions. The leftmost dashed curve shows the first Gaussian model which is very narrow, see also Figure 4.42.

The variance of the scaled dBCS is  $-0.15 \text{ ns}^2$ . As a consequence, the integral of this function, the backscatter cross-section, becomes incalculable for this scatterer, since the integral is unbound.

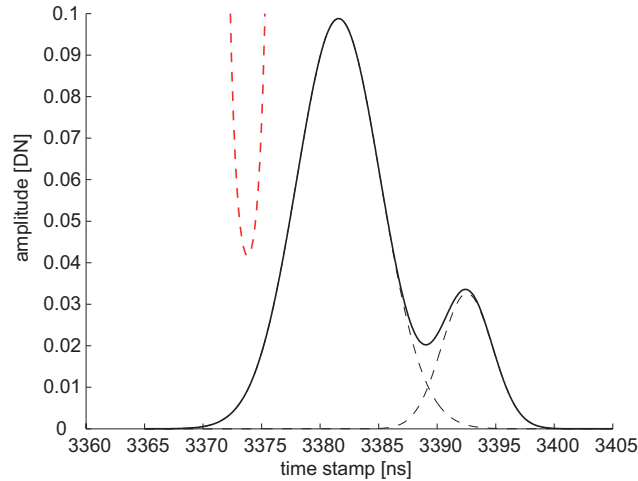


**Figure 4.42:** Deconvolution results of Gaussian Decomposition of the example given in Section 4.4.2. The leftmost dashed curve has  $e^{x^2}$  form instead of  $e^{-x^2}$  form since the variance  $s_{i,\sigma}^2 = s_i^2 - s_s^2$  is negative. The solid curve shows the sum of the two other Gaussian functions representing a physically meaningful result.

The example shows one requirement for the Gaussian Decomposition approach: The model complexity, i.e. number of scatterers, has to be determined before fitting, either using heuristics or an optimization (e.g. [Duong et al. 2008; Mallet et al. 2009; Roncat et al. 2008]). In this example, three scatterers were chosen because of three discernible peaks. The width of the second Gaussian is overestimated, and therefore the width of the first Gaussian becomes too small for being physically meaningful. As shown in Figure 4.40, top, five scatterers all together are found by B-spline deconvolution. While a slight asymmetry in these scatterers can also be seen, especially their width and location are the basis for the better description after forward modeling (Figure 4.40, bottom). The second Gaussian therefore does not describe a scattering surface.

## 4.5 Examples for radiometric Calibration of B-spline-based Deconvolution

The examples given below stem from three different flight strips of the already mentioned FWF dataset presented in [Roncat et al. 2013]. The width of the transmitted laser pulse of the Optech ALTM 3100 scanner was around 10 ns (full width at half maximum, FWHM). This is about 2.5 times the pulse width of the instruments in the RIEGL LMS-Q series (FWHM 4 ns) which we have dealt with as well. Accordingly, the knot distance  $\Delta u$  was chosen to  $5 \text{ ns} = 5\Delta t$ . Our test area of size  $100 \text{ m} \times 100 \text{ m}$  was chosen in a forested area in the overlap of three flight strips (see Figures 4.43 and 4.44). As examples, waveforms were chosen where the onboard detector of the scanner recorded three (first flight strip) and four echoes (second and third flight strip), resulting in 24 system and echo waveforms all together.

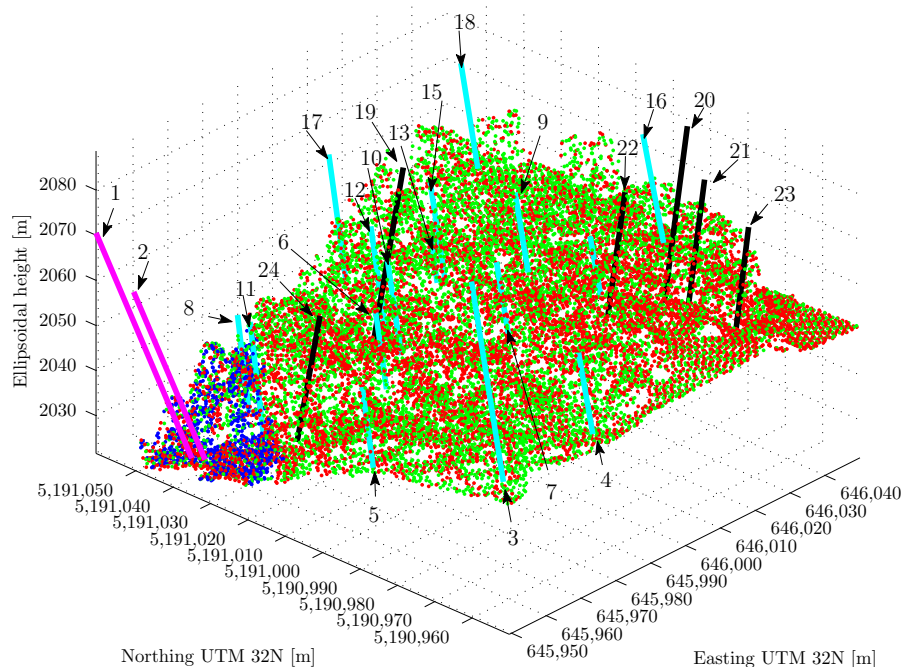


**Figure 4.43:** Test area for radiometric calibration based on B-spline deconvolution. This forested area is in the overlap of three flight strips (points in blue, red and green, respectively). As examples, waveforms were chosen where the on-board detector recorded three (first flight strip) and four echoes (second and third flight strip). Their laser rays are shown as magenta, blue and black lines, according to the flight strips.

The examples of this and the previous section give empirical evidence for that B-spline deconvolution is applicable to both RIEGL and Optech FWF data acquired over



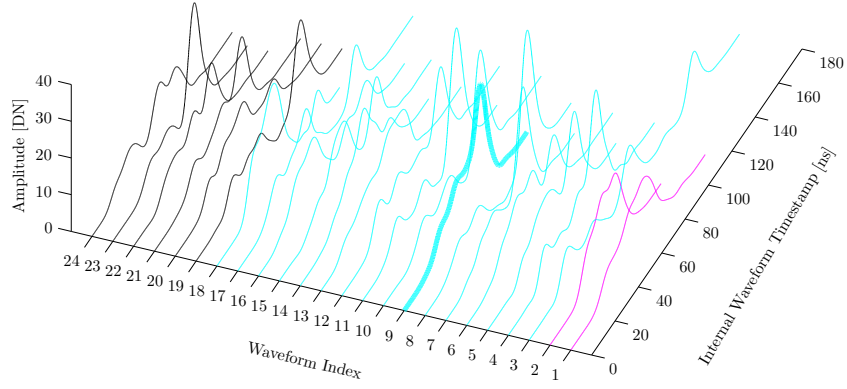


**Figure 4.44:** The  $P_r(t)$  waveforms selected from Figure 4.43 for illustrating radiometric calibration based on B-spline deconvolution.

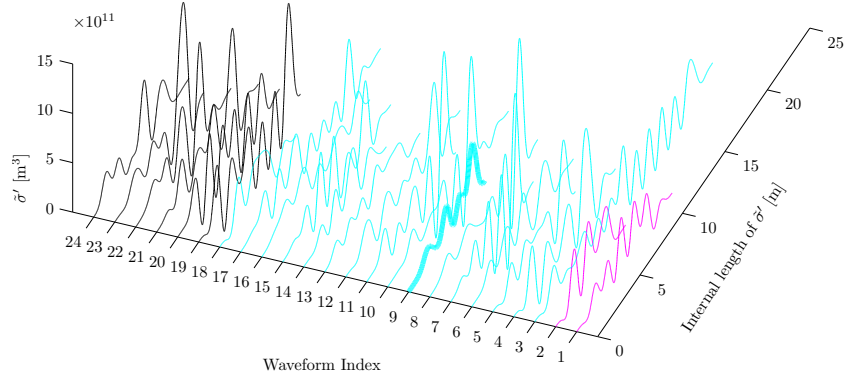


**Figure 4.45:** Range-corrected deconvolution result  $\tilde{\sigma}'(R) = \sigma'(R)/C_{CAL,B}$  for the 24 waveforms from Figure 4.44. Waveform 9 corresponds to Figure 3.10. Numerical values for the BCS  $\sigma$  of these waveforms are given in Table .

Index	$\sigma [m^2] / C_{CAL,B} [m^{-2}]$	Index	$\sigma [m^2] / C_{CAL,B} [m^{-2}]$
1	$1.470660 \times 10^{12}$	13	$1.162442 \times 10^{12}$
2	$1.559547 \times 10^{12}$	14	$1.145049 \times 10^{12}$
3	$1.121289 \times 10^{12}$	15	$1.191023 \times 10^{12}$
4	$1.362496 \times 10^{12}$	16	$1.123303 \times 10^{12}$
5	$1.197656 \times 10^{12}$	17	$1.127921 \times 10^{12}$
6	$1.258688 \times 10^{12}$	18	$1.178015 \times 10^{12}$
7	$1.251359 \times 10^{12}$	19	$1.781822 \times 10^{12}$
8	$1.293170 \times 10^{12}$	20	$1.451291 \times 10^{12}$
9	$1.357094 \times 10^{12}$	21	$1.735836 \times 10^{12}$
10	$1.222455 \times 10^{12}$	22	$1.471636 \times 10^{12}$
11	$1.270203 \times 10^{12}$	23	$1.706954 \times 10^{12}$
12	$1.225000 \times 10^{12}$	24	$1.529070 \times 10^{12}$

**Table 4.11:** BCS  $\sigma$  of the waveforms given in Figure 3.10.

complex terrain and the radiometric calibration of the deconvolution can be performed consequently. The numerical values given in the Figures 3.14 and 4.45 differ significantly because of the different system configurations of the used scanners.

## 4.6 Examples for Target Feature Extraction based on radiometric Calibration

The approach presented in Section 3.3.2.3 was investigated using FWF and discrete-return ALS data from the test area shown in Figure 4.27. The distributions of the BCS and the central moments from degree 2 to 4 show a clear bimodality for the variance and the 4<sup>th</sup> moment which are apparently quadratically dependent (see Figure 4.46). Visual analysis of Figure 4.47 and the orthophoto in Figure 4.27 suggests that the combination of BCS and variance may enable discrimination between the following landcover classes; see Figure 4.47):

- Built-up areas: very low BCS, low variance
- Sparse alpine vegetation: low BCS, low variance
- High vegetation: low BCS, high variance
- Grassland: high BCS, low variance

The third-order moments did only show additional information in the way that positive values (and thus, positive skewness) appeared mainly in higher vegetation. Consequently, these moments were not investigated further.

Moreover, we analysed the geometric performance of the presented approach in comparison to the discrete-return point cloud and an FWF point cloud extracted with Gaussian decomposition of the same flight strip in smooth areas. The B-spline-derived ranges tend to be a few centimetres (mean: 2.5 cm,  $\sigma_{\text{MAD}} = 2$  cm) lower than the corresponding ones of the sensor and of Gaussian Decomposition. The height differences to the discrete-return echoes seem to be slope-dependent whereas this effect was not present in the comparison with the Gaussian Decomposition data, as visible in Figure 4.48.

A detailed geometric cross-validation for the used dataset is given in Chapter 5.

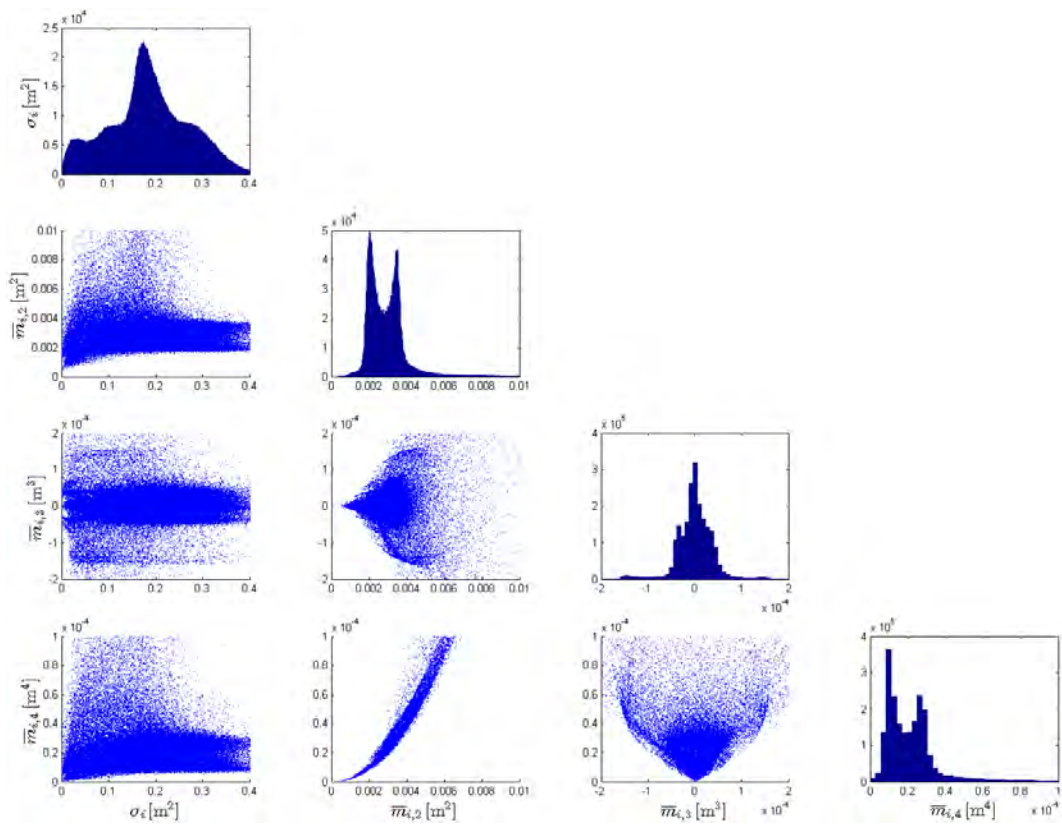


**Figure 4.46:** Distributions of the parameters extracted from the test data set (cf. Figure 4.27): Histograms of the BCS  $\sigma_i$  and the second to fourth central moments of its derivative,  $\bar{m}_{i,2..4}$  (diagonal, from top to bottom). The non-diagonal diagrams show the scatter plots of two of the four variables. The quadratic relationship of  $\bar{m}_{i,2}$  and  $\bar{m}_{i,4}$  is clearly visible.

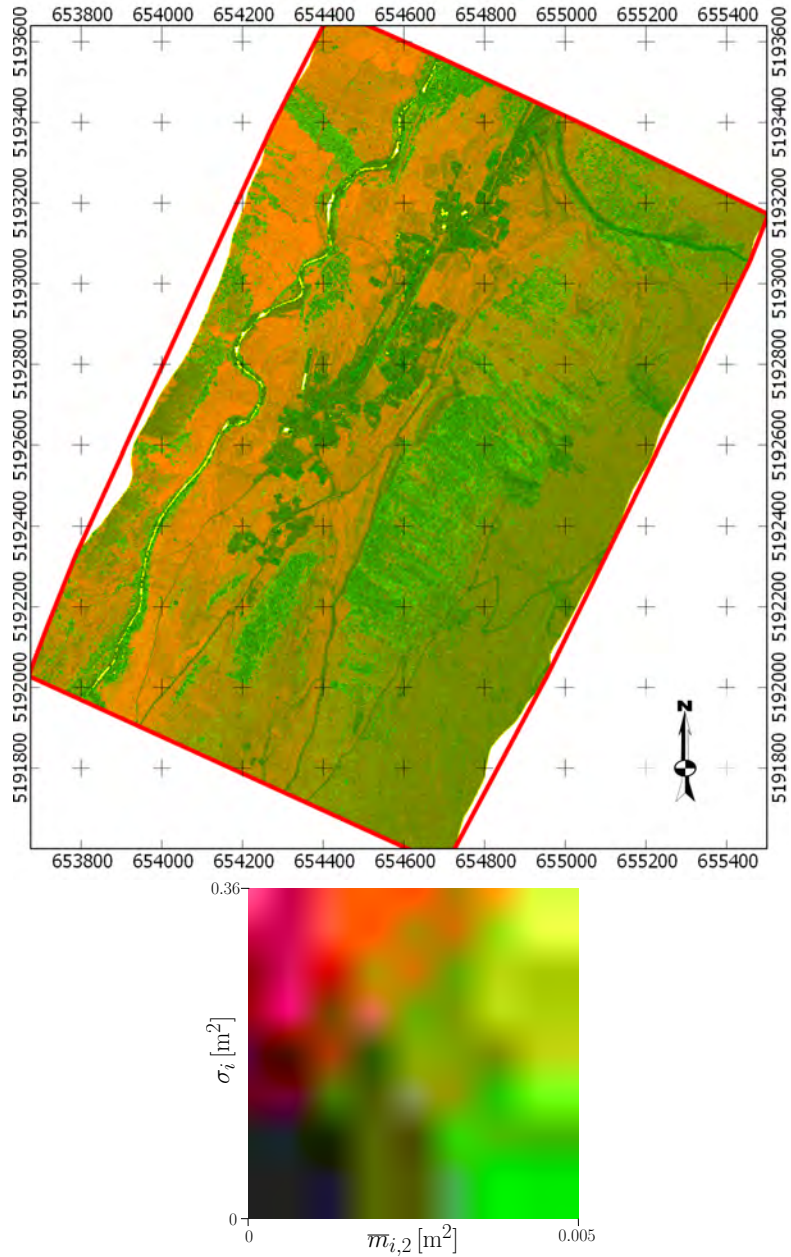


**Figure 4.47:** Top view of the ALS point cloud of the test area (cf. Figure 4.27). While the point locations stem from the first statistical moments of the dBCS segments, the colour coding is composed of the BCS  $\sigma_i$  (red channel) and the variance of the dBCS  $\bar{m}_{i,2}$  (green channel).

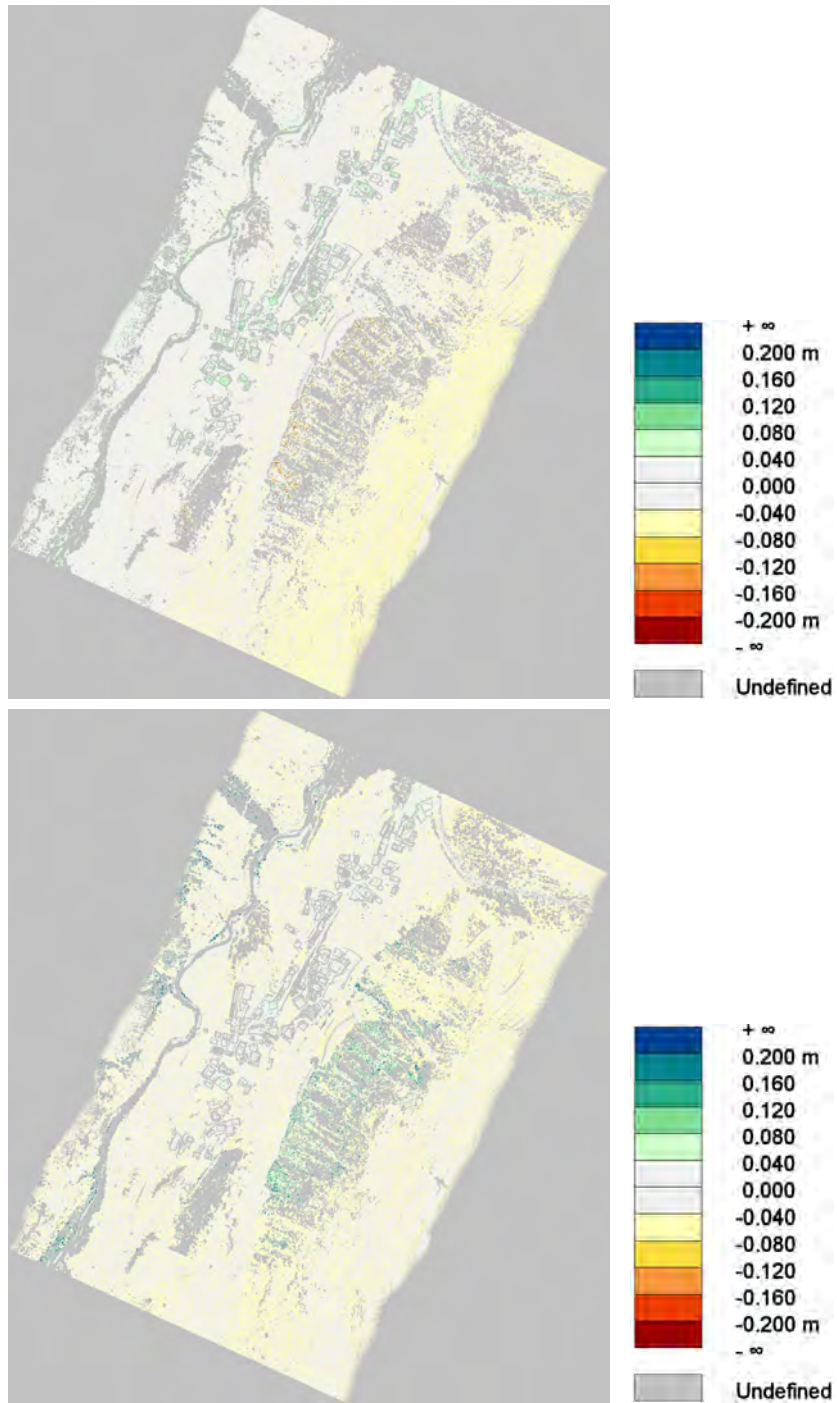


**Figure 4.48:** Height differences (left): moment-derived ALS point cloud in comparison to the discrete-return point cloud of the sensor (top); Gaussian-decomposition derived point cloud in comparison to the discrete-return point cloud of the sensor (bottom). Non-smooth areas were excluded (shown in grey). Right: legend.

## Results and Discussion

The core part of this chapter is dedicated to a cross-validation of four ALS signal processing techniques based on the dataset presented in Section 4.2. These techniques are:

1. Direct ranging and determination of an intensity value as delivered on-line by the sensor; we will refer to this approach with the abbreviation “DR” in the remainder of this chapter,
2. ASDF/Correlation (Section 3.1.2.1, abbreviated by “ASDF”),
3. Gaussian decomposition (Section 3.2.1.1, abbreviated by “GD”) and
4. B-spline deconvolution (Section 3.2.2, abbreviated by “BSP”).

As a first point, the echo count per shot was investigated. While in the case of GD, ASDF and BSP, the maximum echo count is in theory only limited by the minimum separation distances derived in Section 4.1.1, the DR echo count per shot was limited to four by the instrument (first, second, third and last echo). Figure 5.1 illustrates this comparison for the mentioned dataset.

We see that for GD vs. DR, the histogram is practically symmetrical. In the comparison ASDF vs. DR, there are significantly more cases where two echoes have been extracted by DR and one echo by ASDF than the other way round or two echoes by both approaches. By trend, ASDF also delivers fewer echoes than GD; this is understandable by the fact that GD is in principle a *de*-convolution whereas the correlation-based ASDF acts like a convolution and tends to smoothen the input signal  $P_r(t)$ .

The juxtaposition of BSP and DR exhibits that only in the case of single echoes for both techniques the occurrence of an equal number of echoes is the most frequent for

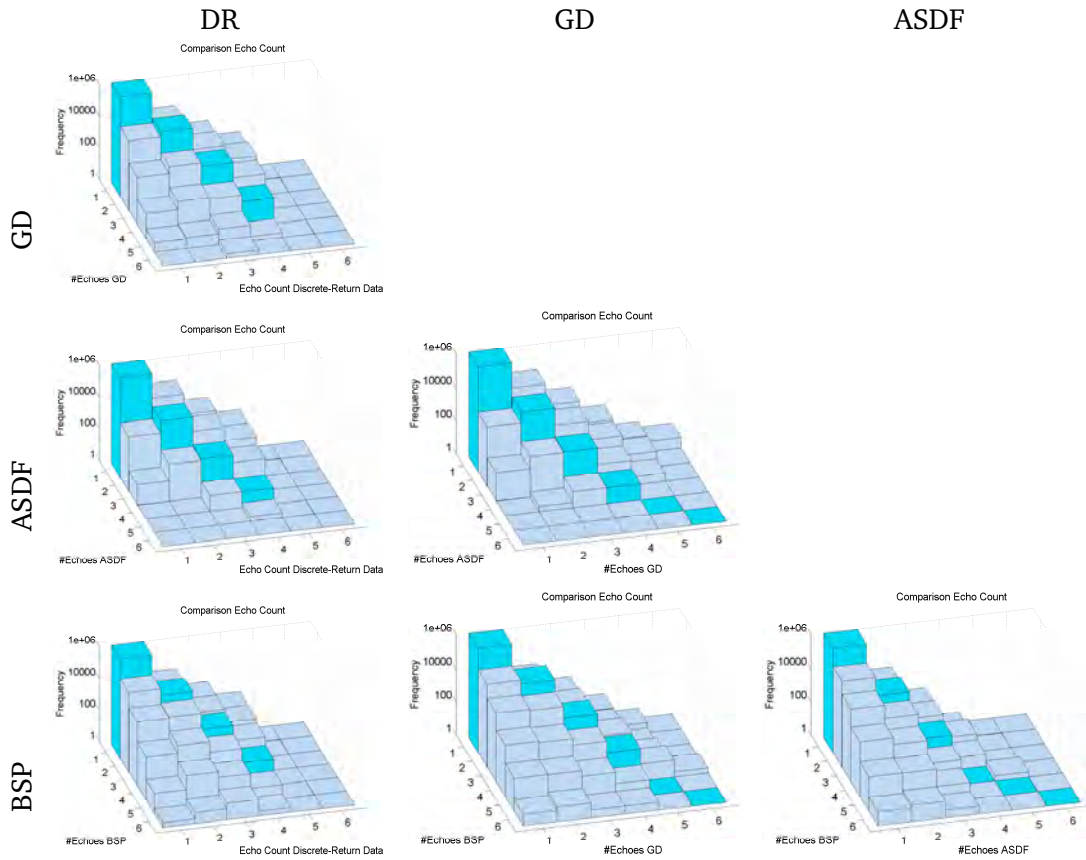


**Figure 5.1:** Comparison of echoes per shot for the four different methods. The vertical axis is given in logarithmic scaling.

the respective row or column in the 2D histogram. By trend, BSP extracts more echoes than DR. Same is valid for the comparison of BSP and GD; this may be a hint for better separability in the BSP case due to the determination of the number of echoes *after* deconvolution.

In the last investigated comparison, i.e. BSP vs. ASDF, there were practically no cases of more than three echoes in ASDF if the corresponding echo count for BSP was lower than the ASDF echo count.

The second part of our geometric cross-validation focuses on the results of range determination for single echoes; histograms of this comparisons are shown in Figure 5.2 and the according statistics for median and  $\sigma_{\text{MAD}}$  (standard deviation of the mean absolute differences w.r.t. the median) are given in Table 5.1; this  $\sigma_{\text{MAD}}$  is a robust estimator of the standard deviation [cf. [Ressl et al. 2011](#)].

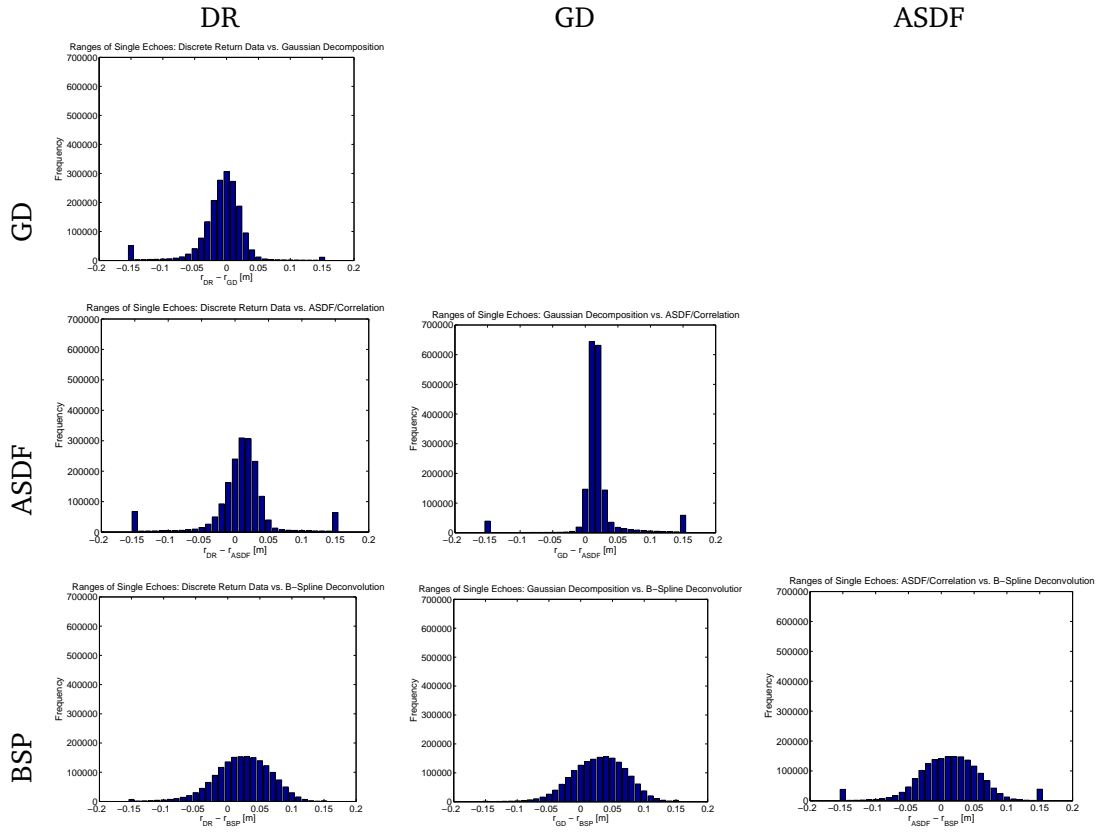


**Figure 5.2:** Histograms of range differences for single echoes, evaluated for the four different methods. Statistical values are given in Table 5.1.

	median [m]	$\sigma_{\text{MAD}}$ [m]
$r_{\text{DR}} - r_{\text{GD}}$	-0.0036	0.0469
$r_{\text{DR}} - r_{\text{ASDF}}$	0.0120	0.0843
$r_{\text{DR}} - r_{\text{BSP}}$	0.0244	0.0516
$r_{\text{GD}} - r_{\text{ASDF}}$	0.0156	0.0643
$r_{\text{GD}} - r_{\text{BSP}}$	0.0305	0.0513
$r_{\text{ASDF}} - r_{\text{BSP}}$	0.0132	0.0892

**Table 5.1:** Median and  $\sigma_{\text{MAD}}$  values of the range differences presented in Figure 5.2.



The comparison of DR and GD ranging showed the best accordance in both median and  $\sigma_{\text{MAD}}$ . The highest  $\sigma_{\text{MAD}}$  values were found for DR vs. ASDF and ASDF vs. BSP in the range of  $\simeq 8$  cm while the medians were in the range of  $\simeq 1.5$  cm for these two comparisons. The highest median value was found for GD vs. BSP with 3.1 cm.

We observe relatively large values in the cases where BSP is involved. A possible reason for this fact might be the poor performance of the BSP approach in the cases where the incidence angle  $\vartheta$  is close to  $0^\circ$  and the (true) dBCS is close to a Dirac impulse. Such a Dirac impulse cannot be represented by a B-spline  $B_l^n(t)$  of positive degree  $n \geq 0$  but only by letting  $n = -1$ . A possible solution for this topic within the framework of B-spline deconvolution will be given in the conclusions (Chapter 6).

## Conclusion and Outlook

The goal of this thesis was to develop new methods in processing full-waveform laser scanning signals that allow improved detection and characterization of echoes and target properties. The presentation summarized the author's contribution to this research area, embedded to the relevant literature in this field.

Special emphasis was laid on the distinction between the approaches extracting *echo* features from those resulting in *target* features. For the latter, a deconvolution is indispensable which further enables for the derivation of physical target attributes such as the differential backscatter cross-section  $\sigma'(t)$  (in m) and its integral, the backscatter cross-section  $\sigma$  (in  $\text{m}^2$ ). Such a derivation is referred to as radiometric calibration. A significant part of this manuscript was dedicated to the detailed presentation of a novel deconvolution technique of linear complexity based on uniform B-spline curves, accompanied by the radiometric calibration of the deconvolution results.

After the presentation of the theoretical frameworks of the mentioned signal processing approaches, their potential was illustrated by numerical examples. The most relevant findings highlighted by these examples are given in the following paragraphs.

The simulated examples have shown that the assumption of a Gaussian-shaped  $\sigma'(t)$  is only justified in case of planar targets and a Gaussian power density distribution within the laser footprint; even for simple configurations such as spherical, cylindrical, or sinusoidal targets the shape of  $\sigma'(t)$  is highly asymmetrical. For a Gaussian configuration, a formula for the minimum separation distance in  $\sigma'(t)$  between two targets hit by the same laser ray can be derived. If additionally the temporal profile of the emitted laser pulse, represented by the system waveform  $S(t)$ , is of Gaussian shape as well, a formula for the minimum distance for echo separation in the recorded echo waveform  $P_r(t)$  can be derived, too.

As the minimum separation distance is significantly shorter in  $\sigma'(t)$  than in  $P_r(t)$ , this fact clearly gives a strong motivation for deconvolution. The actual amount depends on the length of the system waveform, represented e.g. by the standard deviation  $s_s$  of a fitted Gaussian function. A second motivation stems from the increasing availability of ALS systems capable of emitting multiple pulses before recording the echo of the first. As this enables for working with longer distances between sensor and target, it increases the dynamic range present in  $P_r(t)$  which is in a  $1/R^4$  proportionality to the system waveform  $S(t)$ . Thus, the direct usage of *echo* features derived from the recorded echo waveform is even more discouraged than in the case where only one laser pulse is emitted before the recording of its echoes.

A clear evidence has been given for the instability of the system waveform  $S(t)$  from pulse to pulse in the order of some percent of its peak amplitude and even one order of magnitude higher from one flight strip to another. This influence can be partly removed by normalizing the amplitude(s) in  $P_r(t)$  by the one of  $S(t)$ . In order to maintain the number range of the  $P_r(t)$  amplitudes, the normalized amplitudes might be multiplied by e.g. the mean value of a significantly large sample of  $S(t)$  amplitudes.

As the length of  $S(t)$  may vary even for the same instrument at different pulse repetition rates, the usage of a target width is therefore favourable compared to the commonly used echo width. For the Gaussian configuration, this would result in a target width  $s_\sigma = \sqrt{s_i^2 - s_s^2}$  with  $s_i$  being the standard deviation of a Gaussian function fitted to the contribution of the  $i$ -th echo to  $P_r(t)$ .

The most general solution to deal with the instability and shape problem is deconvolution; the mentioned B-spline approach is a very flexible technique working linear in time domain. Its feasibility for processing signals recorded by commercially available ALS systems has been clearly shown in this thesis. Additionally to successful deconvolution, the extraction of targets, radiometric calibration and assignment of additional target features based on the result of radiometric calibration has been proven positively and has shown its potential usefulness for landcover classification.

The mentioned B-spline approach to deconvolution reaches its limits in the case of orthogonal incidence of the laser beam at the target, i.e. the incidence angle  $\vartheta \simeq 0$ ; this circumstances might appear in significantly large parts of the scanned areas. The recorded echo waveform then results in a scaled copy of the system waveform  $S(t)$  and the true deconvolution would be a Dirac impulse. Such a situation cannot be represented correctly by a B-spline  $B_i^n(t)$  of positive degree  $n$  which would result in a bias for range estimation and wrong shape estimation of  $\sigma'(t)$ . However, it can be represented in the framework of B-splines by letting  $n = -1$ . A possible solution to the aforementioned shortcoming may be (a) the detection, approximate localization and scale determination of copies of  $S(t)$  in  $P_r(t)$  by e.g. a correlation technique, and (b) a combined adjustment for curve fitting of  $P_r(t)$  and the deconvolution; the first part of the deconvolution then results in the scaled Dirac impulse(s) while the rest gives a B-spline curve of degree  $n > 1$ , as presented in this thesis.

## Convolution in Time Domain

The convolution of two functions  $f(t)$  and  $g(t)$  is defined as the sliding integral

$$f(t) \otimes g(t) := \int_{-\infty}^{\infty} f(u)g(t-u)du. \quad (\text{A.1})$$

For assuring convergence, one of the two functions is assumed to have compact support, i.e. this function is  $\neq 0$  in a finite interval only. The convolution of two functions shows the following properties [[Weisstein 2014a](#)]:

$$\begin{aligned} f(t) \otimes g(t) &= g(t) \otimes f(t) \\ (f(t) \otimes g(t)) \otimes h(t) &= f(t) \otimes (g(t) \otimes h(t)) \\ f(t) \text{ differentiable} &\Rightarrow f(t) \otimes g(t) \text{ differentiable} \\ \frac{d(f(t) \otimes g(t))}{dt} &= \frac{df(t)}{dt} \otimes g(t) = f(t) \otimes \frac{dg(t)}{dt}. \end{aligned}$$

*Proof.* See [[Wallner 2010](#)]:

For proving the first assumption, we introduce  $s = t - u$  with  $ds = -du$  and retrieve

$$g(t) \otimes f(t) = \int_{u=-\infty}^{\infty} g(u)f(t-u)du = \int_{s=\infty}^{-\infty} f(s)g(t-s)(-ds) = f(t) \otimes g(t).$$

For the second, we set  $x = u - s$  with  $dx = du$ , so that  $t - s - x = t - u$ :

$$\begin{aligned} (f \otimes (g \otimes h))(t) &= \int f(s)(g \otimes h)(t-s)ds = \int \left( \int f(s)g(x)h(t-s-x)dx \right) ds \\ &= \int \int f(s)g(u-s)h(t-u)duds = \int (f \otimes g)(u)h(t-u)du \\ &= ((f \otimes g) \otimes h)(s). \end{aligned}$$

Since  $f(t)$  or  $g(t)$  have compact support, we can write

$$\frac{d(f(t) \otimes g(t))}{dt} = \int \frac{d}{dt} f(u)g(t-u)du = f(t) \otimes \frac{dg(t)}{dt}.$$

Because  $f$  and  $g$  can be used interchangeably, the last statement is proven as well.  $\square$

Let us assume first that both  $f(t)$  and  $g(t)$  have compact support, as shown in the example of Figure A.1:

$$f(t) = \begin{cases} \varphi(t) & t \in [l_\varphi, u_\varphi] \\ 0 & \text{elsewhere} \end{cases} \quad g(t) = \begin{cases} \gamma(t) & t \in [l_\gamma, u_\gamma] \\ 0 & \text{elsewhere} \end{cases}$$

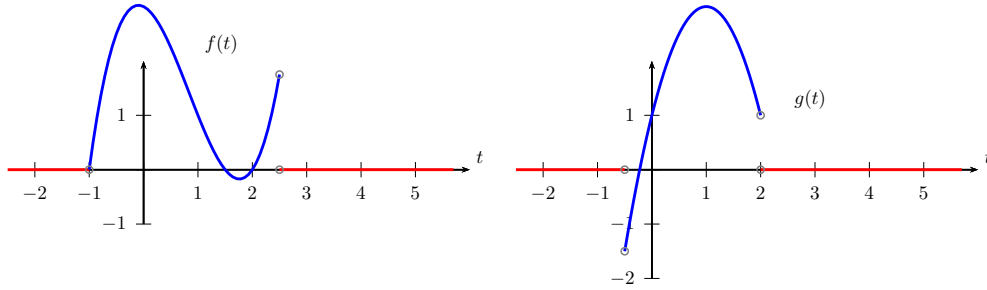


**Figure A.1:** Examples for functions  $f(t)$  (left) and  $g(t)$  (right) with compact support in time domain. The limits of the blue curves  $\varphi(t)$  and  $\gamma(t)$  are  $[-1, 2.5]$  and  $[-0.5, 2]$ , resp.

Without loss of generality, we can say that  $u_\gamma - l_\gamma \leq u_\varphi - l_\varphi$ . For calculating the integral, we need to define the non-zero intervals of  $\varphi(u)$  and  $\gamma(t-u)$ . The first is just  $[l_\varphi, u_\varphi]$  whereas the latter is  $[t-u_\gamma, t-l_\gamma]$  (cf. Figure A.2).

The result of the convolution can only be different from zero where the two intervals overlap, i.e.

$$(t-l_\gamma \geq l_\varphi) \wedge (t-u_\gamma \leq u_\varphi) \Leftrightarrow t \in [l_\gamma + l_\varphi, u_\gamma + u_\varphi].$$

With letting  $h(t) := f(t) \otimes g(t)$ , we get as result

$$h(t) = \begin{cases} \eta_1(t) = \int_{l_\varphi}^{t-l_\gamma} \varphi(u)\gamma(t-u)du & t \in [l_\gamma + l_\varphi, l_\varphi + u_\gamma] \\ \eta_2(t) = \int_{t-u_\gamma}^{t-l_\gamma} \varphi(u)\gamma(t-u)du & t \in [l_\varphi + u_\gamma, l_\gamma + u_\varphi] \\ \eta_3(t) = \int_{t-u_\gamma}^{u_\varphi} \varphi(u)\gamma(t-u)du & t \in [l_\gamma + u_\varphi, u_\gamma + u_\varphi] \\ 0 & \text{elsewhere} \end{cases} \quad (\text{A.2})$$

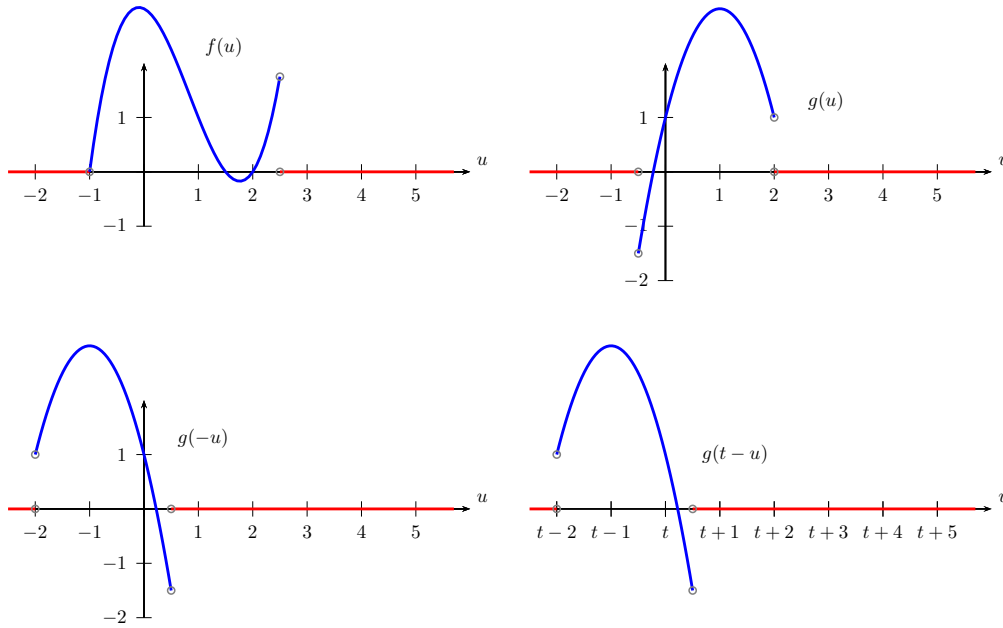


**Figure A.2:** Continuation of Figure A.1. Top Left:  $f(u)$ . Top Right:  $g(u)$ . Bottom:  $g(-u)$  and  $g(t-u)$ . While the limits for  $\varphi(u)$  and  $\gamma(u)$  are the same as for  $\varphi(t)$  and  $\gamma(t)$ , the limits for  $\gamma(-u)$  are  $[-u_\gamma, -l_\gamma] = [-2, 0.5]$ . The limits of  $\gamma(t-u)$  are therefore  $[t-u_\gamma, t-l_\gamma] = [t-2, t+0.5]$ .

Please note that the bounds of integration are dependent on the shift  $t$ .

If  $u_\gamma - l_\gamma = u_\varphi - l_\varphi$ , the non-zero interval of  $\eta_2$  is empty, whereas for global support of  $f(t)$ , i.e.  $l_\varphi = -\infty$  and  $u_\varphi = \infty$ , we retrieve

$$h(t) = \eta_2(t) \quad \forall t.$$

**Numerical Example.** The functions shown in Figure A.1 are

$$f(t) = \begin{cases} \varphi(t) = t^3 - \frac{5}{2}t^2 - \frac{t}{2} + 3 & t \in [-1, 2.5] \\ 0 & \text{elsewhere} \end{cases}$$

$$g(t) = \begin{cases} \gamma(t) = -2t^2 - 4t + 1 & t \in [-0.5, 2] \\ 0 & \text{elsewhere} \end{cases}.$$

The integration term for the convolution integral  $\varphi(u)\gamma(t-u)$  is therefore

$$\varphi(u)\gamma(t-u) = \left(u^3 - \frac{5}{2}u^2 - \frac{u}{2} + 3\right) \left(-2(t-u)^2 - 4(t-u) + 1\right)$$

and its integral equals

$$\int \varphi(u)\gamma(t-u)du = -\frac{1}{3}u^6 - \frac{4t+9}{5}u^5 + \frac{7t+5}{2}u^4 + \frac{2t-7}{2}u^3 + \frac{20t+25}{4}u^2 - (12t-3)u + C.$$

Substituting the actual integration limits gives

$$\begin{aligned} l_\varphi &= -1 & t - l_\gamma &= t + 0.5 \\ t - u_\gamma &= t - 2 & t - l_\gamma &= t + 0.5 \\ t - u_\gamma &= t - 2 & u_\varphi &= 2.5 \end{aligned}$$

and  $h(t)$  consists of the three non-zero functions within the respective limits:

$$\begin{aligned} \eta_1(t) &= -\frac{(2t+3)^2(8t^4 - 16t^3 - 130t^2 + 646t + 717)}{960} & t \in [-1.5, 1) \\ \eta_2(t) &= -\frac{185t^3}{12} + \frac{9655t^2}{96} - \frac{18245t}{96} + \frac{14015}{192} & t \in [1, 2) \\ \eta_3(t) &= \frac{(2t-9)(16t^5 + 88t^4 + 76t^3 - 6618t^2 + 18564t - 7779)}{960} & t \in [2, 4.5] \end{aligned}$$

The graph of  $h(t)$  is shown in Figure A.3.

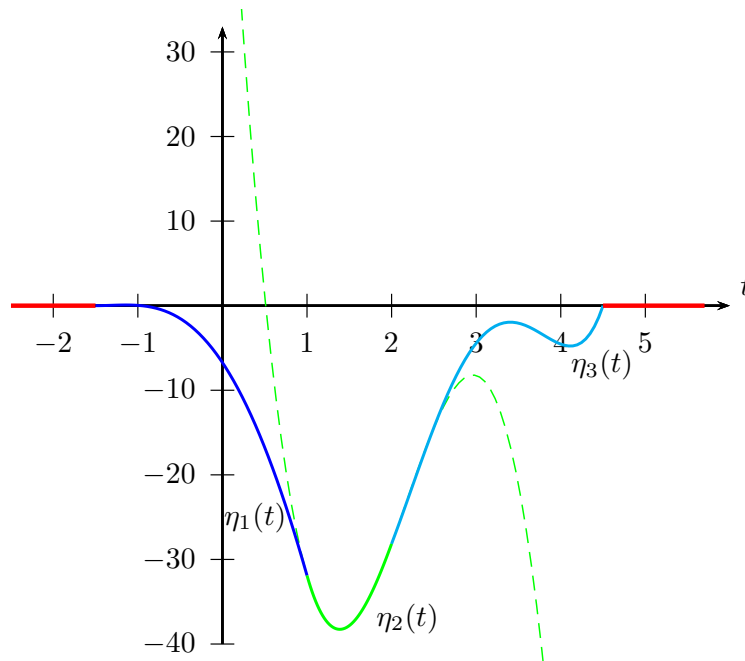


**Figure A.3:** Result of the convolution  $h(t) = f(t) \otimes g(t)$ . The non-zero part of  $h(t)$  is divided into the three segments  $\eta_1(t)$  (blue),  $\eta_2(t)$  (green) and  $\eta_3(t)$  (cyan). The dashed green line indicates the continuation of  $\eta_2(t)$ , i.e. the result of the convolution for infinitive support of  $f(t) = \varphi(t)$ .

## A.1 Construction of uniform B-Splines by repetitive Convolution

A uniform B-spline  $B_l^n(t)$  is a piecewise continuous polynomial function of degree  $n$  and shift  $l$ . It is of  $C^{n-1}$  continuity and is  $\geq 0$  in the interval  $[l\Delta t; (n+l+1)\Delta t]$  where  $\Delta t$  is the *knot distance* [Farin 2002; Zorin and Schröder 2000].

The uniform B-spline of degree 0 is defined as the step function,

$$B_l^0(t) = \begin{cases} 1 & t \in [(l-1)\Delta t; l\Delta t] \\ 0 & \text{elsewhere} \end{cases} \quad (\text{A.3})$$

and the uniform B-splines of higher degrees are constructed by recursive convolution [Zorin and Schröder 2000]:

$$B_l^n(t) = B_l^0(t) \otimes B_l^{n-1}(t). \quad (\text{A.4})$$

The uniform B-Splines of degree 0 to 7 are depicted in Figures A.4 and A.5.

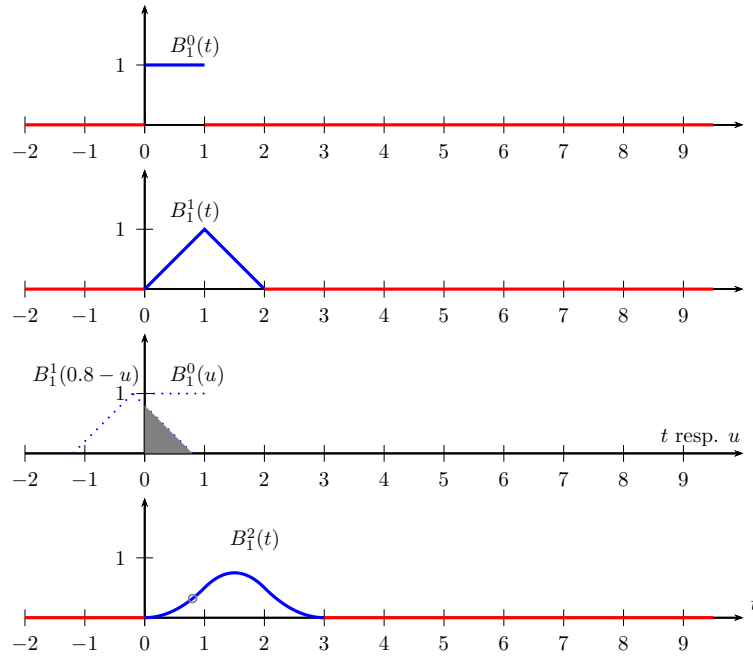


**Figure A.4:** Uniform B-splines of different degrees as result of convolution. The knot distance  $\Delta t$  was set to 1. From top to bottom:  $B_1^0(t)$ ,  $B_1^1(t)$ ,  $B_1^2(0.8)$  – as result of the product  $B_1^0(u)$  and  $B_1^1(0.8 - u)$  – and  $B_1^2(t)$ . The function value of  $B_1^2(0.8)$  (indicated by the grey circle) corresponds to the grey-hatched area in the third plot.

As an interesting result, for  $n = 0$  and  $l = 1$  we retrieve

$$B_1^0(t) = B_1^0(t) \otimes B_1^{-1}(t).$$



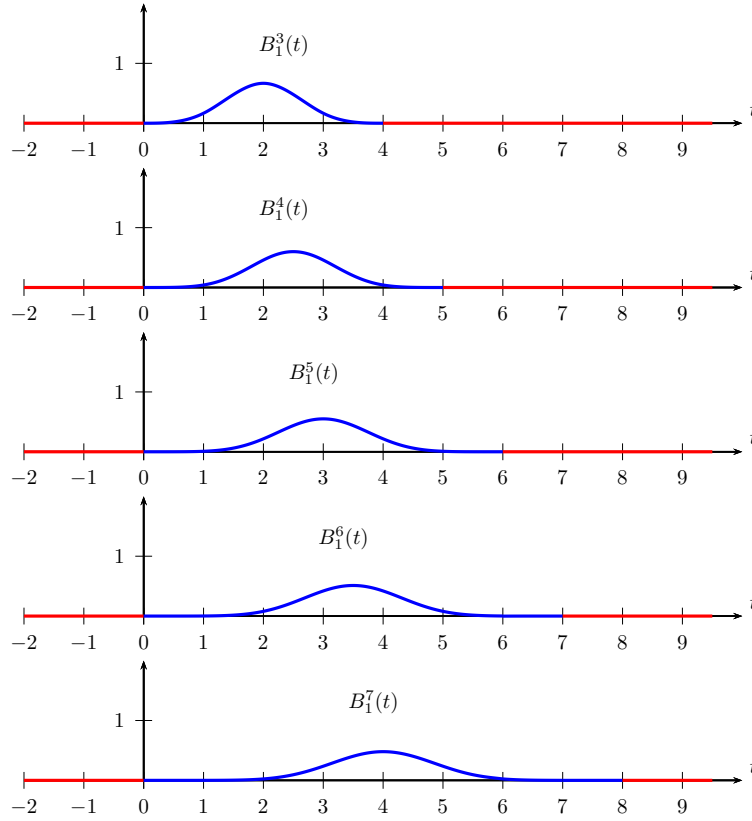


**Figure A.5:** Uniform B-splines of degrees 3 to 7 (from top to bottom). The knot distance  $\Delta t$  was set to 1.

Thus,  $B_1^{-1}(t)$  corresponds to the identity element of convolution, i.e. the *Dirac distribution*  $\delta(t)$ :

$$\delta(t) = B_1^{-1}(t) = \begin{cases} \infty & t = 0 \\ 0 & \text{elsewhere} \end{cases}.$$

For  $l \neq 1$ , convolution with  $B_l^{-1}(t)$  results in the shift about  $(l - 1)\Delta t$  along the  $t$  axis.

Given a uniform B-spline  $f(t) = B_{l_f}^{n_f}(t)$  and another one  $g(t) = B_{l_g}^{n_g}(t)$ , their convolution results to

$$f(t) \otimes g(t) = B_{l_f+l_g+1}^{n_f+n_g+1}(t). \quad (\text{A.5})$$

The integral of a B-spline,

$$\int_{-\infty}^{\infty} B_l^n(t) dt = 1 \quad (\text{A.6})$$

for all shifts  $l \in \mathbb{R}$  and degrees  $n \in \mathbb{N}$ , which follows from the construction by recursive convolution. As a consequence, the integral of a *scaled* uniform B-spline  $cB_l^n(t)$  equals

the scaling factor  $c$ . Thus, the convolution of two scaled uniform B-splines  $c_f B_{l_f}^{n_f}(t)$  and  $c_g B_{l_g}^{n_g}(t)$  results in

$$\int_{-\infty}^{\infty} (c_f B_{l_f}^{n_f}(t)) \otimes (c_g B_{l_g}^{n_g}(t)) dt = c_f c_g \int_{-\infty}^{\infty} \underbrace{B_{l_f}^{n_f}(t) \otimes B_{l_g}^{n_g}(t)}_{B_{l_f+l_g+1}^{n_f+n_g+1}(t)} dt = c_f c_g. \quad (\text{A.7})$$

If scaling is applied in  $t$  direction, equivalent to a parameter change from  $t$  to  $\bar{c}t$ , the integral of the scaled uniform B-spline  $B_l^n(\bar{c}t)$  results to  $1/\bar{c}$ .

## A.2 Convolution of Gaussian Distributions and Functions

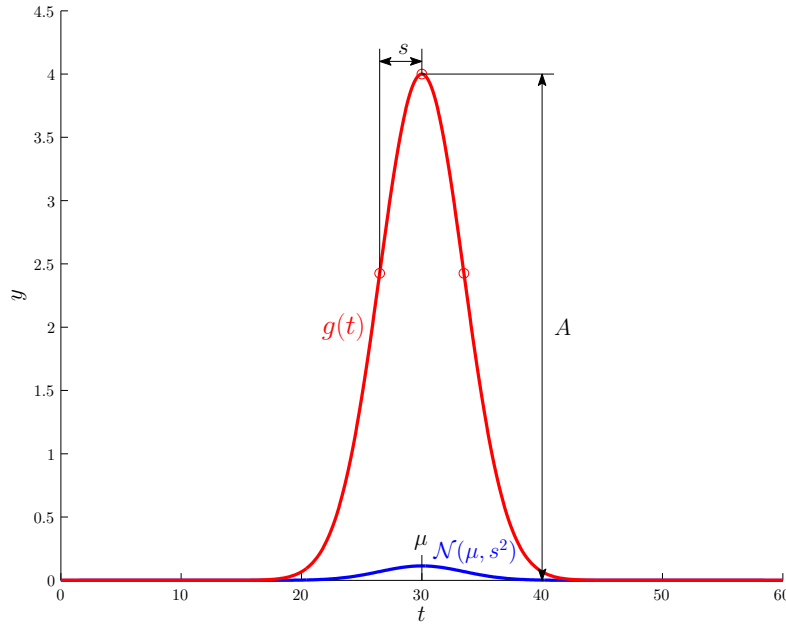


**Figure A.6:** Gaussian function  $g(t)$  (red) with peak amplitude  $A$  as scaled version of a normal distribution  $\mathcal{N}(\mu, s^2)$  (blue). The scaling of  $g(t)$  w.r.t. the normal distribution is  $A\sqrt{2\pi}s$ .

Let  $f(t)$  be a *Gaussian* or *normal distribution* with mean  $\mu_f$  and variance  $\sigma_f^2$  (cf. Figure A.6), i.e.

$$f(t) = \frac{1}{\sqrt{2\pi}\sigma_f} e^{-\frac{(t-\mu_f)^2}{2\sigma_f^2}} = \mathcal{N}(\mu_f, \sigma_f^2),$$

and  $g(t) = \mathcal{N}(\mu_g, \sigma_g^2)$ . Their convolution  $h(t) = f(t) \otimes g(t)$  is given by

$$h(t) = \frac{1}{\sqrt{2\pi(\sigma_f^2 + \sigma_g^2)}} e^{-\frac{(t-(\mu_f+\mu_g))^2}{2(\sigma_f^2 + \sigma_g^2)}} = \mathcal{N}(\mu_f + \mu_g, \sigma_f^2 + \sigma_g^2), \quad (\text{A.8})$$

so the result is again a Gaussian distribution with mean and variance resulting in the sum of the operands means and variances, resp.

*Proof.* See [Bromiley 2003]:

We use the *Fourier transform*  $\mathcal{F}$  of  $f(t)$ ,

$$\mathcal{F}(f(t)) = \underline{f}(\omega) = \int_{-\infty}^{\infty} f(t)e^{-2\pi i\omega t} dt$$

and of  $g(t)$  for proving the proposition. The Fourier transform of a convolution of two functions is the product of the operands' Fourier transforms (see Chapter B):

$$\mathcal{F}(f(t) \otimes g(t)) = \mathcal{F}(f(t))\mathcal{F}(g(t)) = \underline{f}(\omega)\underline{g}(\omega) \Leftrightarrow f(t) \otimes g(t) = \mathcal{F}^{-1}\left(\underline{f}(\omega)\underline{g}(\omega)\right).$$

With the substitution  $\tau = t - \mu_f$  and  $d\tau = dt$ , we get

$$\underline{f}(\omega) = \frac{1}{\sqrt{2\pi}\sigma_f} \int_{-\infty}^{\infty} e^{-\frac{\tau^2}{2\sigma_f^2}} e^{-2\pi i\omega(\tau-\mu_f)} d\tau = \frac{e^{2\pi i\omega\mu_f}}{\sqrt{2\pi}\sigma_f} \int_{-\infty}^{\infty} e^{-\frac{\tau^2}{2\sigma_f^2}} e^{-2\pi i\omega\tau} d\tau.$$

Using the *Euler formula*, we can write  $e^{i\vartheta}$  as

$$e^{i\vartheta} = \cos \vartheta + i \sin \vartheta$$

and as a consequence,

$$\underline{f}(\omega) = \frac{e^{2\pi i\omega\mu_f}}{\sqrt{2\pi}\sigma_f} \int_{-\infty}^{\infty} e^{-\frac{\tau^2}{2\sigma_f^2}} (\cos 2\pi\omega\tau - i \sin 2\pi\omega\tau) d\tau.$$

Since the sine function is odd, the imaginary part does not contribute to the result and the above formula simplifies to

$$\underline{f}(\omega) = \frac{e^{2\pi i\omega\mu_f}}{\sqrt{2\pi}\sigma_f} \int_{-\infty}^{\infty} e^{-\frac{\tau^2}{2\sigma_f^2}} \cos 2\pi\omega\tau d\tau.$$

Using

$$\int_{-\infty}^{\infty} e^{-\alpha x^2} \cos 2\lambda x dx = \sqrt{\frac{\pi}{\alpha}} e^{-\frac{\lambda^2}{\alpha}},$$

we finally get

$$\underline{f}(\omega) = \frac{e^{2\pi i\omega\mu_f}}{\sqrt{2\pi}\sigma_f} \sqrt{2\pi}\sigma_f e^{-2\pi^2\omega^2\sigma_f^2} = e^{2\pi i\omega\mu_f} e^{-2\pi^2\omega^2\sigma_f^2} \quad (\text{A.9})$$

and

$$\underline{f}(\omega)\underline{g}(\omega) = e^{2\pi i\omega(\mu_f+\mu_g)} e^{-2\pi^2\omega^2(\sigma_f^2+\sigma_g^2)}. \quad (\text{A.10})$$

This is the Fourier transform of a Gaussian distribution with mean

$$\mu_h = \mu_f + \mu_g$$

and variance

$$\sigma_h^2 = \sigma_f^2 + \sigma_g^2.$$

□

The result corresponds to the law of error propagation for the sum of two independent normally distributed random variables [Mikhail 1976]. Be  $z = x + y$  with the operands  $x \sim \mathcal{N}(\mu_x, \sigma_x^2)$  and  $y \sim \mathcal{N}(\mu_y, \sigma_y^2)$ . For  $z$ , we retrieve as mean  $\mu_z = \mu_x + \mu_y$  and as variance

$$\sigma_z^2 = (\sigma_x, \sigma_y) \begin{pmatrix} \frac{\partial z}{\partial x} & 0 \\ 0 & \frac{\partial z}{\partial y} \end{pmatrix} \begin{pmatrix} \sigma_x \\ \sigma_y \end{pmatrix} = \sigma_x^2 + \sigma_y^2.$$

Let us look at the more general example of Gaussian functions  $f(t)$  and  $g(t)$  with arbitrary amplitude, i.e.

$$f(t) = A_f e^{-\frac{(t-\mu_f)^2}{2\sigma_f^2}} \quad \text{and} \quad g(t) = A_g e^{-\frac{(t-\mu_g)^2}{2\sigma_g^2}}.$$

We can re-write the two expressions as scaled Gaussian distributions (cf. Figure A.6):

$$f(t) = (A_f \sqrt{2\pi} \sigma_f) \frac{1}{\sqrt{2\pi} \sigma_f} e^{-\frac{(t-\mu_f)^2}{2\sigma_f^2}} \quad \text{and} \quad g(t) = (A_g \sqrt{2\pi} \sigma_g) \frac{1}{\sqrt{2\pi} \sigma_g} e^{-\frac{(t-\mu_g)^2}{2\sigma_g^2}},$$

resp. The scaling factors  $A_f \sqrt{2\pi} \sigma_f$  and  $A_g \sqrt{2\pi} \sigma_g$  are constants, so we can use Equation (A.8) for calculating their convolution  $h(t) = f(t) \otimes g(t)$ :

$$h(t) = (A_f \sqrt{2\pi} \sigma_f)(A_g \sqrt{2\pi} \sigma_g) e^{-\frac{(t-(\mu_f+\mu_g))^2}{2(\sigma_f^2+\sigma_g^2)}} = (2\pi A_f A_g \sigma_f \sigma_g) e^{-\frac{(t-(\mu_f+\mu_g))^2}{2(\sigma_f^2+\sigma_g^2)}}. \quad (\text{A.11})$$

So, again we have retrieved a Gaussian function as result of the convolution of two scaled Gaussian functions where

- the resulting mean is the sum of the operands' means,
- the resulting variance is the sum of the operands' variances, and
- the resulting scaling factor is the product of the operands' scaling factors.

## The Convolution Theorem

In this chapter, we give the proof for the convolution theorem which connects convolution and multiplication in time and frequency domain by means of the Fourier transform  $\mathcal{F}$  [Weisstein 2014b]:

$$f(t) \otimes g(t) = \mathcal{F}^{-1}(\underline{f}(\omega) \underline{g}(\omega)) \text{ and } \mathcal{F}(f(t) g(t)) = \underline{f}(\omega) \otimes \underline{g}(\omega), \quad (\text{B.1})$$

i.e. the convolution of two functions in time domain is equivalent to the multiplication of the Fourier transforms of these two functions in frequency domain, and the other way round.

*Proof.* See [Weisstein 2014b]:

With  $f(t)$  being the inverse Fourier transform of its equivalent in frequency domain  $\underline{f}(\omega)$ , i.e.

$$f(t) = \mathcal{F}^{-1}(\underline{f}(\omega)) = \int_{-\infty}^{\infty} \underline{f}(\omega) e^{2\pi i \omega t} d\omega,$$

we can write the convolution  $f(t) \otimes g(t)$  as

$$f(t) \otimes g(t) = \int_{-\infty}^{\infty} g(\tau) \left( \int_{-\infty}^{\infty} \underline{f}(\omega) e^{2\pi i \omega (t-\tau)} d\omega \right) d\tau.$$

Changing the order of integration in the above formula gives

$$\int_{-\infty}^{\infty} \underline{f}(\omega) \left( \int_{-\infty}^{\infty} g(\tau) e^{-2\pi i \omega \tau} d\tau \right) e^{2\pi i \omega t} d\omega = \int_{-\infty}^{\infty} \underline{f}(\omega) \underline{g}(\omega) e^{2\pi i \omega t} d\omega.$$

Thus, we finally get

$$f(t) \otimes g(t) = \int_{-\infty}^{\infty} \underline{f}(\omega) \underline{g}(\omega) e^{2\pi i \omega t} d\omega = \mathcal{F}^{-1}(\underline{f}(\omega) \underline{g}(\omega)).$$

The proof for the second proposition in Equation (B.1) is found analogously.  $\square$

# Examples of dBCS Synthesis in Detail

## C.1 Simulated dBCS for extended planar Targets

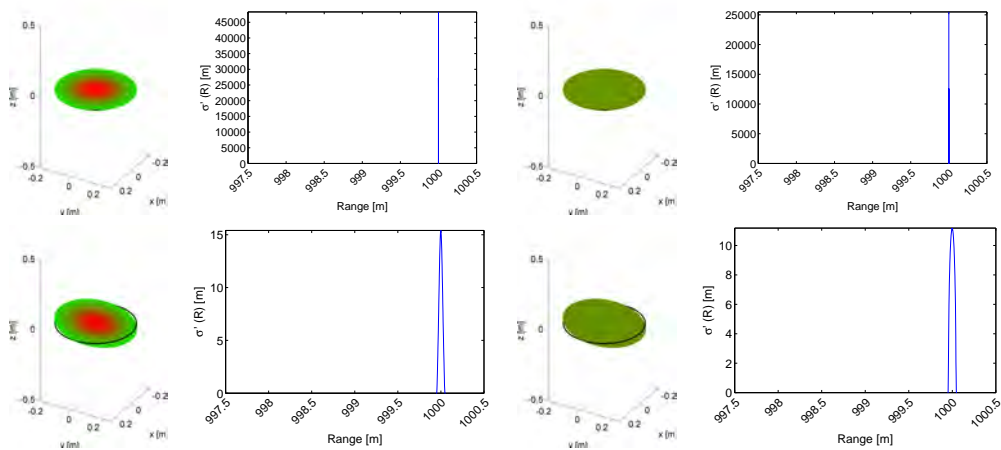


**Figure C.1:** Differential backscatter cross-section for extended planar targets. The incidence angle  $\vartheta$  varies from  $0^\circ$  to  $10^\circ$  from top to bottom in steps of  $10^\circ$ . The images in the 1<sup>st</sup> and 3<sup>rd</sup> column illustrate the laser illumination geometry and local incidence angle for Gaussian and uniform power density distribution within the laser footprint, resp. The images in the 2<sup>nd</sup> and 4<sup>th</sup> column show the resulting dBCS for the respective case. The example is continued for higher incidence angles in Figure C.2.

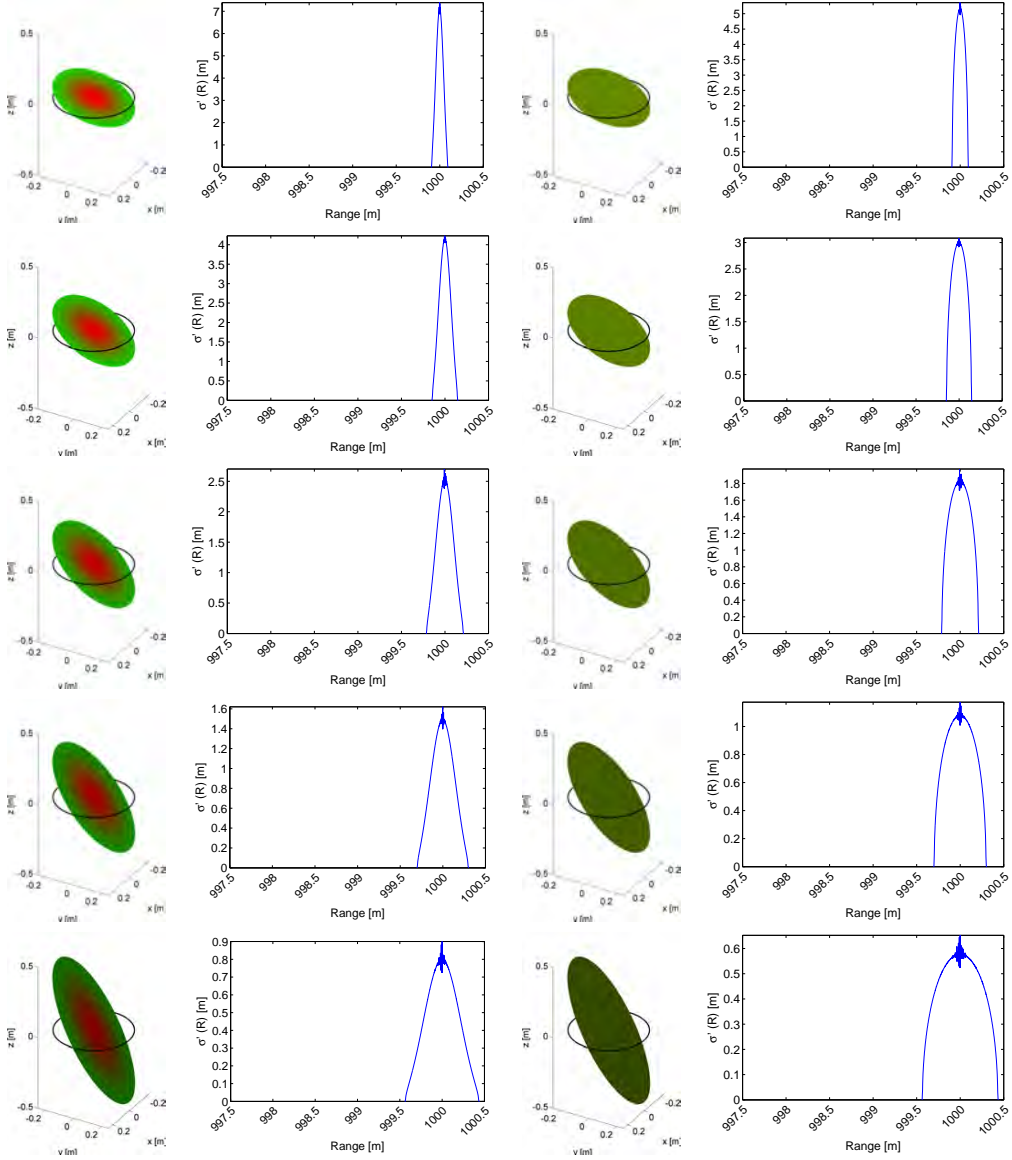


**Figure C.2:** Continuation of the dBCS examples shown in Figure C.1 for incidence angles of  $20^\circ$  to  $60^\circ$  (from top to bottom).



## C.2 Simulated dBCS for parallel planar Targets with Offsets

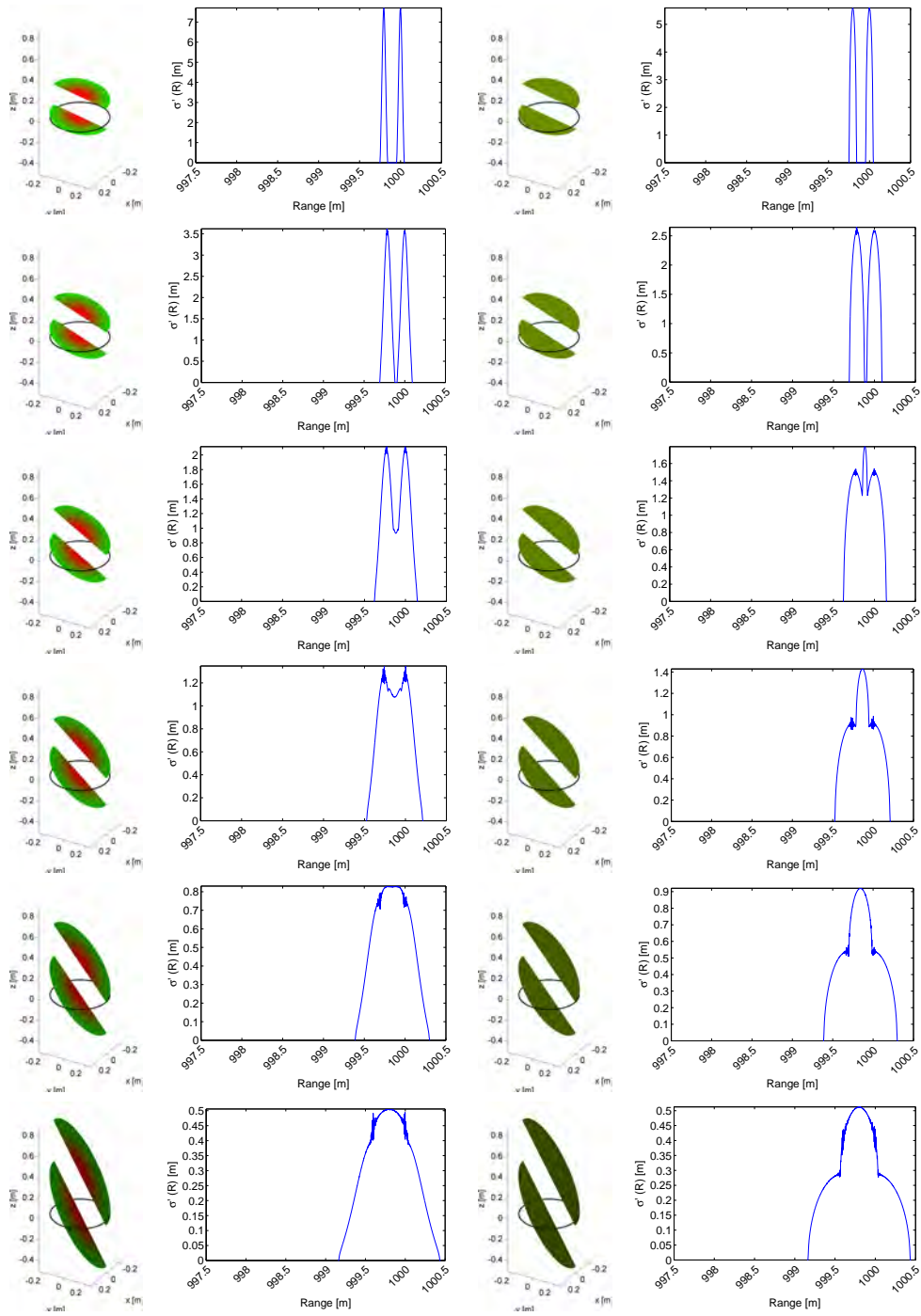


**Figure C.3:** Continuation of Figures C.1 and C.2 for parallel planar targets with an offset of 0.20 m to each other. The incidence angle varies from  $10^\circ$  to  $60^\circ$  in steps of  $10^\circ$ .

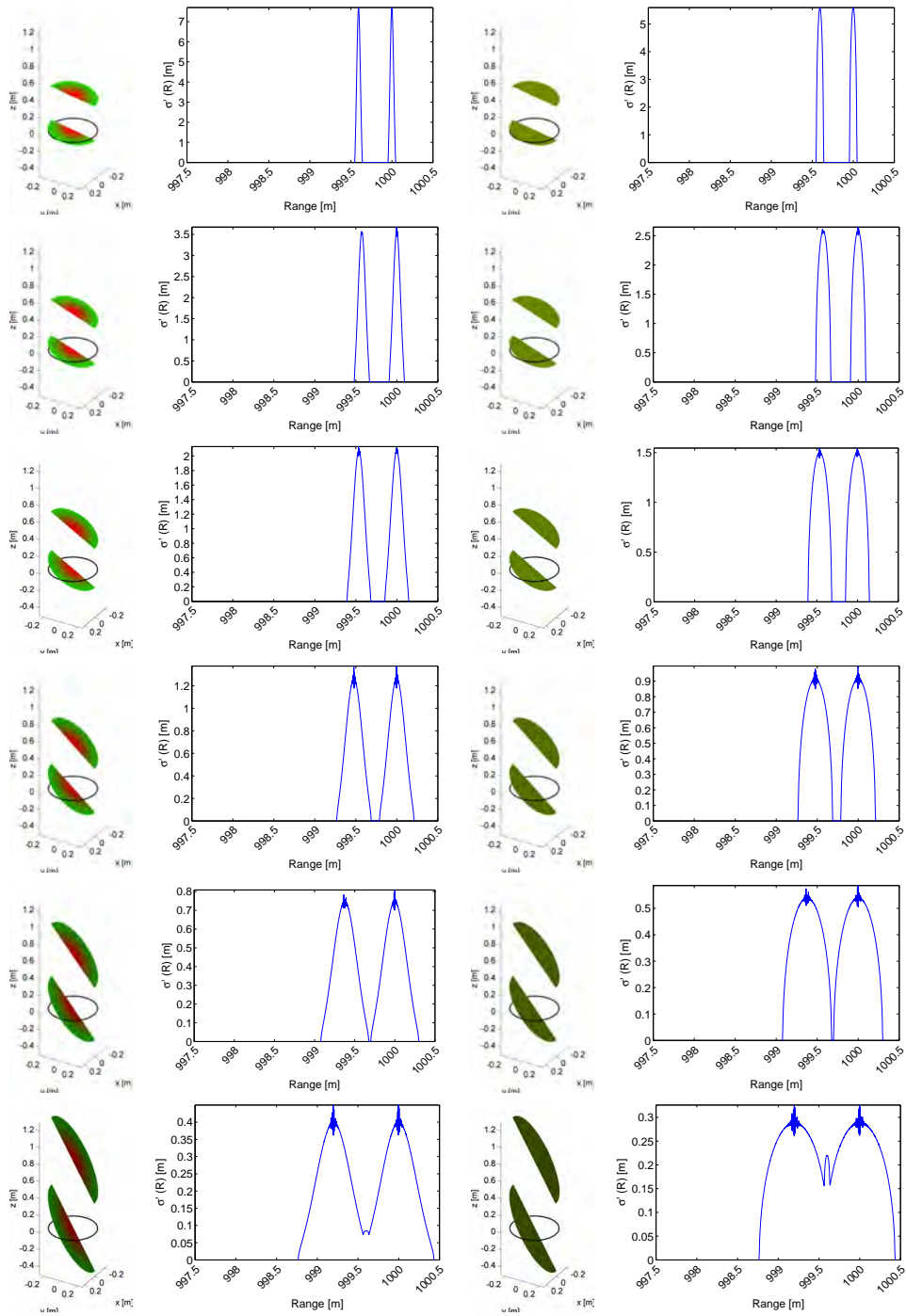


**Figure C.4:** Continuation of Figures C.1 and C.2 for parallel planar targets with an offset of 0.40 m to each other. The incidence angle varies from  $10^\circ$  to  $60^\circ$  in steps of  $10^\circ$ .

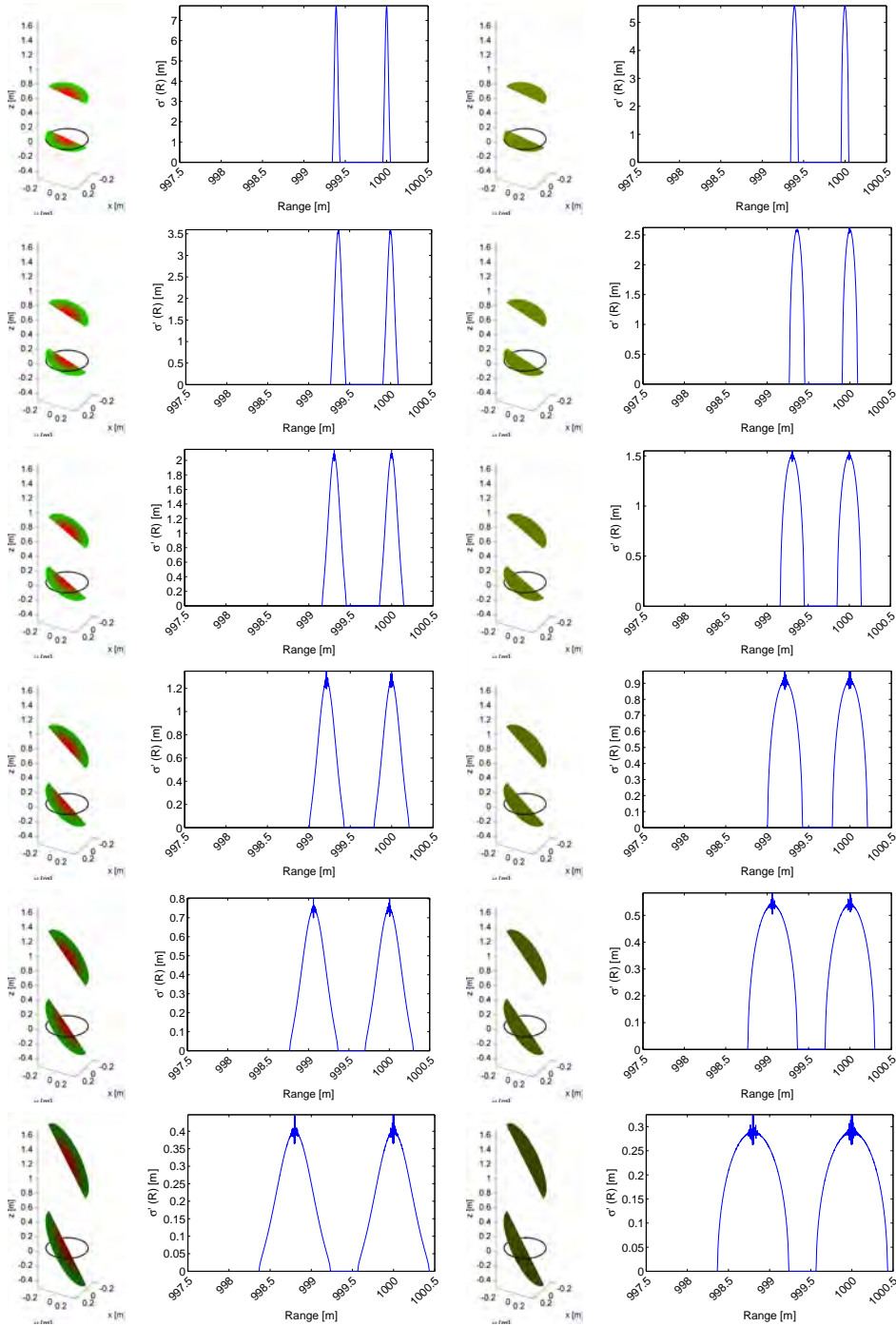


**Figure C.5:** Continuation of Figures C.1 and C.2 for parallel planar targets with an offset of 0.60 m to each other. The incidence angle varies from  $10^\circ$  to  $60^\circ$  in steps of  $10^\circ$ .

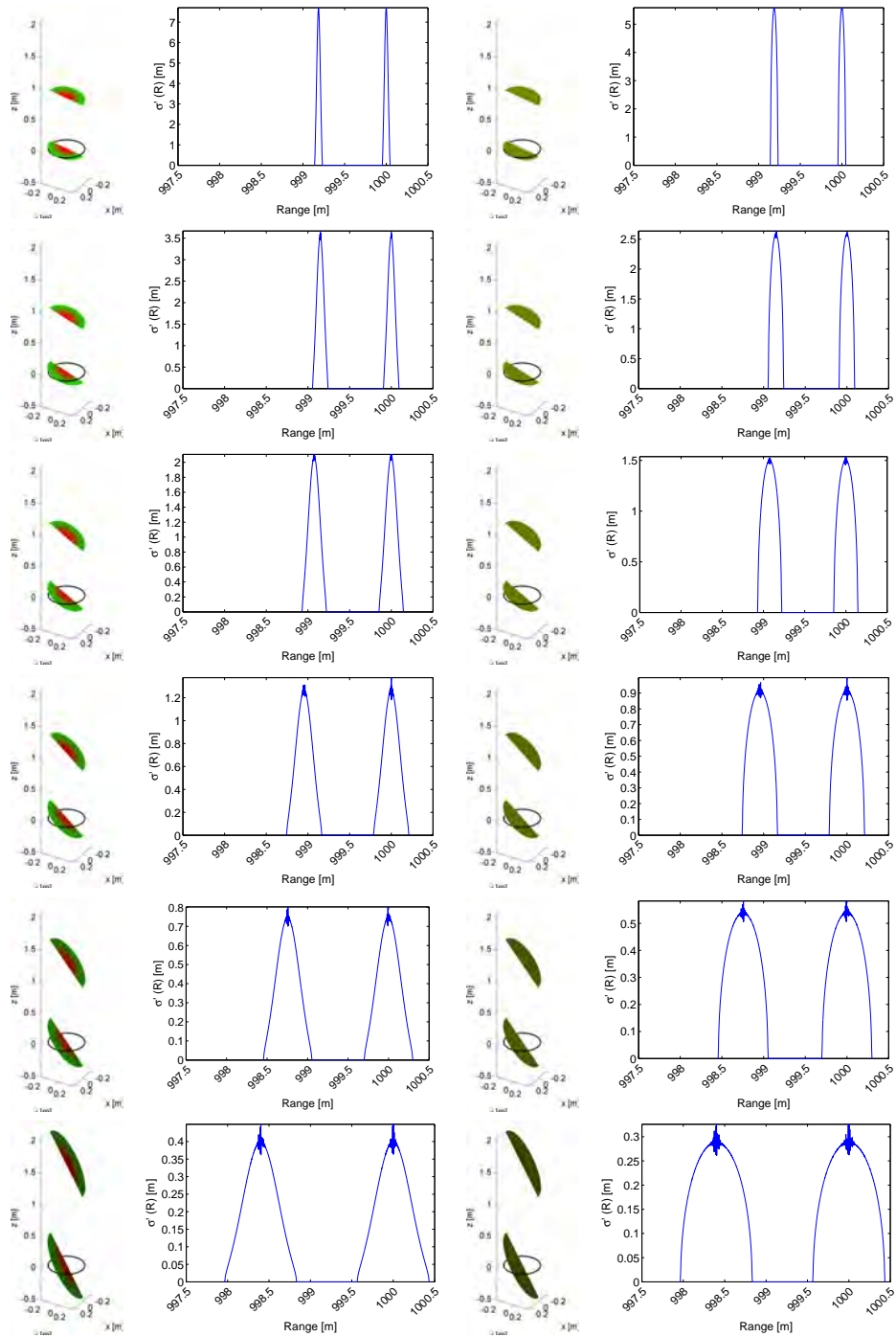


**Figure C.6:** Continuation of Figures C.1 and C.2 for parallel planar targets with an offset of 0.80 m to each other. The incidence angle varies from  $10^\circ$  to  $60^\circ$  in steps of  $10^\circ$ .

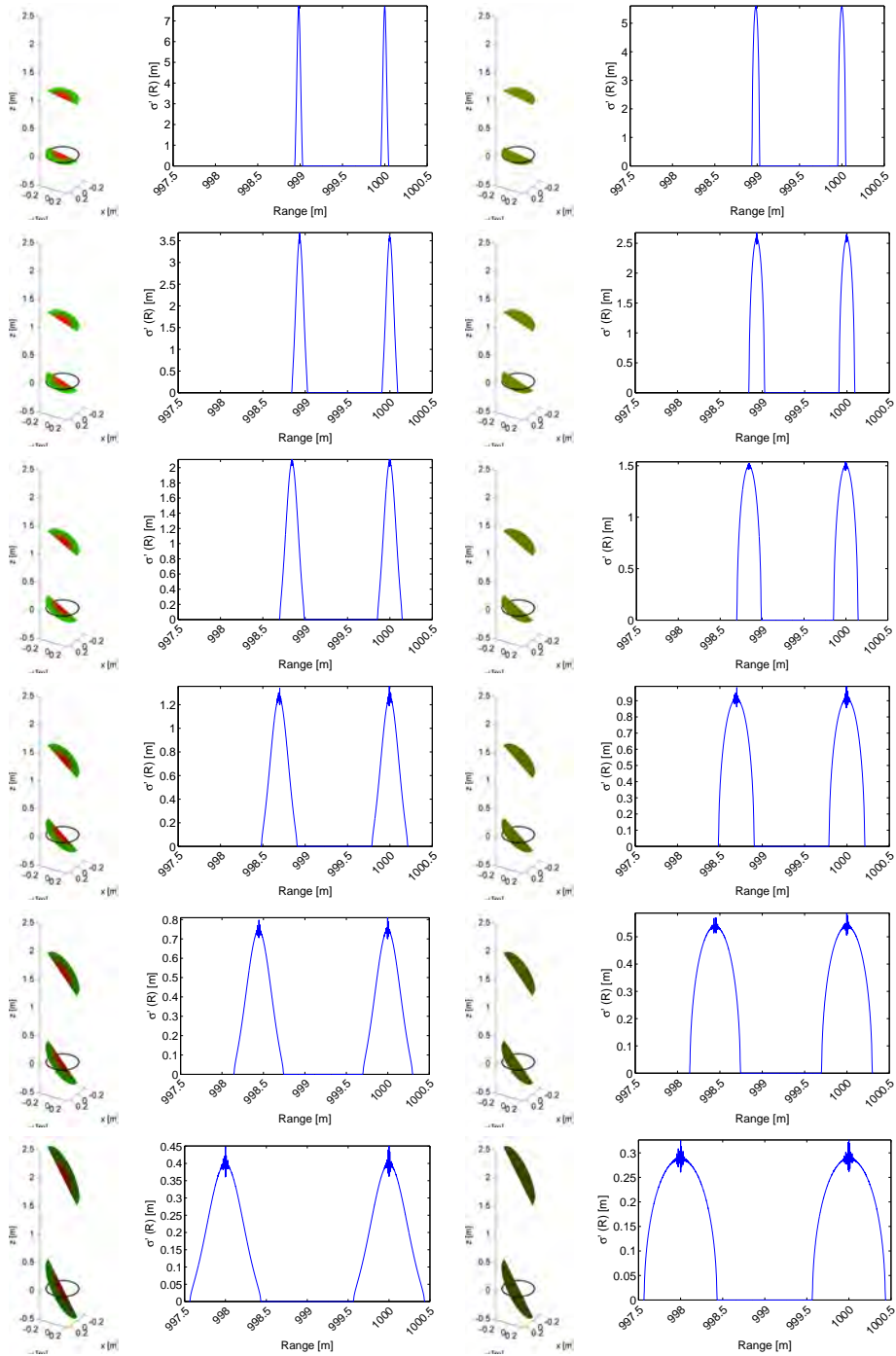
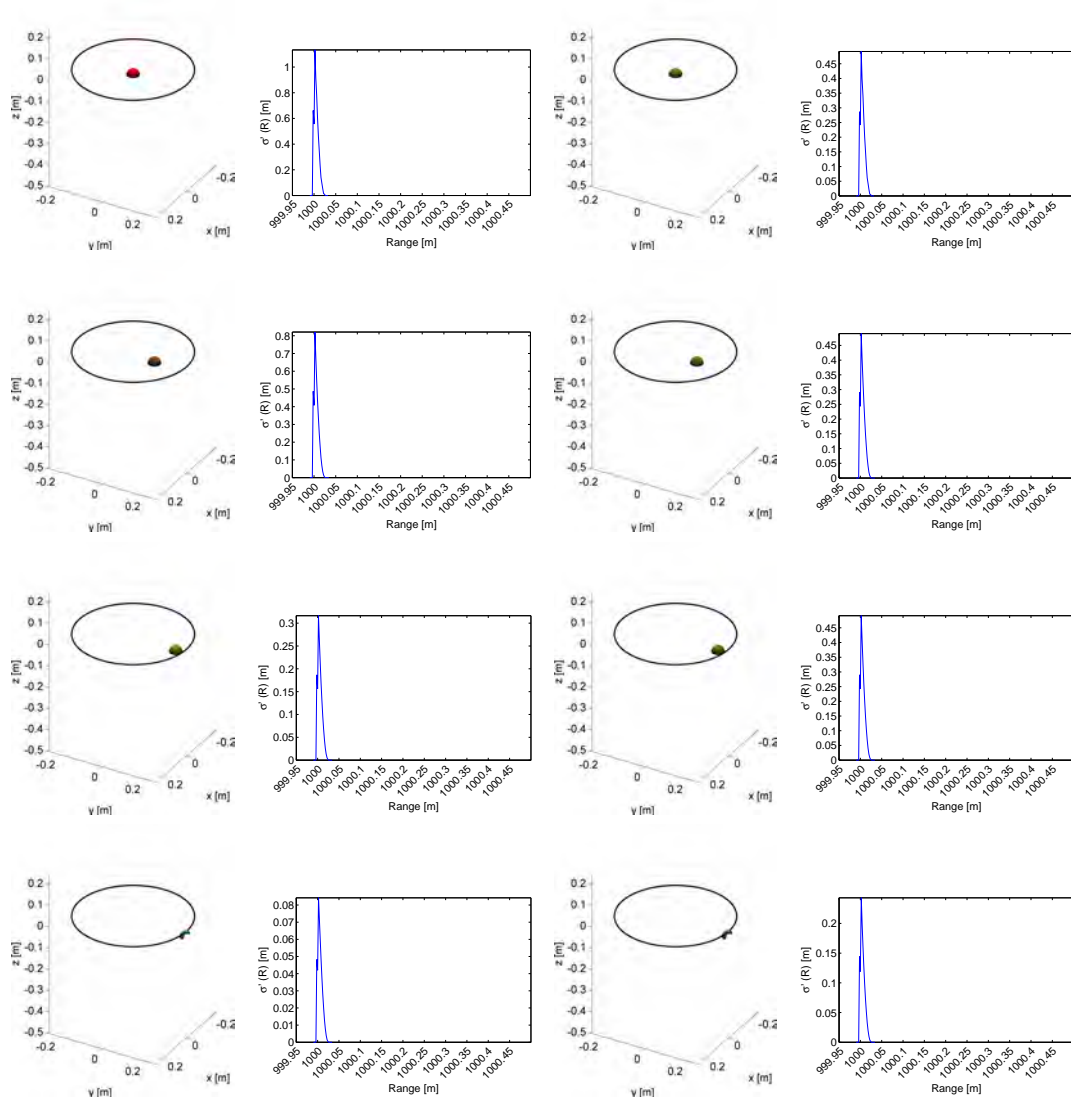
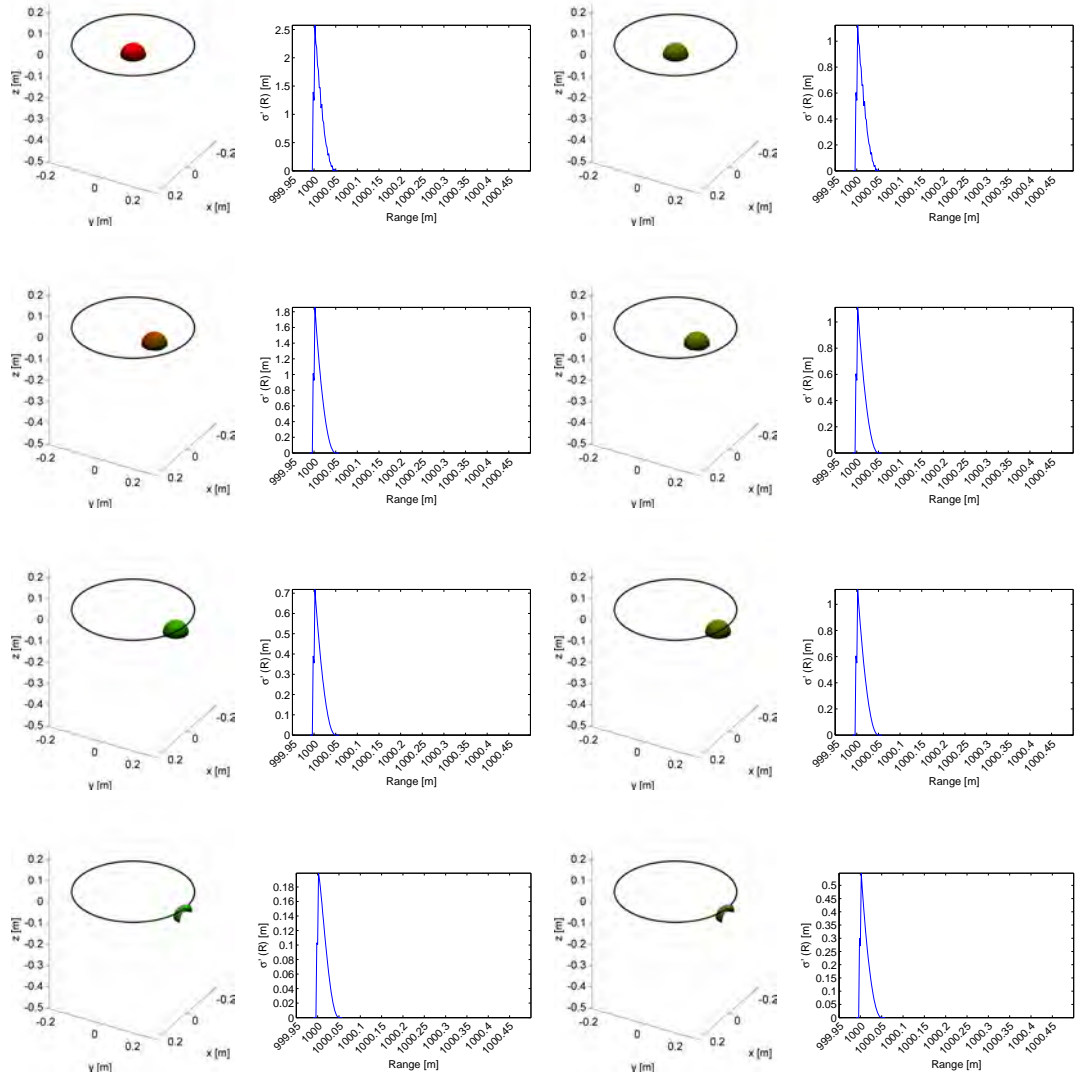


Figure C.7: Continuation of Figures C.1 and C.2 for parallel planar targets with an offset of 1 m to each other. The incidence angle varies from  $10^\circ$  to  $60^\circ$  in steps of  $10^\circ$ .

### C.3 Simulated dBCS for spherical Targets



**Figure C.8:** Differential backscatter cross-section for spherical targets of radius  $r = 0.025$  m. The offset of the sphere's center from the laser beam axis increases from 0 (top) to 0.25 m (bottom) in steps of 0.10 m. The example is continued for spheres of bigger radii in Figures C.9 to C.14.



**Figure C.9:** Continuation of the dBCS examples shown in Figure C.8 for radius  $r = 0.05$  m.

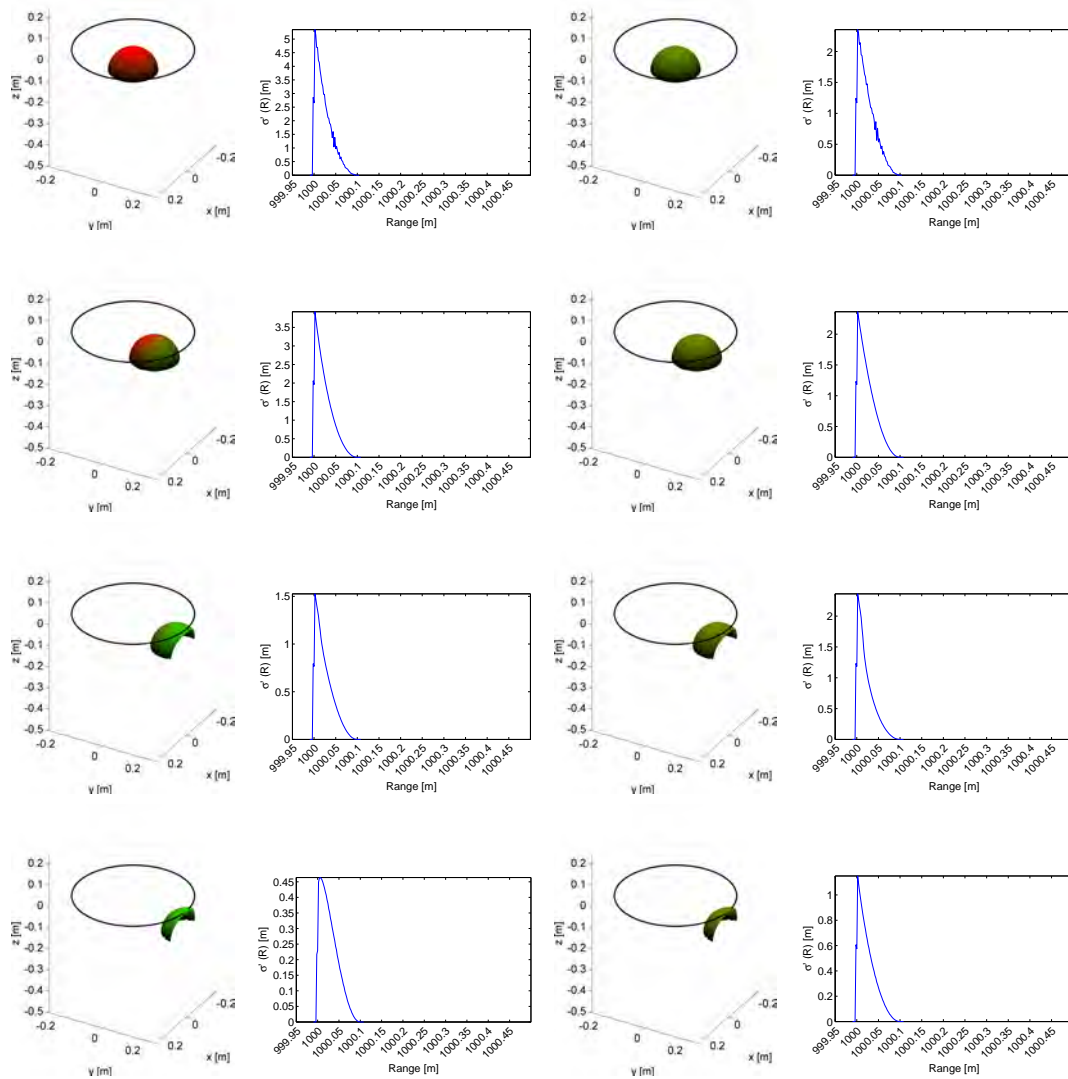


Figure C.10: Continuation of the dBSC examples shown in Figure C.8 for radius  $r = 0.10$  m.



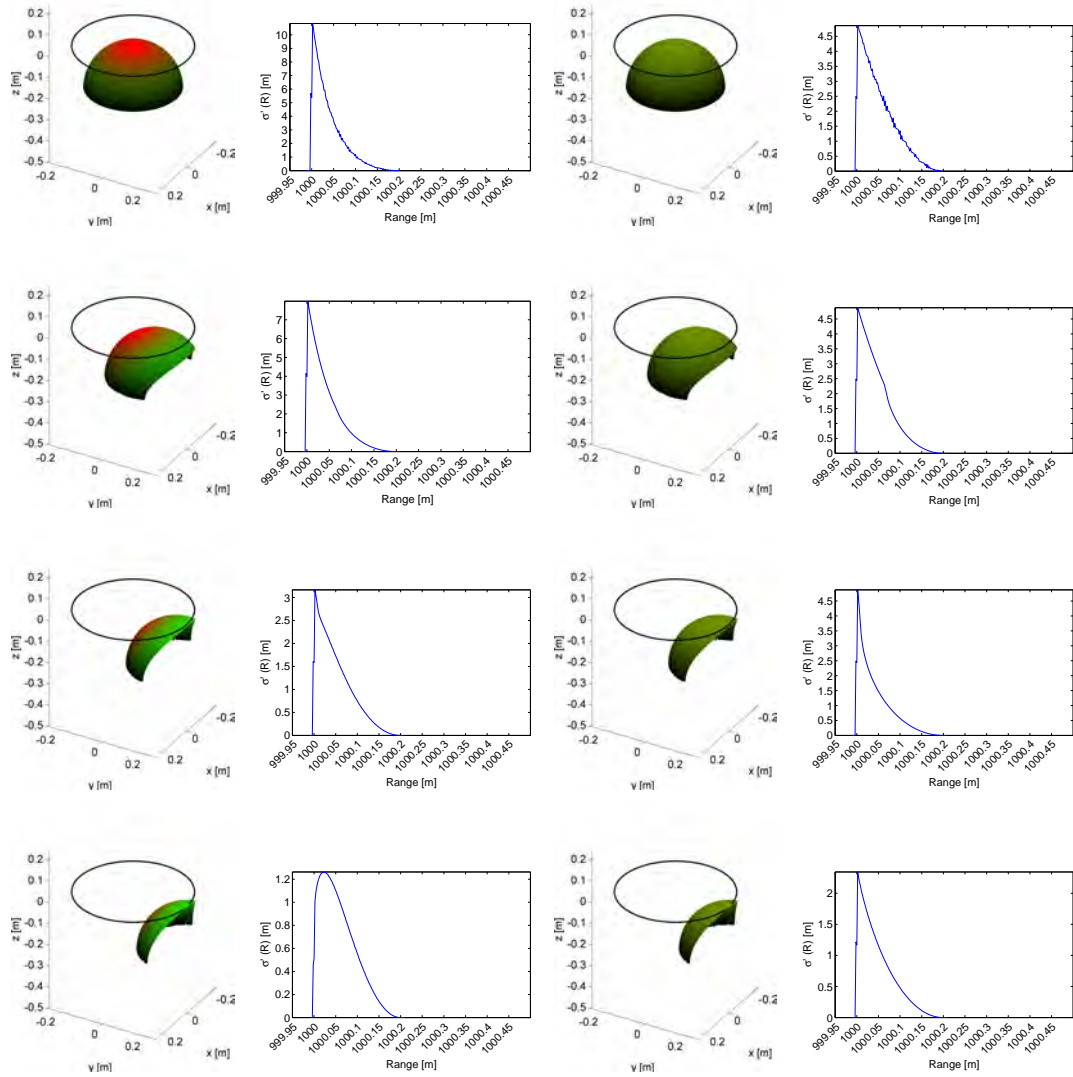


Figure C.11: Continuation of the dBSCS examples shown in Figure C.8 for radius  $r = 0.2$  m.

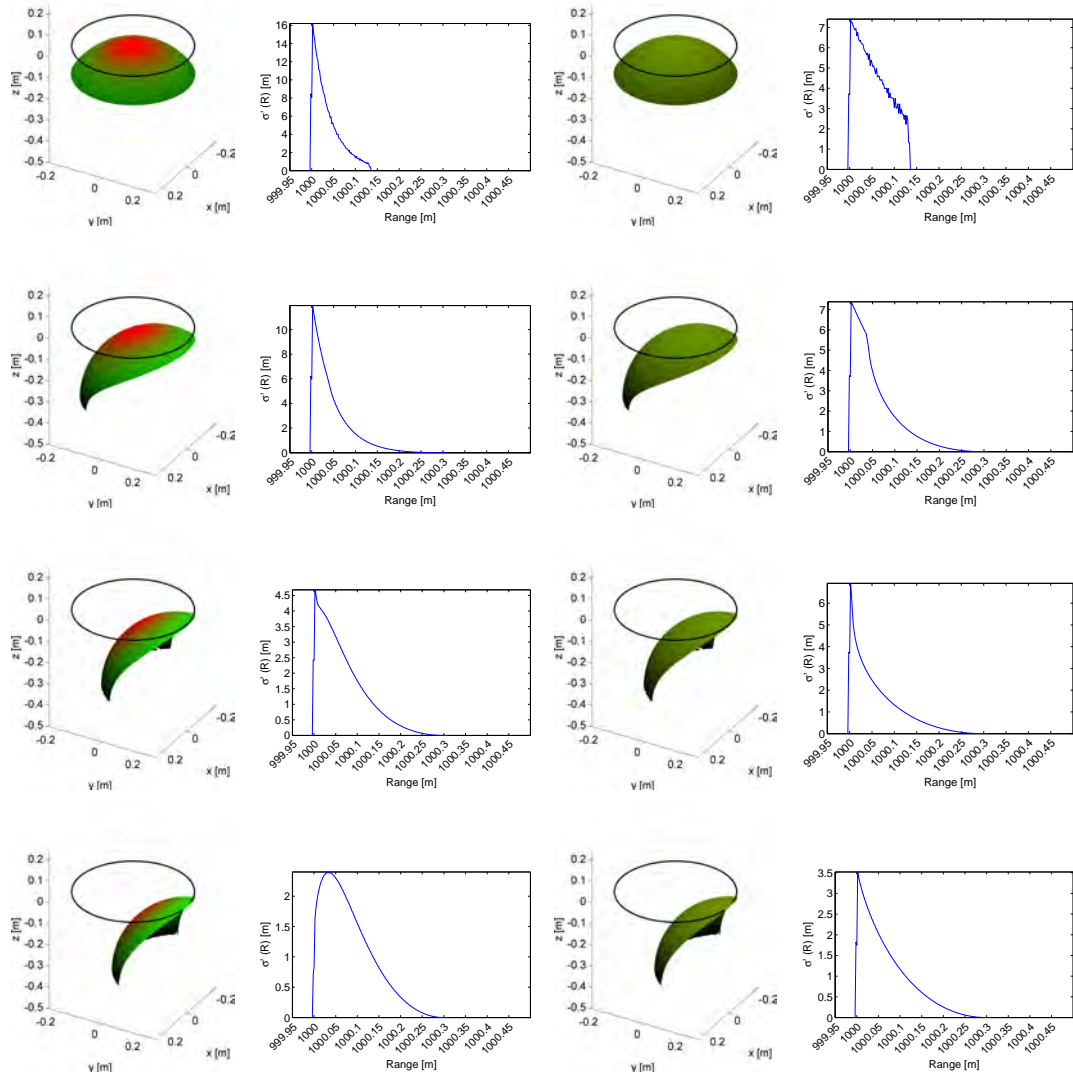
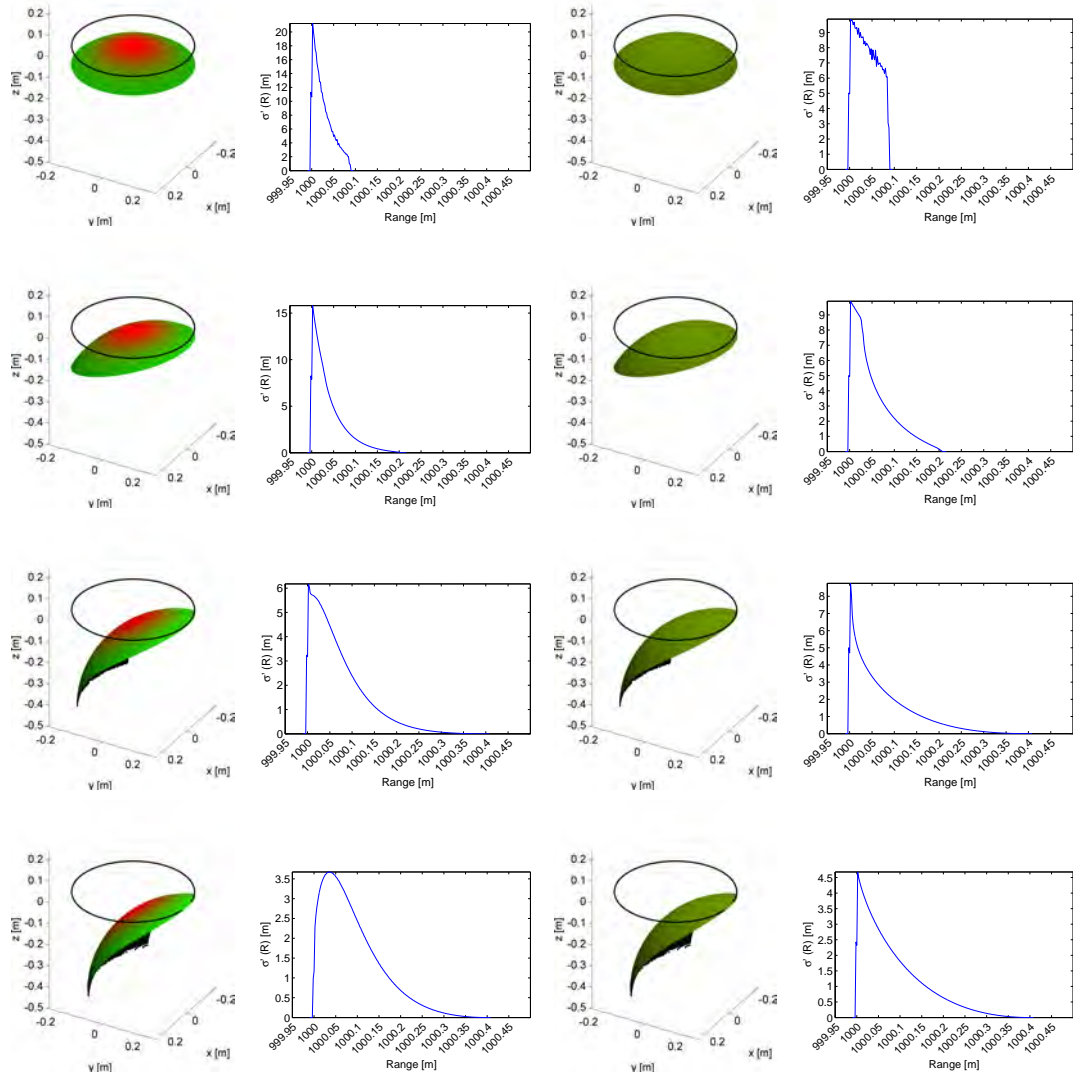
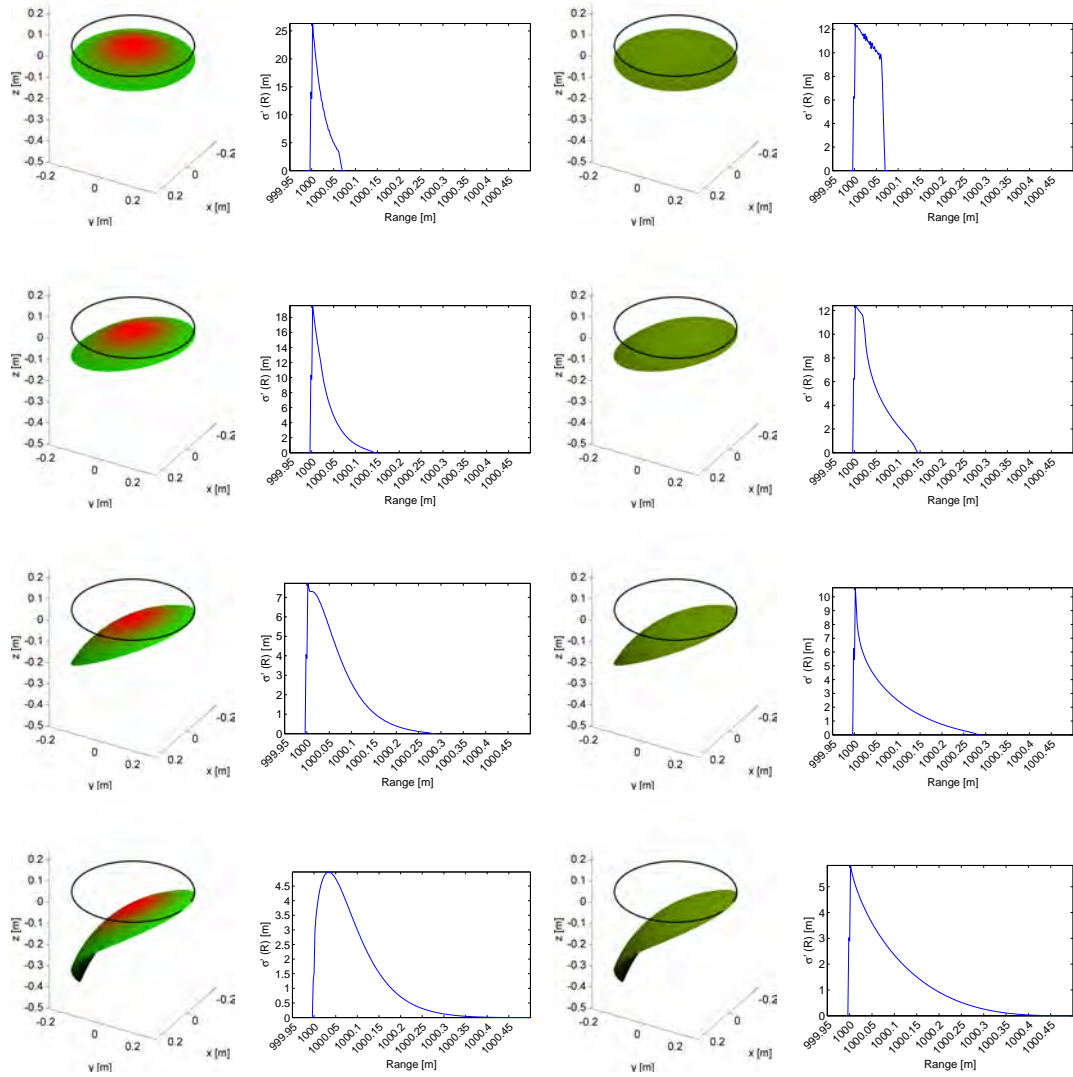


Figure C.12: Continuation of the dBSCS examples shown in Figure C.8 for radius  $r = 0.30$  m.



**Figure C.13:** Continuation of the dBSCS examples shown in Figure C.8 for radius  $r = 0.40$  m.



**Figure C.14:** Continuation of the dBSCS examples shown in Figure C.8 for radius  $r = 0.50$  m.

## C.4 Simulated dBCS for cylindrical Targets

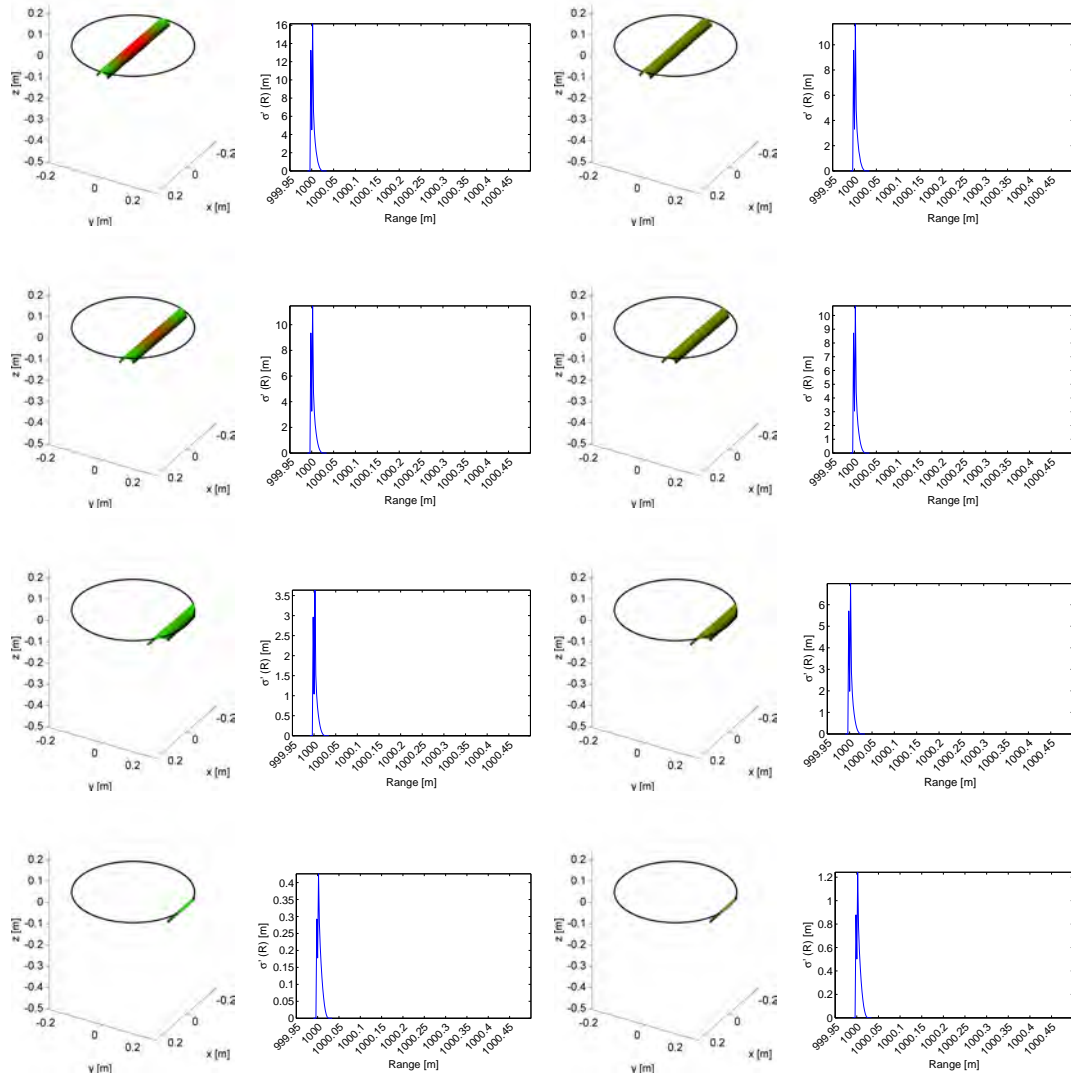


**Figure C.15:** Differential backscatter cross-section for cylindrical targets of radius  $r = 0.025$  m. The offset of the cylinder's center from the laser beam axis increases from 0 (top) to 0.25 m (bottom) in steps of 0.05 m. The example is continued for cylinders of bigger radii in Figures C.16 to C.21.

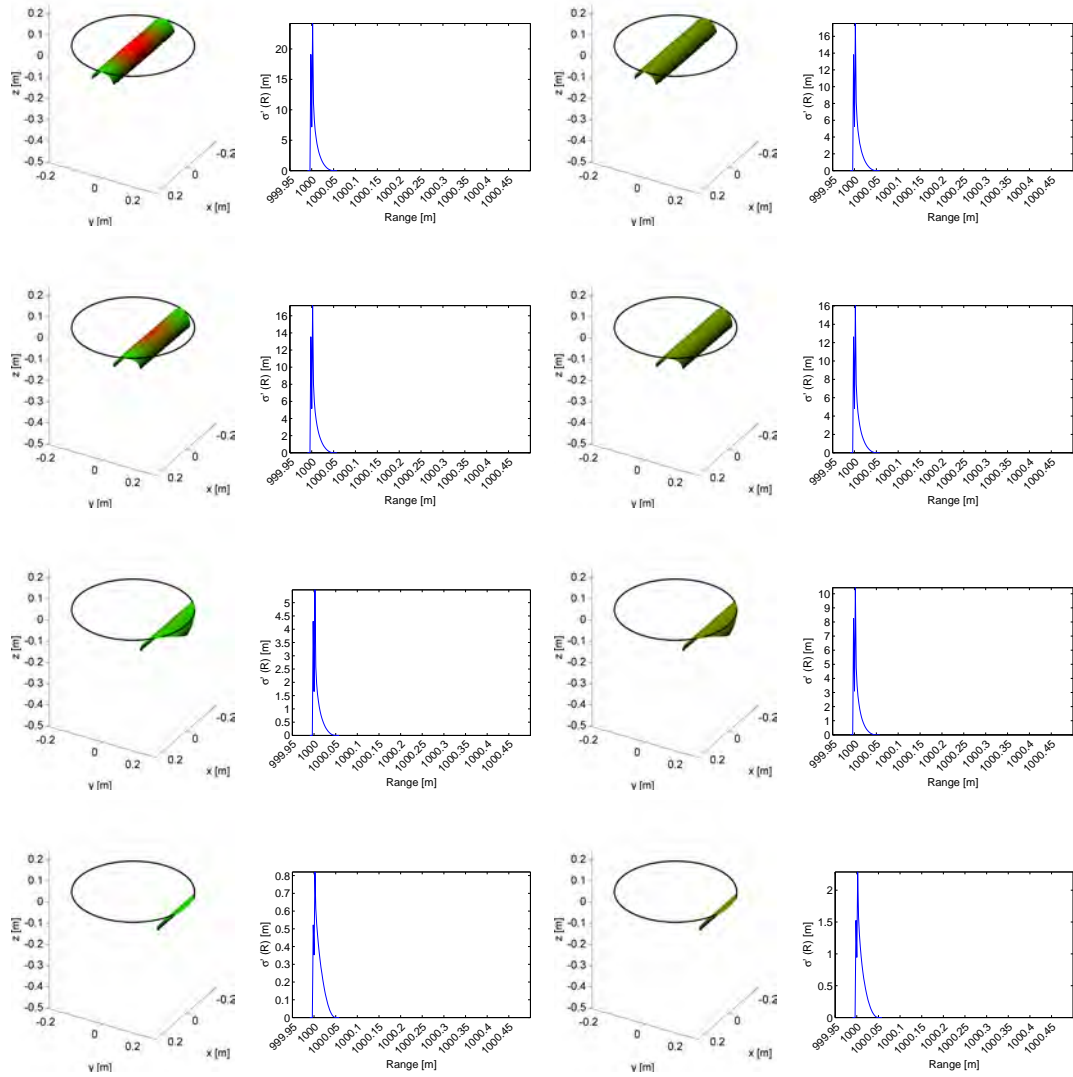


**Figure C.16:** Continuation of the dBCS examples shown in Figure C.15 for radius  $r = 0.05$  m.

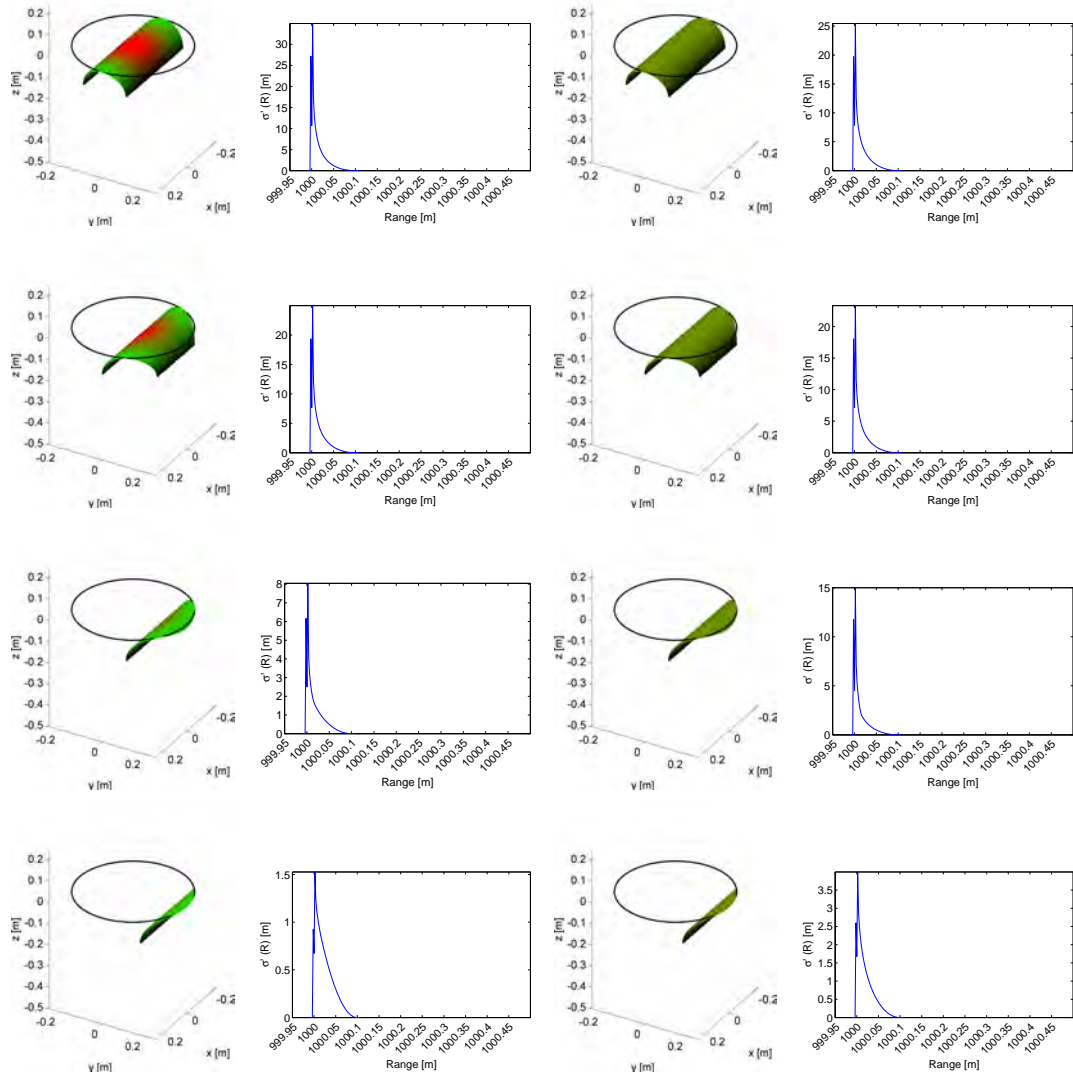


**Figure C.17:** Continuation of the dBSCS examples shown in Figure C.15 for radius  $r = 0.10$  m.

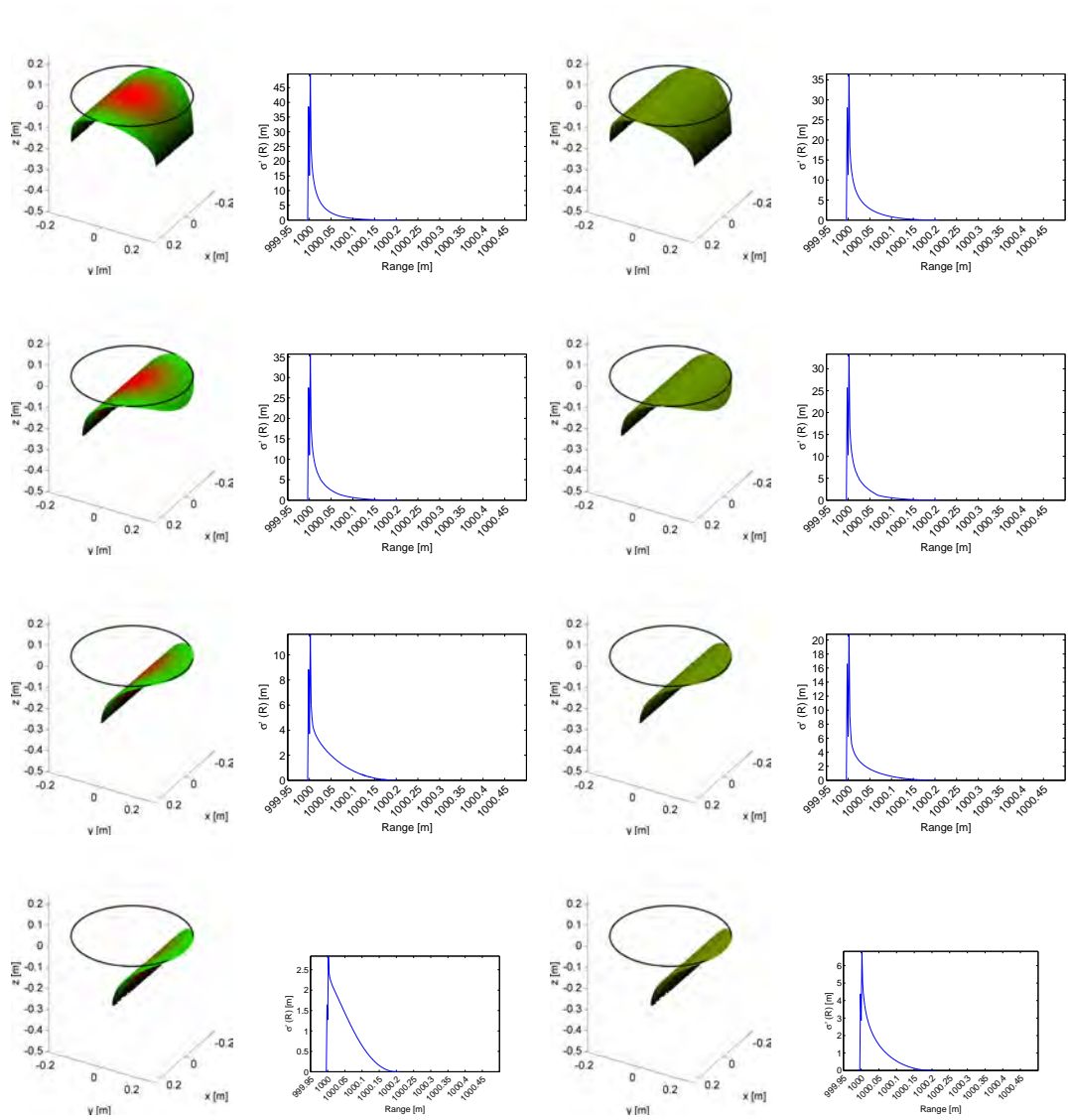


**Figure C.18:** Continuation of the dBCS examples shown in Figure C.15 for radius  $r = 0.2$  m.



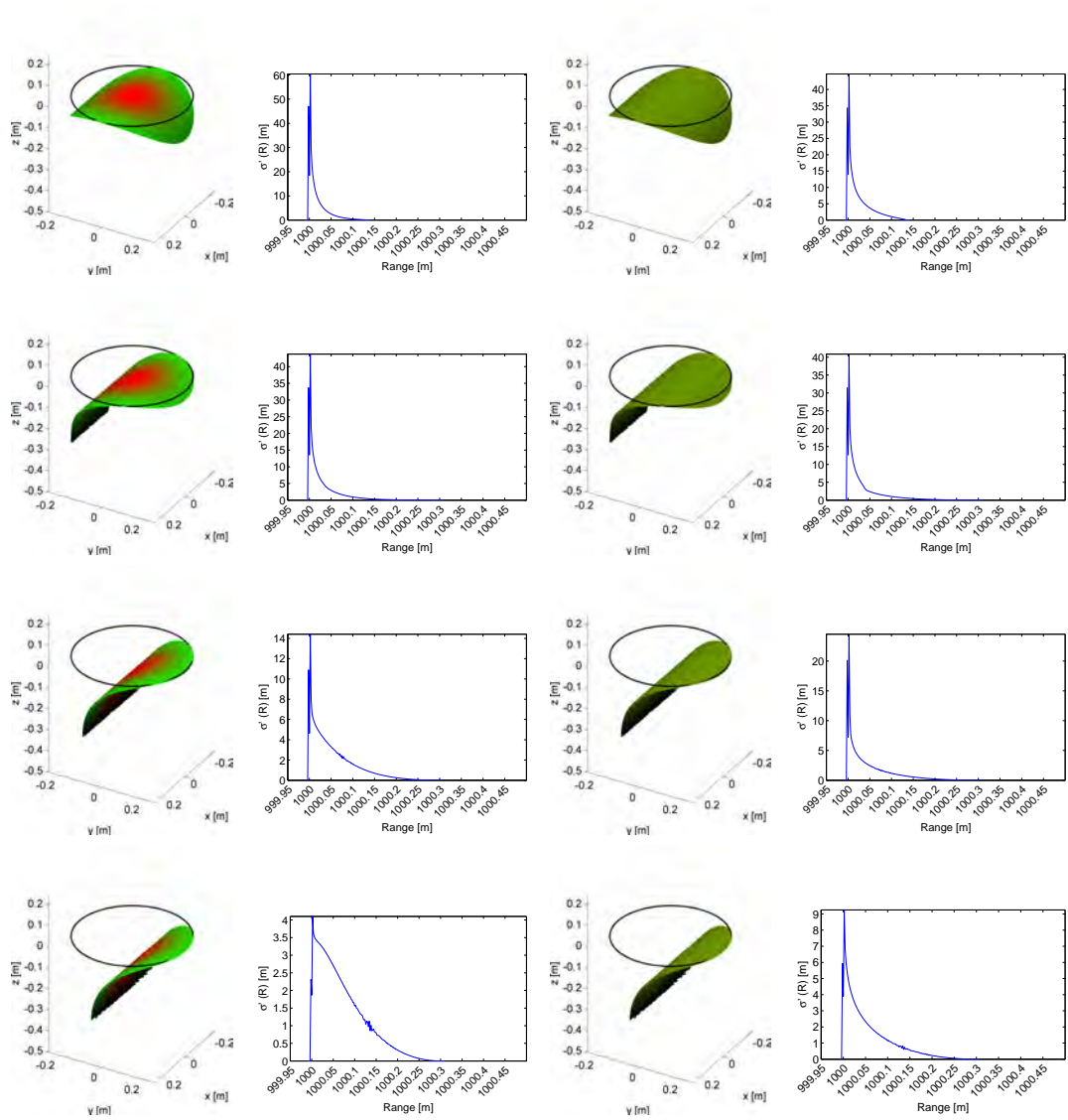


**Figure C.19:** Continuation of the dBCS examples shown in Figure C.15 for radius  $r = 0.30$  m.

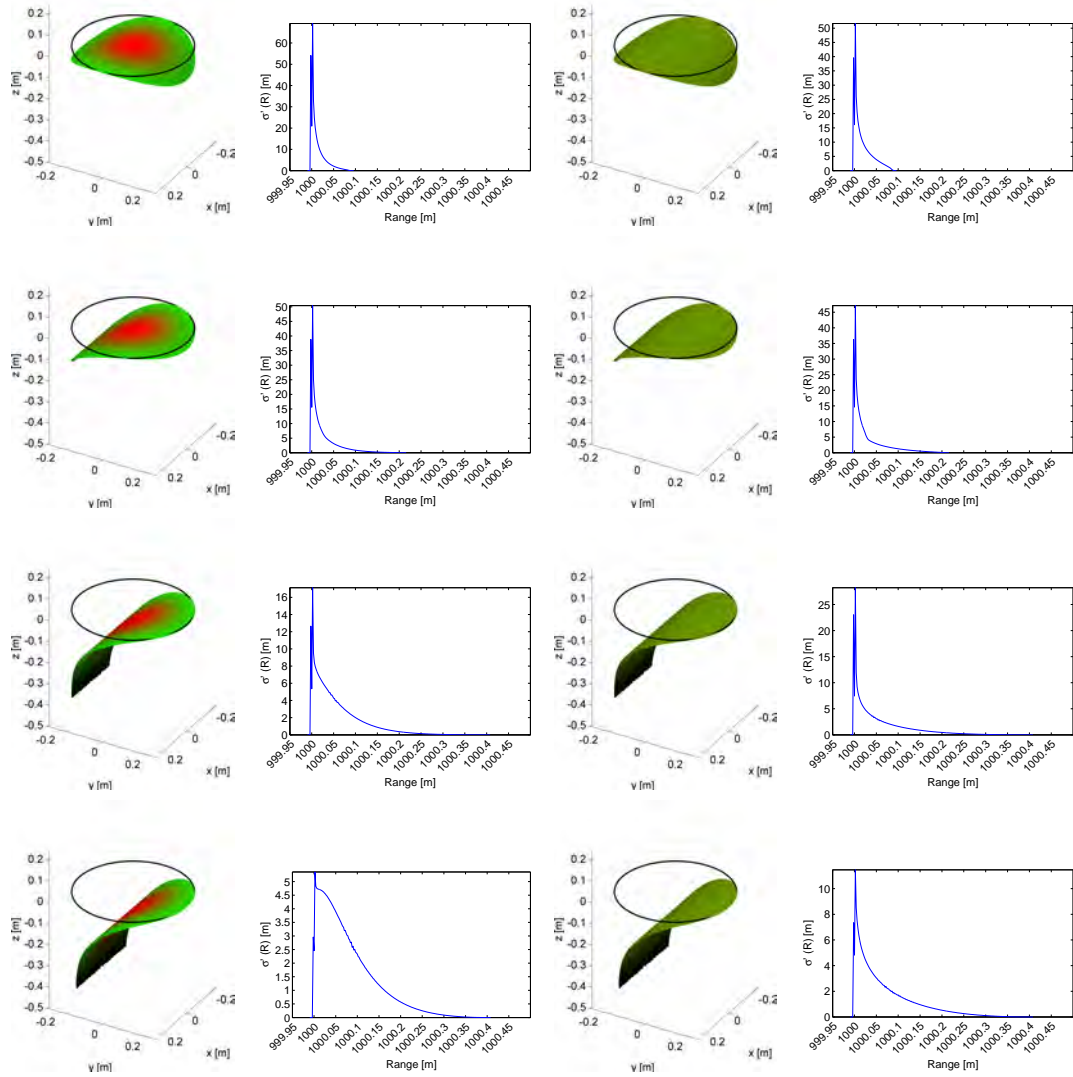


**Figure C.20:** Continuation of the dBCS examples shown in Figure C.15 for radius  $r = 0.40$  m.

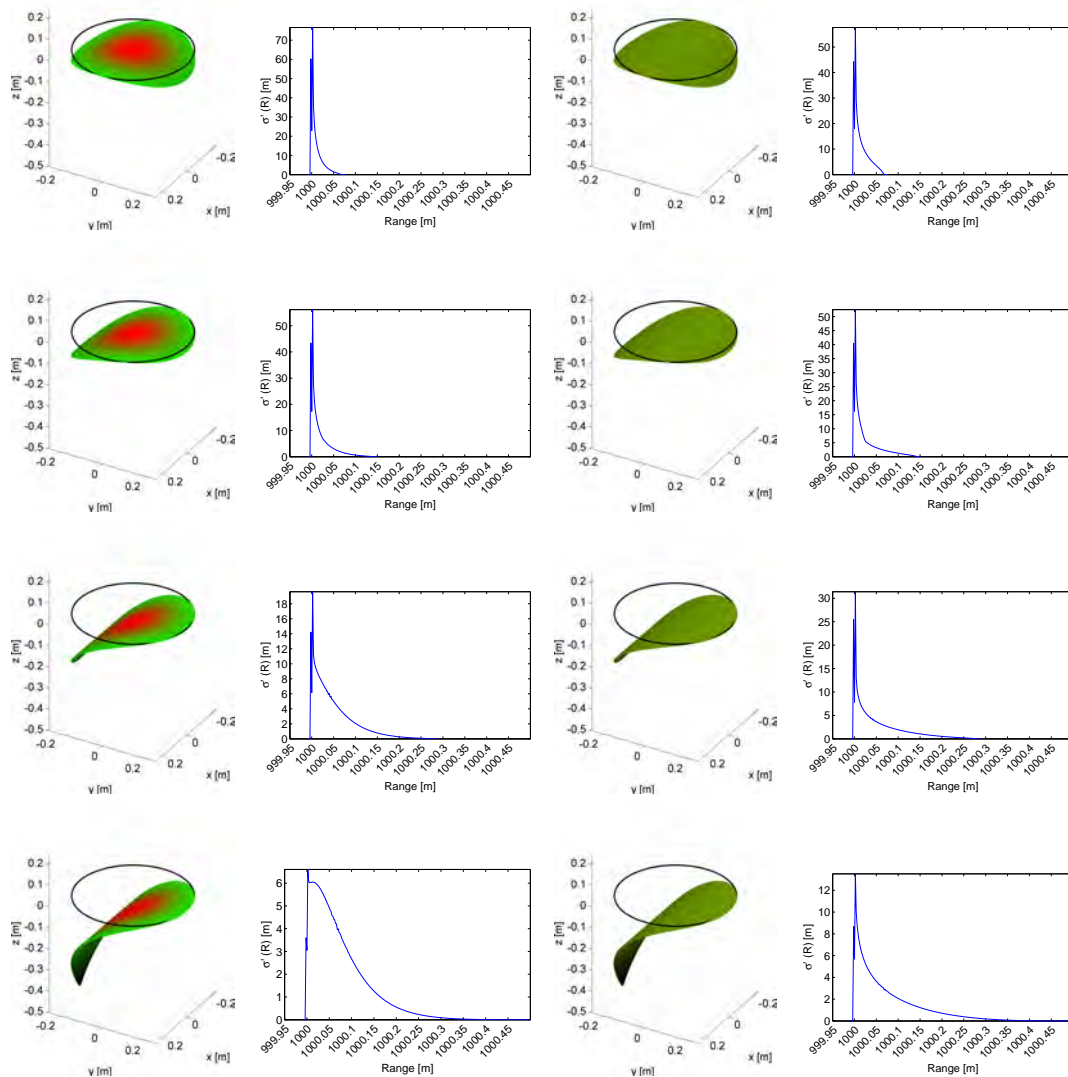


**Figure C.21:** Continuation of the dBCS examples shown in Figure C.15 for radius  $r = 0.50$  m.

## C.5 Simulated dBCS for sinusoidal Targets

### C.5.1 Circular Wavefronts

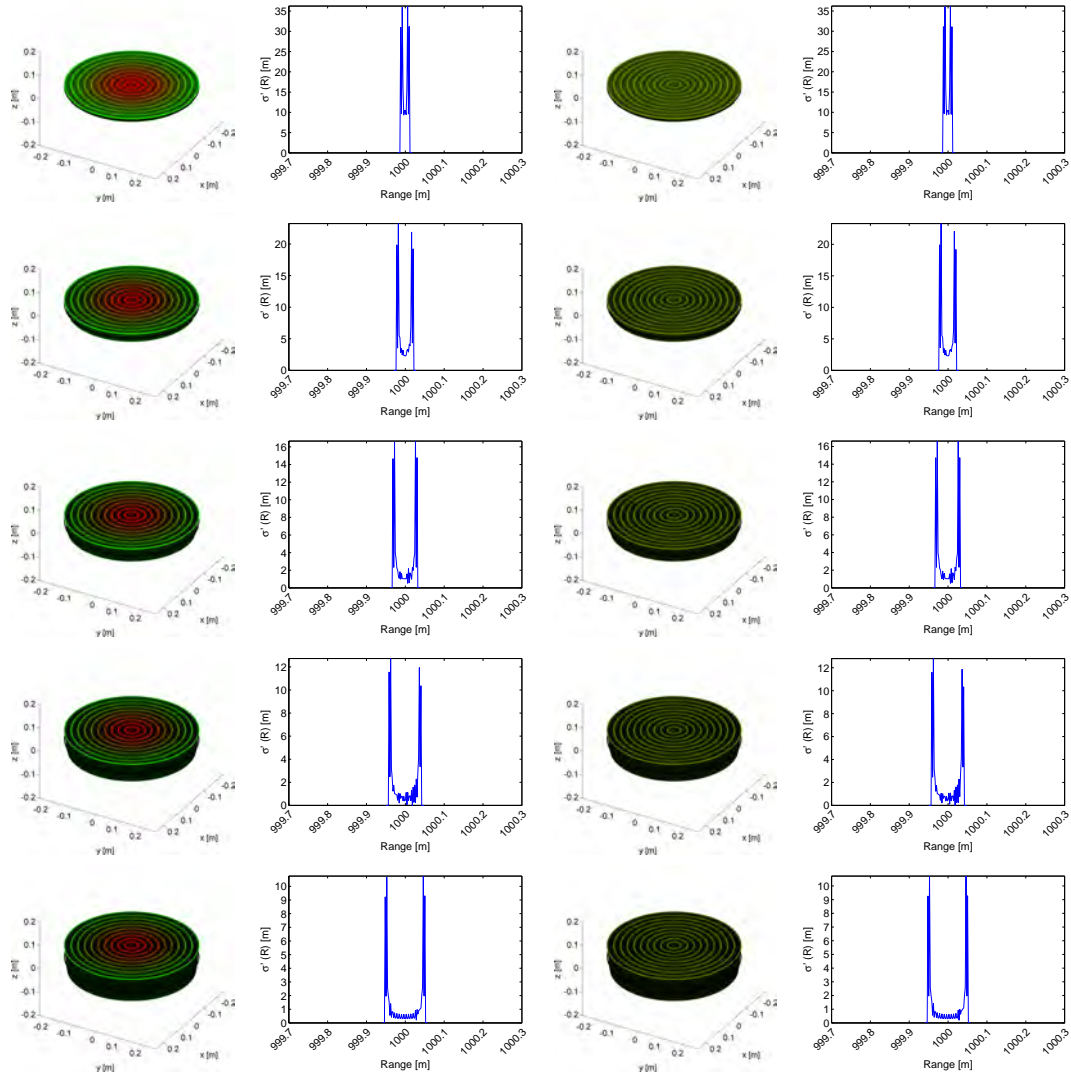


**Figure C.22:** From left to right: Illumination and backscatter geometry and dBCS for the Gaussian and uniform energy distribution within the laser footprint for a sinusoidal target with circular wavefronts; wavelength  $\lambda = 0.025$  m. The amplitude increases from 0.01 m (top) to 0.05 m (bottom) in steps of 0.01 m.

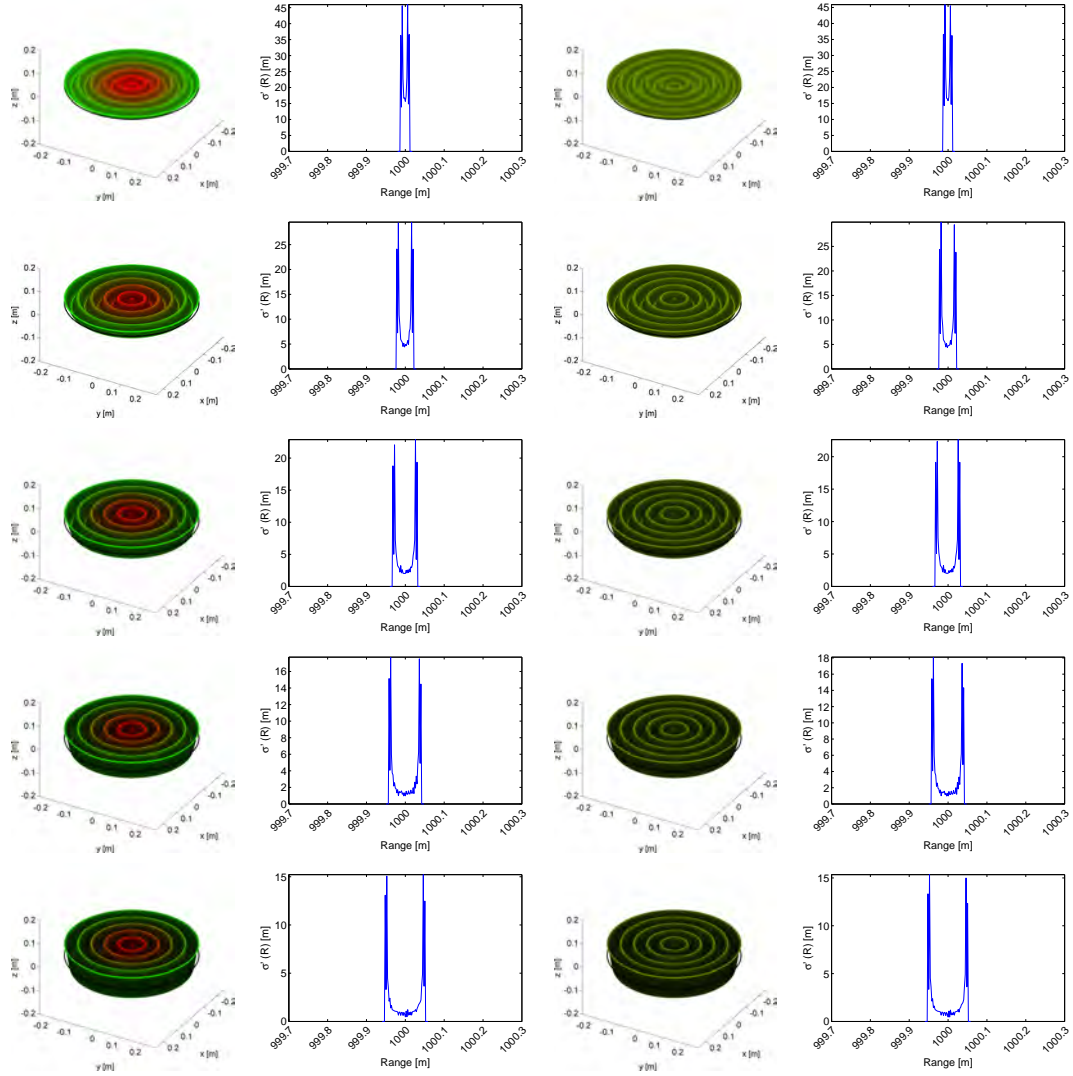


**Figure C.23:** From left to right: Illumination and backscatter geometry and dBCS for the Gaussian and uniform energy distribution within the laser footprint for a sinusoidal target with circular wavefronts; wavelength  $\lambda = 0.05$  m. The amplitude increases from 0.01 m (top) to 0.05 m (bottom) in steps of 0.01 m.

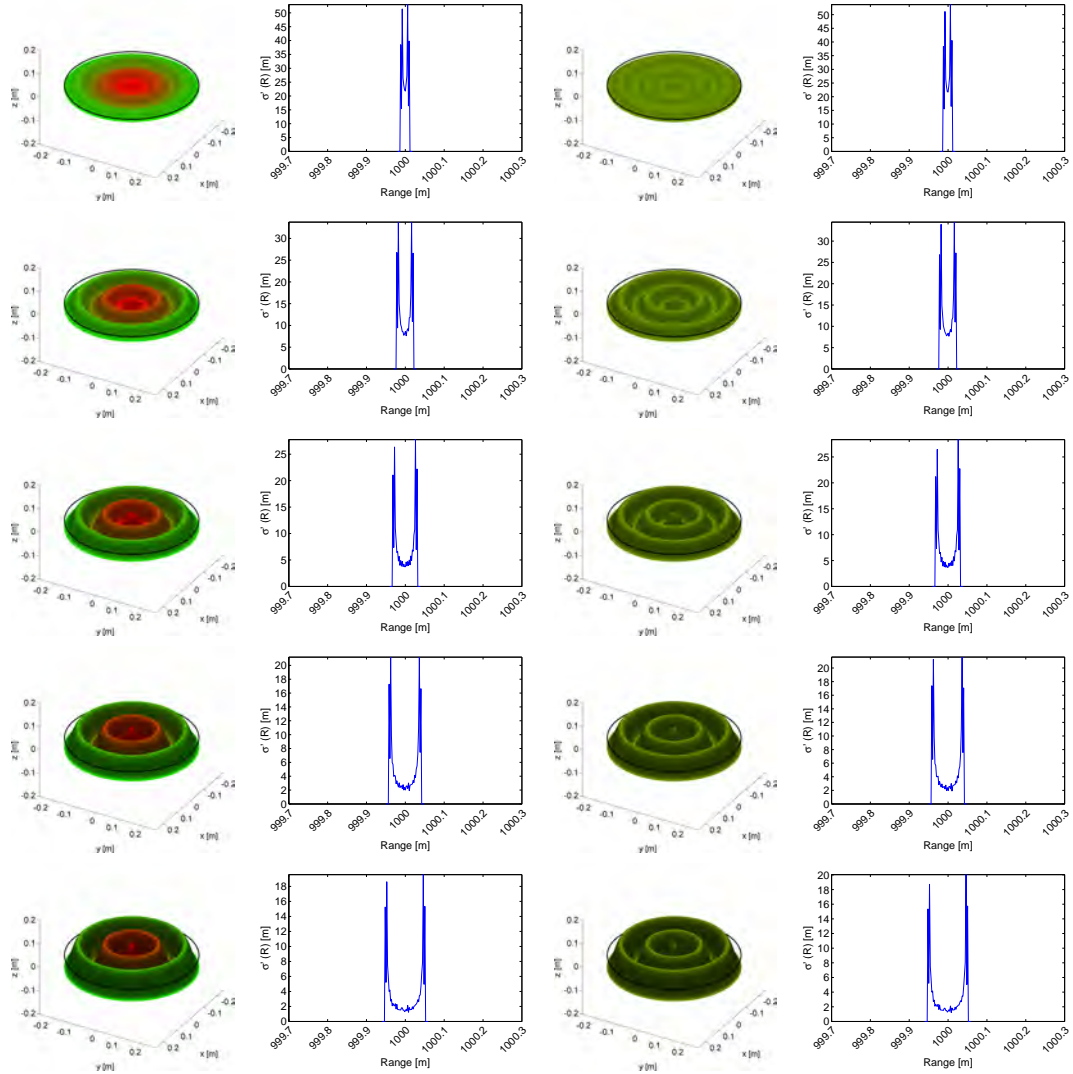


**Figure C.24:** From left to right: Illumination and backscatter geometry and dBCS for the Gaussian and uniform energy distribution within the laser footprint for a sinusoidal target with circular wavefronts; wavelength  $\lambda = 0.10$  m. The amplitude increases from 0.01 m (top) to 0.05 m (bottom) in steps of 0.01 m.

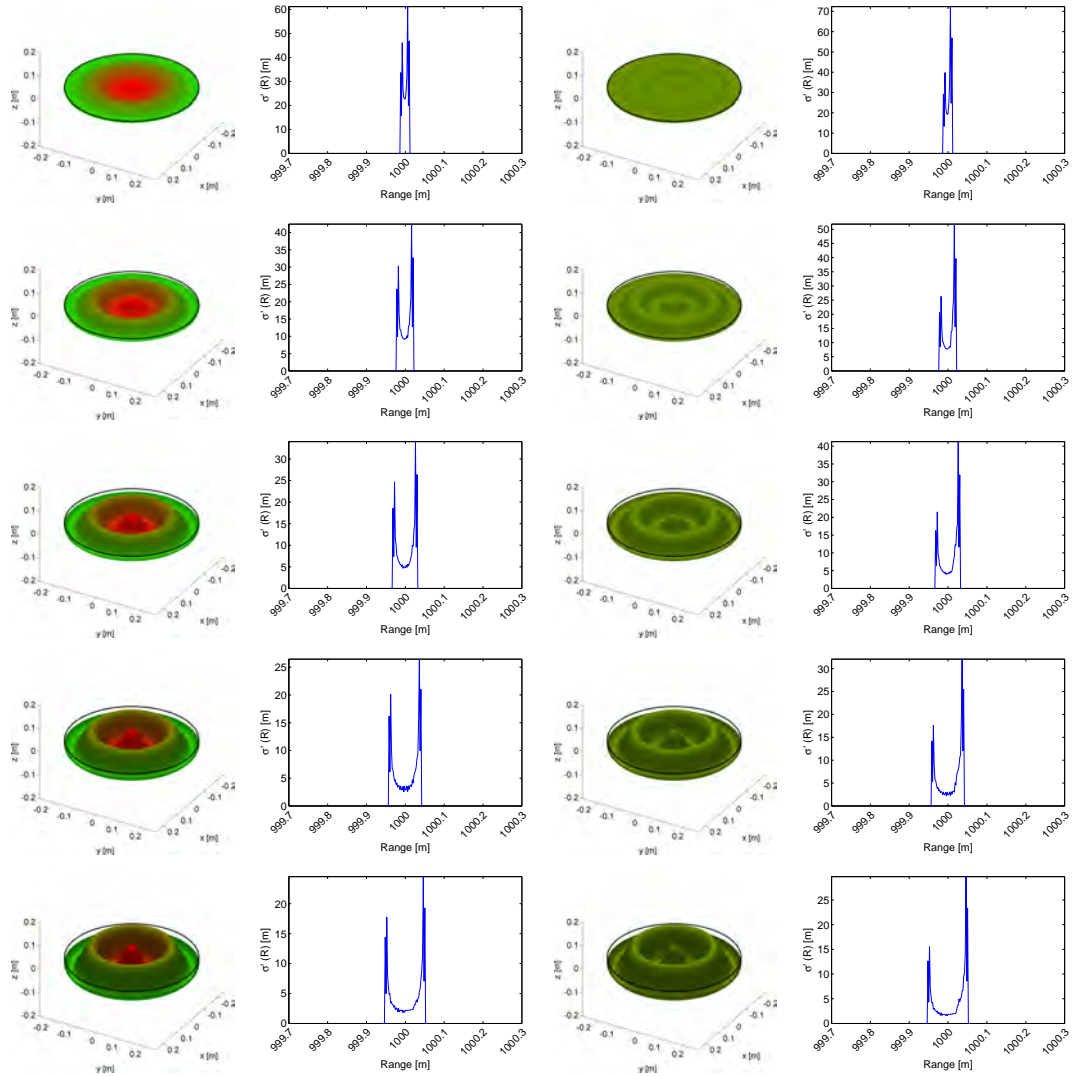


**Figure C.25:** From left to right: Illumination and backscatter geometry and dBCS for the Gaussian and uniform energy distribution within the laser footprint for a sinusoidal target with circular wavefronts; wavelength  $\lambda = 0.15$  m. The amplitude increases from 0.01 m (top) to 0.05 m (bottom) in steps of 0.01 m.

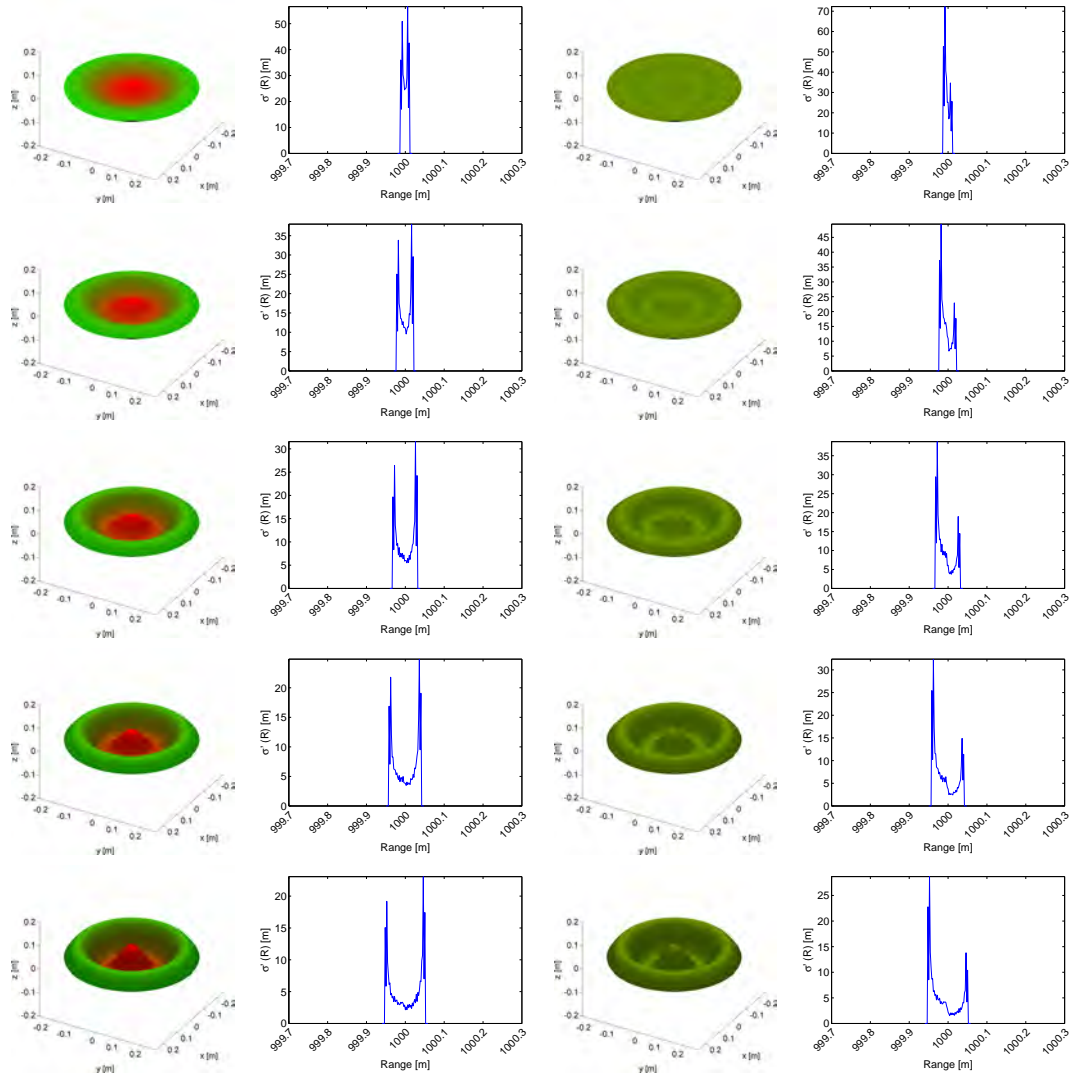


**Figure C.26:** From left to right: Illumination and backscatter geometry and dBCS for the Gaussian and uniform energy distribution within the laser footprint for a sinusoidal target with circular wavefronts; wavelength  $\lambda = 0.2$  m. The amplitude increases from 0.01 m (top) to 0.05 m (bottom) in steps of 0.01 m.



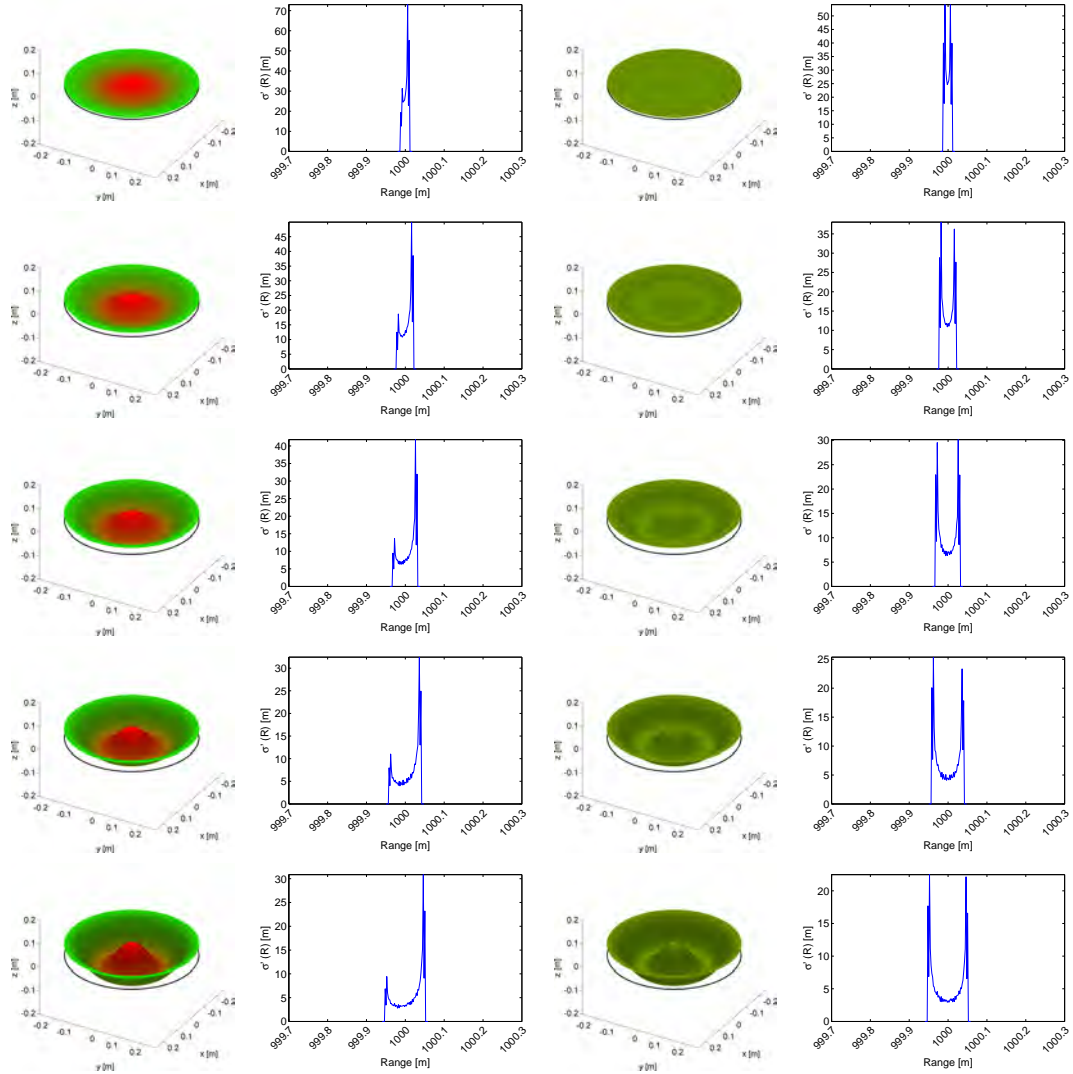


**Figure C.27:** From left to right: Illumination and backscatter geometry and dBCS for the Gaussian and uniform energy distribution within the laser footprint for a sinusoidal target with circular wavefronts; wavelength  $\lambda = 0.25$  m. The amplitude increases from 0.01 m (top) to 0.05 m (bottom) in steps of 0.01 m.

## C.5.2 Parallel Wavefronts

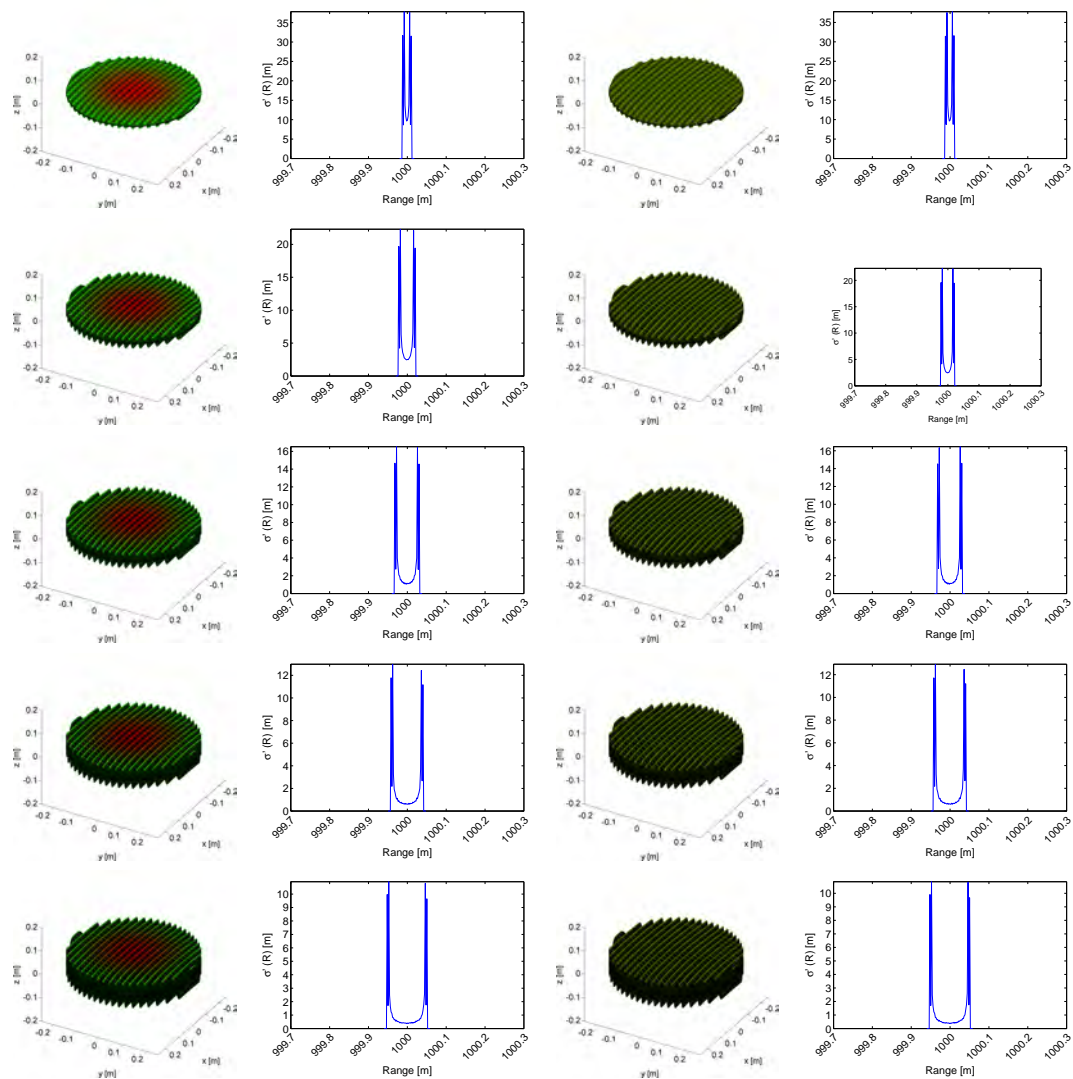


**Figure C.28:** From left to right: Illumination and backscatter geometry and dBCS for the Gaussian and uniform energy distribution within the laser footprint for a sinusoidal target with parallel wavefronts; wavelength  $\lambda = 0.025$  m. The amplitude increases from 0.01 m (top) to 0.05 m (bottom) in steps of 0.01 m.

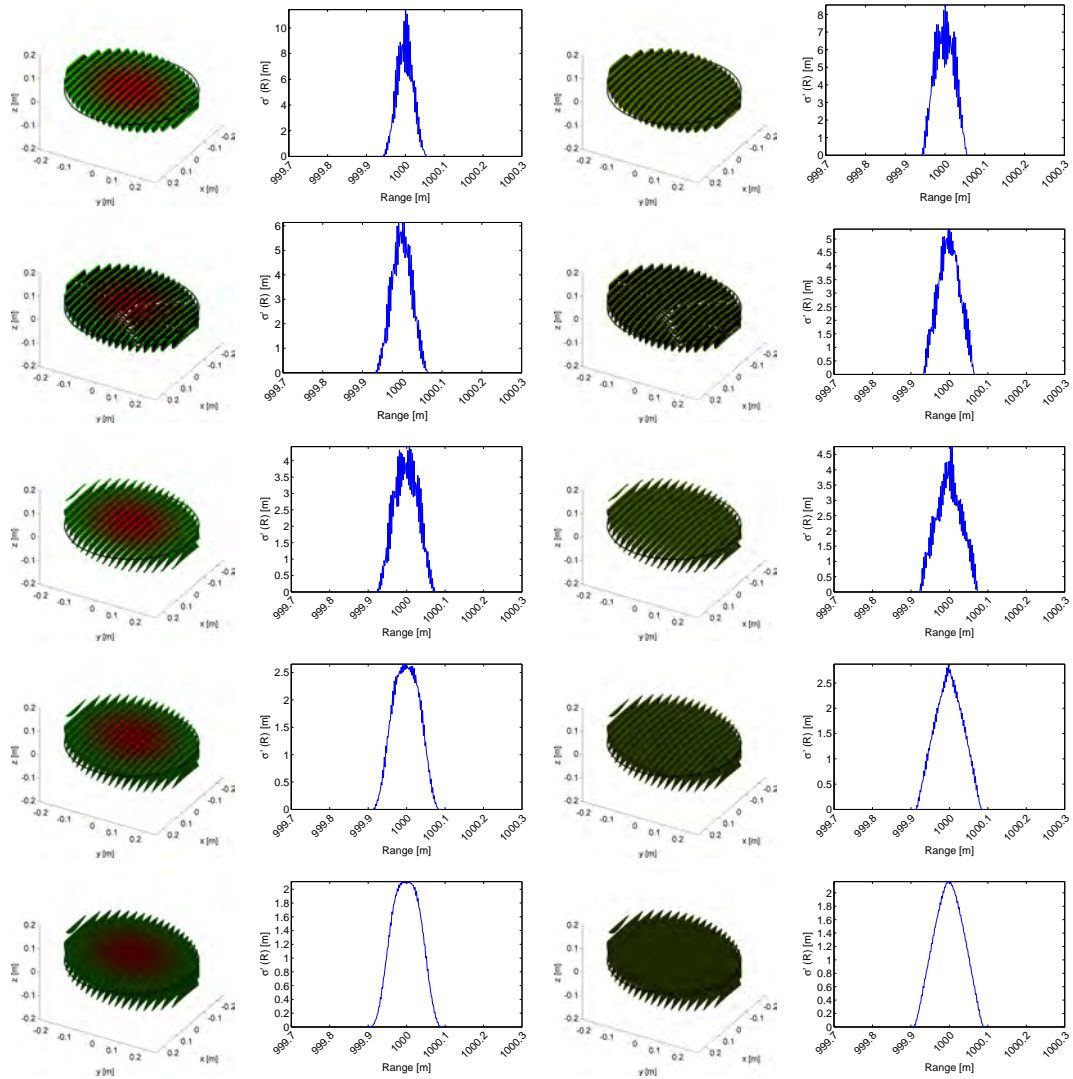


**Figure C.29:** From left to right: Illumination and backscatter geometry and dBCS for the Gaussian and uniform energy distribution within the laser footprint for a tilted sinusoidal target with parallel wavefronts; wavelength  $\lambda = 0.025$  m, tilt angle  $10^\circ$ . The amplitude increases from 0.01 m (top) to 0.05 m (bottom) in steps of 0.01 m.

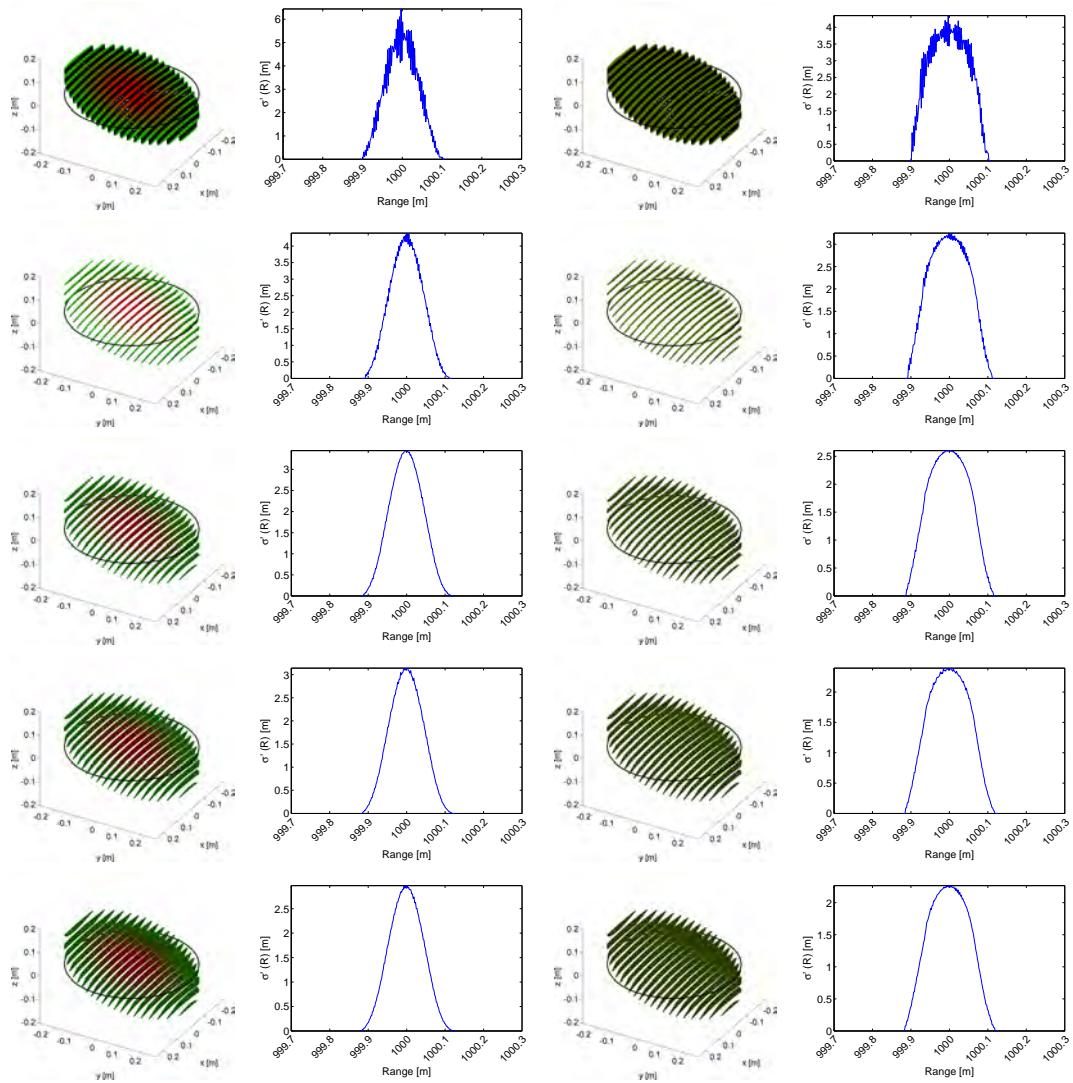


**Figure C.30:** From left to right: Illumination and backscatter geometry and dBCS for the Gaussian and uniform energy distribution within the laser footprint for a tilted sinusoidal target with parallel wavefronts; wavelength  $\lambda = 0.025$  m, tilt angle  $20^\circ$ . The amplitude increases from 0.01 m (top) to 0.05 m (bottom) in steps of 0.01 m.

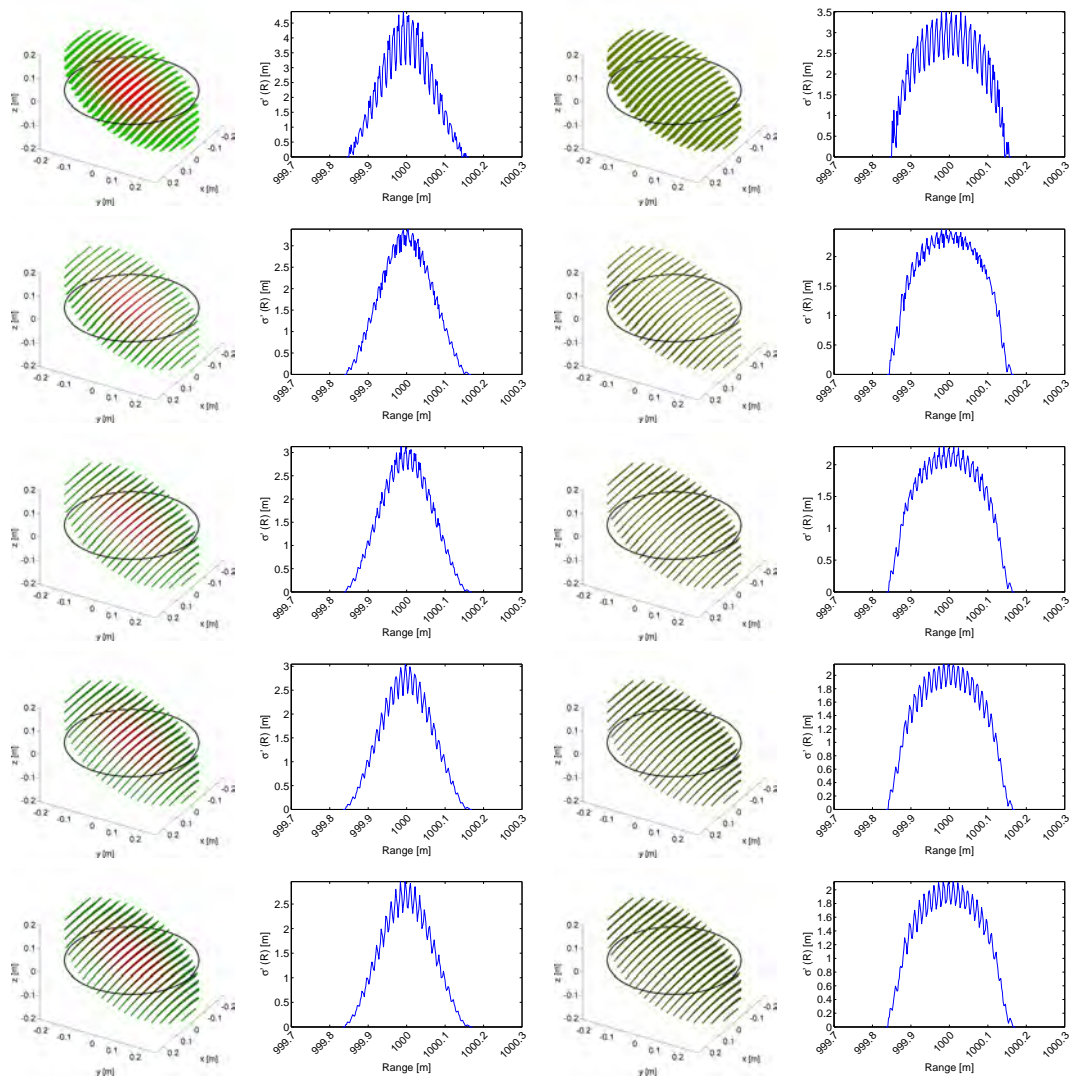


**Figure C.31:** From left to right: Illumination and backscatter geometry and dBCS for the Gaussian and uniform energy distribution within the laser footprint for a tilted sinusoidal target with parallel wavefronts; wavelength  $\lambda = 0.025$  m, tilt angle  $30^\circ$ . The amplitude increases from 0.01 m (top) to 0.05 m (bottom) in steps of 0.01 m.

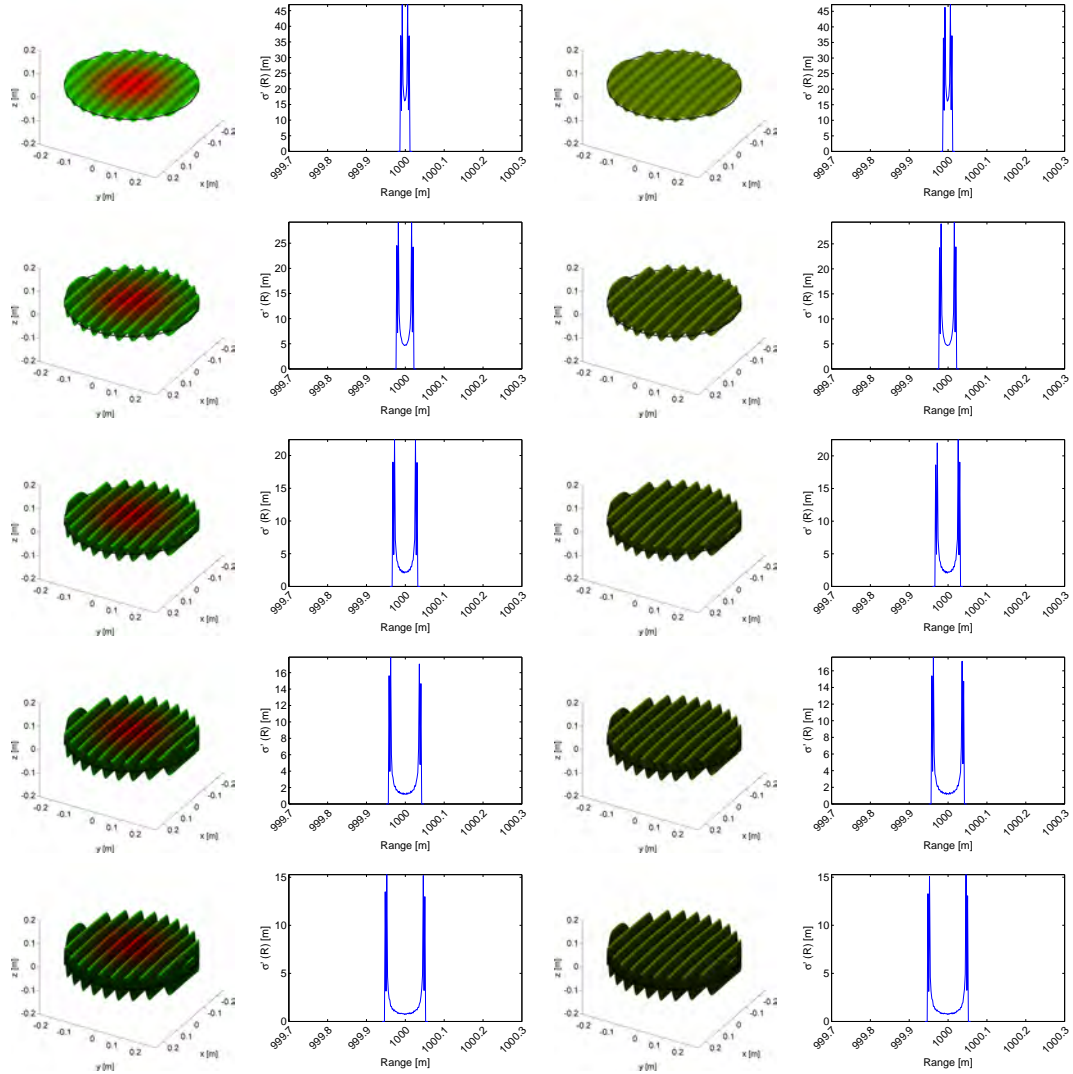


**Figure C.32:** From left to right: Illumination and backscatter geometry and dBCS for the Gaussian and uniform energy distribution within the laser footprint for a sinusoidal target with parallel wavefronts; wavelength  $\lambda = 0.05$  m. The amplitude increases from 0.01 m (top) to 0.05 m (bottom) in steps of 0.01 m.

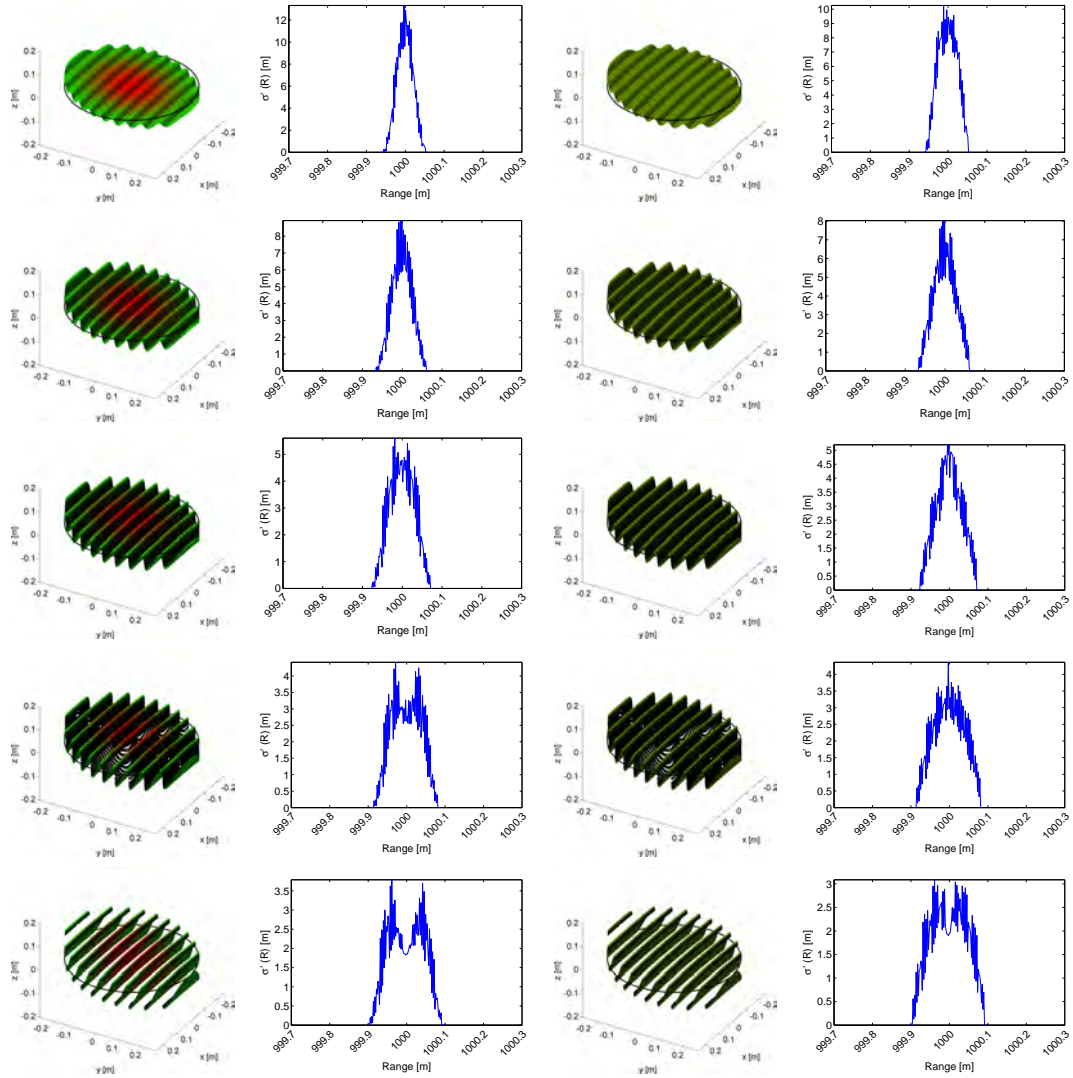


**Figure C.33:** From left to right: Illumination and backscatter geometry and dBCS for the Gaussian and uniform energy distribution within the laser footprint for a tilted sinusoidal target with parallel wavefronts; wavelength  $\lambda = 0.05$  m, tilt angle  $10^\circ$ . The amplitude increases from 0.01 m (top) to 0.05 m (bottom) in steps of 0.01 m.

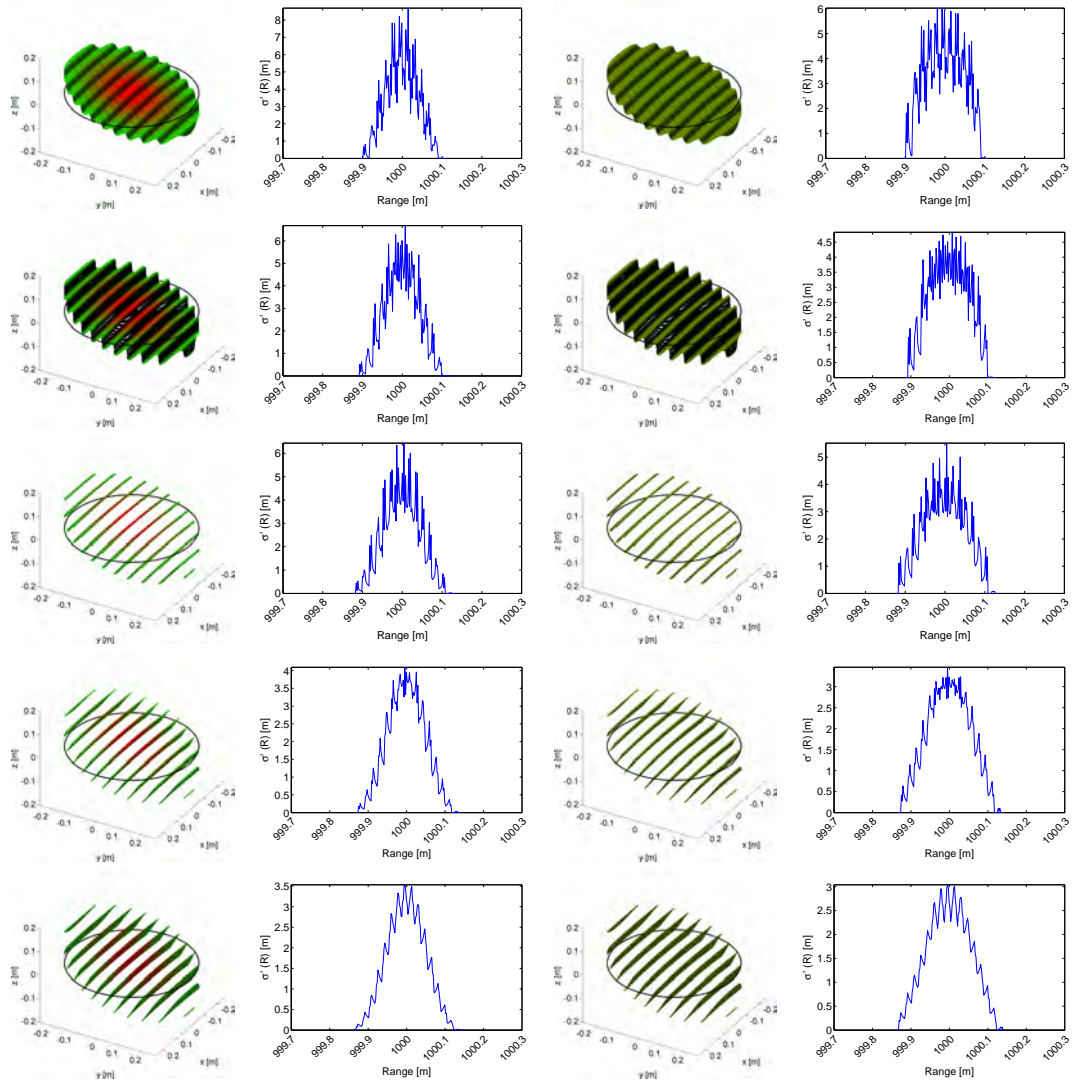


**Figure C.34:** From left to right: Illumination and backscatter geometry and DBCS for the Gaussian and uniform energy distribution within the laser footprint for a tilted sinusoidal target with parallel wavefronts; wavelength  $\lambda = 0.05$  m, tilt angle  $20^\circ$ . The amplitude increases from 0.01 m (top) to 0.05 m (bottom) in steps of 0.01 m.



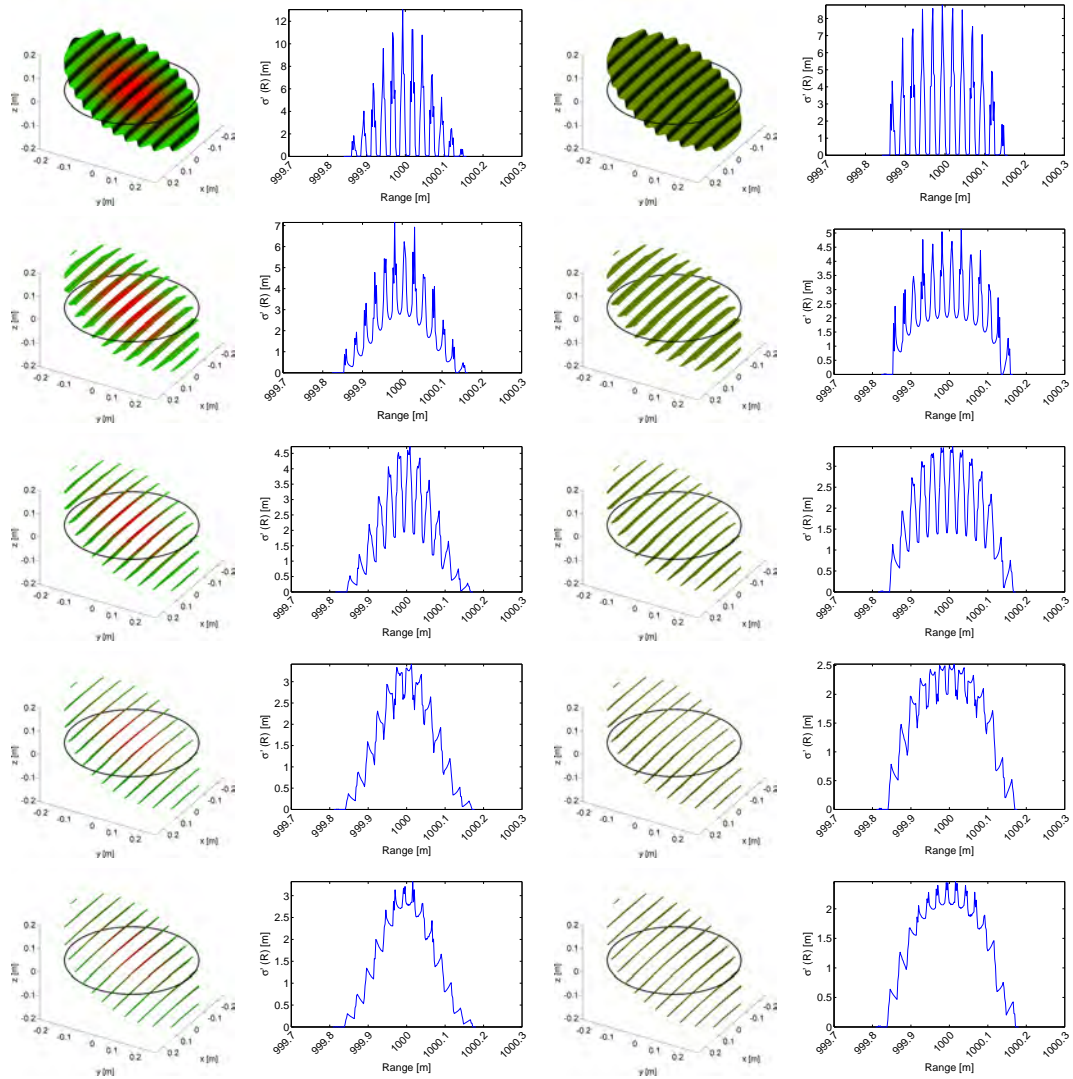


**Figure C.35:** From left to right: Illumination and backscatter geometry and dBCS for the Gaussian and uniform energy distribution within the laser footprint for a tilted sinusoidal target with parallel wavefronts; wavelength  $\lambda = 0.05$  m, tilt angle  $30^\circ$ . The amplitude increases from 0.01 m (top) to 0.05 m (bottom) in steps of 0.01 m.

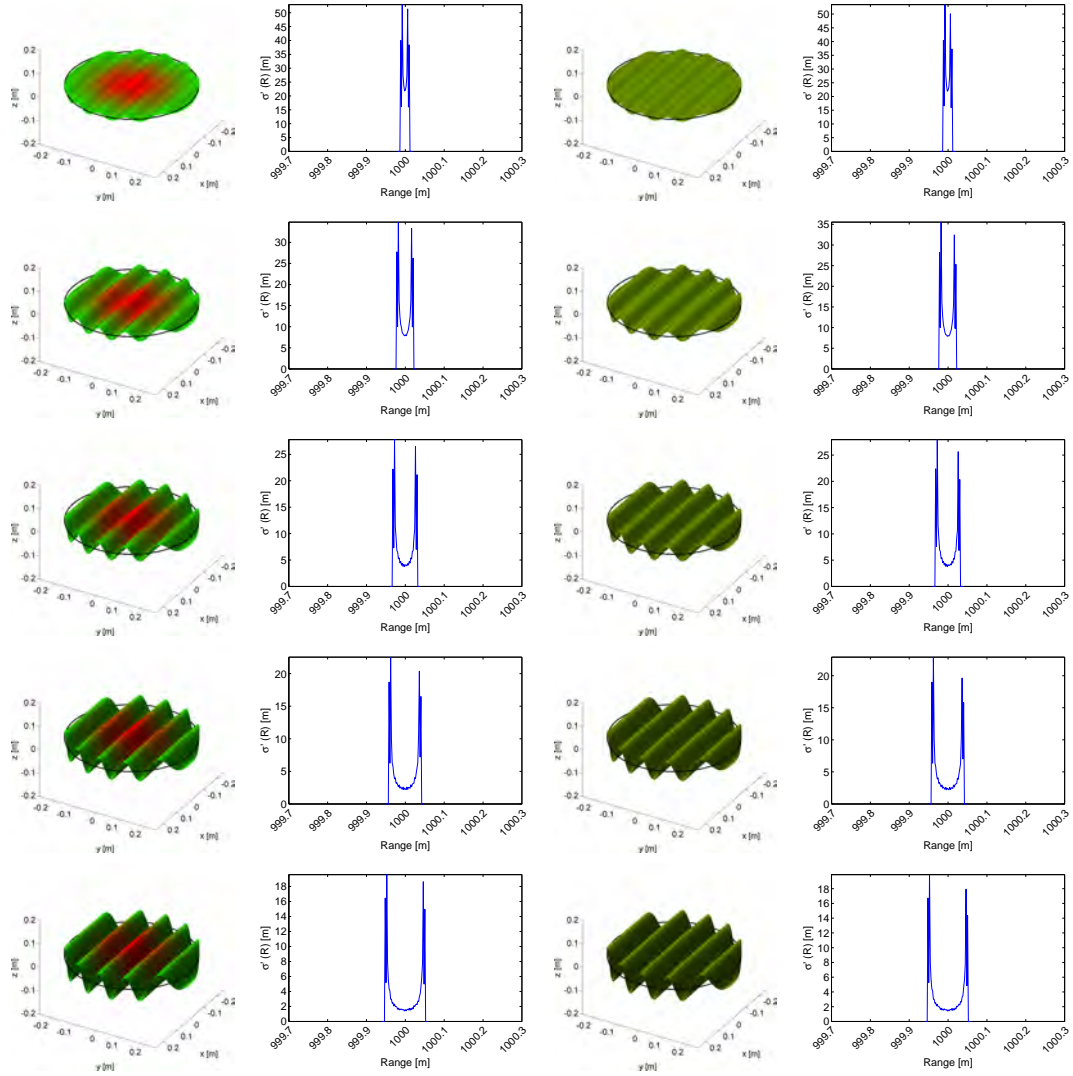


**Figure C.36:** From left to right: Illumination and backscatter geometry and dBCS for the Gaussian and uniform energy distribution within the laser footprint for a sinusoidal target with parallel wavefronts; wavelength  $\lambda = 0.1$  m. The amplitude increases from 0.01 m (top) to 0.05 m (bottom) in steps of 0.01 m.

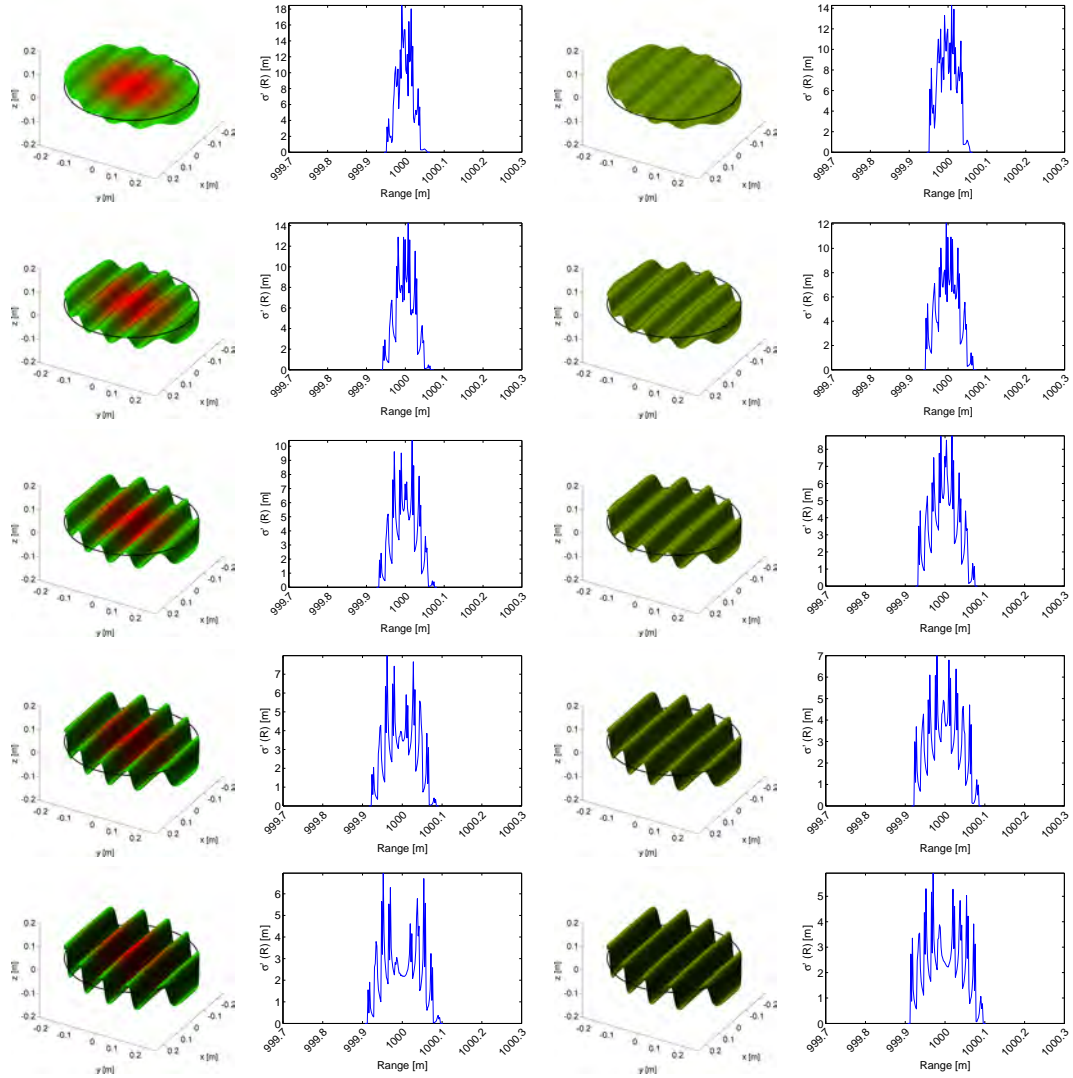


**Figure C.37:** From left to right: Illumination and backscatter geometry and dBDS for the Gaussian and uniform energy distribution within the laser footprint for a tilted sinusoidal target with parallel wavefronts; wavelength  $\lambda = 0.1$  m, tilt angle  $10^\circ$ . The amplitude increases from 0.01 m (top) to 0.05 m (bottom) in steps of 0.01 m.

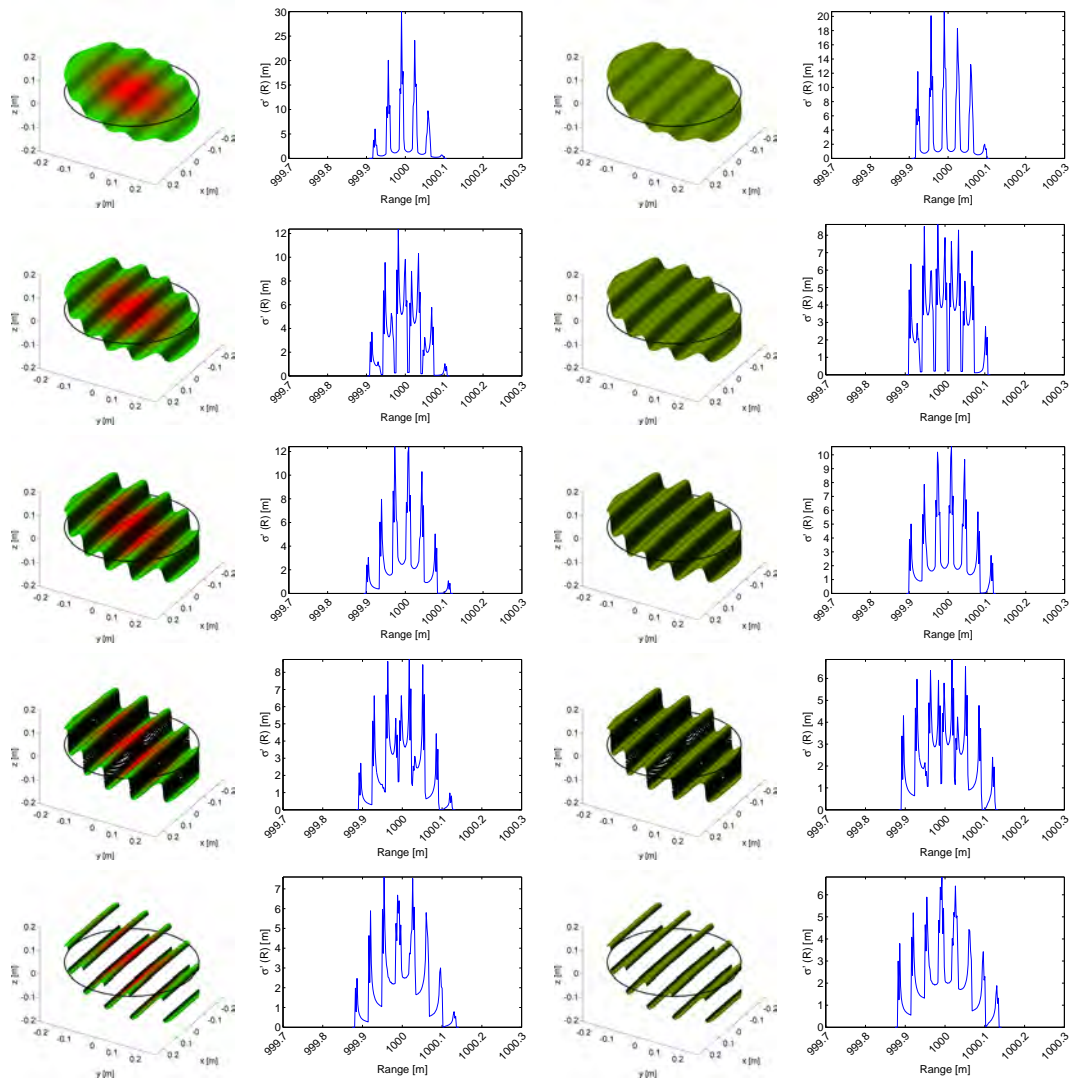


**Figure C.38:** From left to right: Illumination and backscatter geometry and dBCS for the Gaussian and uniform energy distribution within the laser footprint for a tilted sinusoidal target with parallel wavefronts; wavelength  $\lambda = 0.1$  m, tilt angle  $20^\circ$ . The amplitude increases from 0.01 m (top) to 0.05 m (bottom) in steps of 0.01 m.

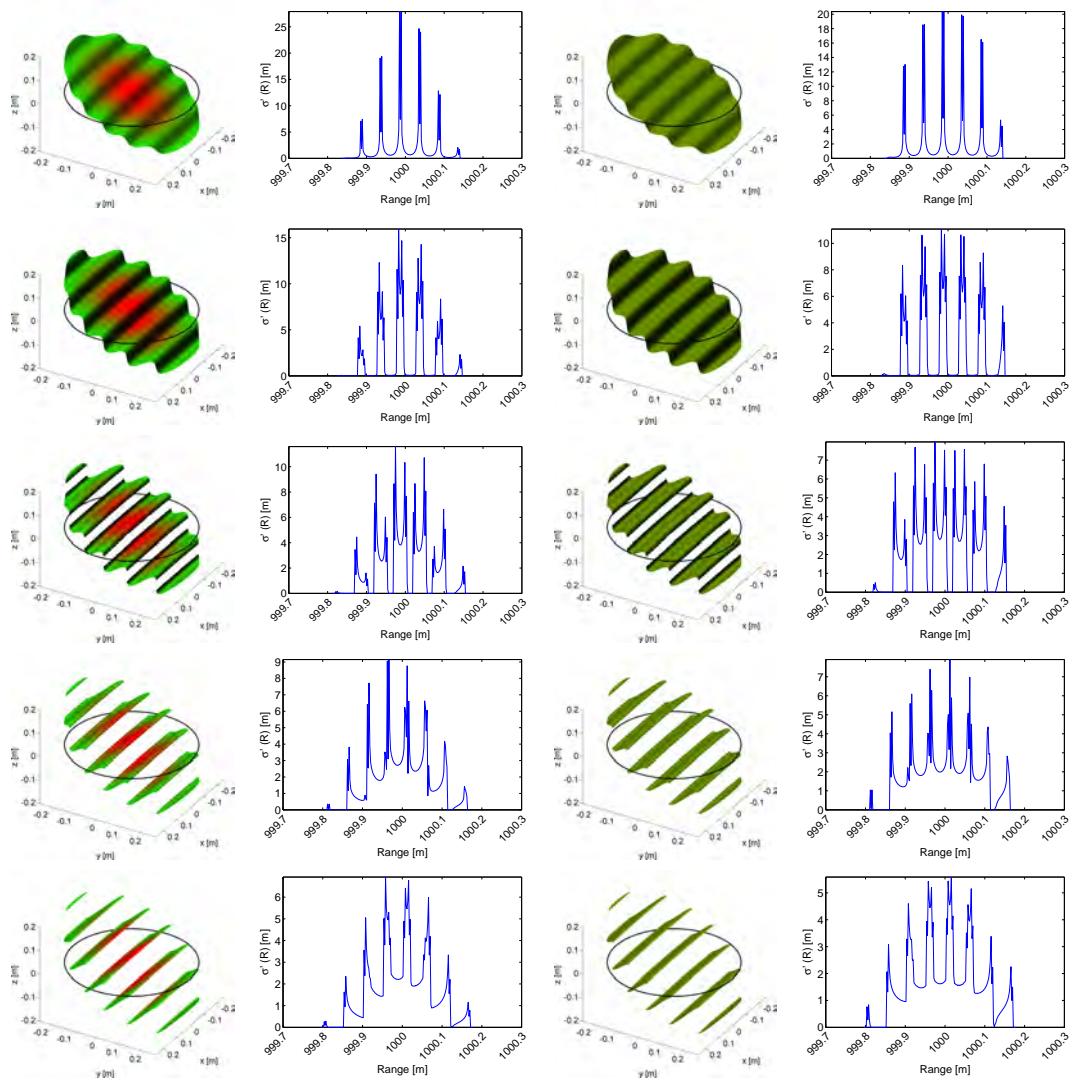


**Figure C.39:** From left to right: Illumination and backscatter geometry and dBCS for the Gaussian and uniform energy distribution within the laser footprint for a tilted sinusoidal target with parallel wavefronts; wavelength  $\lambda = 0.1$  m, tilt angle  $30^\circ$ . The amplitude increases from 0.01 m (top) to 0.05 m (bottom) in steps of 0.01 m.

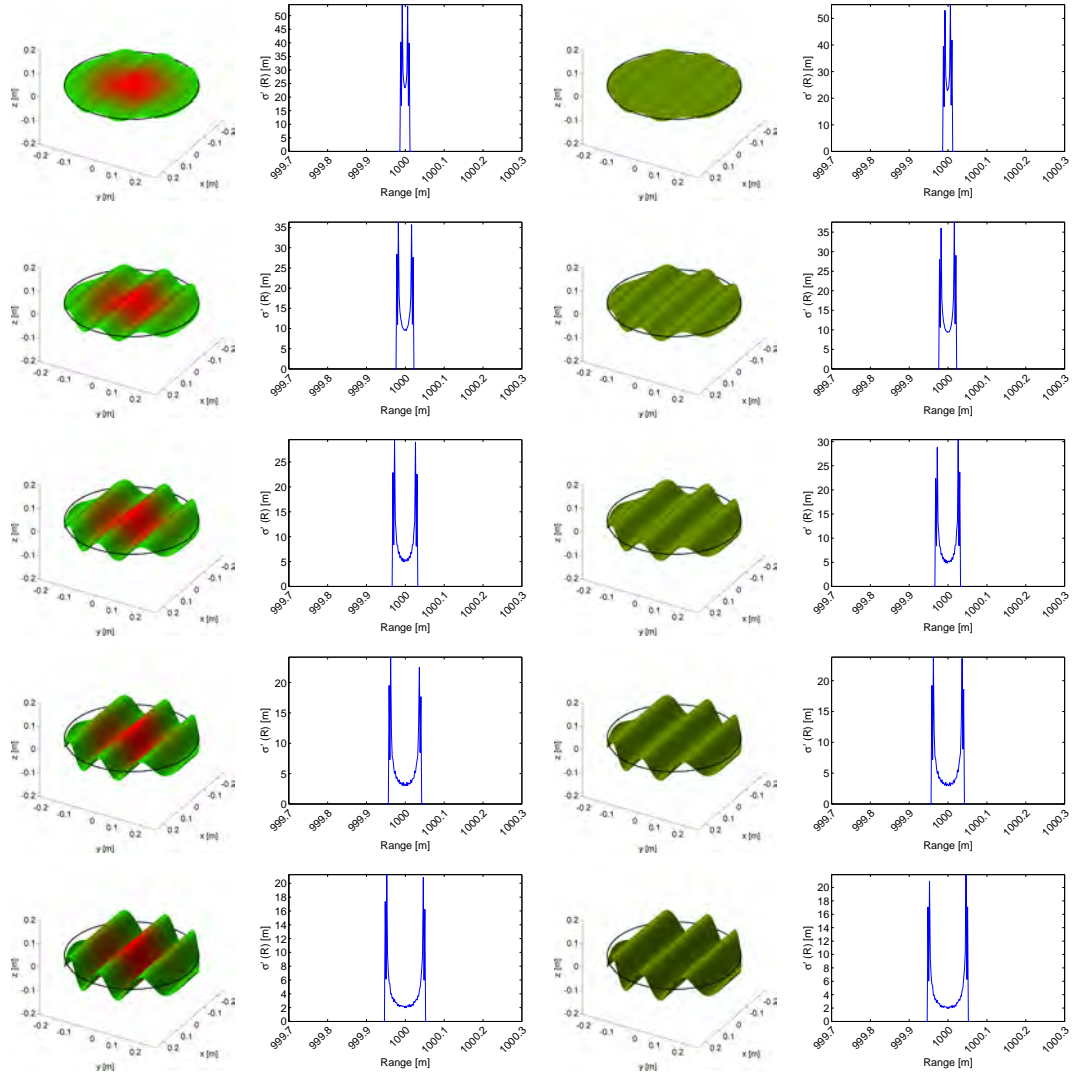


**Figure C.40:** From left to right: Illumination and backscatter geometry and dBCS for the Gaussian and uniform energy distribution within the laser footprint for a sinusoidal target with parallel wavefronts; wavelength  $\lambda = 0.15$  m. The amplitude increases from 0.01 m (top) to 0.05 m (bottom) in steps of 0.01 m.

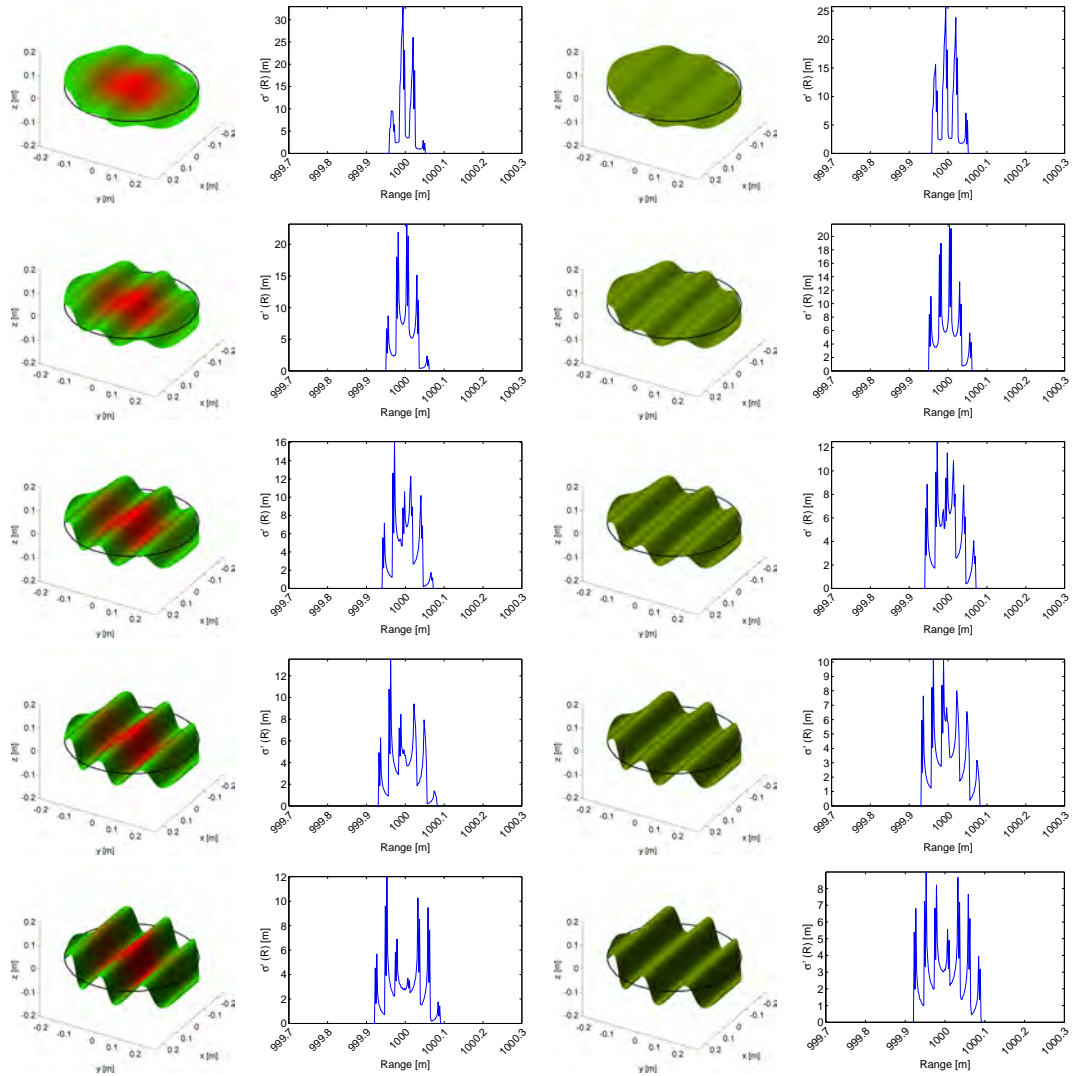


**Figure C.41:** From left to right: Illumination and backscatter geometry and dBCS for the Gaussian and uniform energy distribution within the laser footprint for a tilted sinusoidal target with parallel wavefronts; wavelength  $\lambda = 0.15$  m, tilt angle  $10^\circ$ . The amplitude increases from 0.01 m (top) to 0.05 m (bottom) in steps of 0.01 m.

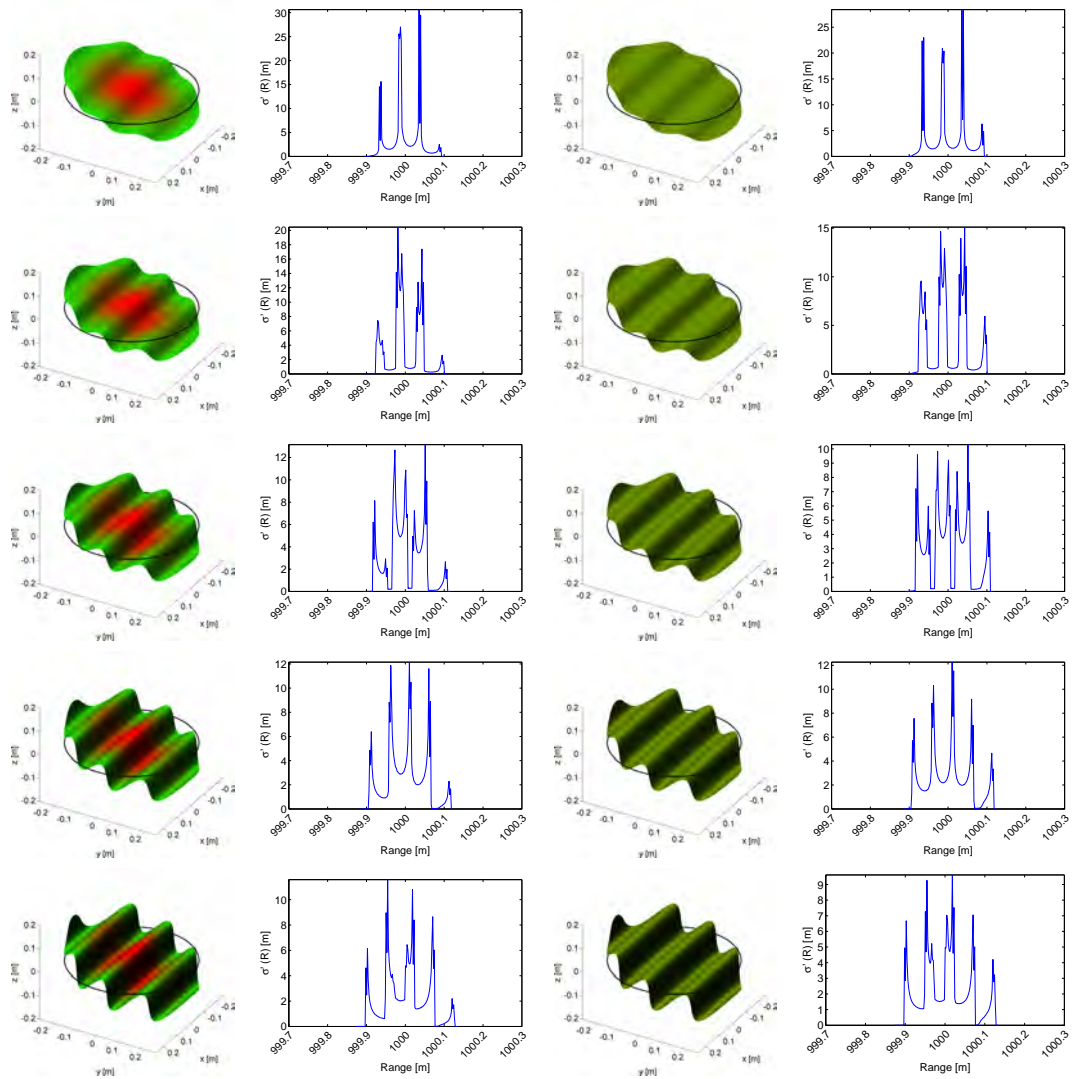


**Figure C.42:** From left to right: Illumination and backscatter geometry and dBCS for the Gaussian and uniform energy distribution within the laser footprint for a tilted sinusoidal target with parallel wavefronts; wavelength  $\lambda = 0.15$  m, tilt angle  $20^\circ$ . The amplitude increases from 0.01 m (top) to 0.05 m (bottom) in steps of 0.01 m.



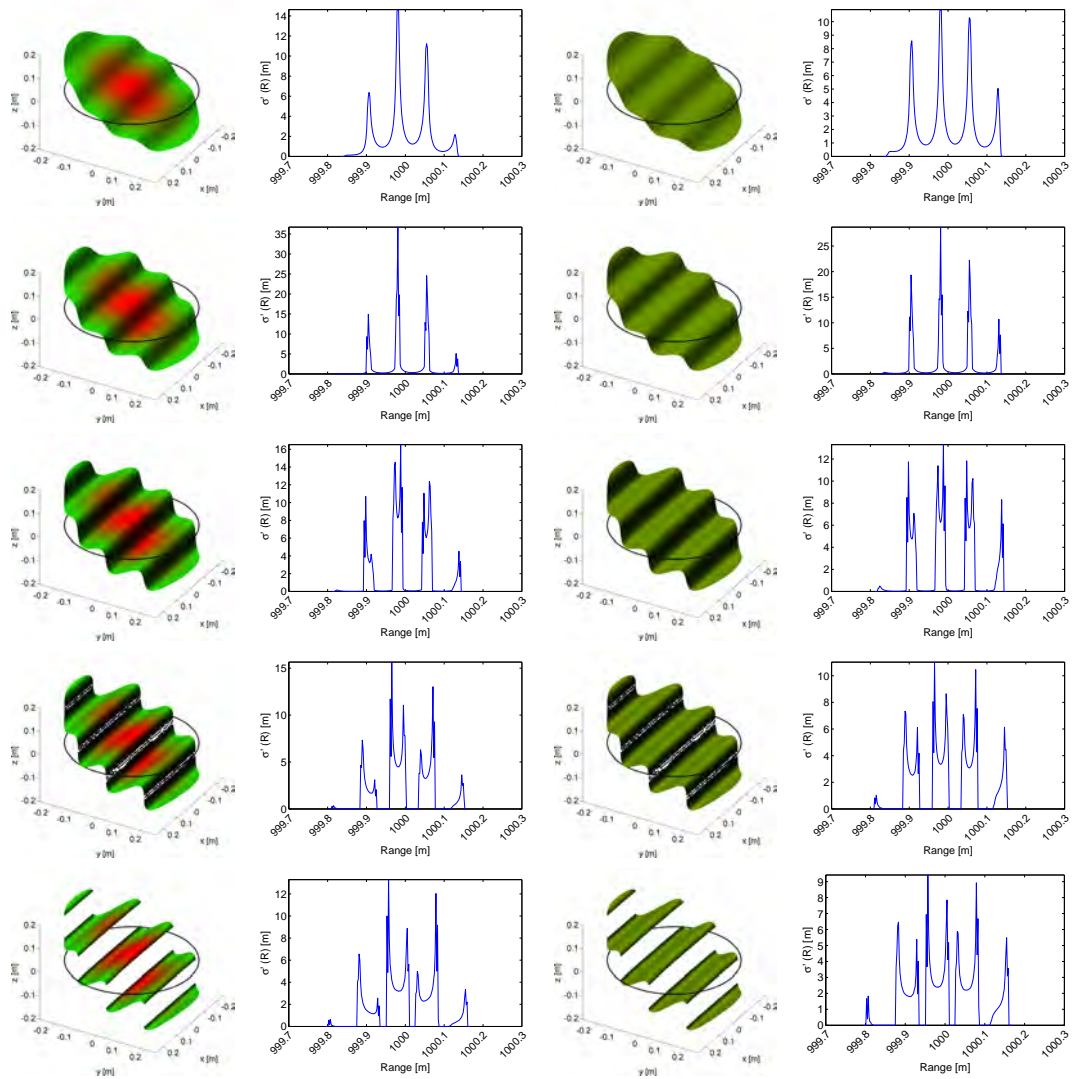


**Figure C.43:** From left to right: Illumination and backscatter geometry and dBCS for the Gaussian and uniform energy distribution within the laser footprint for a tilted sinusoidal target with parallel wavefronts; wavelength  $\lambda = 0.15$  m, tilt angle  $30^\circ$ . The amplitude increases from 0.01 m (top) to 0.05 m (bottom) in steps of 0.01 m.

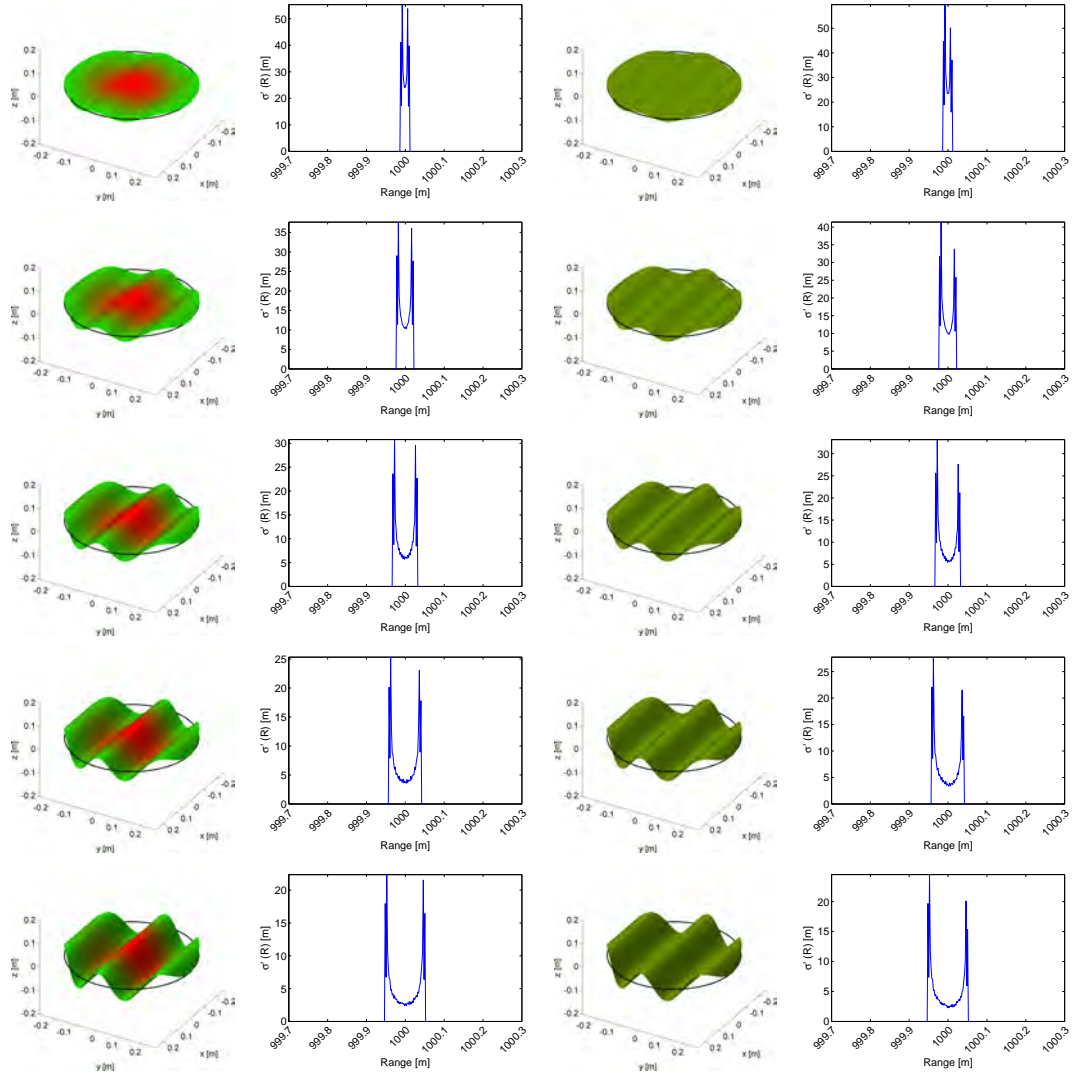


**Figure C.44:** From left to right: Illumination and backscatter geometry and dBCS for the Gaussian and uniform energy distribution within the laser footprint for a sinusoidal target with parallel wavefronts; wavelength  $\lambda = 0.2$  m. The amplitude increases from 0.01 m (top) to 0.05 m (bottom) in steps of 0.01 m.

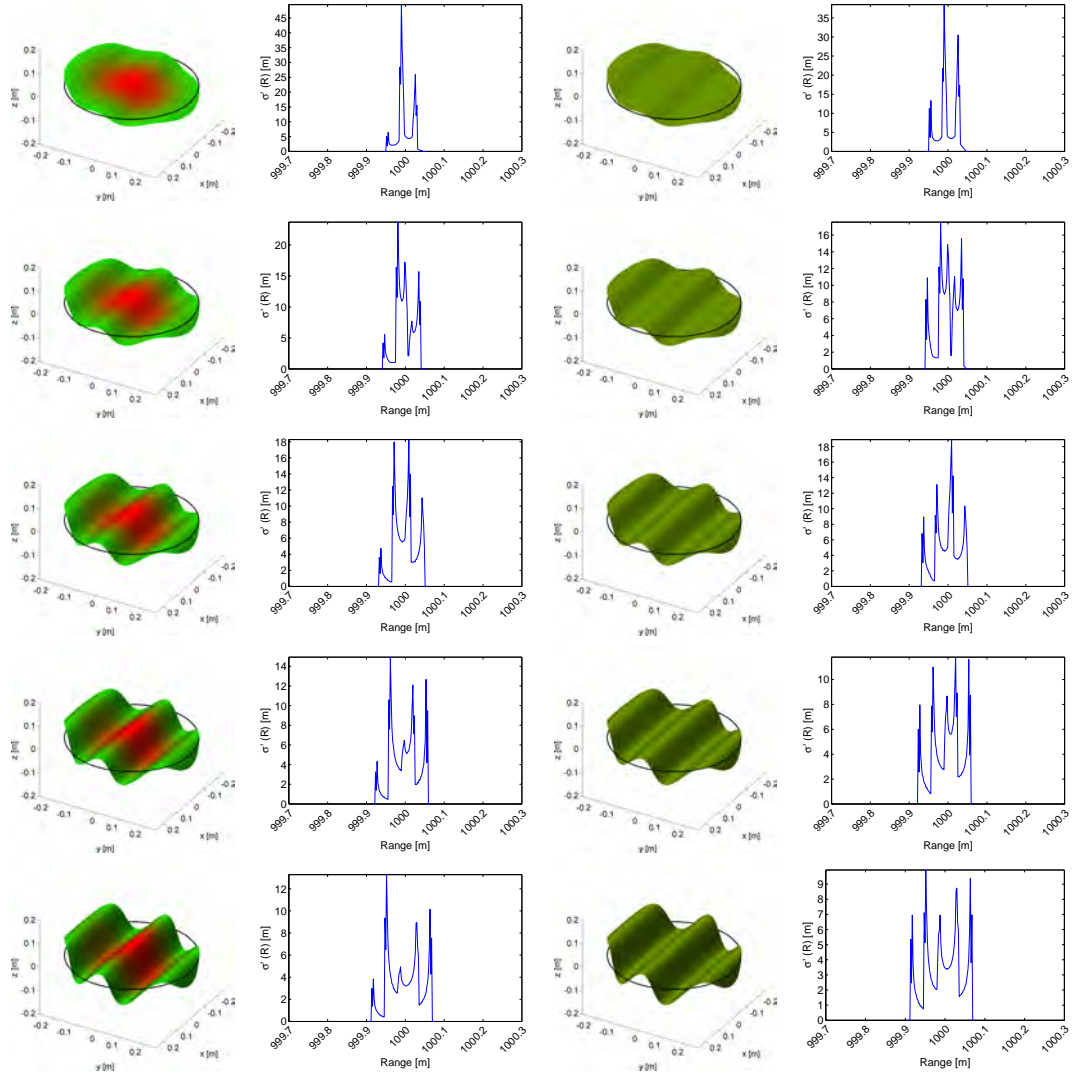


**Figure C.45:** From left to right: Illumination and backscatter geometry and DBCS for the Gaussian and uniform energy distribution within the laser footprint for a tilted sinusoidal target with parallel wavefronts; wavelength  $\lambda = 0.2$  m, tilt angle  $10^\circ$ . The amplitude increases from 0.01 m (top) to 0.05 m (bottom) in steps of 0.01 m.

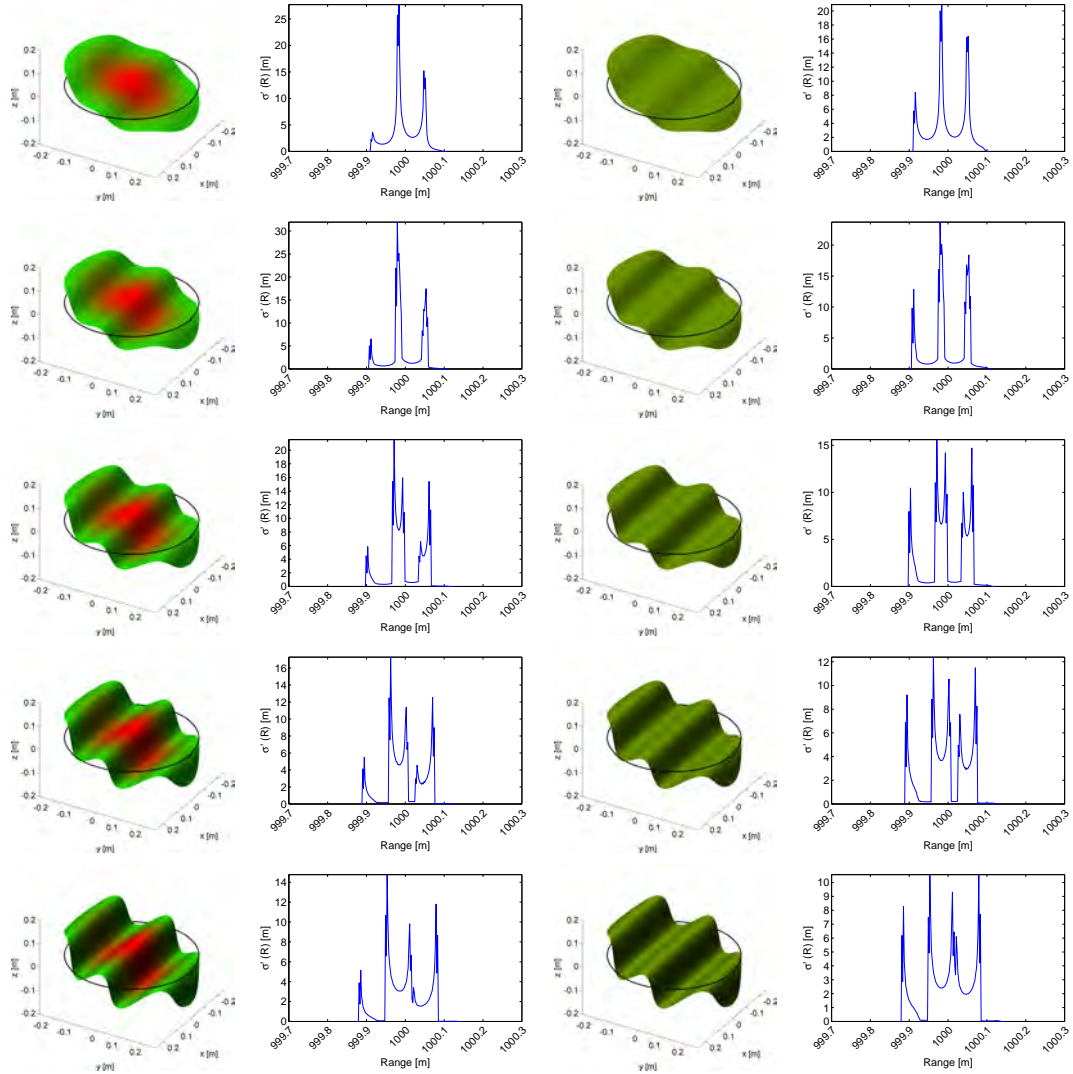


**Figure C.46:** From left to right: Illumination and backscatter geometry and dB backscatter coefficient for the Gaussian and uniform energy distribution within the laser footprint for a tilted sinusoidal target with parallel wavefronts; wavelength  $\lambda = 0.2$  m, tilt angle  $20^\circ$ . The amplitude increases from 0.01 m (top) to 0.05 m (bottom) in steps of 0.01 m.

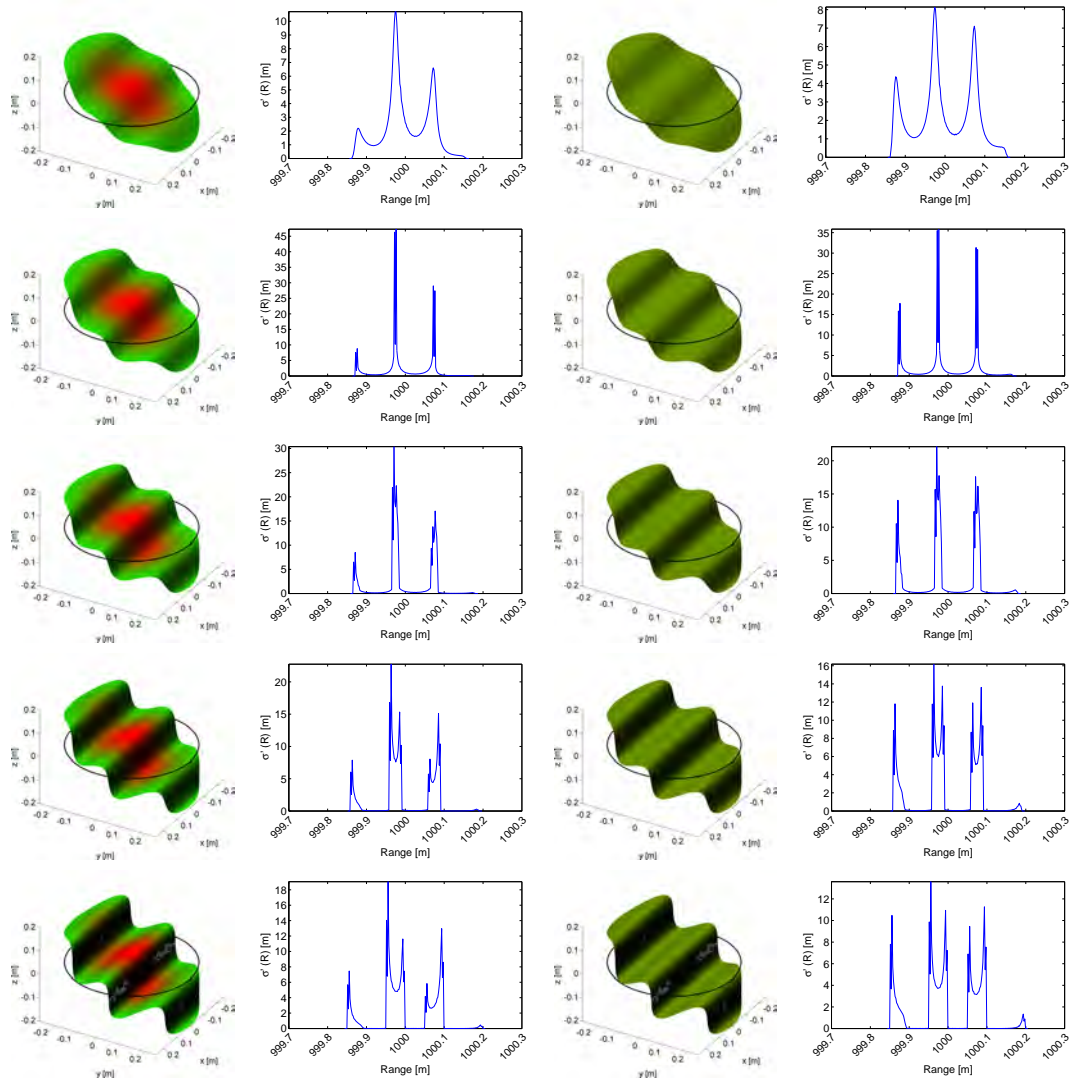


**Figure C.47:** From left to right: Illumination and backscatter geometry and dBBS for the Gaussian and uniform energy distribution within the laser footprint for a tilted sinusoidal target with parallel wavefronts; wavelength  $\lambda = 0.2$  m, tilt angle  $30^\circ$ . The amplitude increases from 0.01 m (top) to 0.05 m (bottom) in steps of 0.01 m.

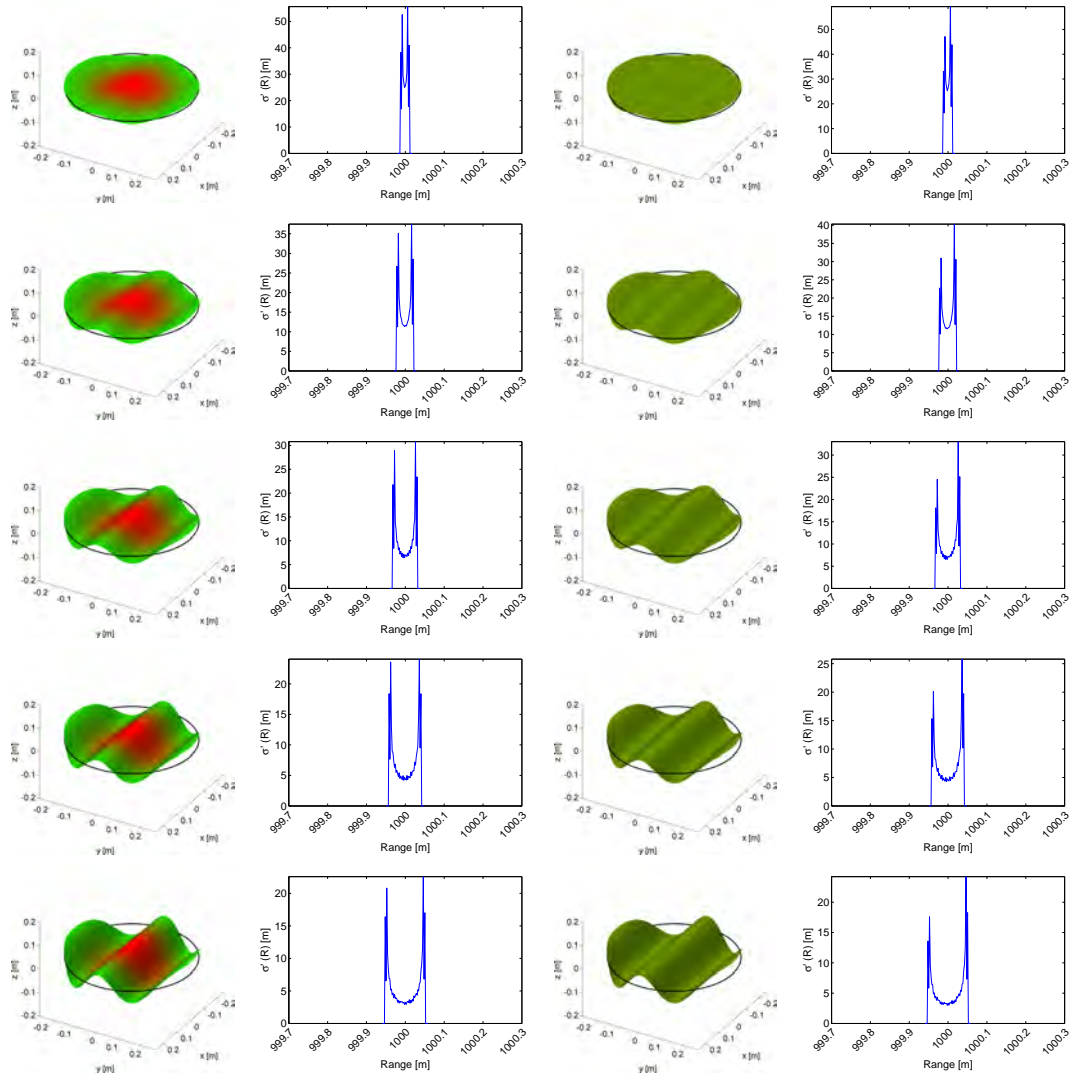


**Figure C.48:** From left to right: Illumination and backscatter geometry and dBCS for the Gaussian and uniform energy distribution within the laser footprint for a sinusoidal target with parallel wavefronts; wavelength  $\lambda = 0.25$  m. The amplitude increases from 0.01 m (top) to 0.05 m (bottom) in steps of 0.01 m.

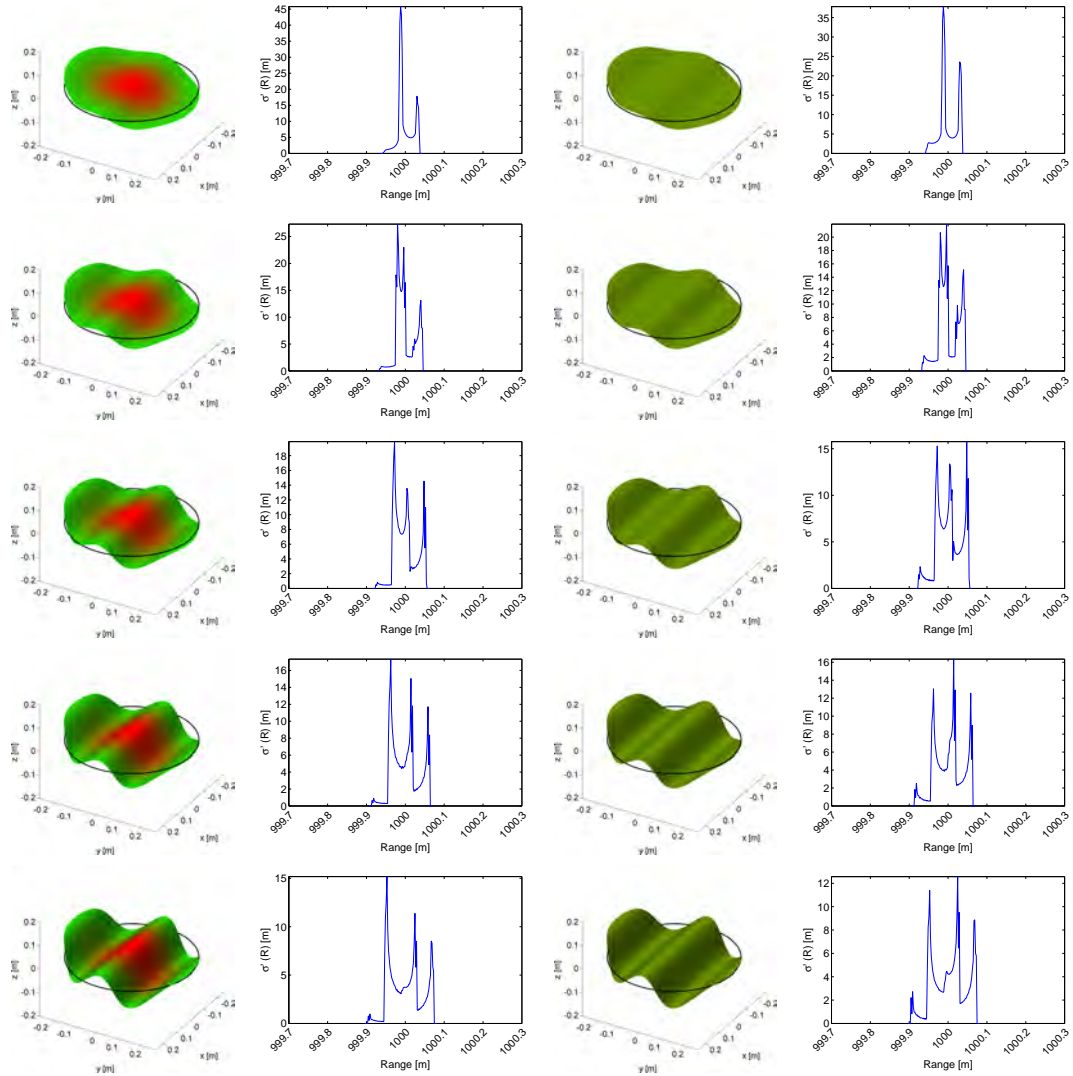


**Figure C.49:** From left to right: Illumination and backscatter geometry and dBDS for the Gaussian and uniform energy distribution within the laser footprint for a tilted sinusoidal target with parallel wavefronts; wavelength  $\lambda = 0.25$  m, tilt angle  $10^\circ$ . The amplitude increases from 0.01 m (top) to 0.05 m (bottom) in steps of 0.01 m.

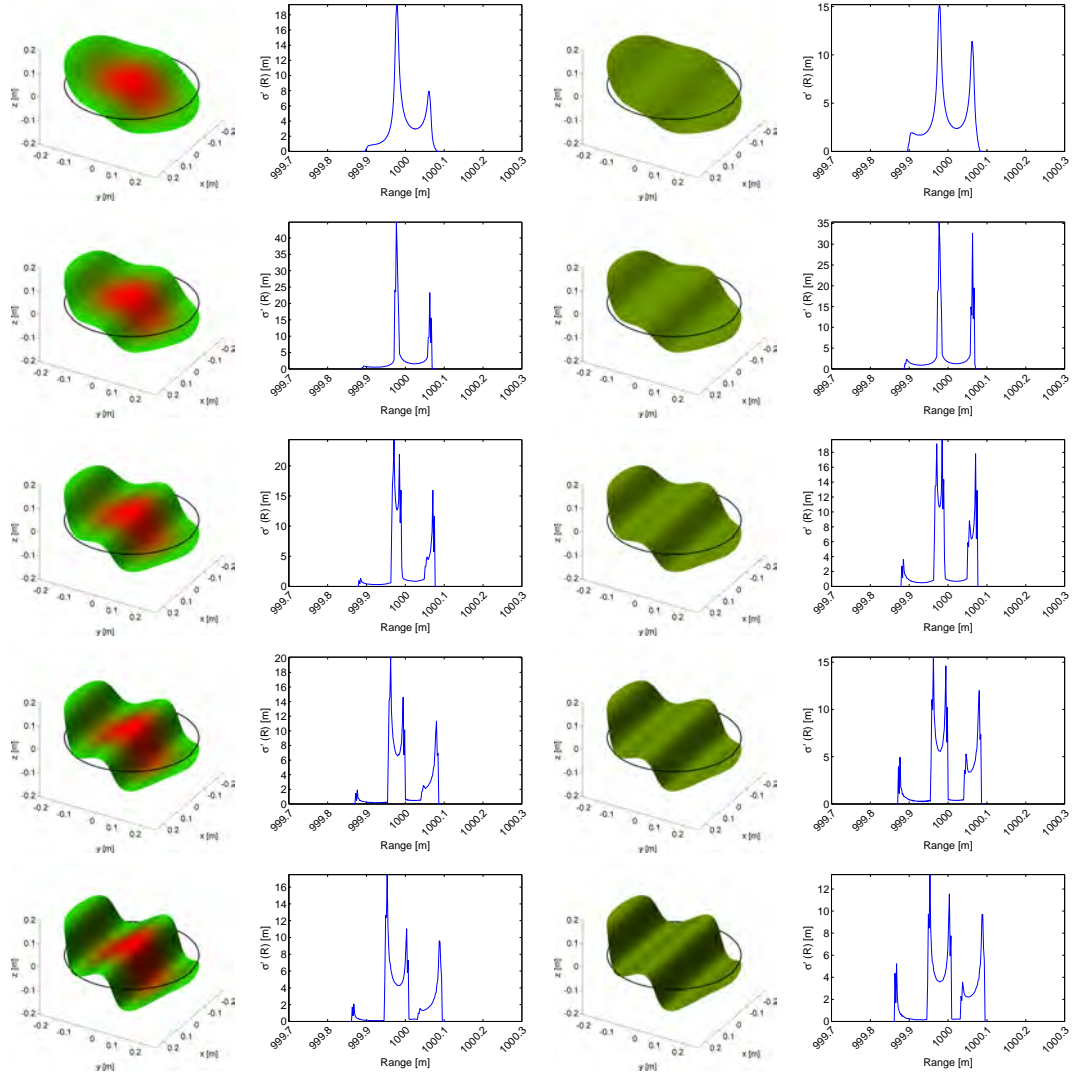


**Figure C.50:** From left to right: Illumination and backscatter geometry and dBCS for the Gaussian and uniform energy distribution within the laser footprint for a tilted sinusoidal target with parallel wavefronts; wavelength  $\lambda = 0.25$  m, tilt angle  $20^\circ$ . The amplitude increases from 0.01 m (top) to 0.05 m (bottom) in steps of 0.01 m.



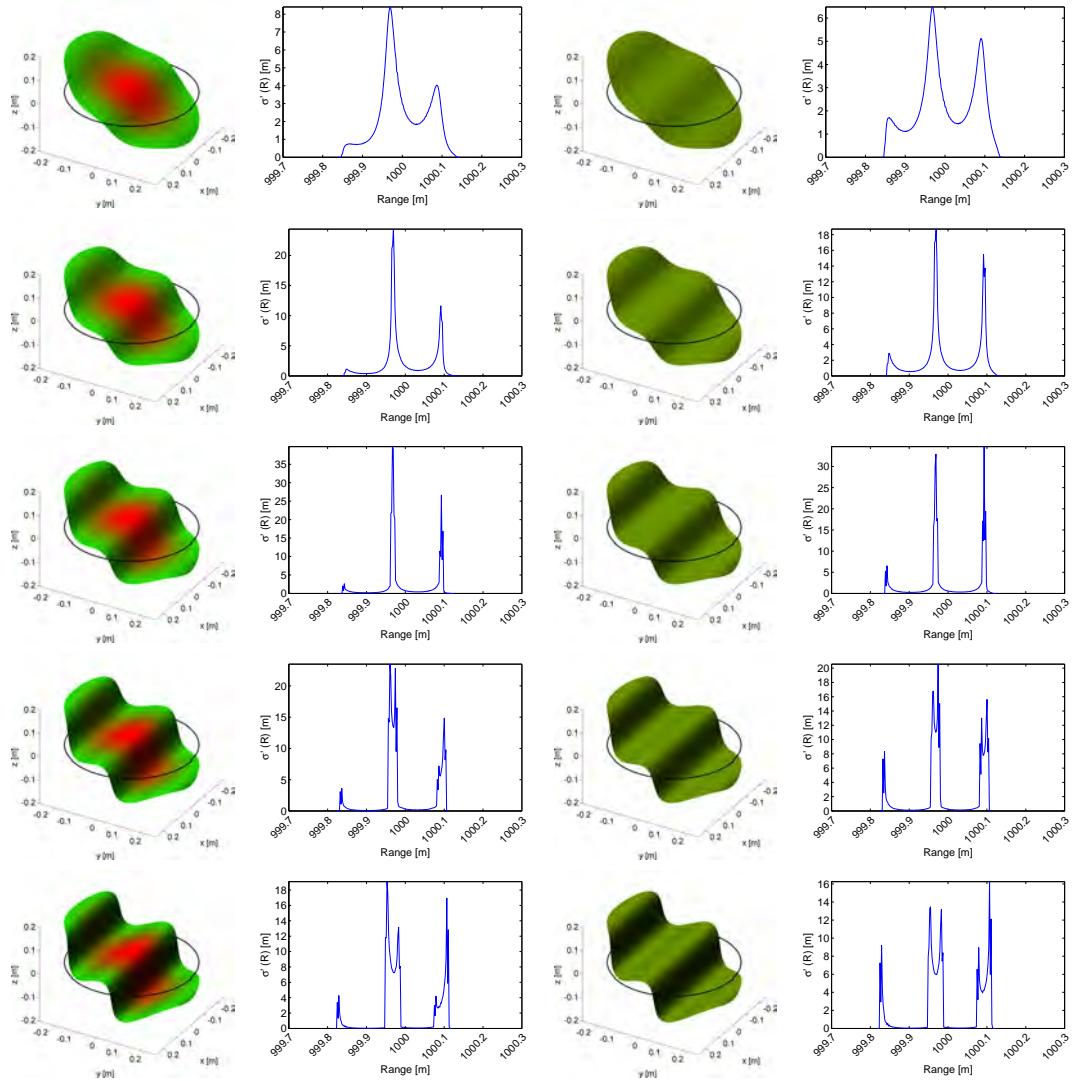


**Figure C.51:** From left to right: Illumination and backscatter geometry and dBCS for the Gaussian and uniform energy distribution within the laser footprint for a tilted sinusoidal target with parallel wavefronts; wavelength  $\lambda = 0.25$  m, tilt angle  $30^\circ$ . The amplitude increases from 0.01 m (top) to 0.05 m (bottom) in steps of 0.01 m.

# Examples for simulated recorded Echo Waveforms in Detail

## D.1 Simulated recorded Echo Waveforms for planar Targets

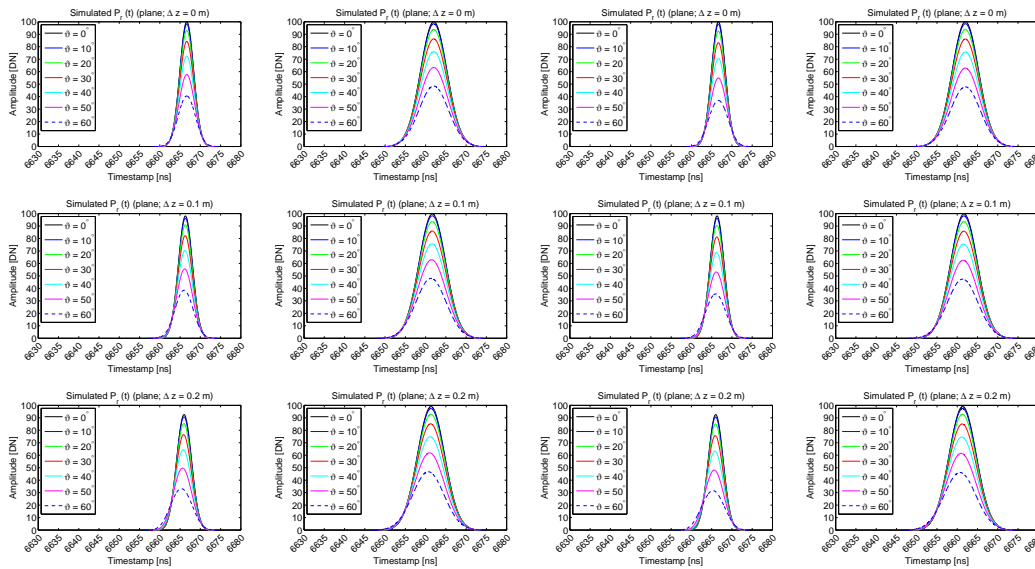


**Figure D.1:** Simulated recorded echo waveforms  $P_r(t)$  for planar targets, retrieved by convolution of the simulated dBCS of the various configurations and Gaussian-shaped (standard deviation  $s_s$ ) system waveform  $S(t)$ . From left to right:  $s_s = 1.7$  ns (Gauss),  $s_s = 4.8$  ns (Gauss),  $s_s = 1.7$  (uniform),  $s_s = 4.8$  (uniform). The offset  $\Delta z$  varies from 0 to 0.2 m in steps of 0.1 m.

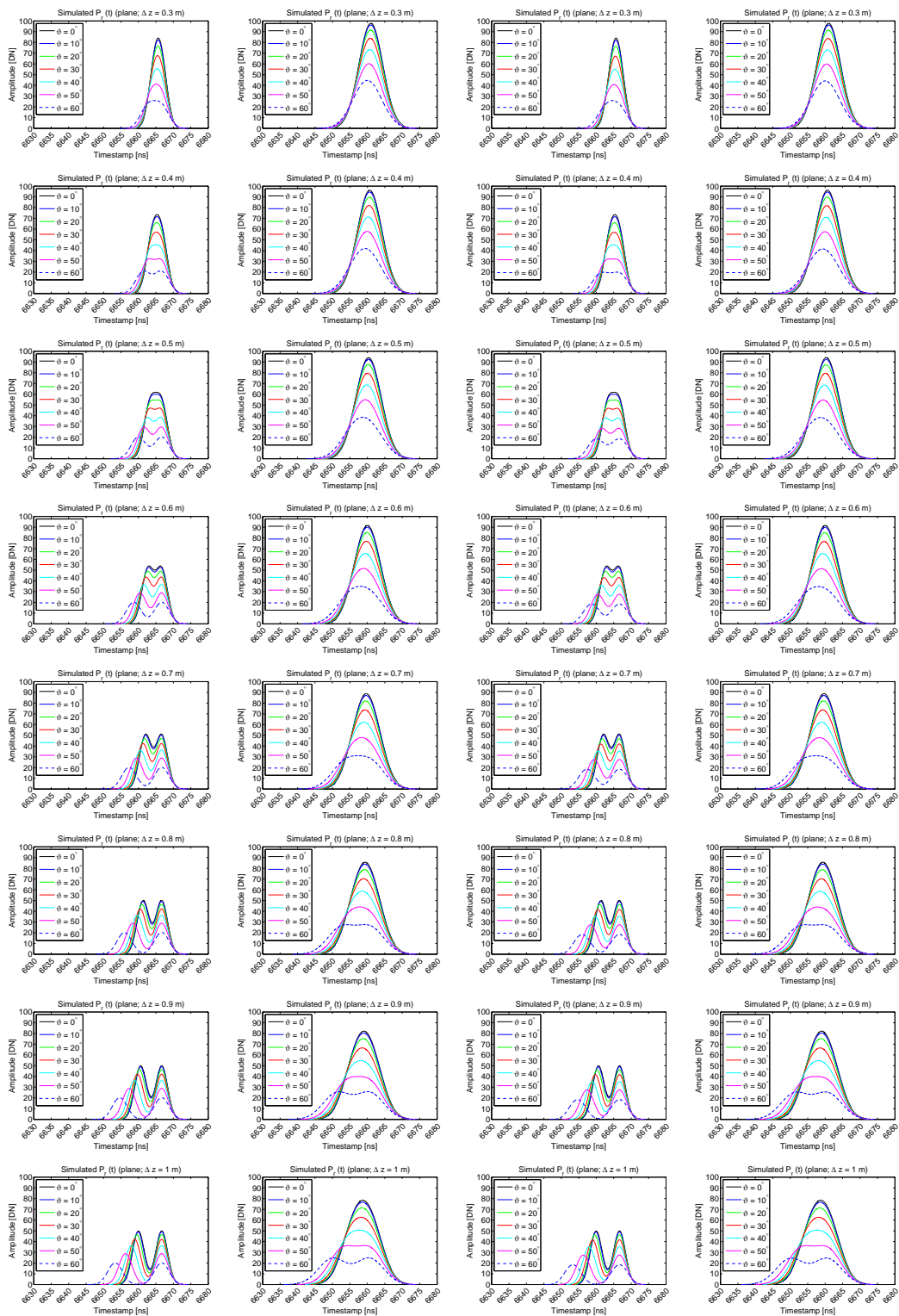
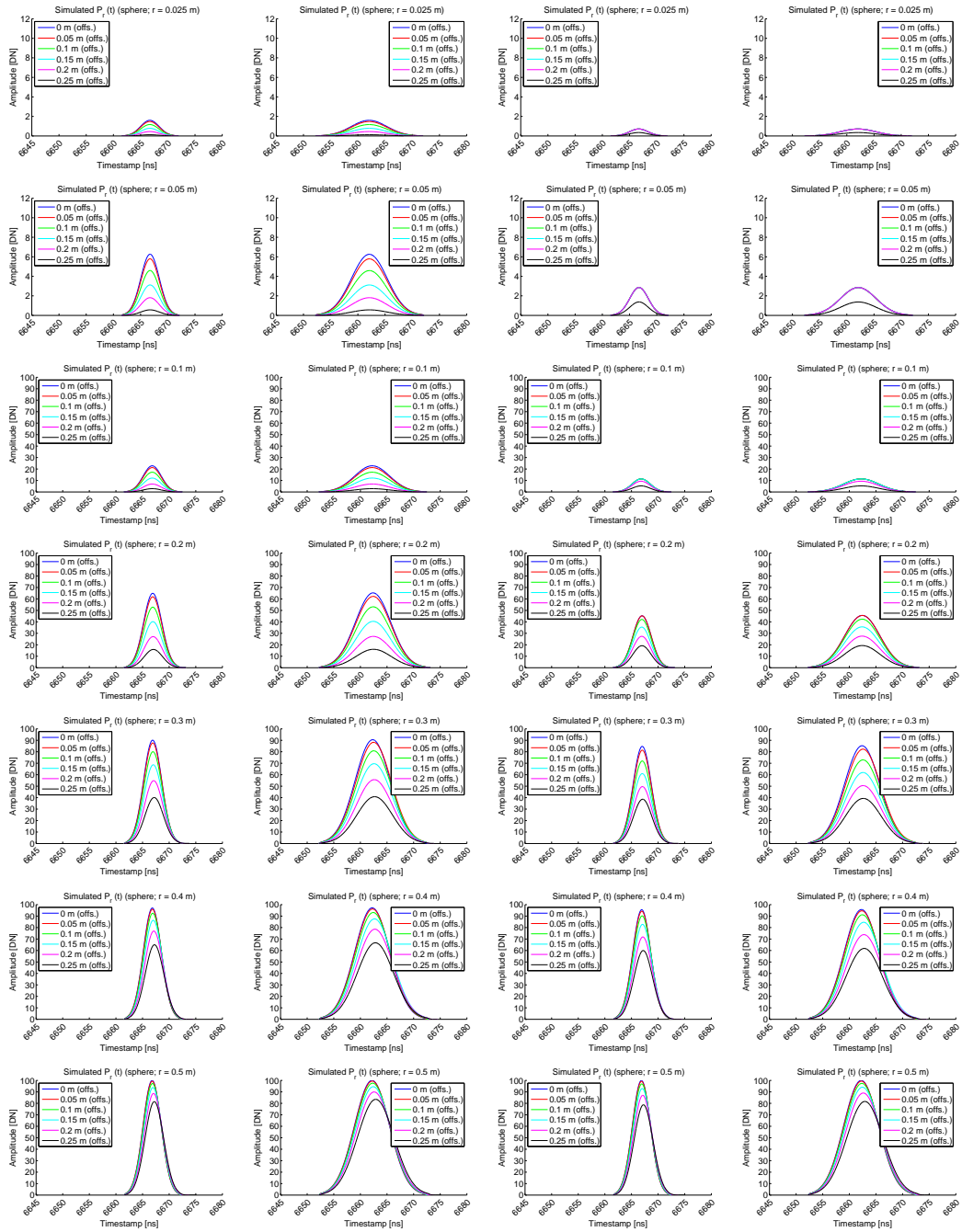


Figure D.2: Continuation of Figure D.1 for offsets  $\Delta z$  from 0.3 m to 1 m.

## D.2 Simulated recorded Echo Waveforms for spherical Targets



**Figure D.3:** Simulated recorded echo waveforms  $P_r(t)$  for spherical targets, retrieved by convolution of the simulated dBCS of the various configurations and Gaussian-shaped (standard deviation  $s_s$ ) system waveform  $S(t)$ . From left to right:  $s_s = 1.7$  ns (Gauss),  $s_s = 1.7$  (uniform),  $s_s = 4.8$  ns (Gauss),  $s_s = 4.8$  (uniform). The radius  $r$  varies from 0.025 to 0.1, 0.2, 0.3, 0.4 and 0.5 m (from top to bottom).

## D.3 Simulated recorded Echo Waveforms for cylindrical Targets

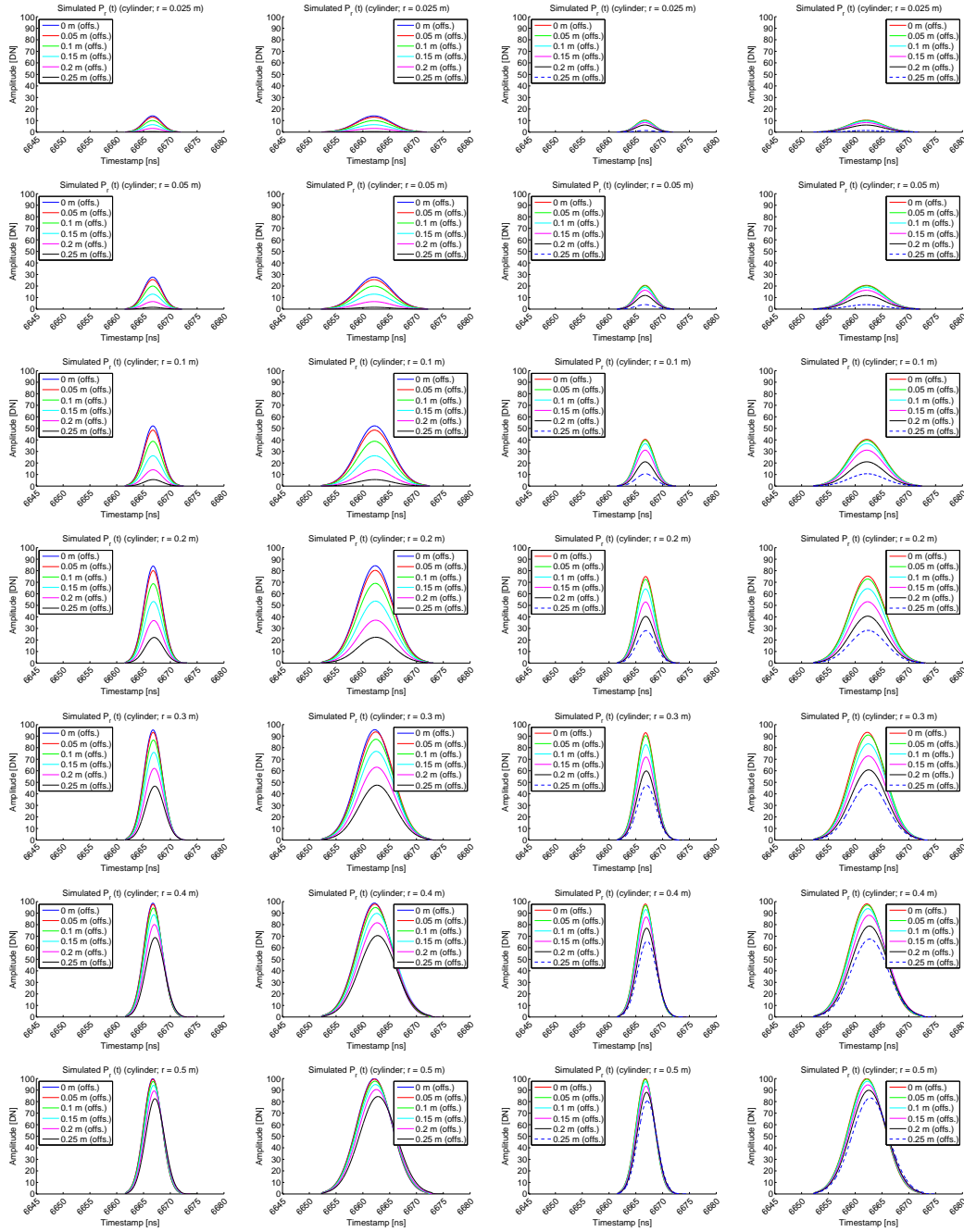


**Figure D.4:** Simulated recorded echo waveforms  $P_r(t)$  for cylindrical targets, retrieved by convolution of the simulated dBDCS of the various configurations and Gaussian-shaped (standard deviation  $s_s$ ) system waveform  $S(t)$ . From left to right:  $s_s = 1.7$  ns (Gauss),  $s_s = 1.7$  (uniform),  $s_s = 4.8$  ns (Gauss),  $s_s = 4.8$  (uniform). The radius  $r$  varies from 0.025 to 0.1, 0.2, 0.3, 0.4 and 0.5 m.

## D.4 Simulated recorded Echo Waveforms for sinusoidal Targets

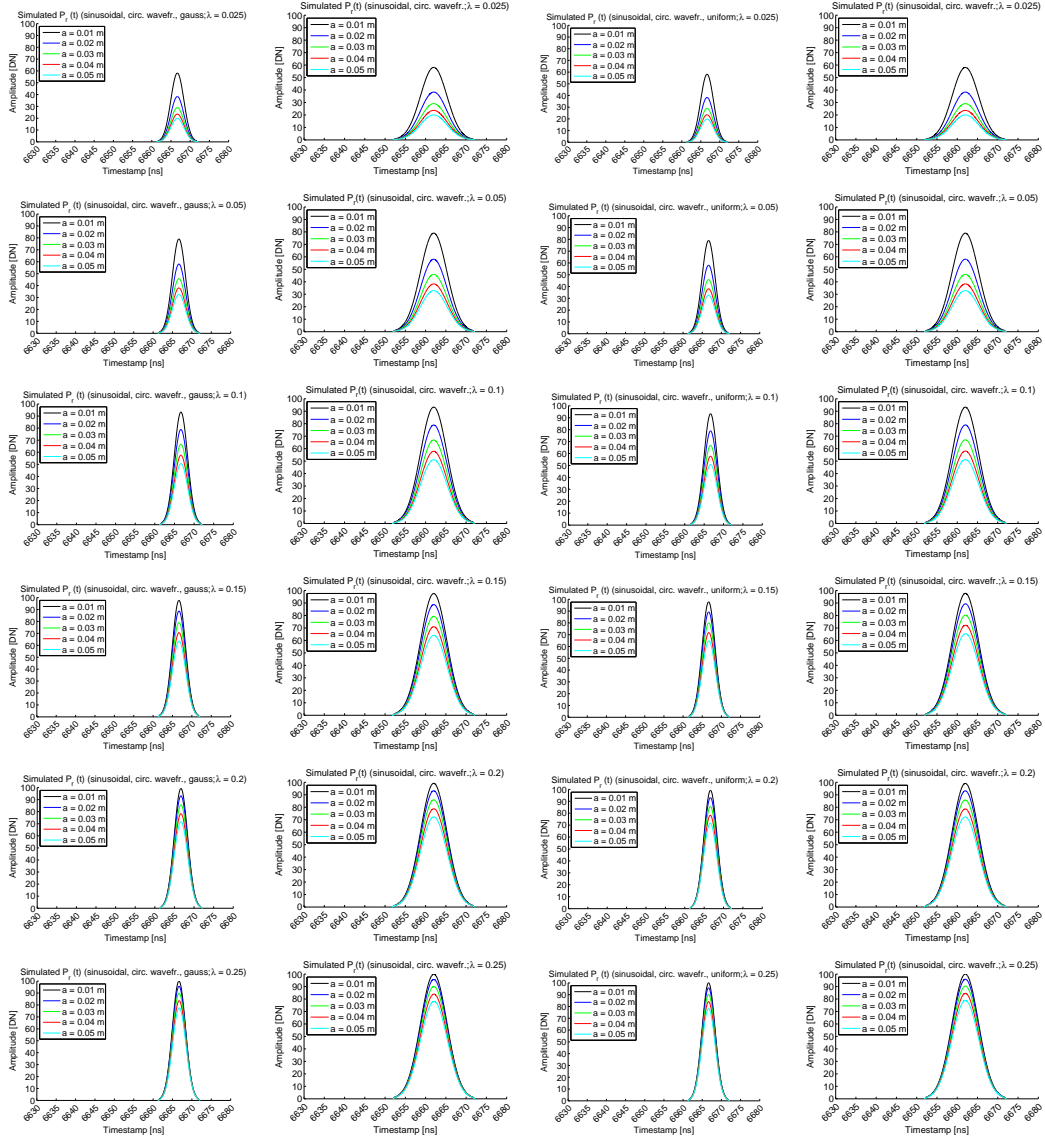


**Figure D.5:** Simulated recorded echo waveforms  $P_r(t)$  for sinusoidal targets with circular wavefronts, retrieved by convolution of the simulated dBCS of the various configurations and Gaussian-shaped (standard deviation  $s_s$ ) system waveform  $S(t)$ . From left to right:  $s_s = 1.7$  ns (Gauss),  $s_s = 1.7$  ns (uniform),  $s_s = 4.8$  ns (Gauss),  $s_s = 4.8$  ns (uniform). The wavelength  $\lambda$  varies from 0.025 to 0.1, 0.15, 0.2 and 0.25 m.

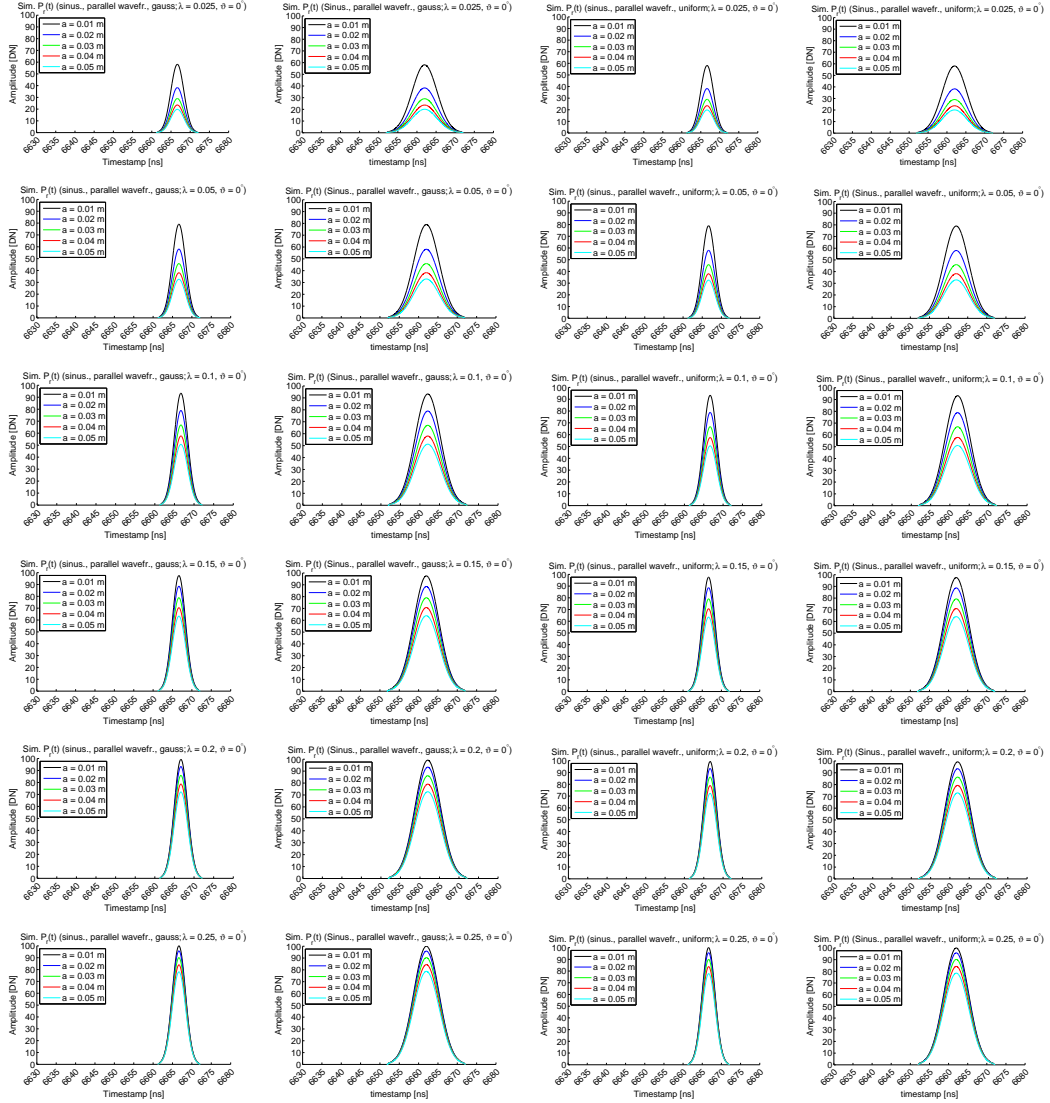


**Figure D.6:** Simulated recorded echo waveforms  $P_r(t)$  for sinusoidal targets with parallel wavefronts, retrieved by convolution of the simulated dBCS of the various configurations and Gaussian-shaped (standard deviation  $s_s$ ) system waveform  $S(t)$ . From left to right:  $s_s = 1.7$  ns (Gauss),  $s_s = 1.7$  ns (uniform),  $s_s = 4.8$  ns (Gauss),  $s_s = 4.8$  ns (uniform). The wavelength  $\lambda$  varies from 0.025 to 0.1, 0.15, 0.2 and 0.25 m. The example is continued in Figures D.7 to D.9 for incidence angles of 10, 20 and 30°, resp.

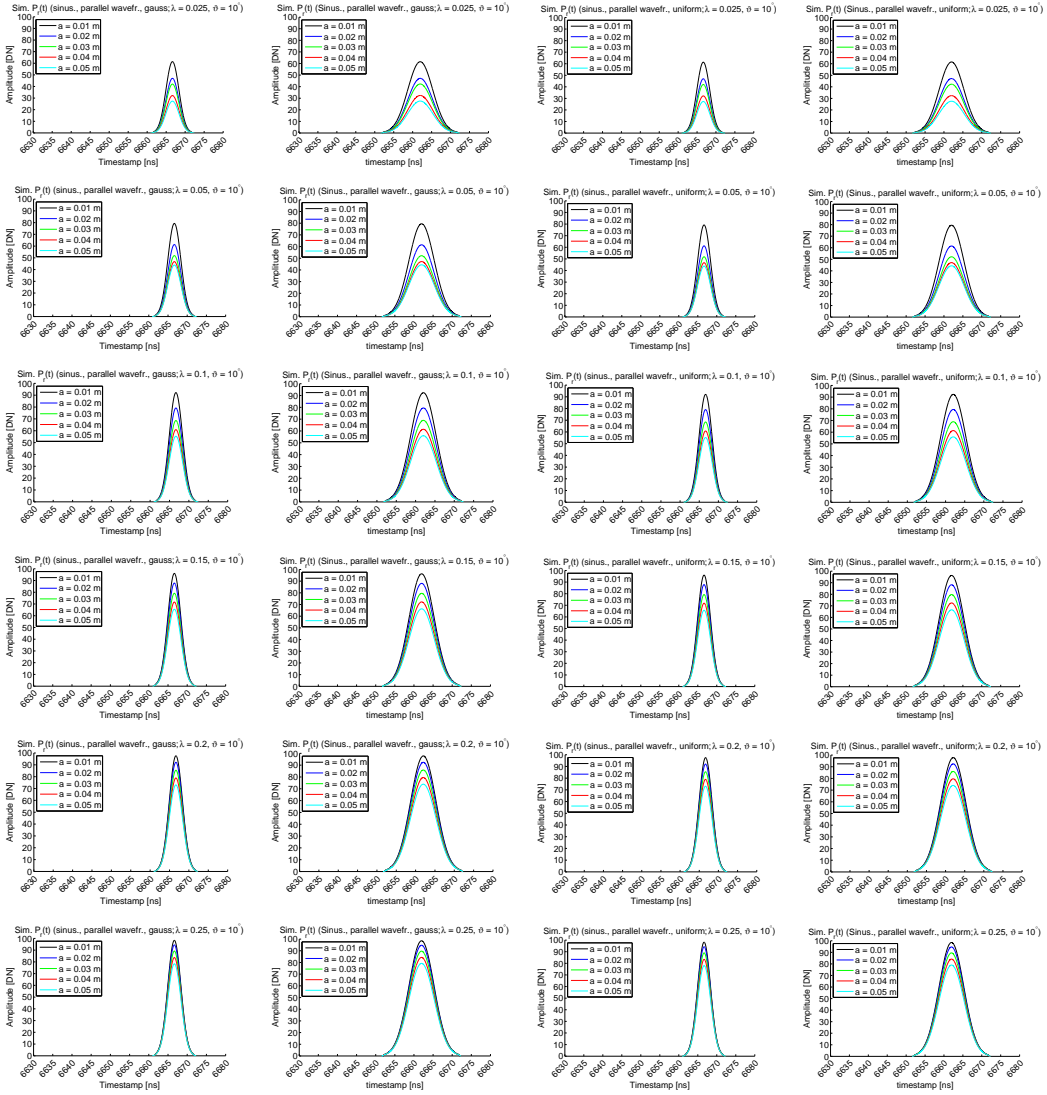


Figure D.7: Continuation of Figure D.6 for incidence angle  $\vartheta = 10^\circ$ .



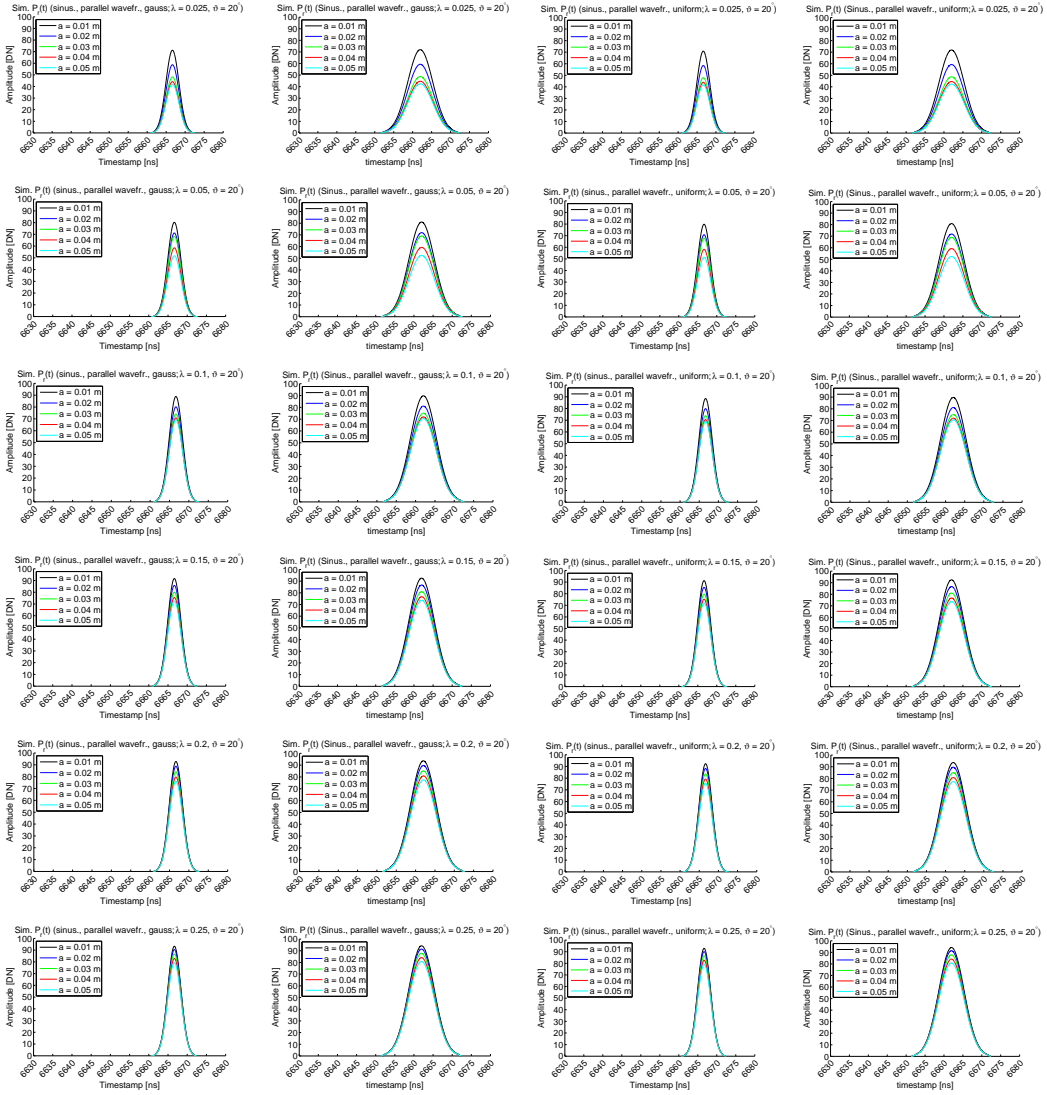


Figure D.8: Continuation of Figure D.6 for incidence angle  $\vartheta = 20^\circ$ .

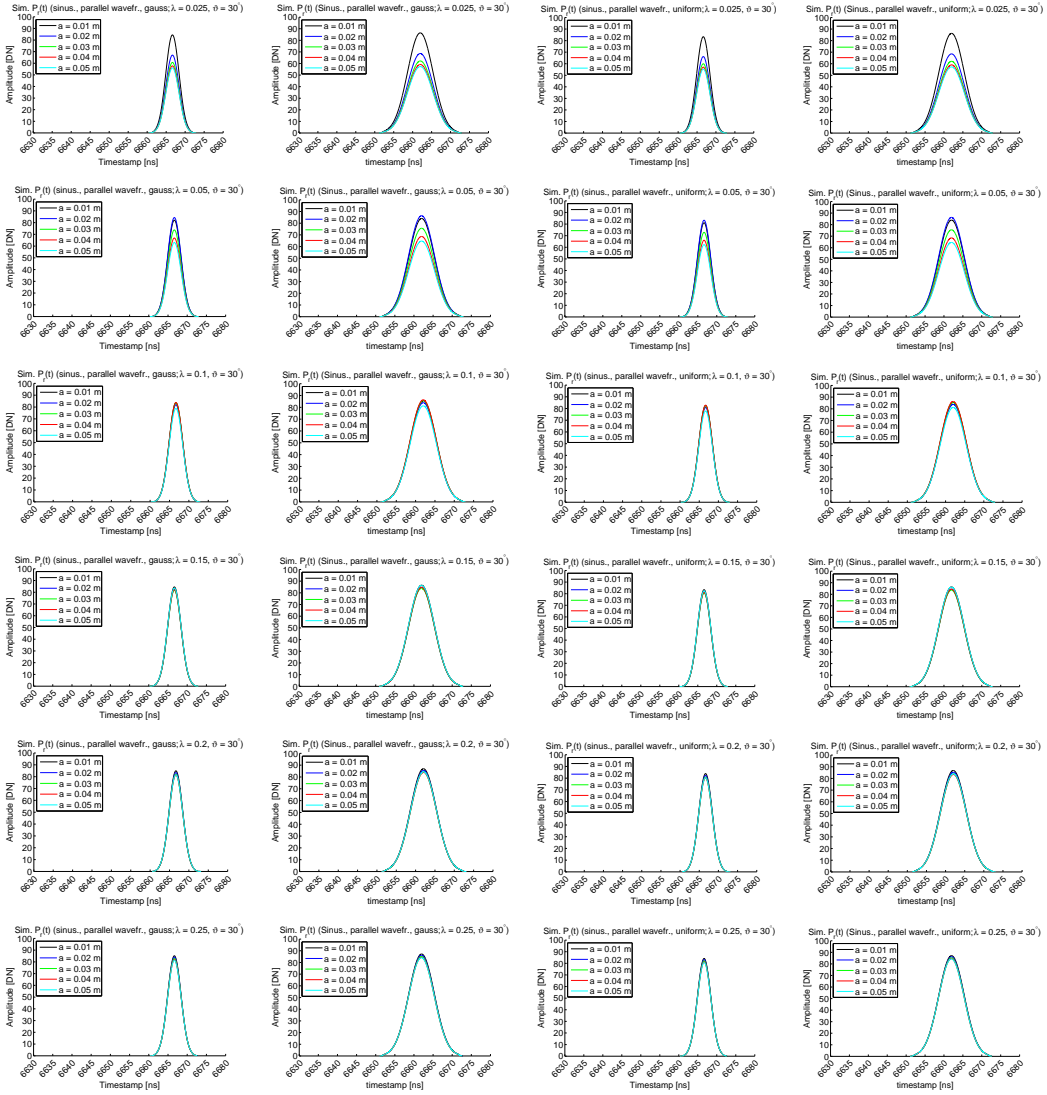


Figure D.9: Continuation of Figure D.6 for incidence angle  $\vartheta = 30^\circ$ .

# Bibliography

- Abed, F. M., Mills, J. P., and Miller, P. E. [2012]. “Echo Amplitude Normalization of Full-Waveform Airborne Laser Scanning Data Based on Robust Incidence Angle Estimation”. In: *IEEE Transactions in Geosciences and Remote Sensing* 50 (7), pp. 2910–2918. doi: [10.1109/TGRS.2011.2175232](https://doi.org/10.1109/TGRS.2011.2175232).
- Ahokas, E., Kaasalainen, S., Hyyppä, J., and Suomalainen, J. [2006]. “Calibration of the Optech ALTM 3100 laser scanner intensity data using brightness targets”. In: *International Archives of the Photogrammetry, Remote Sensing and Spatial Information Sciences* 36 (Part 1). Paris, France. url: <http://www.isprs.org/proceedings/XXXVI/part1/Papers/T03-11.pdf>.
- Beraldin, J.-A., Blais, F., and Lohr, U. [2010]. “Laser Scanning Technology”. In: *Airborne and terrestrial laser scanning*. Ed. by G. Vosselman and H.-G. Maas. Whittles. Chap. 1, pp. 1–42. isbn: 1-904-44587-X.
- Blair, J. B., Rabine, D. L., and Hofton, M. A. [1999]. “The Laser Vegetation Imaging Sensor: a medium-altitude, digitisation-only, airborne laser altimeter for mapping vegetation and topography”. In: *ISPRS Journal of Photogrammetry and Remote Sensing* 54 (2–3), pp. 115–122. doi: [10.1016/S0924-2716\(99\)00002-7](https://doi.org/10.1016/S0924-2716(99)00002-7).
- Bretar, F., Chauve, A., Bailly, J.-S., Mallet, C., and Jacome, A. [2009]. “Terrain surfaces and 3-D landcover classification from small footprint full-waveform lidar data: Application to badlands”. In: *Hydrology and Earth System Sciences* 13 (8), pp. 1531–1545. doi: [10.5194/hess-13-1531-2009](https://doi.org/10.5194/hess-13-1531-2009).
- Briese, C., Höfle, B., Lehner, H., Wagner, W., and Pfennigbauer, M. [2008]. “Calibration of full-waveform airborne laser scanning data for object classification”. In: *SPIE: Laser Radar Technology and Applications XIII*. doi: [10.1117/12.781086](https://doi.org/10.1117/12.781086).
- Briese, C., Pfennigbauer, M., Lehner, H., Ullrich, A., Wagner, W., and Pfeifer, N. [2012]. “Radiometric Calibration of Multi-Wavelength Airborne Laser Scanning Data”. In: *ISPRS Annals of the Photogrammetry, Remote Sensing and Spatial Information Sciences* 1 (Part 7). ISSN: 1682-1750. Melbourne, Australia, pp. 335–340. doi: [10.5194/isprsannals-I-7-335-2012](https://doi.org/10.5194/isprsannals-I-7-335-2012).

- Bromiley, P. [2003]. *Products and Convolutions of Gaussian Distributions*. Internal Report Tina Memo No. 2003-003. Manchester, UK: Imaging Science and Biomedical Engineering Division, Medical School, University of Manchester. url: <http://www.tina-vision.net/docs/memos/2003-003.pdf>.
- Chauve, A., Mallet, C., Bretar, F., Durrieu, S., Pierrot-Deseilligny, M., and Puech, W. [2007]. "Processing full-waveform lidar data: modelling raw signals". In: *ISPRS Workshop "Laser Scanning 2007 and SilviLaser 2007"*. *International Archives of the Photogrammetry, Remote Sensing and Spatial Information Sciences 36 (Part 3/W52)*, pp. 102–107. url: [http://www.isprs.org/proceedings/XXXVI/3-W52/final\\_papers/Chauve\\_2007.pdf](http://www.isprs.org/proceedings/XXXVI/3-W52/final_papers/Chauve_2007.pdf).
- Cobby, D. M., Mason, D. C., and Davenport, I. J. [2001]. "Image processing of airborne scanning laser altimetry data for improved river flood modelling". In: *ISPRS Journal of Photogrammetry and Remote Sensing 56 (2)*, pp. 121–138. issn: 0924-2716. doi: [10.1016/S0924-2716\(01\)00039-9](https://doi.org/10.1016/S0924-2716(01)00039-9).
- Demantké, J., Mallet, C., David, N., and Vallet, B. [2011]. "Dimensionality based Scale Selection in 3D Lidar Point Clouds". In: *ISPRS Workshop Laser Scanning 2011. International Archives of the Photogrammetry, Remote Sensing and Spatial Information Sciences 38 (Part 5/W12)*. Ed. by D. D. Lichti and A. F. Habib, pp. 97–102. doi: [10.5194/isprsarchives-XXXVIII-5-W12-97-2011](https://doi.org/10.5194/isprsarchives-XXXVIII-5-W12-97-2011).
- Doneus, M., Briese, C., Fera, M., and Janner, M. [2008]. "Archaeological prospection of forested areas using full-waveform airborne laser scanning". In: *Journal of Archaeological Science 35 (4)*, pp. 882–893. doi: [10.1016/j.jas.2007.06.013](https://doi.org/10.1016/j.jas.2007.06.013).
- Dorninger, P. and Pfeifer, N. [2008]. "A comprehensive automated 3D approach for building extraction, reconstruction, and regularization from airborne laser scanning point clouds". In: *Sensors 8 (11)*, pp. 7323–7343. doi: [10.3390/s8117323](https://doi.org/10.3390/s8117323).
- Duong, H. V., Lindenbergh, R., Pfeifer, N., and Vosselman, G. [2008]. "Single and two epoch analysis of ICESat full waveform data over forested areas". In: *International Journal of Remote Sensing 29 (5)*, pp. 1453–1473. doi: [10.1080/01431160701736372](https://doi.org/10.1080/01431160701736372).
- Farin, G. [2002]. *Curves and Surfaces for CAD. A Practical Guide*. 5th. San Francisco, USA: Morgan Kaufmann Publishers, p. 520.
- Filin, S. and Pfeifer, N. [2005]. "Neighborhood systems for airborne laser data". In: *Photogrammetric Engineering & Remote Sensing 71 (6)*, pp. 743–755. doi: [10.14358/PERS.71.6.743](https://doi.org/10.14358/PERS.71.6.743).
- Gonzalez, R. C. and Woods, R. E. [2008]. *Digital Image Processing*. 3rd ed. Upper Saddle River, NJ: Pearson Prentice Hall, pp. 954+xxii. isbn: 0-131-68728-X.
- Habib, A. F., Kersting, A. P., Bang, K.-I., Zhai, R., and Al-Durgham, M. [2009]. "A strip adjustment procedure to mitigate the impact of inaccurate mounting parameters in

- parallel lidar strips”. In: *The Photogrammetric Record* 24 (126), pp. 171–195. doi: [10.1111/j.1477-9730.2009.00529.x](https://doi.org/10.1111/j.1477-9730.2009.00529.x).
- Hakala, T., Suomalainen, J., Kaasalainen, S., and Chen, Y. [2012]. “Full waveform hyperspectral LiDAR for terrestrial laser scanning”. In: *Optics Express* 20 (7), pp. 7119–7127. doi: [10.1364/OE.20.007119](https://doi.org/10.1364/OE.20.007119).
- Hernández-Marín, S., Wallace, A. M., and Gibson, G. J. [2007]. “Bayesian Analysis of Lidar Signals with Multiple Returns”. In: *IEEE Transactions on Pattern Analysis and Machine Intelligence* 29 (12), pp. 2170–2180. doi: [10.1109/TPAMI.2007.1122](https://doi.org/10.1109/TPAMI.2007.1122).
- Höfle, B. and Rutzinger, M. [2011]. “Topographic airborne LiDAR in geomorphology: A technological perspective”. In: *Zeitschrift für Geomorphologie/Annals of Geomorphology* 55 (Supplementary Issue 2), pp. 1–29. doi: [10.1127/0372-8854/2011/0055-0031](https://doi.org/10.1127/0372-8854/2011/0055-0031).
- Hofton, M., Minster, J., and Blair, J. [2000]. “Decomposition of laser altimeter waveforms”. In: *IEEE Transactions on Geoscience and Remote Sensing* 38, pp. 1989–1996. doi: [10.1109/36.851780](https://doi.org/10.1109/36.851780).
- Hollaus, M., Mücke, W., Roncat, A., Pfeifer, N., and Brieese, C. [2014]. “Full-Waveform Airborne Laser Scanning Systems and Their Possibilities in Forest Applications”. In: *Forestry Applications of Airborne Laser Scanning – Concepts and Case Studies*. Vol. 27. Ed. by M. Maltamo, E. Næsset, and J. Vauhkonen. Managing Forest Ecosystems. Dordrecht, The Netherlands: Springer Netherlands. Chap. 3, pp. 43–61. isbn: 978-94-017-8662-1. doi: [10.1007/978-94-017-8663-8\\_3](https://doi.org/10.1007/978-94-017-8663-8_3).
- Irish, J. L. and Lillycrop, W. J. [1999]. “Scanning laser mapping of the coastal zone: the SHOALS system”. In: *ISPRS Journal of Photogrammetry and Remote Sensing* 54 (2–3), pp. 123–129. doi: [10.1016/S0924-2716\(99\)00003-9](https://doi.org/10.1016/S0924-2716(99)00003-9).
- Jacovitti, G. and Scarano, G. [1993]. “Discrete time techniques for time delay estimation”. In: *IEEE Transactions on Signal Processing* 41 (2), pp. 525–533. doi: [10.1109/78.193195](https://doi.org/10.1109/78.193195).
- Jelalian, A. V. [1992]. *Laser Radar Systems*. Boston: Artech House.
- Jutzi, B. and Stilla, U. [2003]. “Laser pulses Analysis for reconstruction and classification of urban objects”. In: *International Archives of the Photogrammetry, Remote Sensing and Spatial Information Sciences* 34 (Part 3/W8). Munich, Germany, pp. 151–156. url: [http://www.isprs.org/proceedings/XXXIV/3-W8/papers/pia03\\_s6p3.pdf](http://www.isprs.org/proceedings/XXXIV/3-W8/papers/pia03_s6p3.pdf).
- Jutzi, B. [2007]. “Analyse der zeitlichen Signalform von rückgestreuten Laserpulsen”. PhD thesis. Technical University Munich. url: [http://www.pf.bv.tum.de/pub/2007/jutzi\\_phd07\\_dis.pdf](http://www.pf.bv.tum.de/pub/2007/jutzi_phd07_dis.pdf).
- Jutzi, B. and Stilla, U. [2006]. “Range determination with waveform recording laser systems using a Wiener Filter”. In: *ISPRS Journal of Photogrammetry and Remote Sensing* 61 (1), pp. 95–107. doi: [10.1016/j.isprsjprs.2006.09.001](https://doi.org/10.1016/j.isprsjprs.2006.09.001).

- Kaasalainen, S., Hyyppä, J., Litkey, P., Hyyppä, H., Ahokas, E., Kukko, A., and Kaartinen, H. [2007]. “Radiometric calibration of ALS intensity”. In: *ISPRS Workshop “Laser Scanning 2007 and SilviLaser 2007”*. *International Archives of the Photogrammetry, Remote Sensing and Spatial Information Sciences 36 (Part 3/W52)*. Ed. by P. Rönholm, H. Hyyppä, and J. Hyyppä, pp. 201–205. url: [http://www.isprs.org/proceedings/XXXVI/3-W52/final\\_papers/Kaasalainen\\_2007.pdf](http://www.isprs.org/proceedings/XXXVI/3-W52/final_papers/Kaasalainen_2007.pdf).
- Kaasalainen, S., Hyyppä, H., Kukko, A., Litkey, P., Ahokas, E., Hyyppä, J., Lehner, H., Jaakkola, A., Suomalainen, J., Akujarvi, A., Kaasalainen, M., and Pyysalo, U. [2009]. “Radiometric Calibration of LIDAR Intensity With Commercially Available Reference Targets”. In: *IEEE Transactions on Geoscience and Remote Sensing 47 (2)*, pp. 588–598. issn: 0196-2892. doi: [10.1109/TGRS.2008.2003351](https://doi.org/10.1109/TGRS.2008.2003351).
- Kaasalainen, S., Suomalainen, J., Hakala, T., and Chen, Y. [2010]. “Active hyperspectral LIDAR methods for object classification”. In: *2nd Workshop on Hyperspectral Image and Signal Processing: Evolution in Remote Sensing (WHISPERS)*. Reykjavik, Iceland, p. 4. doi: [10.1109/WHISPERS.2010.5594863](https://doi.org/10.1109/WHISPERS.2010.5594863).
- Kager, H. [2004]. “Discrepancies Between Overlapping Laser Scanning Strips - Simultaneous Fitting of Aerial Laser Scanner Strips”. In: *International Archives of the Photogrammetry, Remote Sensing and Spatial Information Sciences 35 (Part B1)*. Istanbul, Turkey, pp. 555–560. url: <http://www.isprs.org/proceedings/XXXV/congress/comml/papers/99.pdf>.
- Kay, S. M. [1993]. *Fundamentals of Statistical Signal Processing: Estimation Theory*. Vol. 1. Prentice Hall Signal Processing Series. Englewood Cliffs, NY: Prentice Hall, pp. 595+xii. isbn: 0-133-45711-7.
- Kirchhof, M., Jutzi, B., and Stilla, U. [2008]. “Iterative processing of laser scanning data by full waveform analysis”. In: *ISPRS Journal of Photogrammetry and Remote Sensing 63 (1)*. Theme Issue: Terrestrial Laser Scanning, pp. 99–114. issn: 0924-2716. doi: [10.1016/j.isprsjprs.2007.08.006](https://doi.org/10.1016/j.isprsjprs.2007.08.006).
- Kukko, A. and Hyyppä, J. [2007]. “Laser Scanner Simulator for System Analysis and Algorithm Development: A Case with Forest Measurements”. In: *ISPRS Workshop “Laser Scanning 2007 and SilviLaser 2007”*. *International Archives of the Photogrammetry, Remote Sensing and Spatial Information Sciences 36 (Part 3/W52)*. Ed. by P. Rönholm, H. Hyyppä, and J. Hyyppä, pp. 234–240. url: [http://www.isprs.org/proceedings/XXXVI/3-W52/final\\_papers/Kukko\\_2007a.pdf](http://www.isprs.org/proceedings/XXXVI/3-W52/final_papers/Kukko_2007a.pdf).
- Lehner, H. and Briese, C. [2010]. “Radiometric calibration of Full-Waveform Airborne Laser Scanning Data based on natural surfaces”. In: *ISPRS Technical Commission VII Symposium 2010: 100 Years ISPRS – Advancing Remote Sensing Science*. *International Archives of the Photogrammetry, Remote Sensing and Spatial Information Sciences 38 (Part 7B)*. Vienna, Austria, pp. 360–365. url: [http://www.isprs.org/proceedings/XXXVIII/part7/b/pdf/360\\_XXXVIII-part7B.pdf](http://www.isprs.org/proceedings/XXXVIII/part7/b/pdf/360_XXXVIII-part7B.pdf).

- Lehner, H., Kager, H., Roncat, A., and Zlinszky, A. [2011]. “Consideration of laser pulse fluctuations and automatic gain control in radiometric calibration of airborne laser scanning data”. In: *Proceedings of 6th ISPRS Student Consortium and WG VI/5 Summer School*. Fayetteville State University, North Carolina. url: [http://publik.tuwien.ac.at/files/PubDat\\_199484.pdf](http://publik.tuwien.ac.at/files/PubDat_199484.pdf).
- Mallet, C. [2011]. “Analyse de données lidar à Retour d’Onde Complète pour la classification en milieu urbain”. PhD thesis. Paris, France: Télécom ParisTech, École Doctorale d’Informatique, Télécommunications et Électronique de Paris. url: [http://recherche.ign.fr/labos/matis/pdf/theses/mallet\\_thesis\\_web.pdf](http://recherche.ign.fr/labos/matis/pdf/theses/mallet_thesis_web.pdf).
- Mallet, C. and Bretar, F. [2009]. “Full-waveform topographic lidar: State-of-the-art”. In: *ISPRS Journal of Photogrammetry and Remote Sensing* 64 (1), pp. 1–16. issn: 0924-2716. doi: [10.1016/j.isprsjprs.2008.09.007](https://doi.org/10.1016/j.isprsjprs.2008.09.007).
- Mallet, C., Lafarge, F., Bretar, F., Roux, M., Soergel, U., and Heipke, C. [2009]. “A Stochastic Approach for Modelling Airborne LIDAR Waveforms”. In: *ISPRS Workshop Laserscanning ’09. International Archives of the Photogrammetry, Remote Sensing and Spatial Information Sciences 38 (Part 3/W8)*. Ed. by F. Bretar, M. Pierrot-Deseilligny, and G. Vosselman, pp. 201–206. url: [http://www.isprs.org/proceedings/XXXVIII/3-W8/papers/201\\_laserscanning09.pdf](http://www.isprs.org/proceedings/XXXVIII/3-W8/papers/201_laserscanning09.pdf).
- Mallet, C., Lafarge, F., Roux, M., Soergel, U., Bretar, F., and Heipke, C. [2010]. “A marked point process for modeling lidar waveforms”. In: *IEEE Transactions on Image Processing* 19 (12), pp. 3204–3221. doi: [10.1109/TIP.2010.2052825](https://doi.org/10.1109/TIP.2010.2052825).
- Mallet, C., Bretar, F., Roux, M., Soergel, U., and Heipke, C. [2011]. “Relevance assessment of full-waveform lidar data for urban area classification”. In: *ISPRS Journal of Photogrammetry and Remote Sensing* 66 (6, Supplement), S71–S84. doi: [10.1016/j.isprsjprs.2011.09.008](https://doi.org/10.1016/j.isprsjprs.2011.09.008).
- Maltamo, M., Næsset, E., and Vauhkonen, J., eds. [2014]. *Forestry Applications of Airborne Laser Scanning – Concepts and Case Studies*. Vol. 27. Managing Forest Ecosystems. Dordrecht, The Netherlands: Springer Netherlands, p. 464. isbn: 978-94-017-8662-1.
- Mandlbürger, G., Hauer, C., Höfle, B., Habersack, H., and Pfeifer, N. [2009]. “Optimisation of LiDAR derived terrain models for river flow modelling”. In: *Hydrology and Earth System Sciences* 13 (8), pp. 1453–1466. doi: [10.5194/hess-13-1453-2009](https://doi.org/10.5194/hess-13-1453-2009).
- Mandlbürger, G., Pfennigbauer, M., Steinbacher, F., and Pfeifer, N. [2011]. “Airborne Hydrographic LiDAR Mapping – Potential of a new technique for capturing shallow water bodies”. In: *Proceedings of ModSim’11*. New Zealand. url: <http://www.mssanz.org.au/modsim2011/E14/mandlbuerger.pdf>.
- Mikhail, E. M. [1976]. *Observations And Least Squares*. New York: IEP-A Dun-Donnelley.
- Morsdorf, F., Frey, O., Koetz, B., and Meier, E. [2007]. “Ray Tracing for Modeling of Small Footprint Airborne Laser Scanning Returns”. In: *ISPRS Workshop “Laser Scanning 2007*

- and SilviLaser 2007". *International Archives of the Photogrammetry, Remote Sensing and Spatial Information Sciences 36 (Part 3/W52)*, pp. 294–299. url: [http://www.isprs.org/proceedings/XXXVI/3-W52/final\\_papers/Morsdorf\\_2007.pdf](http://www.isprs.org/proceedings/XXXVI/3-W52/final_papers/Morsdorf_2007.pdf).
- Morsdorf, F., Nichol, C., Malthus, T., and Woodhouse, I. H. [2009]. "Assessing forest structural and physiological information content of multi-spectral LiDAR waveforms by radiative transfer modelling". In: *Remote Sensing of Environment* 113 (10), pp. 2152–2163. issn: 0034-4257. doi: [10.1016/j.rse.2009.05.019](https://doi.org/10.1016/j.rse.2009.05.019).
- Næsset, E. and Gobakken, T. [2005]. "Estimating forest growth using canopy metrics derived from airborne laser scanner data". In: *Remote Sensing of Environment* 96 (3–4), pp. 453–465. doi: [10.1016/j.rse.2005.04.001](https://doi.org/10.1016/j.rse.2005.04.001).
- Nicodemus, F., Richmond, J., Hsia, J., Ginsberg, I., and Limperis, T. [1977]. *Geometrical Considerations and Nomenclature for Reflectance*. National Bureau of Standards Monograph 166. Washington, D.C.: U.S. Department of Commerce, National Bureau of Standards.
- Nothegger, C. and Dorninger, P. [2007]. "Automated Modeling of Surface Detail from Point Clouds of Historical Objects". In: *21st CIPA Symposium, International Archives of the Photogrammetry, Remote Sensing and Spatial Information Sciences 36 (Part 5/C53)*. Athens, Greece, pp. 538–543. url: <http://www.isprs.org/proceedings/xxxvi/5-c53/papers/fp107.pdf>.
- Otepka, J. [2004]. "Precision Target Mensuration in Vision Metrology". PhD thesis. Institute of Photogrammetry and Remote Sensing, Vienna University of Technology. url: <http://media.obvsg.at/p-AC04346920-2001>.
- Otepka, J., Ghuffar, S., Waldhauser, C., Hochreiter, R., and Pfeifer, N. [2013]. "Georeferenced Point Clouds: A Survey of Features and Point Cloud Management". In: *ISPRS International Journal of Geo-Information* 2 (4), pp. 1038–1065. doi: [10.3390/ijgi2041038](https://doi.org/10.3390/ijgi2041038).
- Parrish, C. E. and Nowak, R. D. [2009]. "Improved Approach to Lidar Airport Obstruction Surveying Using Full-Waveform Data". In: *Journal of Engineering Surveying* 135 (2), pp. 72–82. doi: [10.1061/\(ASCE\)0733-9453\(2009\)135:2\(72\)](https://doi.org/10.1061/(ASCE)0733-9453(2009)135:2(72)).
- Parrish, C. E., Jeong, I., Nowak, R. D., and Brent Smith, R. [2011]. "Empirical Comparison of Full-Waveform Lidar Algorithms: Range Extraction and Discrimination Performance". In: *Photogrammetric Engineering & Remote Sensing* 77 (8), pp. 825–838. doi: [10.14358/PERS.77.8.825](https://doi.org/10.14358/PERS.77.8.825).
- Pfennigbauer, M. and Ullrich, A. [2011]. "Multi-Wavelength Airborne Laser Scanning". In: *International Lidar Mapping Forum (ILMF) 2011*. New Orleans, LA, p. 10.
- Pfennigbauer, M., Wolf, C., and Ullrich, A. [2013]. "Enhancing online waveform processing by adding new point attributes". In: *Proc. SPIE 8731, Laser Radar Technology and Applications XVIII*. Baltimore, MD. doi: [10.1117/12.2015733](https://doi.org/10.1117/12.2015733).



- Prautzsch, H., Boehm, W., and Paluszny, M. [2002]. *Bézier and B-Spline Techniques. Mathematics and Visualization*. Berlin Heidelberg: Springer-Verlag, pp. 296 + XIV. isbn: 978-3-642-07842-2. doi: [10.1007/978-3-662-04919-8](https://doi.org/10.1007/978-3-662-04919-8).
- Ressl, C., Pfeifer, N., and Mandlbürger, G. [2011]. “Applying 3D affine transformation and least squares matching for airborne laser scanning strips adjustment without GNSS/INS trajectory data”. In: *International Archives of the Photogrammetry, Remote Sensing and Spatial Information Sciences 38 (Part 5/W12)*. Calgary, Canada. doi: [10.5194/isprsarchives-XXXVIII-5-W12-67-2011](https://doi.org/10.5194/isprsarchives-XXXVIII-5-W12-67-2011).
- Ritter, M. and Benger, W. [2012]. “Reconstructing Power Cables From LIDAR Data Using Eigenvector Streamlines of the Point Distribution Tensor Field”. In: *Journal of WSCG 20*, pp. 223–230. url: [http://wscg.zcu.cz/wscg2012/!\\_2012-Journal-Full-3.pdf](http://wscg.zcu.cz/wscg2012/!_2012-Journal-Full-3.pdf).
- Roncat, A., Wagner, W., Melzer, T., and Ullrich, A. [2008]. “Echo Detection and Localization in Full-Waveform Airborne Laser Scanner Data using the Averaged Square Difference Function Estimator”. In: *The Photogrammetric Journal of Finland 21 (1)*, pp. 62–75. url: [http://foto.hut.fi/seura/julkaisut/pjf/pjf\\_e/2008/Roncat\\_et\\_al\\_2008\\_PJF.pdf](http://foto.hut.fi/seura/julkaisut/pjf/pjf_e/2008/Roncat_et_al_2008_PJF.pdf).
- Roncat, A., Bergauer, G., and Pfeifer, N. [2010]. “Retrieval of the Backscatter Cross-Section in Full-Waveform Lidar Data using B-Splines”. In: *PCV 2010 – ISPRS Technical Commission III Symposium on Photogrammetric Computer Vision and Image Analysis. International Archives of the Photogrammetry, Remote Sensing and Spatial Information Sciences 38 (Part 3B)*. Ed. by N. Paparoditis, M. Pierrot-Deseilligny, C. Mallet, and O. Tournaire, pp. 137–142. url: [http://www.isprs.org/proceedings/XXXVIII/part3/b/pdf/137\\_XXXVIII-part3B.pdf](http://www.isprs.org/proceedings/XXXVIII/part3/b/pdf/137_XXXVIII-part3B.pdf).
- [2011a]. “B-Spline Deconvolution for Differential Target Cross-Section Determination in Full-Waveform Laser Scanner Data”. In: *ISPRS Journal of Photogrammetry and Remote Sensing 66 (4)*, pp. 418–428. doi: [10.1016/j.isprsjprs.2011.02.002](https://doi.org/10.1016/j.isprsjprs.2011.02.002).
- Roncat, A., Lehner, H., and Briese, C. [2011b]. “Laser Pulse Variations and their Influence on radiometric Calibration of Full-Waveform Laser Scanner Data”. In: *ISPRS Workshop Laser Scanning 2011. International Archives of the Photogrammetry, Remote Sensing and Spatial Information Sciences 38 (Part 5/W12)*. Ed. by D. D. Lichti and A. F. Habib, pp. 137–142. doi: [10.5194/isprsarchives-XXXVIII-5-W12-37-2011](https://doi.org/10.5194/isprsarchives-XXXVIII-5-W12-37-2011).
- Roncat, A., Pfeifer, N., and Briese, C. [2012]. “A linear approach for radiometric calibration of full-waveform Lidar data”. In: *Proc. SPIE 8537, Image and Signal Processing for Remote Sensing XVIII*. doi: [10.1117/12.970305](https://doi.org/10.1117/12.970305).
- Roncat, A., Wieser, M., Briese, C., Bollmann, E., Sailer, R., Klug, C., and Pfeifer, N. [2013]. “Analysing the suitability of radiometrically calibrated full-waveform lidar data for delineating Alpine rock glaciers”. In: *ISPRS Workshop Laser Scanning 2013. ISPRS Annals of the Photogrammetry, Remote Sensing and Spatial Information Sciences 2 (Part 5/W2)*. Ed. by M. Scaioni, R. C. Lindenbergh, S. O. Elberink, D. Schneider, and

- F. Pirotti. Antalya, Turkey, pp. 247–252. doi: [10.5194/isprsannals-II-5-W2-247-2013](https://doi.org/10.5194/isprsannals-II-5-W2-247-2013).
- Roncat, A., Morsdorf, F., Briese, C., Wagner, W., and Pfeifer, N. [2014a]. “Laser Pulse Interaction with Forest Canopy: Geometric and Radiometric Issues”. In: *Forestry Applications of Airborne Laser Scanning – Concepts and Case Studies*. Vol. 27. Ed. by M. Maltamo, E. Næsset, and J. Vauhkonen. Managing Forest Ecosystems. Dordrecht, The Netherlands: Springer Netherlands. Chap. 2, pp. 19–41. isbn: 978-94-017-8662-1. doi: [10.1007/978-94-017-8663-8\\_2](https://doi.org/10.1007/978-94-017-8663-8_2).
- Roncat, A., Briese, C., Jansa, J., and Pfeifer, N. [2014b]. “Radiometrically Calibrated Features of Full-Waveform Lidar Point Clouds based on Statistical Moments”. In: *IEEE Geoscience and Remote Sensing Letters* 11 (2), pp. 549–553. doi: [10.1109/LGRS.2013.2274557](https://doi.org/10.1109/LGRS.2013.2274557).
- Schaepman-Strub, G., Schaepman, M., Painter, T., Dangel, S., and Martonchik, J. [2006]. “Reflectance quantities in optical remote sensing—definitions and case studies”. In: *Remote Sensing of Environment* 103 (1), pp. 27–42. issn: 0034-4257. doi: [10.1016/j.rse.2006.03.002](https://doi.org/10.1016/j.rse.2006.03.002).
- Schanda, E. [1986]. *Physical Foundations of Remote Sensing*. Berlin Heidelberg New York Tokyo: Springer-Verlag, pp. 187+X. isbn: 3-540-16236-4.
- Schmitt, O. H. [1938]. “A thermionic trigger”. In: *Journal of Scientific Instruments* 15 (1), pp. 24–26. doi: [10.1088/0950-7671/15/1/305](https://doi.org/10.1088/0950-7671/15/1/305).
- Shan, J. and Toth, C. K., eds. [2008]. *Topographic Laser Ranging and Scanning: Principles and Processing*. Boca Raton, FL: CRC Press, p. 590. isbn: 1-42005-142-3.
- Steinvall, O. [2000]. “Effects of Target Shape and Reflection on Laser Radar Cross Sections”. In: *Applied Optics* 39 (24), pp. 4381–4391. doi: [10.1364/AO.39.004381](https://doi.org/10.1364/AO.39.004381).
- Stilla, U. and Jutzi, B. [2008]. “Waveform Analysis for Small-Footprint Pulsed Laser Systems”. In: *Topographic Laser Ranging and Scanning: Principles and Processing*. Ed. by J. Shan and C. K. Toth. Boca Raton, FL: CRC Press. Chap. 5, pp. 215–234. isbn: 1-42005-142-3.
- Tikhonov, A. N. and Arsenin, V. Y. [1977]. *Solutions of ill-posed Problems*. Scripta Seris in Mathematics. Washington, D.C.: V. H. Winston & Sons, pp. 259+XIV. isbn: 0-470-99124-0.
- Ullrich, A. and Pfennigbauer, M. [2011]. “Categorisation of Full Waveform Data Provided by Laser Scanning Devices”. In: *Proc. of SPIE Vol. 8186, Electro-Optical Remote Sensing, Photonic Technologies, and Applications*. Ed. by G. W. Kamerman, O. Steinvall, K. L. Lewis, G. J. Bishop, and J. D. Gonglewski. doi: [10.1117/12.898490](https://doi.org/10.1117/12.898490).
- Wagner, W. [2010]. “Radiometric calibration of small-footprint full-waveform airborne laser scanner measurements: Basic physical concepts”. In: *ISPRS Journal of Photogram-*

- metry and Remote Sensing* 65 (6, ISPRS Centenary Celebration Issue), pp. 505–513. doi: [10.1016/j.isprsjprs.2010.06.007](https://doi.org/10.1016/j.isprsjprs.2010.06.007).
- Wagner, W., Briese, C., and Ullrich, A. [2003]. “Der Laserstrahl und seine Interaktion mit der Erdoberfläche”. In: *VGI, Österreichische Zeitschrift für Vermessung & Geoinformation* 91 (4), pp. 223–242.
- Wagner, W., Ullrich, A., Melzer, T., Briese, C., and Kraus, K. [2004]. “From Single-Pulse to Full-Waveform airborne laser scanners: potential and practical challenges”. In: *International Archives of the Photogrammetry, Remote Sensing and Spatial Information Sciences* 35 (Part B3). Istanbul, Turkey, pp. 201–206. url: <http://www.isprs.org/proceedings/XXXV/congress/comm3/papers/267.pdf>.
- Wagner, W., Ullrich, A., Ducic, V., Melzer, T., and Studnicka, N. [2006]. “Gaussian decomposition and calibration of a novel small-footprint full-waveform digitising airborne laser scanner”. In: *ISPRS Journal of Photogrammetry and Remote Sensing* 60 (2), pp. 100–112. doi: [10.1016/j.isprsjprs.2005.12.001](https://doi.org/10.1016/j.isprsjprs.2005.12.001).
- Wagner, W., Roncat, A., Melzer, T., and Ullrich, A. [2007]. “Waveform Analysis Techniques in Airborne Laser Scanning”. In: *ISPRS Workshop “Laser Scanning 2007 and SilviLaser 2007”*. *International Archives of the Photogrammetry, Remote Sensing and Spatial Information Sciences* 36 (Part 3/W52). Ed. by P. Rönholm, H. Hyypä, and J. Hyypä, pp. 413–418. url: [http://www.isprs.org/proceedings/XXXVI/3-W52/final\\_papers/Wagner\\_2007\\_keynote.pdf](http://www.isprs.org/proceedings/XXXVI/3-W52/final_papers/Wagner_2007_keynote.pdf).
- Wagner, W., Hollaus, M., Briese, C., and Ducic, V. [2008]. “3D vegetation mapping using small-footprint full-waveform airborne laser scanners”. In: *International Journal of Remote Sensing* 29 (5), pp. 1433–1452. doi: [10.1080/01431160701736398](https://doi.org/10.1080/01431160701736398).
- Wallner, J. [2010]. “Computer Aided Geometric Design”. Lecture Notes. Institute of Discrete Mathematics and Geometry, Vienna University of Technology.
- Wang, Y., Zhang, J., Roncat, A., Künzer, C., and Wagner, W. [2009]. “Regularizing method for the determination of the backscatter cross section in lidar data”. In: *Journal of the Optical Society of America A* 26 (5), pp. 1071–1079. doi: [10.1364/JOSAA.26.001071](https://doi.org/10.1364/JOSAA.26.001071).
- Woodhouse, I. H. [2006]. *Introduction to Microwave Remote Sensing*. Boca Raton, FL: CRC Press, pp. 370+xxiv. isbn: 0-415-27123-1.
- Wunderlich, W. [1966]. *Darstellende Geometrie I*. Hochschultaschenbücher für den Ingenieur. Mannheim, Germany: Bibliographisches Institut, p. 187.
- Zhou, G., Song, C., Simmers, J., and Cheng, P. [2004]. “Urban 3D GIS From LiDAR and digital aerial images”. In: *Computers & Geosciences* 30 (4), pp. 345–353. issn: 0098-3004. doi: [10.1016/j.cageo.2003.08.012](https://doi.org/10.1016/j.cageo.2003.08.012).

# WWW References

- ASPRS [2014]. *LAS File Format Exchange Activities*. Homepage of ASPRS LAS file format. Last accessed: June 2014. url: <http://www.asprs.org/Committee-General/LASer-LAS-File-Format-Exchange-Activities.html>.
- ISO [2006]. *ISO 11145:2006. Optics and photonics – Lasers and laser-related equipment – Vocabulary and symbols*. url: [http://www.iso.org/iso/home/store/catalogue\\_tc/catalogue\\_detail.htm?csnumber=43006](http://www.iso.org/iso/home/store/catalogue_tc/catalogue_detail.htm?csnumber=43006).
- Leica Geosystems [2014]. *Homepage of the company Leica Geosystems*. Last accessed: June 2014. url: [www.leica-geosystems.com](http://www.leica-geosystems.com).
- Optech Inc. [2014]. *Homepage of the company Optech Inc.* Last accessed: June 2014. url: [www.optech.ca](http://www.optech.ca).
- PulseWaves [2014]. *PulseWaves – no pulse left behind. Homepage of PulseWaves file format*. Last accessed: June 2014. url: [www.pulsegwaves.org](http://www.pulsegwaves.org).
- Riegl LMS [2014]. *Homepage of the company RIEGL Laser Measurement Systems GmbH*. Last accessed: June 2014. url: [www.riegl.com](http://www.riegl.com).
- Weisstein, E. W. [2014a]. *Convolution*. From MathWorld–A Wolfram Web Resource. Last accessed: June 2014. url: <http://mathworld.wolfram.com/Convolution.html>.
- [2014b]. *Convolution Theorem*. From MathWorld–A Wolfram Web Resource. Last accessed: June 2014. url: <http://mathworld.wolfram.com/ConvolutionTheorem.html>.
- Zorin, D. and Schröder, P. [2000]. *Subdivision for Modeling and Animation*. SIGGRAPH 2000 Course Notes. url: <http://www.multires.caltech.edu/pubs/sig00notes.pdf>.